

Preface – The ‘Gatekeeper’ of Express Polymer Letters is 65

T. Czigány*

Department of Polymer Engineering, Faculty of Mechanical Engineering, Budapest University of Technology and Economics, Műegyetem rkp. 3., H-1111 Budapest, Hungary

Dear Readers,

The 2015 March issue of *eXPRESS Polymer Letters* is dedicated to our editor in chief, Prof. Dr. Dr. h.c. József Karger-Kocsis on the occasion of his 65th birthday. This is the 99th issue of this journal, and to its appearance credit should be given to professor Karger-Kocsis. His genius consistence, his strict standards in quality were guaranties of the continuous development of the journal. The gatekeeper supervises which papers may even enter the gates and from those which will be published in the end. The legendary devotion of professor Karger-Kocsis to everything belonging to his profession raised *eXPRESS Polymer Letters* to the level of best journals and made it reputable all over the world.

Professor Karger-Kocsis was born in March 1950 in Budapest, received his diploma from the Faculty of Chemical Engineering of the Budapest Technical University. He received his Dr. techn. in 1977, became candidate in science in 1983 and the acquired the DSc degree of the Hungarian Academy of Science in 1991. He worked in the industry and in an industrial research institute. Then he was granted a Humboldt Research Fellowship and worked afterwards at the TU Hamburg-Harburg, at the Institute of Composite Materials of the TU Kaiserslautern in Germany, and at the Tshwane University of Technology in South Africa. At present, he is a professor of the Department of Polymer Engineering of the Faculty of Mechanical Engineering at the Budapest University of Technology and Economics and he is also a member of the Composite Technology Research Group of the Hungarian

Academy of Science. His main research interest covers the improvement of the properties of polymers and their composites, their testing and applications; development of material testing methods; investigation of matrix/reinforcement interfacial interactions and utilization of plastics and rubber wastes. The quality of his research is shown by the fact that he is the author of more than 500 publications (books, book chapters, journal articles and conference proceedings). His cumulative impact factor is at about 500, and his number of independent citations is close to 10 000. He has

more than 30 patents, several of them being used by the industry. Professor Karger-Kocsis is an internationally renowned scientist, who, in addition to his Hungarian mother tongue, is fluent in six further languages. He established his own school, having dozens of PhD students who inherited his specific professional world-view and propagated it all over the world. Recognizing his work, the Novofer Foundation hon-



ored him with the Dennis Gábor prize – 2014 which was handed over in the Parliament by the president of the Hungarian Academy of Sciences and the curator of the Novofer Foundation (see the photo).

The authors of this issue are professor Karger-Kocsis' friends, present and former colleagues, and students, who selected topics representing the main research fields belonging to professor Karger-Kocsis.

With this issue, in the name of the authors and the scientific community, I would like to express my best wishes to professor Karger-Kocsis on his birthday.

Prof. Dr. Tibor Czigány
editor (one of the disciples)

*Corresponding author, e-mail: czigany@eik.bme.hu
© BME-PT

Solid particle erosion and viscoelastic properties of thermoplastic polyurethanes

G. Arena¹, K. Friedrich^{2*}, D. Acierno³, E. Padenko², P. Russo⁴, G. Filippone^{1,3}, J. Wagner⁵

¹Department of Chemical, Materials and Production Engineering, University of Naples Federico II, P.le Vincenzo Tecchio 80, 80125 Naples, Italy

²Institute for Composite Materials (IVW GmbH), Technical University of Kaiserslautern, 67663 Kaiserslautern, Germany

³INSTM – Reference Centre for Processing Technologies of Polymer and Composites, University of Naples Federico II, P.le V. Tecchio 80, 80125 Naples, Italy

⁴Institute for Polymers, Composites and Biomaterials, National Council of Research, Via Campi Flegrei 34, 80078 Pozzuoli, Naples, Italy

⁵Bayer MaterialScience Aktiengesellschaft, BMS-CAS-SB-SF-SP, Leverkusen, Germany

Received 15 September 2014; accepted in revised form 31 October 2014

Abstract. The wear resistance of several thermoplastic polyurethanes (TPUs) having different chemical nature and micron-scale arrangement of the hard and soft segments has been investigated by means of erosion and abrasion tests. The goal was correlating the erosion performances of the materials to their macroscopic mechanical properties. Unlike conventional tests, such as hardness and tensile measurements, viscoelastic analysis proved to be a valuable tool to study the erosion resistance of TPUs. In particular, a strict correlation was found between the erosion rate and the high-frequency ($\sim 10^7$ Hz) loss modulus. The latter reflects the actual ability of TPU to dissipate the impact energy of the erodent particles.

Keywords: damage mechanism, solid particle erosion, thermoplastic polyurethanes, wear, material testing

1. Introduction

Erosion is a dynamic process that causes material removal from a target solid surface. The most severe erosion case is that occurring as a consequence of the impingement of solid particles, having a high momentum and, in particular, a very high velocity. This process causes wear of materials, surface degradations and reduction in functional life of the structural components. As pointed out by Barkoula and Karger-Kocsis [1], solid particle erosion, similarly to other tribological processes, is a combined process: the mechanical load may be associated with secondary thermal, chemical and physical phenomena between the counterparts involved in the tribological system.

The classification of various materials with reference to their erosive wear shows remarkably differences, particularly when the variation in the impact-angle and impact-time is taken into account. The mechanisms can be categorized as ductile and brittle. The ductile erosion may involve an incubation period whereby the mass of the target initially increases, and then sets down to a steady state condition; for normal impacts, the latter is due to an early embedding of particles in the relatively soft target surface [2]. It is also known that in ductile mode the maximum material removal occurs at low impingement angles, whereas this maximum is found at high impingement angles when brittle erosion dominates. Fiber reinforced polymers are con-

*Corresponding author, e-mail: klaus.friedrich@ivw.uni-kl.de
© BME-PT

sidered as having a semi-ductile erosion behaviour, for which the maximum is at an angle between ca. 45 to 60° [3, 4].

Polymer-based materials can be profitably used as coating of components subjected to erosion as they provide them with a high impact absorbing ability [5–7]. Among other polymers, thermoplastic polyurethanes (TPUs) have attracted a significant attention in this respect, due to their good processability and unique properties deriving from their peculiar molecular structure. TPUs are multiphase block copolymers characterized by a sequence of hard and soft blocks having glass transition temperature (T_g) and melting point (T_m) well below and well above the room temperature, respectively [8]. Due to these unique features, TPU exhibits high impact absorbing ability and, at the same time, a sufficiently high modulus. This makes TPUs suitable for protective coating or films with minimal erosive wear, which can strongly limit the consequences of erosion processes in environments where high-speed particles may hit surfaces [9].

The amount of material removal during erosion depends on many interrelated factors, which include the properties and structures of the target material as well as the physical and chemical characteristics of the erodent particles. The difficulty to control and model so many factors and processes makes the tribological system generally complex. This aspect appears even more pronounced for coating made of TPUs. Several attempts have been done in the last years aimed at correlating their performances with their morphological and mechanical features, but there is a lack of general agreement in the role played by the various parameters involved [1]. The T_g , in terms of both its absolute value and its relative position with respect to the operating temperature, certainly affects the erosion rate. In addition, molecular and morphological parameters, such as presence of crosslinks, relative content of hard and soft phase, and degree of phase separation between soft and hard segments (that in turn depends on the molecular weight of the elastomer and its chemical composition) have a strong influence on the erosion behaviour [9, 10]. Besides, macroscopic mechanical features affect the solid particle erosion resistance. In particular, a correlation was found between the erosion resistance and the rebound resilience, defined as the absorbed amount of initial energy of the impact particles [11]. Viscoelasticity was consid-

ered to be important as well. Comparing different kinds of elastomers Slikkerveer *et al.* [6] concluded that polymers having a pronounced ‘rubber-like’ behaviour generally exhibit a better erosion resistance. Generally speaking, softer elastomers usually show a better solid particle erosion resistance because of less crack propagation and more elastic/plastic deformation [9], while harder TPU’s systems normally exhibit higher wear resistance [12].

To resume, although some interesting trends have emerged about the effects of different factors influencing polyurethanes erosion, identifying general trends and relationships remains an ambitious challenge. A serious attempt in this direction has been recently done by Cizmas and Slattery [13], who proposed a dimensionless elastic modulus to rationalize the results by Li and Hutchings [14] on a series of polyurethanes. This study aims for the same goal, that is looking for general relationships between the erosion behavior and the main properties of different kinds of TPUs. In particular, the sand erosion of seven commercial grade TPUs has been investigated at different impingement angles. Before erosion testing, the materials were thoroughly characterized by means of different techniques, including their microstructural analysis and their dynamic-mechanical properties. This resulted finally in a clear relationship between the erosion mass loss and the viscoelastic properties, in particular with the loss flexural modulus E'' (provided the latter was estimated on the proper timescale).

2. Experimental

2.1. Raw materials and preliminary characterization

Seven different TPUs, all produced by Bayer MaterialScience AG and commercialized with the trade name of DESMOPAN[®], were examined in this study. The pure materials were subjected to a preliminary characterization, whose results are summarized in Table 1.

2.2. Microstructural analyses

Transmission electron microscopy (TEM) analysis was carried out using a Philips EM 208S TEM apparatus. In details, after embedding in acrylic resin, small pieces of samples, pre-conditioned at 120°C for 72 h, were trimmed into pyramidal shapes. Ultra-thin sections (60 nm thick), obtained using a Reichert-Jung ultramicrotome fitted with a diamond

Table 1. Main TPU properties

Code name	Grade name	Chemical basis ¹	Density ² [g/cm ³]	Hardness ³ [Shore A]	Elastic modulus ⁴ [MPa]	Tensile stress ⁴ [MPa]	Deformation at break ⁴ [%]	Degradation temperature ⁵ [°C]	T _g (soft segments) ⁶ [°C]
TPU 1	9385A	ether	1.12	86	27.8±1	47.9±3	773.3±17	292	-50
TPU 2	487	ester	1.20	85	23.2±3	55.9±5	633.2±34	304	-41
TPU 3	385S	ester	1.21	84	25.4±0.2	43.3±8	691.6±61	300	-42
TPU 4	DP2587A	ester	1.19	86	29.3±3	60.4±5	737.0±24	300	-43
TPU 5	DP1085A	ester	1.20	83	23.5±2	44.9±1	857.6±8	286	-42
TPU 6	1089A	ester	1.20	88	43.6±0.4	54.0±3	710.7±20	292	-40
TPU 7	786E	carbonate	1.15	86	28.8±3	35.6±1	647.5±10	282	-36

¹According to producers. ²From technical datasheet. ³Measured through hardness Shore A. ⁴Measured from tensile tests. ⁵Measured through TGA analyses. ⁶Measured through DSC analyses.

knife, were placed on a copper grid and stained with uranyl acetate and lead citrate which preferentially dyes the soft segments [15].

Small angle X-ray scattering (SAXS) analyses were performed using a SAXSess diffractometer (Anton Paar, Austria) equipped with a CuK_α radiation source ($\lambda = 0.1542$ nm). The spectra were collected at 30°C in transmission. The average distance between contiguous soft phase domains (d_i) was estimated from the angular location of the maximum intensity peak in the scattering curve, according to the Bragg's law.

Further, a scanning electron microscope (SEM; JSM 5400 of Jeol, Tokyo, Japan) was used to analyze the surface of the TPUs before and after erosion. Prior to SEM, the specimens were sputtered with a thin Pt/Pd alloy layer in a Balzers SCD-050 (Balzers, Liechtenstein) sputtering device for 150 s.

2.3. Viscoelastic analysis

Linear viscoelastic analyses were carried out using a dynamic mechanical analyser Metravib DMA + 1000 (ACOEM Group, France). The frequency dependent storage (E') and loss (E'') flexural moduli were evaluated in three-point bending mode by imposing a static stress of 10^5 N/m² and a dynamic stress of $5 \cdot 10^4$ N/m². For each sample the tests were performed in a frequency range ω between 1 and 50 Hz, at temperatures from -50 to 50°C, i.e. a temperature range within which the glass transition of the amorphous soft phase of the different TPUs took place. The time-temperature superposition principle (TTS) was then used to generate master curves of E' and E'' in a broad frequency range. As reference temperature, $T = 25^\circ\text{C}$ was chosen.

2.4. Solid particle erosion tests

The erosive wear tests were conducted within a sand-blasting type facility (ST 800, Paul Auer GmbH, Mannheim, Germany) [7]. The erodent particles were driven and accelerated by compressed air, exiting from a steel nozzle (length 66 mm, diameter 10 mm) and impacting on the sample surface. The measurements were done according to the ASTM G76-83 standard [16].

The erodent particles utilized for the tests were angular grainy grit quartz sand F36, having different shape and a wide size range (125–355 μm). The average velocity of the particles, determined by using the double disc method [17] amounted to ~ 160 m/s. All the specimen were impacted in the erosive wear chamber at room temperature. A fixed area of 20 mm in diameter was exposed to a sand flow rate of 6.45 g/min at different impact angles in a range between 15 and 90°. The angle 0° could not be reliably determined, so that it was not further tested. The mass loss of the samples after erosion (Δm) was measured through a precision balance (AT261 Mettler Toledo, United States), and then related to the mass of erodent (m_E), leading to the erosion rate $\Delta m/m_E$.

2.5. Abrasion tests

For comparison purposes, the low velocity abrasion behaviour of the samples was also investigated by means of a custom-built scratch machine (Surface Machine Systems, LLC, Texas, USA). A square sample (5×5 mm²) was scratched in the y -direction against an abrasive SiC – paper P180 (average particle diameter 82 μm). The normal load was 12.5 N (equivalent to a nominal pressure of 0.5 MPa), and

the velocity amounted to 1 mm/s. The sample changes its x -position after each cycle to always meet a fresh portion of abrasive paper.

3. Results

3.1. Microstructural analyses

TEM analyses were carried out with the aim to identify the space arrangement of the soft and hard phases in the selected TPUs. Some representative micrographs are reported in Figure 1.

The bright and dark regions represent the hard and soft domains, respectively. The samples differ in terms of relative amounts and space arrangement of the phases. Both drop-matrix (Figure 1a and 1d) and co-continuous (Figure 1b and 1c) morphologies can be recognized: in the former, isolated domains (dark) of the soft phase are suspended in the hard matrix (bright); in the latter, the phases are both continuous and appear interpenetrated. Further quantitative information can be collected through SAXS analy-

sis, which is often employed when dealing with polyurethane systems [8, 18]. The one-dimensional SAXS patterns of intensity $I(q)$ vs. q of the various TPUs are shown in Figure 2.

An intensity maximum in the scattering curve indicates a phase separated morphology. The peak intensity is particularly high for the samples TPU 1 and TPU 7, which clearly exhibit a drop-matrix morphology. Less intensive and broader peaks are instead

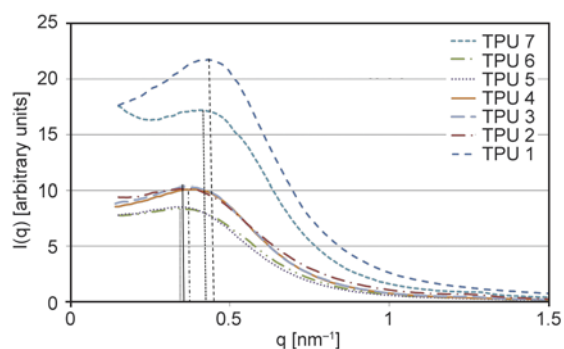


Figure 2. SAXS patterns of the TPUs

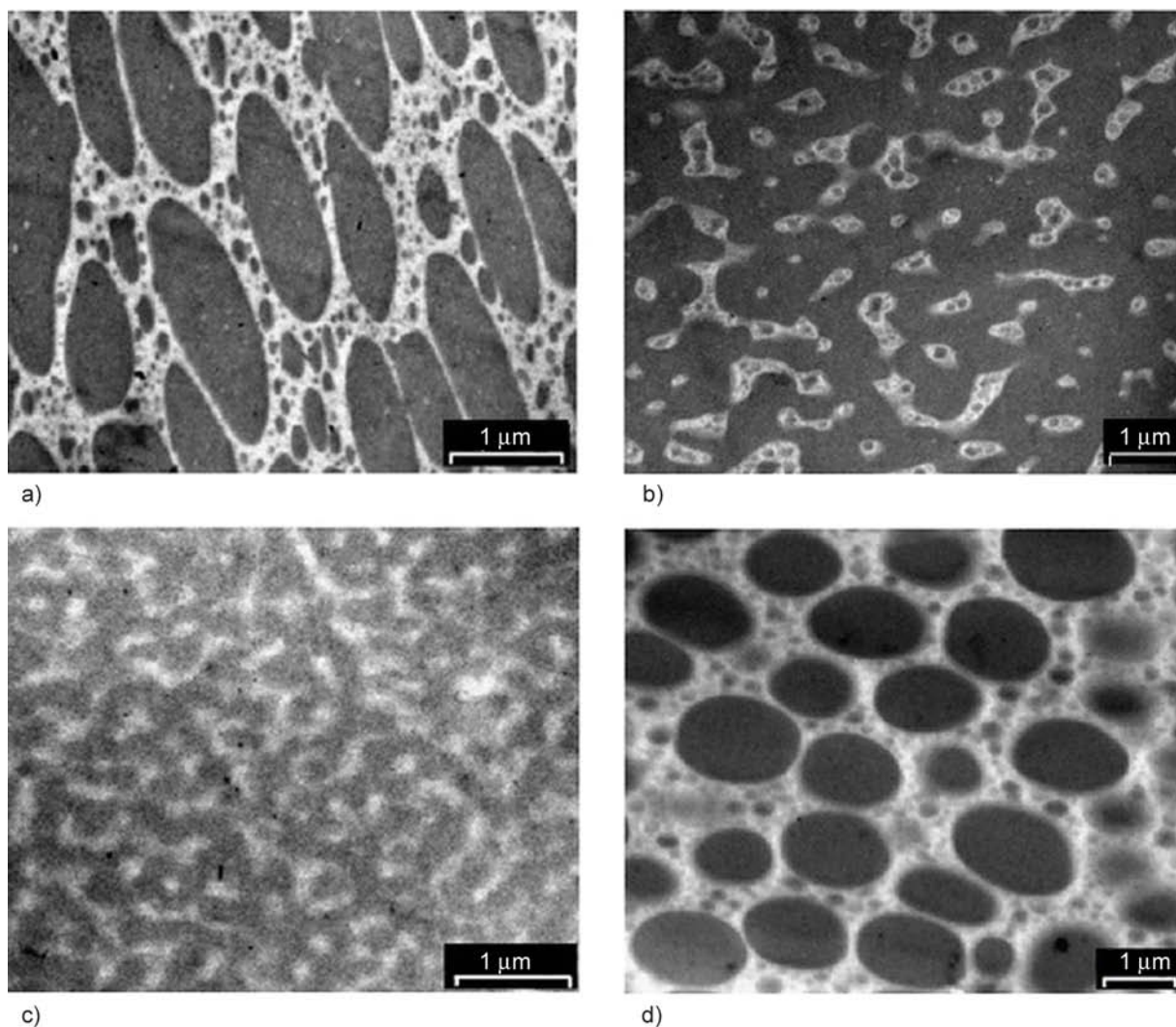


Figure 1. TEM images of TPU 1 (a), TPU 3 (b), TPU 6 (c), and TPU 7 (d)

Table 2. Average inter-domain distance computed from the SAXS spectra

	TPU 1	TPU 2	TPU 3	TPU 4	TPU 5	TPU 6	TPU 7
q_{\max} [nm ⁻¹]	0.43	0.37	0.35	0.39	0.33	0.33	0.40
d_i [nm]	14.54	16.92	17.78	16.25	18.82	18.82	15.66

noticed for the other samples, suggesting more homogeneous structures in which ordered crystalline and/or para-crystalline hard domains appear randomly dispersed in a continuous soft matrix. An approximate estimate of the average inter-domain distance can be inferred from the position of the intensity peak [18]. The data, computed by means of the Bragg's law, are listed in Table 2.

All the samples exhibit phase separation at nanoscale in addition to the superimposed morphology in larger lateral scale as depicted in the TEM-pictures, so that the d_i – data cannot be correlated directly to any features seen on the low magnification TEM pictures. The samples TPU 1 and TPU 7, i.e. those with a drop-matrix morphology, possess slightly smaller inter-domain spacing.

In general, the TEM and SAXS results reveal significant microstructural differences among the commercial TPU samples investigated, which are also reflected in a different macroscopic response of the materials, as shown in Table 1.

3.2. Viscoelastic behavior

Viscoelastic analysis is a powerful tool to collect mechanical information in a wide range of time-scale or, alternatively, over different length scales. The time-temperature equivalence was exploited to enlarge the experimental time window. An example of the output of a series of viscoelastic tests is shown in Figure 3, where E' and the loss factor $\tan \delta$ of the sample TPU 4 are shown as a function of frequency and temperature.

Invoking the time-temperature superposition principle, the frequency dependence of the viscoelastic moduli was estimated in a wide range of frequency. In particular, the very short timescale involved in the erosion phenomenon produced by high momentum particles suggested to focus on the high-frequency viscoelastic behaviour, which was probed

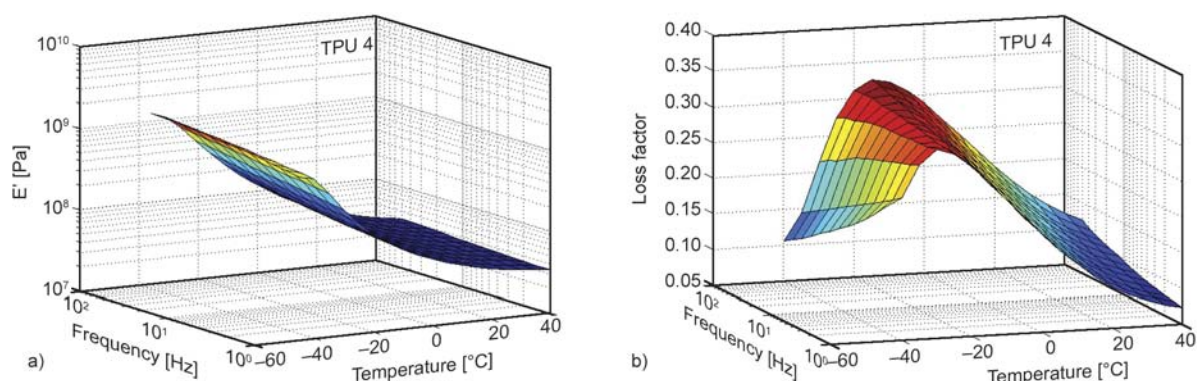


Figure 3. E' (a) and $\tan \delta$ (b) as function of temperature and frequency for the sample TPU 4

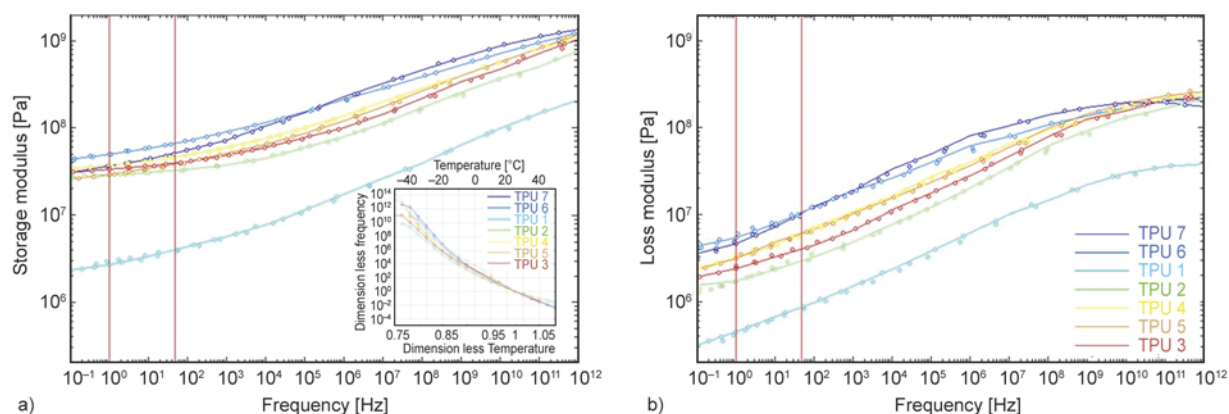


Figure 4. Master curves of E' (a) and for E'' (b) for the various TPUs. The reference curves at $T_{\text{ref}} = 25^\circ\text{C}$ are highlighted. The T -dependence of the shift factors aT are shown in the inset.

by performing low-temperature tests. The master curves of E' and E'' are shown in Figure 4 for the various TPUs. The reference temperature was $T_{\text{ref}} = 25^\circ\text{C}$, that is the temperature at which erosion and abrasion tests were performed.

Although the curves cross each other in several points, the materials essentially share the same overall behaviour, whereby both moduli generally increase with frequency, denoting a typical viscoelastic behaviour. More precisely, the samples exhibit a predominant elastic feature, E' being much higher than E'' in the whole range of frequencies investigated. However, only the polycarbonate-based sample TPU 7 starts losing its viscous feature at $\sim 10^{10}\text{Hz}$, where E'' exhibits a maximum. Moreover, it is interesting to notice that the polyether-based sample TPU 1 differs from the others because of its relatively low moduli, which is probably due to a higher flexibility of the ether bonds in comparison with the ester and carbonate bonds of the other samples.

3.3. Solid particle erosion

Solid particle erosion tests have been carried out for about 30 minutes at a value of particle impact velocity of 160 m/s. Previous studies [7, 19] have shown that the wear rate does not change appreciably above values of the impingement angle $\alpha > 45^\circ$. This can be explained by the partial embedding of the eroding silica particles into the sample, which is mostly pronounced at normal angles of impact [7]. As a consequence, the erosion tests were performed at values of α ranging from 15 to 45° . Corresponding results are shown in Figure 5.

The maximum erosion rate was found at $\alpha = 15^\circ$, and it is assumed that it will still slightly increase with angles lower than 15° . This suggests that the

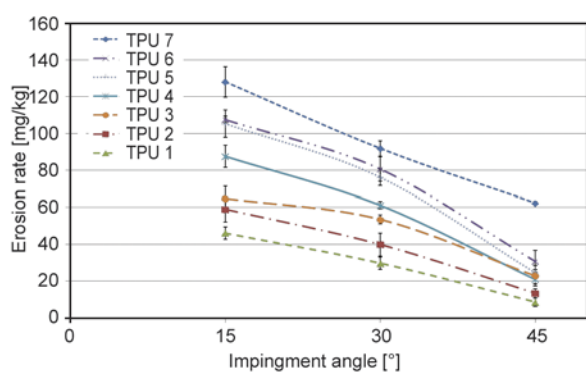


Figure 5. Erosive wear rate of TPUs as function of impingement angle. The points are average values of three independent tests.

thermoplastic elastomers possess the lowest erosion resistance when the impingement conditions are similar to that of surface abrasion. Among the different TPUs, the polyether-based TPU 1 showed the lowest erosion rate, whereas the polycarbonate system TPU 7 exhibited the poorest erosion behaviour. The erosion rate of the various polyester-based TPUs ranged in between these two extremes.

When considering the appearance of the surfaces at the end of the tests, in the initial stage of the erosion process some particles were embedded. Once a steady state condition was reached, small cracks and a high degree of plastic deformation occurred. During the initial stage, also ridges were formed, and in the successive steps the particles impacting the surface deformed these ridges and caused some cracks normal to the erosion direction. The latter started to grow at the ridge bases. In this way, the cyclic impact caused a fatigue crack growth, with cracks intersecting to each other and causing material removal [9, 19, 20]. All these features can be found on the SEM micrographs of the worn surfaces, in this case for material TPU 4, at three different values of α (Figure 6). The micro-cracks and plastic deformations caused by the erosion are similar for all the impingement angles, being more intense at $\alpha = 15^\circ$. Fracture and chipping off over the surface are ascribed to the succession of impacts, which gradually increase the strain until the removal of the material.

SEM micrographs of the surfaces of the samples TPU 1 and 7 after erosion test at $\alpha = 45^\circ$ are shown in Figure 7. Cracks, ridges and debris are visible over all the eroded surfaces. Micro-tearing and micro-cracks under the surface, caused by the cyclic impact of silica sand, can also be observed. The worn surface of TPU 1 mainly shows plastic deformation, with a rather limited presence of cracks and debris in comparison to TPU 7. In particular, TPU 7 shows the mostly damaged surface after erosion. This is consistent with the low erosion resistance exhibited by this sample (see Figure 5).

3.4. Abrasion tests

The results of the abrasion tests are reported in Figure 8 in comparison to the erosion mass loss data at 15° .

It is noteworthy that the TPU resistances to erosive and abrasive wear approximately follow the same trend. This confirms that, especially when the abra-

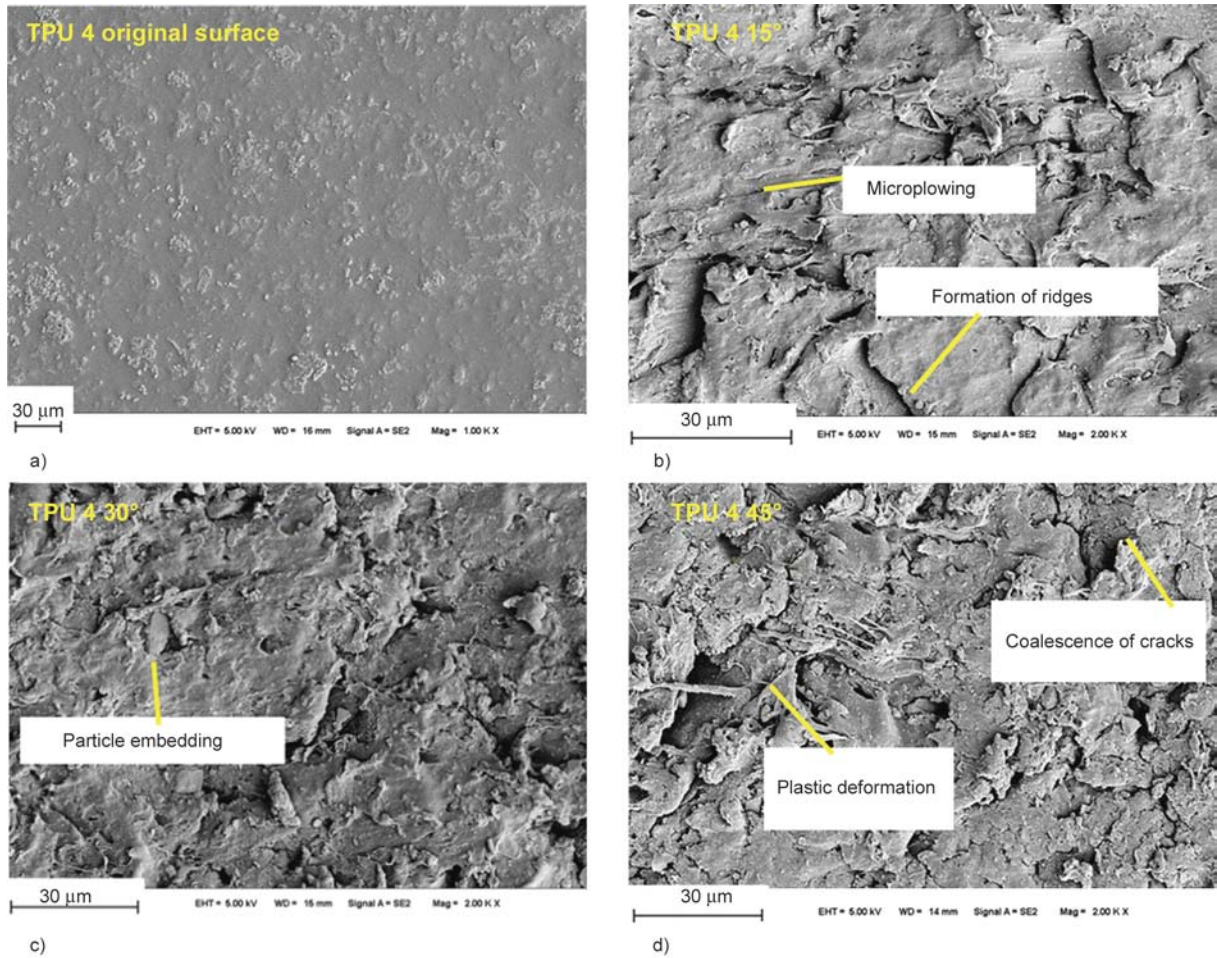


Figure 6. SEM micrographs showing the surface of the sample TPU 4 before (a) and after erosion tests at $\alpha = 15^\circ$ (b), $\alpha = 30^\circ$ (c) and $\alpha = 45^\circ$ (d)

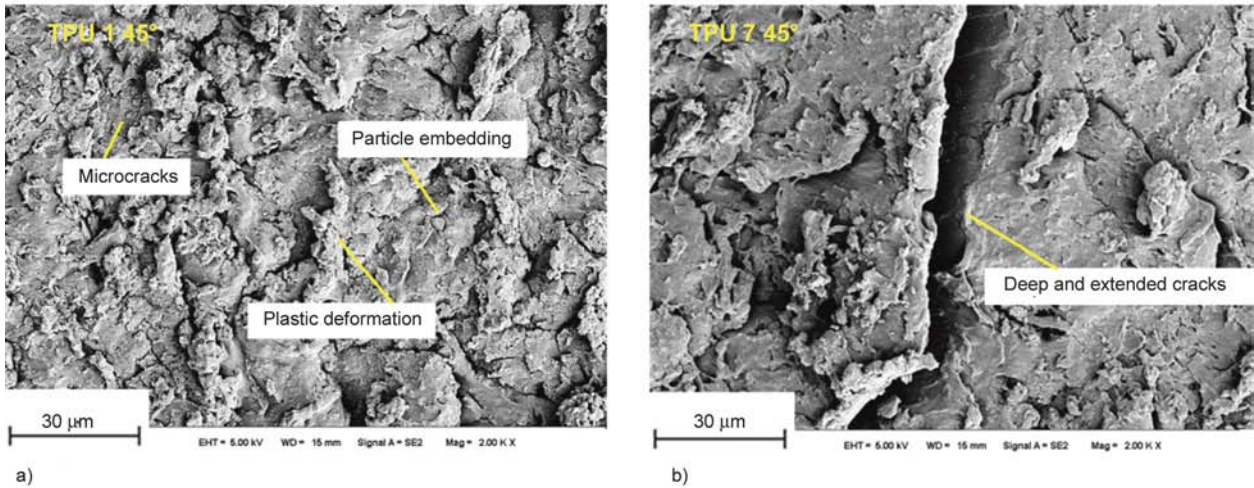


Figure 7. Surfaces of the sample TPU 1 (a) and TPU 7 (b), after erosion tests at $\alpha = 45^\circ$

sive wear is compared with the erosion at glancing impingement angles, the resistances against removal of material are quite similar.

The SEM images of TPU 2 and TPU 7 after abrasion testing are compared in Figure 9. Both samples

exhibit long ploughed furrows. The lower abrasive wear resistance of sample TPU 7 is reflected in larger fragments before final removal from the specimen surface.

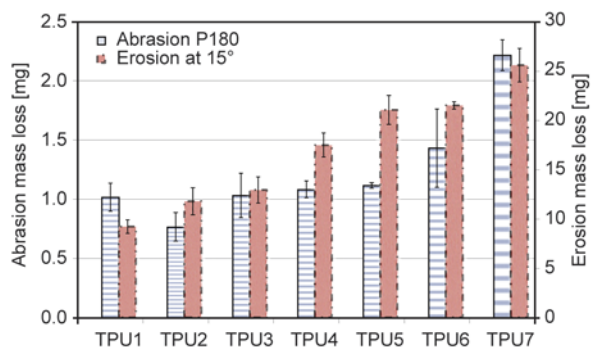


Figure 8. Comparison between the mass loss showed by the selected TPUs during erosion tests at $\alpha = 15^\circ$ for 31 min (red columns) and abrasion tests on 500 mm of P180 abrasive paper (blue columns)

4. Discussion

4.1. Comparison between mechanical properties, microstructural details and erosion rate

When comparing the erosion rates of the TPU samples, represented by their value under 30° impact angle (see Figure 5) with the mechanical properties, as listed in Table 1, no direct correlation in the trends can be found (Figure 10). This means that only a complex combination of various properties, as it has been proposed in some previous papers for a comparison of a broad variety of different polymers, e.g. [2], could help. In the present case, however, only one specific class of polymers (TPU) with slightly different chemical composition is compared, whereby all of the polymers in this class are generally very resistant against erosion. Therefore a correlation approach as mentioned above seems to be not successful at all.

Another approach to correlate the erosive wear rates with differences in the microstructural details

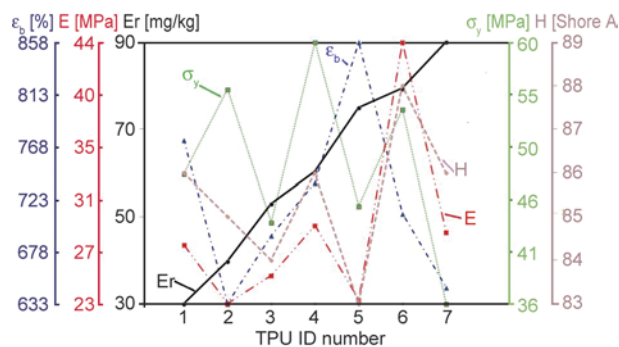


Figure 10. Comparison between erosion rate (Er) at 30° , and mechanical properties such deformation at break (ϵ_b), elastic modulus (E), tensile strength (σ_y) and hardness (H)

(as found by TEM or SAXS) is also misleading. E.g. when comparing the TEM images of TPU 1 and TPU 7 with their erosion rates, their morphologies look very similar, but their erosion rates are totally opposite. The same is true for TPU 3 and TPU 6. And also a comparison between the erosion rates and the inter-domain spacings does not lead to any success.

In the following, it was therefore tested if the viscoelastic data, which also showed clear differences between the different TPUs allow a meaningful correlation.

4.2. Correlation between erosion rate and viscoelastic properties

In order to rank the samples on the basis of their viscoelastic behaviour shown in Figure 4, first of all the identification of the correct timescale relevant to the erosion testing conditions is required. The characteristic duration τ of each impact of an eroding particle on the surface of the sample can be roughly

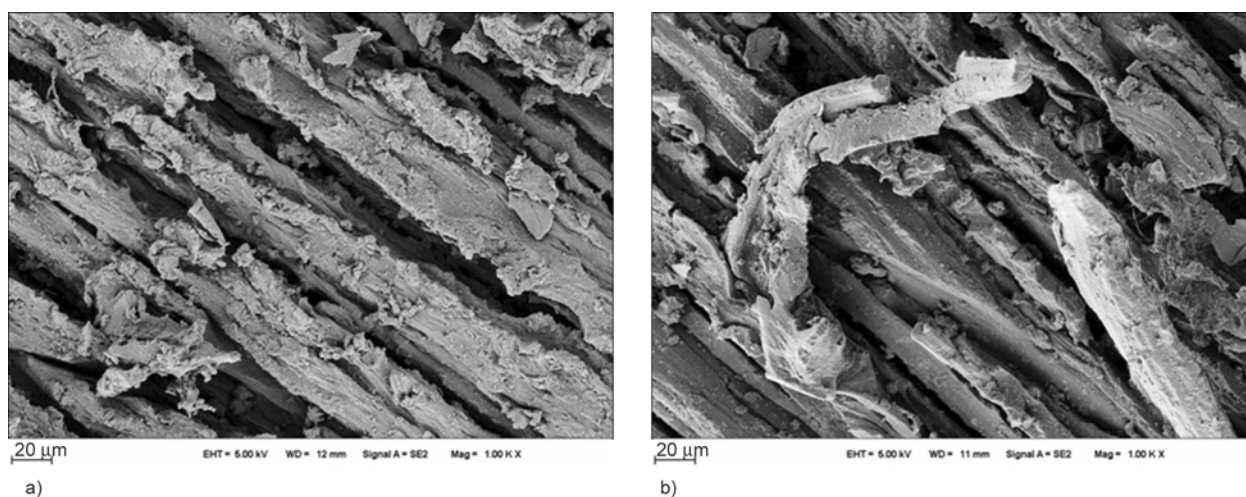


Figure 9. SEM images of TPU 2 (a) and TPU 7 (b) after abrasion test on abrasive paper P180

estimated as the ratio between the impact depth h_i and the impact velocity v_i . Looking at the roughness profile of the samples at the end of the erosion test, i.e. after continued impacts have hit the surface, one can reasonably assume that $h_i \sim 10 \mu\text{m}$. We recognise that inferring h_i from head-on SEM pictures is difficult. Actually profilometry or AFM analysis would be much more appropriate. However, it can be observed that the correlation shown in Figures 11 and 12 is quite strong, i.e. it keeps holding true even if the order of magnitude of the h_i is wrong. For example, if h_i (that we inferred to be $\sim 10 \mu\text{m}$ from SEM visual inspection) would be either 1 or $100 \mu\text{m}$, then $\tau = h_i/v_i$ would be 10^{-6} or 10^{-8} s, or alternatively the relevant frequency would be 10^6 or 10^8 Hz. Looking at Figure 4, it can be concluded that this would not affect our conclusions in terms of ranking of various TPUs. Being $v_i \sim 160$ m/s, one gets a value of $\tau \sim 10^{-7}$ s. This means that a meaningful comparison among the various TPU samples must be done at a frequency of 10^7 Hz. Therefore the viscoelastic moduli at $\omega = 10^7$ Hz were plotted in Figure 11 as a function of the mass loss (after 30 min of erosion testing).

In fact, a linear correlation is noticed between the mass loss and the viscoelastic moduli at the frequency of interest, irrespective of the impingement angle. In particular, the higher the viscoelastic moduli, the higher the erosion rate. It is important to observe that such a direct correlation is quite robust, persisting in a pretty wide range of frequencies around $\omega = 10^7$ Hz. Consequently, even non-negligible uncertainty on h_i or v_i does not invalidate our main conclusions. The strict relationship becomes even more evident by considering the viscoelastic moduli divided by Δm (Figure 12). More specifi-

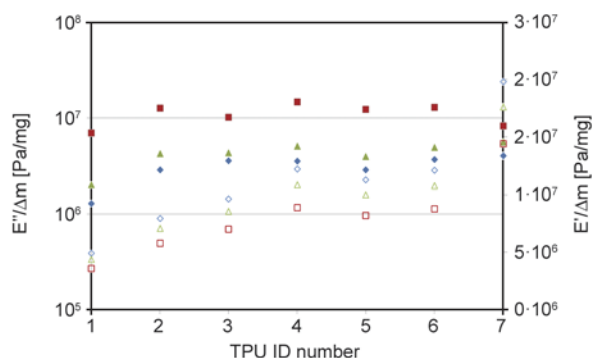


Figure 12. Storage (empty symbols) and loss (full symbols) modulus at $\omega = 10^7$ Hz divided by the mass loss for all the TPUs tested at the various angles of impact: 15° (diamonds), 30° (squares) and 45° (triangles)

cally, an essential independence on the type of TPU and impingement angle can be noticed for the parameter $E''/\Delta m$. In other words, all the TPUs share the same erosion resistance if the comparison is done in terms of their loss modulus.

Provided to be estimated at the proper frequency, the loss modulus seems to be the critical property for the erosion resistance of the studied TPUs. The relevance of E'' could reflect the noticeable propensity to plasticization exhibited by polymeric materials even in case of impulsive loads [21]. It is worth noting that the importance of energy dissipation was also highlighted by Karger-Kocsis and Kuleznev [22], who noticed a good correlation between impact strength and $\tan \delta$ in impact modified polypropylene.

5. Conclusions

Various commercial TPUs were studied in terms of morphological and tribological features and linear viscoelastic behavior. TEM and SAXS analyses

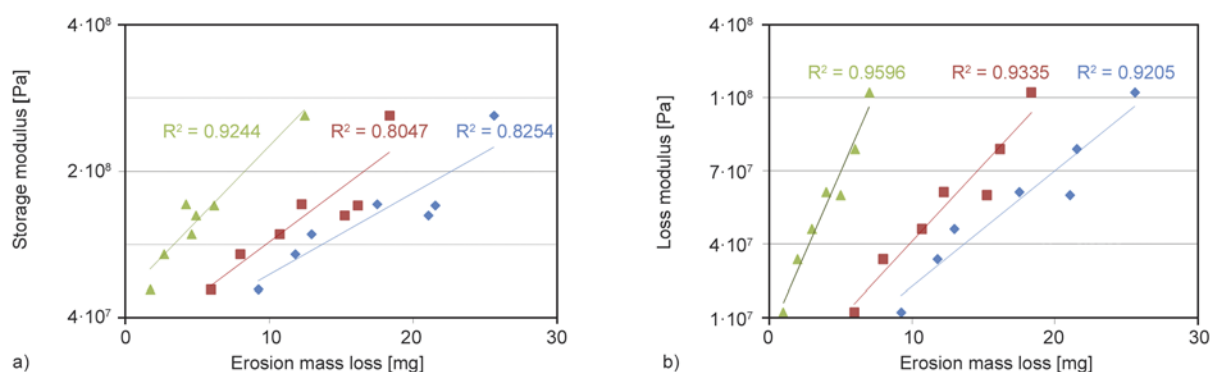


Figure 11. Storage (a) and loss (b) modulus at $\omega = 10^7$ Hz as a function of the mass loss at various impingement angles: 15° (blue diamonds), 30° (red squares) and 45° (green triangles). Lines are linear fittings to the experimental data. The coefficient of determination R^2 is reported for each dataset.

revealed that the samples exhibit different morphologies. In particular, the soft phase can be in the form of either isolated drops or continuous domains interpenetrated with the hard phase. Abrasion tests showed a good correlation with erosion measurements carried out at impingement angle below about 15°. This means that abrasion tests can be used for a first screening of ductile polymeric materials, which are supposed to have their erosion maximum close to an angle of 0 to 15°. The analysis of the viscoelastic behavior revealed a good relationship between the erosion mass loss and the loss modulus, provided the latter is estimated in the proper timescale, i.e. the one of the impacts of the erodent particles. Accordingly, we focused on the viscoelastic properties at about 10⁷ Hz. Good linear correlation was found between *E''* and the mass loss in the course of the erosion tests irrespective of the impingement angle. The ability to rationalize erosion data of many different TPUs suggests that the viscous modulus is the key parameter in the erosion resistance of the studied materials. This has been explained by invoking the inherent propensity to plasticization of the elastomers.

Acknowledgements

This work was partially supported by the Italian Ministry of University (MIUR) through the project PON01_00519 SCILLA_M. Authors are grateful to Dr. Luigi Sanguigno for his precious support in the DMA analyses and the precious discussions about the TTS principle. One of us, G. Arena, is especially grateful to the ERASMUS Program, allowing him the nine months research stay at the Institute for Composite Materials (IVW GmbH), Kaiserslautern, Germany, where many of the experiments were carried out.

References

- [1] Barkoula N-M., Karger-Kocsis J.: Review processes and influencing parameters of the solid particle erosion of polymers and their composites. *Journal of Materials Science*, **37**, 3807–3820 (2002). DOI: [10.1023/A:1019633515481](https://doi.org/10.1023/A:1019633515481)
- [2] Friedrich K.: Erosive wear of polymer surfaces by steel ball blasting. *Journal of Materials Science*, **21**, 3317–3332 (1986). DOI: [10.1007/BF00553375](https://doi.org/10.1007/BF00553375)
- [3] Barkoula N-M., Karger-Kocsis J.: Solid particle erosion of unidirectional GF reinforced EP composites with different fiber/matrix adhesion. *Journal of Reinforced Plastics and Composites*, **21**, 1377–1388 (2002). DOI: [10.1177/0731684402021015779](https://doi.org/10.1177/0731684402021015779)
- [4] Pei X-Q., Friedrich K.: Erosive wear properties of unidirectional carbon fiber reinforced PEEK composites. *Tribology International*, **55**, 135–140 (2012). DOI: [10.1016/j.triboint.2012.05.020](https://doi.org/10.1016/j.triboint.2012.05.020)
- [5] Stachowiak G. W., Batchelor A. W.: *Engineering tribology*. Butterworth-Heinemann, Dordrecht (2005).
- [6] Slikkerveer P. J., van Dongen M. H. A., Touwslager F. J.: Erosion of elastomeric protective coatings. *Wear*, **236**, 189–198 (1999). DOI: [10.1016/S0043-1648\(99\)00268-9](https://doi.org/10.1016/S0043-1648(99)00268-9)
- [7] Friedrich K., Pei X-Q., Almajid A. A.: Specific erosive wear rate of neat polymer films and various polymer composites. *Journal of Reinforced Plastics and Composites*, **32**, 631–643 (2013). DOI: [10.1177/0731684413478478](https://doi.org/10.1177/0731684413478478)
- [8] Prisacariu C.: *Polyurethane elastomers. From morphology to mechanical aspects*. Springer, Wien (2011). DOI: [10.1007/978-3-7091-0514-6](https://doi.org/10.1007/978-3-7091-0514-6)
- [9] Sigamani N. S.: *Characterization of polyurethane at multiple scales for erosion mechanisms under sand particle impact*. Master's thesis, Texas A&M University, USA (2010). DOI: <http://hdl.handle.net/1969.1/ETD-TAMU-2010-05-8008>
- [10] Kontou E., Spathis G., Niaounakis M., Kefalas V.: Physical and chemical cross-linking effects in polyurethane elastomers. *Colloid and Polymer Science*, **298**, 636–644 (1990). DOI: [10.1007/BF01410405](https://doi.org/10.1007/BF01410405)
- [11] Hutchings I. M., Deuchards W. T., Muhr A. H.: Erosion of unfilled elastomers by solid particle impact. *Journal of Materials Science*, **22**, 4071–4076 (1987). DOI: [10.1007/BF01133360](https://doi.org/10.1007/BF01133360)
- [12] Karger-Kocsis J.: Dry friction and sliding behavior of organoclay reinforced thermoplastic polyurethane rubbers. *Kautschuk, Gummi, Kunststoffe*, **59**, 537–543 (2006).
- [13] Cizmas P. G., Slattery J. C.: Dimensionless correlation for sand erosion of families of polymers. *Wear*, **262**, 316–319 (2007). DOI: [10.1016/j.wear.2006.05.008](https://doi.org/10.1016/j.wear.2006.05.008)
- [14] Li J., Hutchings I. M.: Resistance of cast polyurethane elastomers to solid particle erosion. *Wear*, **135**, 293–303 (1990). DOI: [10.1016/0043-1648\(90\)90032-6](https://doi.org/10.1016/0043-1648(90)90032-6)
- [15] Li C., Goodman S. L., Albrecht R. M., Cooper S. L.: Morphology of segmented polybutadiene-polyurethane elastomers. *Macromolecules*, **21**, 2367–2375 (1988). DOI: [10.1021/ma00186a012](https://doi.org/10.1021/ma00186a012)
- [16] ASTM-G76-83: Standard practice for conducting erosion tests by solid particle impingement using gas jets (1989).
- [17] Ruff A. W., Ives L. K.: Measurement of solid particle velocity in erosive wear. *Wear*, **35**, 195–199 (1975). DOI: [10.1016/0043-1648\(75\)90154-4](https://doi.org/10.1016/0043-1648(75)90154-4)

- [18] Saiani A., Rochas C., Eeckhaut G., Daunch W. A., Leenslag J-W., Higgins J. S.: Origin of multiple melting endotherms in a high hard block content polyurethane. 2. Structural investigation. *Macromolecules*, **37**, 1411–1421 (2004).
DOI: [10.1021/ma034604+](https://doi.org/10.1021/ma034604+)
- [19] Acierno D., Sanguigno L., Arena G., Friedrich K., Padenko E., Russo P.: Erosion behavior and mechanical properties of thermoplastic polyurethanes. In ‘Proceedings of the 7th International Conference on Times of Polymers (TOP) and Composites, Ischia, Italy’. AIP Publishing Vol. 1599, 110–113 (2014).
DOI: [10.1063/1.4876790](https://doi.org/10.1063/1.4876790)
- [20] Arnoldt J. C., Hutchings I. M.: A model for the erosive wear of rubber at oblique impact angles. *Journal of Physics D: Applied Physics*, **25**, A222–A229 (1992).
DOI: [10.1088/0022-3727/25/1A/034](https://doi.org/10.1088/0022-3727/25/1A/034)
- [21] Grellmann W., Seidler S.: Deformation and fracture behaviour of polymers. Springer, Berlin (2001).
DOI: [10.1007/978-3-662-04556-5](https://doi.org/10.1007/978-3-662-04556-5)
- [22] Karger-Kocsis J., Kuleznev V. N.: Dynamic mechanical and impact properties of polypropylene/EPDM blends. *Polymer*, **23**, 699–705 (1982).
DOI: [10.1016/0032-3861\(82\)90054-4](https://doi.org/10.1016/0032-3861(82)90054-4)

Fatigue life extension of epoxy materials using ultrafast epoxy-SbF₅ healing system introduced by manual infiltration

X. J. Ye^{1,2}, Y. Zhu¹, Y. C. Yuan³, Y. X. Song¹, G. C. Yang¹, M. Z. Rong¹, M. Q. Zhang^{1*}

¹Key Laboratory for Polymeric Composite and Functional Materials of Ministry of Education, GD HPPC Lab, School of Chemistry and Chemical Engineering, Sun Yat-Sen University, 510275 Guangzhou, P. R. China

²Guangdong Provincial Public Laboratory of Analysis and Testing Technology, China National Analytical Center, 510070 Guangzhou, P. R. China

³College of Materials Science and Engineering, South China University of Technology, 510640 Guangzhou, P. R. China

Received 7 September 2014; accepted in revised form 7 November 2014

Abstract. The present paper is devoted to the verification of the capability of epoxy-SbF₅ system as a healing chemistry for rapidly retarding and/or arresting fatigue cracks in epoxy materials at room temperature. Owing to the very fast curing speed of epoxy catalyzed by SbF₅, epoxy monomer and the hardener (ethanol solution of SbF₅-ethanol complex) are successively infiltrated into the fracture plane under cyclic loading during the tension-tension fatigue test. As a result, the mechanisms including hydrodynamic pressure crack tip shielding, polymeric wedge and adhesive bonding of the healing agent are revealed. It is found that the healing agent forms solidified wedge at the crack tip within 20 s after start of polymerization of the epoxy monomer, so that the highest healing effect is offered at the moment. The epoxy-SbF₅ system proves to be effective in rapidly obstructing fatigue crack propagation (despite that its cured version has lower fracture toughness than the matrix), and satisfies the requirement of constructing fast self-healing polymeric materials.

Keywords: smart polymers, fracture and fatigue, self-healing, epoxy

1. Introduction

Polymers and polymer composites used for structural application are often subjected to cyclic loading. As a result, fatigue cracks might start to grow at a stress intensity that is significantly lower than the critical stress intensity [1, 2]. To prevent the catastrophic failure of these materials under the circumstances, integration of self-healing capability within the system has been explored [3, 4].

Brown *et al.* [5] examined the effect of fluidic dicyclopentadiene (DCPD) on fatigue life extension of cured epoxy. The chemical was manually infiltrated into the crack tip of tapered double cantilever beam (TDCB) specimen. Viscous flow of DCPD in the

crack plane retarded crack growth, and its polymerized version further acted as a wedge at the crack tip for artificial crack closure. In a latter report of the same group of authors [6], DCPD-loaded microcapsules and particulate Grubbs' catalyst were embedded in epoxy to fabricate self-healing epoxy. It allowed for responding to propagating fatigue cracks by autonomic processes that led to higher endurance limit and life extension, or even complete arrest of crack.

Subsequently, epoxy filled with the dual-microcapsules consisting of epoxy-capsules and mercaptan/tertiary amine-capsules also exhibited in-situ fatigue crack retardancy at room temperature [7]. The mech-

*Corresponding author, e-mail: ceszmq@mail.sysu.edu.cn

anisms of hydrodynamic pressure crack tip shielding, polymeric wedge and adhesive bonding of the healing agent were revealed [7, 8]. Very recently, Neuser and Michaud [9] showed the fatigue response of the epoxy resin containing ethyl phenylacetate (EPA)-capsules. Diffusion of EPA solvent into the crack tip induced local plasticization of the epoxy and hence stopped cracking.

In addition to the strategy based on microencapsulated healing agent, thermoplastic poly(ethylene-co-methacrylic acid) (EMAA) particles and fibers were respectively added into carbon fiber/epoxy laminates [10]. The thermally activated healing at 150°C of double cantilever beam (DCB) after fatigue test fully restored the fatigue resistance of delamination cracks. Infusion of EMAA along the crack plane under the high pressure delivery mechanism and strong EMAA/epoxy bonding were believed to account for the rehabilitation. James *et al.* [11] dispersed zirconium titanate powder in Zn ionomer to form a piezoelectric composite. The degraded piezoelectric property after high strain tensile cyclic loading was found to be recovered to a significant degree upon annealing at 70°C due to the thermal healing capability of Zn-containing ionomer matrix. In fact, the approach no longer belongs to the extrinsic self-healing as most works discussed above, but intrinsic self-healing [12].

Considering the fact that the extent and speed of mechanical properties restoration are equally important, but the latter factor has not yet aroused intense interest [13–16], the authors applied epoxy-SbF₅ cure as the healing chemistry for cured epoxy [17]. The epoxy composite with embedded epoxy-capsules [18] and SbF₅·HOC₂H₅/HOC₂H₅ (ethanol solution of SbF₅-ethanol complex)-capsules [19] proved to be able to re-bonding cracked epoxy within seconds. To have better understanding of the role of the epoxy-SbF₅ system under cyclic loading, manual infiltration of the healing agent at crack tip of cured epoxy is investigated in this work. The knowledge might benefit further development of ultrafast self-healing polymeric materials for practical usage.

2. Experimental

2.1. Materials

Epoxy, diglycidyl ether of bisphenol A (trade name: EPON 828; epoxy equivalent mass: 188 g/mol), was purchased from Shell Co., acting as both the composite's matrix and the polymerizable component of

healing agent. SbF₅ was supplied by Tianjin Institute of Physical and Chemical Engineering of Nuclear Industry, China. Methyl hexahydrophthalic anhydride (MHHPA, anhydride equivalent mass: 168 g/mol) and borontrifluoride-2,4-dimethylaniline-complex (BF₃·DMA) were supplied by Energy Chemical, Shanghai, China.

2.2. Specimen preparation

TDCB specimens with groove length of 55 mm [20, 21] were cast from the stoichiometric mixture of 100 parts EPON 828, 80 parts curing agent MHHPA and 5 parts accelerant BF₃·DMA. The compound was firstly degassed, and then poured into a preheated closed silicone rubber mold and cured at 50°C for 60 h and 70°C for 12 h.

SbF₅·HOC₂H₅/HOC₂H₅ (concentration of SbF₅ = 5 wt%), the hardener component of the healing agent, was prepared by the method mentioned in ref. [17].

2.3. Characterization

Healing of the materials under cyclic stress was studied during fatigue test on the TDCB specimens with a Shimadzu air servo fatigue and endurance testing system ADT-AV02K1S5 at room temperature (25°C). The specimens were pre-cracked (~2.5 mm long) by a razor blade while ensuring the pre-crack tip was centered in the groove. A triangular waveform of 5 Hz was applied with a stress ratio, R , of 0.1 ($R = K_{\min}/K_{\max}$, where K_{\min} and K_{\max} denote the minimum and maximum values of the cyclic stress intensity, respectively). Fatigue cracks were grown within constant mode-I stress intensity factor range, ΔK_I ($\Delta K_I = K_{\max} - K_{\min}$). The optically measured crack tip position and specimen compliance were plotted against number of cycles. The linear relationship between optically measured crack length and specimen compliance was used to calculate the crack tip position of the specimens at all times during the experiment [6]. Healing efficiency, λ , was defined by fatigue life extension [5]: $\lambda = (N_{\text{healed}} - N_{\text{control}})/N_{\text{control}}$, where N_{healed} and N_{control} denote the total number of cycles to failure of the healed specimen and that of a similar control specimen without healing, respectively. The manual infiltration of the healing agent was conducted as follows. About 0.5 μL EPON 828 was injected into the crack plane by using a microsyringe after a crack growth increment of about 8 mm. In this case, both the growth rate and crack closure response settled down to steady state values. The

injection was completed within 5 s. With the repeated opening and closing of the fracture plane, the infiltrated epoxy flowed backward and forward and instantaneously evenly penetrated into the crack. Thereby the effect of hydrodynamic pressure crack tip shielding could be observed. Furthermore, the effects of polymeric wedge and adhesive bonding of the healing agent were studied by injecting 0.5 μL $\text{SbF}_5 \cdot \text{HOC}_2\text{H}_5/\text{HOC}_2\text{H}_5$ into the crack plane about 60 s after the injection of EPON 828. For each test, the result was an average of five specimens. Temperature variation at the crack tip was monitored by an infrared camera ImageIR[®] 8300 (InfraTec GmbH, Germany). Morphologies of the fracture surfaces were observed by a Hitachi Model S-4800 field emission scanning electron microscope (SEM).

3. Results and discussion

3.1. Effect of hydrodynamic pressure crack-tip shielding

In our previous work on the epoxy composite filled with epoxy monomer loaded microcapsules and $\text{SbF}_5 \cdot \text{HOC}_2\text{H}_5/\text{HOC}_2\text{H}_5$ loaded microcapsules [17], the healing agent was found to be liberated upon fracture of the specimen, spreading over the fractured surface and rejoining the broken specimen at room temperature. Due to the very fast curing characteristic of the healing system, however, the effect of hydrodynamic pressure crack-tip shielding cannot be clearly identified. For this purpose, uncured epoxy component of the healing agent alone was firstly injected into the crack plane without the interference of any hardener.

It has been known that the forces required to drive viscous liquid into the crack during loading and to draw the fluid out of the crack during unloading would provide effective crack-tip shielding [22, 23]. This hydrodynamic pressure effect decreases the effective mode-I stress intensity factor range, ΔK_{eff} , and hence slows down the expansion of the fatigue crack and increases the fatigue life of materials. The dependences of fatigue crack length on loading cycle in Figure 1 illustrate the influence of the epoxy monomer on the fracture plane. Upon the injection of the fluidic epoxy monomer, the rate of crack growth remarkably declines as compared with that of the control specimen. As a result, the infiltrated specimen fails after $3.6 \cdot 10^5$ cycles instead of $2.1 \cdot 10^5$ cycles, leading to a fatigue life extension of 73.5%.

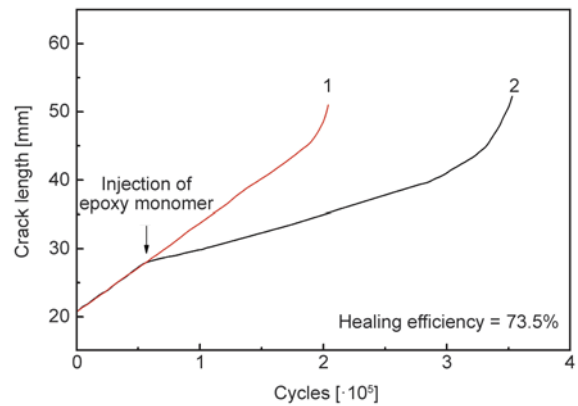


Figure 1. Crack length vs. fatigue cycles of (1) control specimen and (2) the specimen with manually injected epoxy monomer. Testing condition: $K_{\text{max}} = 2.58 \cdot 10^{-1} \text{ MPa} \cdot \text{m}^{1/2}$ ($= 0.56 K_{\text{IC}}$ of the matrix), $K_{\text{min}} = 2.60 \cdot 10^{-2} \text{ MPa} \cdot \text{m}^{1/2}$, $\Delta K_{\text{I}} = 2.32 \cdot 10^{-1} \text{ MPa} \cdot \text{m}^{1/2}$.

It is worth noting that our early study of manual infiltration of the same epoxy monomer, EPON 828, into cured epoxy under cyclic loading yielded a fatigue life extension of 246% [8]. The difference should result from the different ductility of the matrix epoxy. In the present work, fracture toughness, K_{IC} , of the epoxy cured by MHPA and $\text{BF}_3 \cdot \text{DMA}$ is $4.59 \cdot 10^{-1} \text{ MPa} \cdot \text{m}^{1/2}$, which is lower than the value of the former cured by diethylenetriamine (i.e. $5.87 \cdot 10^{-1} \text{ MPa} \cdot \text{m}^{1/2}$). Although the ΔK_{I} applied for the fatigue test of the current material is reduced to $2.32 \cdot 10^{-1} \text{ MPa} \cdot \text{m}^{1/2}$, lower than that applied for the former material (i.e. $4.54 \cdot 10^{-1} \text{ MPa} \cdot \text{m}^{1/2}$), the measured fatigue life extension is still lower. Clearly, the hydrodynamic pressure crack-tip shielding mechanism is less effective in more brittle material, which is more sensitive to the fatigue loading.

The load-displacement curve shown in Figure 2 further shows the hydrodynamic pressure effect from another angle. Before injecting the epoxy monomer, the loading-unloading curves of the epoxy specimen recorded at each fatigue cycle overlap (refer to curves a and b in Figure 2). After injection of the epoxy monomer, the fatigue crack can neither be fully opened at the maximum load nor be fully closed at the minimum load. Consequently, hysteresis loops appear on the load-displacement relationship between the initial phase of crack opening and the end phase of crack closing (see curves c~e in Figure 2). As the injected epoxy monomer has to inevitably adhere to the crack plane, the amount of the viscous fluid at the crack tip gradually decreases

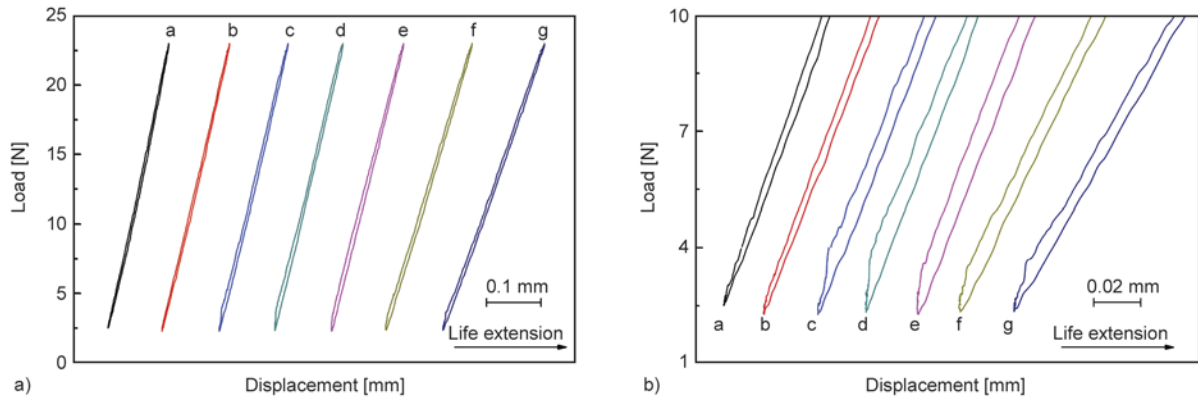


Figure 2. (a) Load-displacement curves measured during selected cycles of curve 2 in Figure 1. Number of the fatigue cycles and time after manual infiltration of the epoxy monomer: (a) 600; (b) 57 400; (c) 60 000, 0.5 min; (d) 61 500, 5 min; (e) 101 400, 138.5 min; (f) 199 800, 466.5 min; (g) 299 400, 798.5 min. (b) Partially enlarged view of (a). Testing condition: $K_{\max} = 2.58 \cdot 10^{-1} \text{ MPa}\cdot\text{m}^{1/2}$ ($= 0.56 K_{IC}$ of the matrix), $K_{\min} = 2.60 \cdot 10^{-2} \text{ MPa}\cdot\text{m}^{1/2}$, $\Delta K_I = 2.32 \cdot 10^{-1} \text{ MPa}\cdot\text{m}^{1/2}$.

with advance of crack. The hysteresis loops become thinner with time (refer to curves f and g in Figure 2), representing weakening of the hydrodynamic pressure crack-tip shielding effect.

3.2. Effects of polymeric wedge and adhesive bonding

It has been known that the effective stress intensity factor range can be greatly reduced by a wedge with adhesiveness at the crack tip [24–26]. Here in this work, the wedge of crosslinked epoxy forms shortly after injection of $\text{SbF}_5 \cdot \text{HOC}_2\text{H}_5 / \text{HOC}_2\text{H}_5$ into the fracture plane, because the epoxy monomer has been infiltrated in advance. Therefore, significant retardation of fatigue crack occurs (Figure 3a), leading to a fatigue life extension of 82.8%, which is ~9% higher than the value offered by merely injecting epoxy monomer (Figure 1). The marginal increase of the healing efficiency owing to the incorporation of

the hardener should be attributed to the incomplete polymerization of epoxy monomer in the case of the ultrafast curing speed. Fully developed network structure in conventional cured epoxy is absent in the present cured healing agent, so that the polymeric wedge and adhesive bonding effects become weaker in comparison with the case of slower curing speed [8]. It seems there is a dilemma that how the healing system can simultaneously provide high healing efficiency and high healing speed.

To have more detailed information of the crack growth behavior affected by the infiltrated healing agent, partially enlarged view of Figure 3a is plotted in Figure 3b. It is seen that after the injection of epoxy monomer but before the injection of the curing agent $\text{SbF}_5 \cdot \text{HOC}_2\text{H}_5 / \text{HOC}_2\text{H}_5$, the aforesaid hydrodynamic pressure effect is present as characterized by the reduced slope of the dependences of fatigue crack length on loading cycle (refer to curve 2

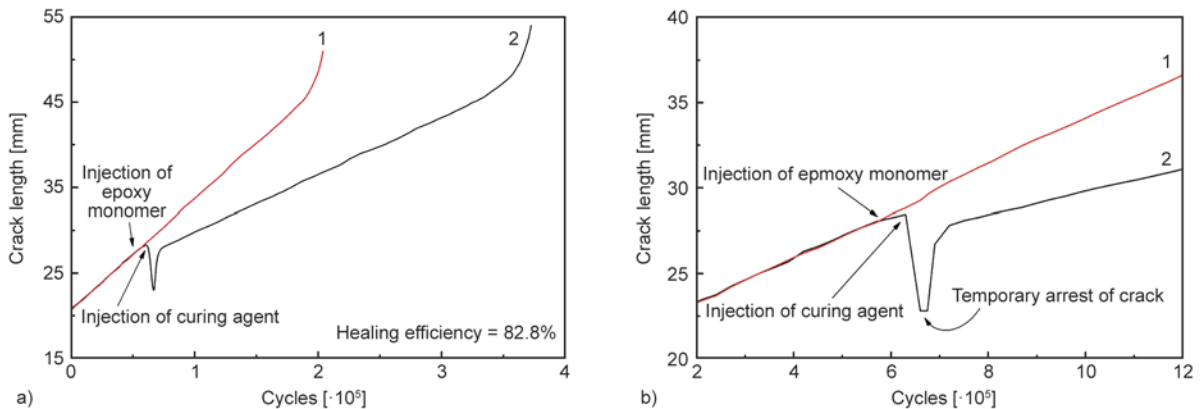


Figure 3. (a) Crack length vs. fatigue cycles of (1) control specimen and (2) the specimen with manually injected epoxy monomer and $\text{SbF}_5 \cdot \text{HOC}_2\text{H}_5 / \text{HOC}_2\text{H}_5$. (b) Partially enlarged view of (a). Testing condition: $K_{\max} = 2.58 \cdot 10^{-1} \text{ MPa}\cdot\text{m}^{1/2}$ ($= 0.56 K_{IC}$ of the matrix), $K_{\min} = 2.60 \cdot 10^{-2} \text{ MPa}\cdot\text{m}^{1/2}$, $\Delta K_I = 2.32 \cdot 10^{-1} \text{ MPa}\cdot\text{m}^{1/2}$.

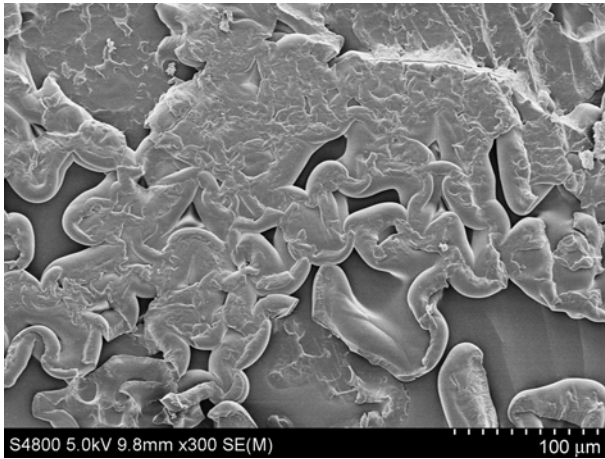


Figure 4. SEM micrograph of fatigue fracture surface of the specimen with successive manual injection of epoxy monomer and $\text{SbF}_5 \cdot \text{HOC}_2\text{H}_5/\text{HOC}_2\text{H}_5$

in Figure 3b). When the curing agent is injected, curing reaction of the epoxy monomer takes place rapidly. The infiltrated epoxy that flows backward in the course of crack closing is consolidated instantly, so that the measured crack length is shortened by about 6 mm. Additionally, temporary arrest of fatigue crack also appear (refer to the terrace on curve 2 in Figure 3b).

With the proceeding of the fatigue test, the crack eventually travels through the polymeric wedge and leaves cohesively ruptured wedge behind (Figure 4). Due to the high affinity of the cured healing agent for the epoxy matrix, however, the remains of the ruptured wedge still stay on the cracked plane, and take effect to reduce the effective stress intensity factor range at the crack tip to a certain degree. It

explains the significantly lower crack growth rate of the majority of curve 2 in Figure 3 after injection of $\text{SbF}_5 \cdot \text{HOC}_2\text{H}_5/\text{HOC}_2\text{H}_5$, as compared with that of the control specimen (i.e. curve 1 in Figure 3).

To understand the time of the polymeric wedge formation, load-displacement relationships measured during selected cycles of curve 2 in Figure 3 are given in Figure 5. Prior to injection of the healing agent into the crack tip, nearly no hysteresis loop is detected (see curve a in Figure 5). Following the epoxy monomer injection, the fluid rapidly flows throughout the cracked plane and penetrates into the crack tip under cycling load. Accordingly, the hydrodynamic pressure effect comes into existence and hysteresis loop is evidently visible (curve b in Figure 5). When the curing agent $\text{SbF}_5 \cdot \text{HOC}_2\text{H}_5/\text{HOC}_2\text{H}_5$ is injected into the crack plane, the pre-injected epoxy monomer starts to be polymerized. As the fluidic healing agent becomes more and more viscous, the effect of hydrodynamic pressure crack tip shielding is enhanced and the areas of the hysteresis loops increase (curves c and d in Figure 5). Meanwhile, obvious tearing traces formed by the healing agent in the rubbery state are found on the fracture plane (Figure 4).

It is interesting to see that a knee point appears on the loading part of curve e in Figure 5, which results from the crack closure effect contributed by the polymeric wedge and adhesion at the crack tip [27]. In contrast, injection of epoxy monomer alone could not lead to the same effect (Figure 2), which evidences that the knee point is related to solidification

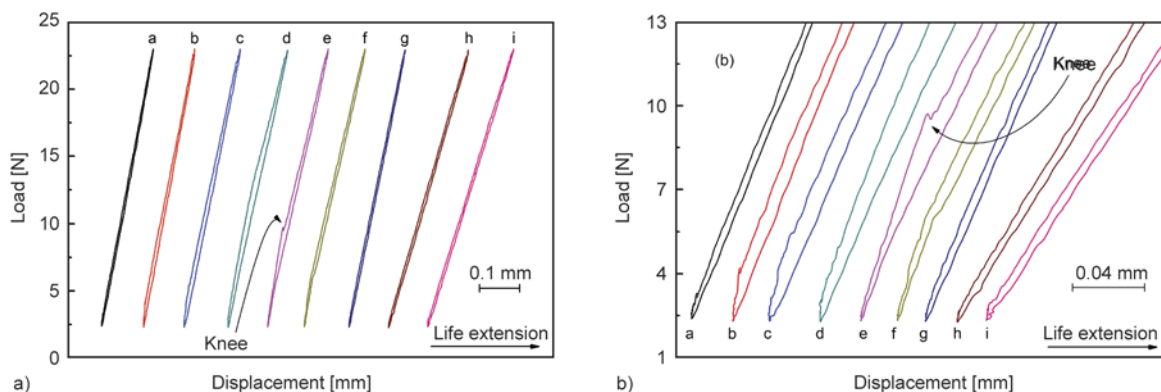


Figure 5. (a) Load-displacement curves measured during selected cycles of curve 2 in Figure 3. Number of the fatigue cycles and time after the manual infiltration of healing agent: (a) 54 000; (b) 60 000, 1 min after epoxy monomer injection; (c) 65 950, 10 s after injection of $\text{SbF}_5 \cdot \text{HOC}_2\text{H}_5/\text{HOC}_2\text{H}_5$; (d) 65 975, 15 s; (e) 66 000, 20 s; (f) 66 025, 25 s; (g) 73 400, 25 min; (h) 299 300, 998 min; (i) 345 000, 1150 min. The times indicated for curves (d)~(i) represent those counting from the injection of the curing agent $\text{SbF}_5 \cdot \text{HOC}_2\text{H}_5/\text{HOC}_2\text{H}_5$. (b) Partially enlarged view of (a). Testing conditions: $K_{\max} = 2.58 \cdot 10^{-1} \text{ MPa} \cdot \text{m}^{1/2}$ ($= 0.56 K_{IC}$ of the matrix), $K_{\min} = 2.60 \cdot 10^{-2} \text{ MPa} \cdot \text{m}^{1/2}$, $\Delta K_I = 2.32 \cdot 10^{-1} \text{ MPa} \cdot \text{m}^{1/2}$.

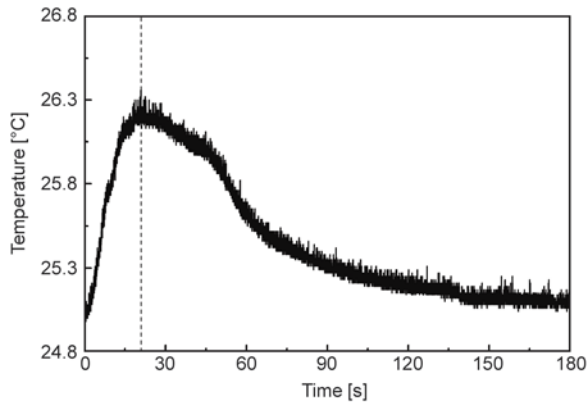


Figure 6. Time dependence of the temperature at fatigue crack tip of the specimen. The time is counted from injection of $\text{SbF}_5 \cdot \text{HOC}_2\text{H}_5/\text{HOC}_2\text{H}_5$. Epoxy monomer has been injected into the fracture plane prior to the injection of the curing agent.

of the injected healing agent. It can thus be concluded that the highest healing effect offered by the epoxy-SF₅ healing agent is achieved 20 s after their contact. With a further rise in time, the wedge is damaged and the effects of polymeric wedge and adhesive bonding have to be decreased. Not only the knee point disappears but also the areas of the hysteresis loops become smaller (refer to curves f~i in Figure 5).

The rapid healing capability of the healing system revealed above is supported by the in-situ measurement of the temperature of the crack tip, which peaks at about 20 s (Figure 6). It means that the exothermic polymerization of the injected epoxy monomer happens as soon as it contacts $\text{SbF}_5 \cdot \text{HOC}_2\text{H}_5/\text{HOC}_2\text{H}_5$ and the reaction degree reaches the maximum after 20 s. As no additional reactants are supplemented, the heat given by the curing reaction gradually reduces with time.

3.3. Effect of applied range of cyclic stress intensity

In the course of fatigue test, healing chemical kinetics and crack growth rate are the major factors affecting the crack retardation performance of self-healing materials [5, 8]. Considering that crack growth rate is closely related to stress intensity factor range, ΔK_I , crack growth behavior of the specimen was studied at additional two levels of applied range of stress intensity using manual infiltration of the healing agent (Figure 7), so as to have better understanding of the healing system. During the tests, the maximum cyclic stress intensity was changed, but the stress ratio, R , was kept at 0.1.

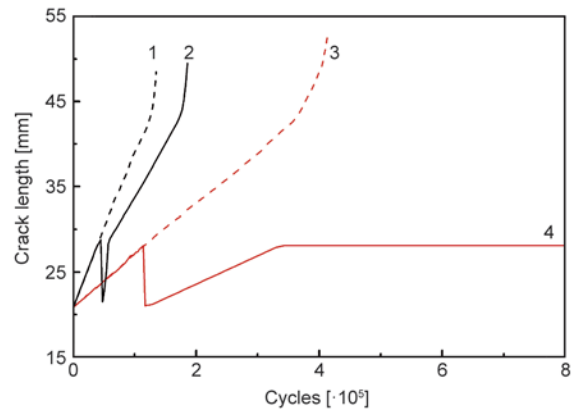


Figure 7. Crack length vs. fatigue cycles of control specimens (dashed lines) and the specimens with manually injected epoxy monomer and $\text{SbF}_5 \cdot \text{HOC}_2\text{H}_5/\text{HOC}_2\text{H}_5$ (solid lines). Testing conditions: for curves 1 and 2, $K_{\max} = 2.80 \cdot 10^{-1} \text{ MPa} \cdot \text{m}^{1/2}$ ($= 0.61 K_{IC}$ of the matrix), $K_{\min} = 2.80 \cdot 10^{-2} \text{ MPa} \cdot \text{m}^{1/2}$, $\Delta K_I = 2.52 \cdot 10^{-1} \text{ MPa} \cdot \text{m}^{1/2}$; for curves 3 and 4, $K_{\max} = 2.24 \cdot 10^{-1} \text{ MPa} \cdot \text{m}^{1/2}$ ($= 0.49 K_{IC}$ of the matrix), $K_{\min} = 2.20 \cdot 10^{-2} \text{ MPa} \cdot \text{m}^{1/2}$, $\Delta K_I = 2.02 \cdot 10^{-1} \text{ MPa} \cdot \text{m}^{1/2}$.

For $K_{\max} = 2.80 \cdot 10^{-1} \text{ MPa} \cdot \text{m}^{1/2}$ ($= 0.61 K_{IC}$ of the matrix) that is higher than the value in Figure 3 (i.e. $2.58 \cdot 10^{-1} \text{ MPa} \cdot \text{m}^{1/2}$), the repairing efficiency of the specimen is about 37.8% at room temperature relative to the control specimen. It is lower than 82.8% given in Figure 3 because (i) the mechanical kinetics of crack propagation is dominant in this case, and (ii) the polymeric wedge formed by the healing agent is easier to be destroyed by higher stress and the shielding effect of the crack tip has to be weakened accordingly.

When K_{\max} is reduced to $2.24 \cdot 10^{-1} \text{ MPa} \cdot \text{m}^{1/2}$ ($= 0.49 K_{IC}$ of the matrix), the deformation rate and damaging of polymeric wedge are greatly slowed

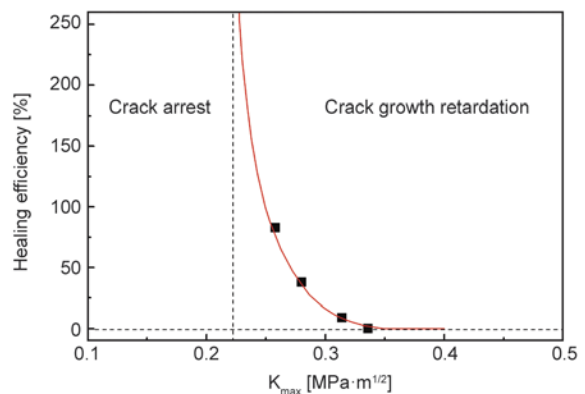


Figure 8. Healing efficiency of fatigue specimens vs. maximum cyclic stress intensity

down, thus the healing kinetics predominates and the crack tip shielding effect is more apparent. The crack does not grow even when fatigue cycles are greater than 10^7 , meaning that it is arrested. The repair efficiency tends to be infinite. In contrast, the crack in the control specimen that cannot be healed develops at a constant speed. The maximum cyclic stress intensity of $\sim 2.24 \cdot 10^{-1} \text{ MPa} \cdot \text{m}^{1/2}$ becomes the watershed between fatigue crack growth retardation and crack arrest (Figure 8).

4. Conclusions

By successive manual infiltration of epoxy monomer and $\text{SbF}_5 \cdot \text{HOC}_2\text{H}_5/\text{HOC}_2\text{H}_5$ into fracture plane of cured epoxy specimen subjected to cyclic loading, crack tip shielding effects resulting from hydrodynamic pressure, polymeric wedge and adhesive bonding are clearly identified. Under certain stress intensity factor range, the fatigue crack can even be fully arrested. More importantly, the healing agent proves to be converted into polymeric wedge within 20 s after the polymerization starts. This demonstrates the extremely fast operation feature of the healing system. The information helps to understand well the healing mechanisms of self-healing composites with dual microencapsulated healing agent under fatigue loading [17, 28], and to optimize the healant formulation accordingly. In authentic self-healing composites, reaction of the healing agent released from ruptured microcapsules proceeds too fast to accurately analyze the healing mechanisms. Compared to the case with healing capsules [17], the fatigue life extension is less in the present work. This might be due the fact that the capsules rupture along the crack growth whereas the injection is done once. Accordingly, the fatigue crack retardation mechanisms (i.e. hydrodynamic pressure, polymeric wedge and adhesive bonding) appear repeatedly during the tests of the former material. In contrast, only the polymeric wedge still takes effect to a certain extent as crack passes the wedge in the pure epoxy specimen healed by manual infiltration. The difference highlights the role of individual factors in retarding fatigue crack propagation, and hence the usefulness of this work.

Acknowledgements

The authors thank the support of the Natural Science Foundation of China (Grants: 51273214 and 51333008), Doctoral Fund of Ministry of Education of China (Grant: 20090171110026), the Science and Technology Program of Guangdong Province (Grants: 2010B010800021, 2010A011300004, 2011A091102001, 2011A091102003 and S2013020013029), the Science and Technology Program of Guangzhou (Grant: 2014J4100121), and the Basic Scientific Research Foundation in Colleges and Universities of Ministry of Education of China (Grant: 12lgjc08).

References

- [1] Karger-Kocsis J., Friedrich K.: Microstructure-related fracture toughness and fatigue crack growth behaviour in toughened, anhydride-cured epoxy resins. *Composites Science and Technology*, **48**, 263–272 (1993). DOI: [10.1016/0266-3538\(93\)90143-5](https://doi.org/10.1016/0266-3538(93)90143-5)
- [2] Karger-Kocsis J., Friedrich K.: Fatigue crack propagation and related failure in modified, anhydride-cured epoxy resins. *Colloid and Polymer Science*, **270**, 549–562 (1992). DOI: [10.1007/BF00658286](https://doi.org/10.1007/BF00658286)
- [3] Zhang M. Q., Rong M. Z.: *Self-healing polymers and polymer composites*. Wiley, Hoboken (2011).
- [4] Yuan Y. C., Yin T., Rong M. Z., Zhang M. Q.: Self healing in polymers and polymer composites. Concepts, realization and outlook: A review. *Express Polymer Letters*, **2**, 238–250 (2008). DOI: [10.3144/expresspolymlett.2008.29](https://doi.org/10.3144/expresspolymlett.2008.29)
- [5] Brown E. N., White S. R., Sottos N. R.: Retardation and repair of fatigue cracks in a microcapsule toughened epoxy composite – Part I: Manual infiltration. *Composites Science and Technology*, **65**, 2466–2473 (2005). DOI: [10.1016/j.compscitech.2005.04.020](https://doi.org/10.1016/j.compscitech.2005.04.020)
- [6] Brown E. N., White S. R., Sottos N. R.: Retardation and repair of fatigue cracks in a microcapsule toughened epoxy composite – Part II: *In situ* self-healing. *Composites Science and Technology*, **65**, 2474–2480 (2005). DOI: [10.1016/j.compscitech.2005.04.053](https://doi.org/10.1016/j.compscitech.2005.04.053)
- [7] Yuan Y. C., Rong M. Z., Zhang M. Q., Yang G. C., Zhao J. Q.: Self-healing of fatigue crack in epoxy materials with epoxy/mercaptan system. *Express Polymer Letters*, **5**, 47–59 (2011). DOI: [10.3144/expresspolymlett.2011.6](https://doi.org/10.3144/expresspolymlett.2011.6)
- [8] Yuan Y. C., Rong M. Z., Zhang M. Q., Yang G. C., Zhao J. Q.: Healing of fatigue crack in epoxy materials with epoxy/mercaptan system *via* manual infiltration. *Express Polymer Letters*, **4**, 644–658 (2010). DOI: [10.3144/expresspolymlett.2010.79](https://doi.org/10.3144/expresspolymlett.2010.79)
- [9] Neuser S., Michaud V.: Fatigue response of solvent-based self-healing smart materials. *Experimental Mechanics*, **54**, 293–304 (2014). DOI: [10.1007/s11340-013-9787-5](https://doi.org/10.1007/s11340-013-9787-5)

- [10] Pingkarawat K., Wang C. H., Varley R. J., Mouritz A. P.: Self-healing of delamination fatigue cracks in carbon fibre–epoxy laminate using mendable thermoplastic. *Journal of Materials Science*, **47**, 4449–4456 (2012). DOI: [10.1007/s10853-012-6303-8](https://doi.org/10.1007/s10853-012-6303-8)
- [11] James N. K., Lafont U., van der Zwaag S., Groen W. A.: Piezoelectric and mechanical properties of fatigue resistant, self-healing PZT–ionomer composites. *Smart Materials and Structures*, **23**, 055001/1–055001/9 (2014). DOI: [10.1088/0964-1726/23/5/055001](https://doi.org/10.1088/0964-1726/23/5/055001)
- [12] Zhang M. Q., Rong M. Z.: Intrinsic self-healing of covalent polymers through bond reconnection towards strength restoration. *Polymer Chemistry*, **4**, 4878–4884 (2013). DOI: [10.1039/c3py00005b](https://doi.org/10.1039/c3py00005b)
- [13] Xiao D. S., Yuan Y. C., Rong M. Z., Zhang M. Q.: Hollow polymeric microcapsules: Preparation, characterization and application in holding boron trifluoride diethyl etherate. *Polymer*, **50**, 560–568 (2009). DOI: [10.1016/j.polymer.2008.11.022](https://doi.org/10.1016/j.polymer.2008.11.022)
- [14] Xiao D. S., Yuan Y. C., Rong M. Z., Zhang M. Q.: A facile strategy for preparing self-healing polymer composites by incorporation of cationic catalyst-loaded vegetable fibers. *Advanced Functional Materials*, **19**, 2289–2296 (2009). DOI: [10.1002/adfm.200801827](https://doi.org/10.1002/adfm.200801827)
- [15] Xiao D. S., Yuan Y. C., Rong M. Z., Zhang M. Q.: Self-healing epoxy based on cationic chain polymerization. *Polymer*, **50**, 2967–2975 (2009). DOI: [10.1016/j.polymer.2009.04.029](https://doi.org/10.1016/j.polymer.2009.04.029)
- [16] Xiao D. S., Rong M. Z., Zhang M. Q.: A novel method for preparing epoxy-containing microcapsules *via* UV irradiation-induced interfacial copolymerization in emulsions. *Polymer*, **48**, 4765–4776 (2007). DOI: [10.1016/j.polymer.2007.06.018](https://doi.org/10.1016/j.polymer.2007.06.018)
- [17] Ye X. J., Zhang J-L., Zhu Y., Rong M. Z., Zhang M. Q., Song Y. X., Zhang H-X.: Ultrafast self-healing of polymer toward strength restoration. *ACS Applied Materials and Interfaces*, **6**, 3661–3670 (2014). DOI: [10.1021/am405989b](https://doi.org/10.1021/am405989b)
- [18] Yuan Y. C., Rong M. Z., Zhang M. Q., Yang G. C.: Study of factors related to performance improvement of self-healing epoxy based on dual encapsulated healant. *Polymer*, **50**, 5771–5781 (2009). DOI: [10.1016/j.polymer.2009.10.019](https://doi.org/10.1016/j.polymer.2009.10.019)
- [19] Ye X-J., Ma Z-X., Song Y-X., Huang J-J., Rong M-Z., Zhang M-Q.: SbF₅-loaded microcapsules for ultrafast self-healing of polymer. *Chinese Chemical Letters*, **25**, 1565–1568 (2014). DOI: [10.1016/j.ccllet.2014.07.002](https://doi.org/10.1016/j.ccllet.2014.07.002)
- [20] Brown E. N., Sottos N. R., White S. R.: Fracture testing of a self-healing polymer composite. *Experimental Mechanics*, **42**, 372–379 (2002). DOI: [10.1177/001448502321548193](https://doi.org/10.1177/001448502321548193)
- [21] Brown E. N.: Use of the tapered double-cantilever beam geometry for fracture toughness measurements and its application to the quantification of self-healing. *Journal of Strain Analysis for Engineering Design*, **46**, 167–186 (2011). DOI: [10.1177/0309324710396018](https://doi.org/10.1177/0309324710396018)
- [22] Tzou J-L., Hsueh C. H., Evans A. G., Ritchie R. O.: Fatigue crack propagation in oil environments – II. A model for crack closure induced by viscous fluids. *Acta Metallurgica*, **33**, 117–127 (1985). DOI: [10.1016/0001-6160\(85\)90225-1](https://doi.org/10.1016/0001-6160(85)90225-1)
- [23] Davis F. H., Ellison E. G.: Hydrodynamic pressure effects of viscous fluid flow in a fatigue crack. *Fatigue and Fracture of Engineering Materials and Structures*, **12**, 527–542 (1989). DOI: [10.1111/j.1460-2695.1989.tb00561.x](https://doi.org/10.1111/j.1460-2695.1989.tb00561.x)
- [24] Shin C. S., Cai C. Q.: A model for evaluating the effect of fatigue crack repair by the infiltration method. *Fatigue and Fracture of Engineering Materials and Structures*, **23**, 835–845 (2000). DOI: [10.1046/j.1460-2695.2000.00347.x](https://doi.org/10.1046/j.1460-2695.2000.00347.x)
- [25] Sharp P. K., Clayton J. Q., Clark G.: Retardation and repair of fatigue cracks by adhesive infiltration. *Fatigue and Fracture of Engineering Materials and Structures*, **20**, 605–614 (1997). DOI: [10.1111/j.1460-2695.1997.tb00292.x](https://doi.org/10.1111/j.1460-2695.1997.tb00292.x)
- [26] Shin C. S., Hsu S. H.: Fatigue life extension by an artificially induced retardation mechanism. *Engineering Fracture Mechanics*, **43**, 677–684 (1992). DOI: [10.1016/0013-7944\(92\)90210-6](https://doi.org/10.1016/0013-7944(92)90210-6)
- [27] Wolf E.: Fatigue crack closure under cyclic tension. *Engineering Fracture Mechanics*, **2**, 37–45 (1970). DOI: [10.1016/0013-7944\(70\)90028-7](https://doi.org/10.1016/0013-7944(70)90028-7)
- [28] Ye X. J., Song Y. X., Zhu Y., Yang G. C., Rong M. Z., Zhang M. Q.: Self-healing epoxy with ultrafast and heat-resistant healing system processable at elevated temperature. *Composites Science and Technology*, **104**, 40–46 (2014). DOI: [10.1016/j.compscitech.2014.08.028](https://doi.org/10.1016/j.compscitech.2014.08.028)

Ductile-brittle transition behaviour of PLA/o-MMT films during the physical aging process

M. Ll. MasPOCH^{1*}, O. O. Santana¹, J. Cailloux¹, E. Franco-Urquiza¹, C. Rodriguez², J. Belzunce², A. B. Martínez¹

¹Centre Català del Plàstic (CCP), Universitat Politècnica de Catalunya (ETSEIB-UPC), C/Colom 114, 08222 Terrassa, Spain

²SIMUMECAMAT, Universidad de Oviedo, Edificio Departamental Oeste, nº 7, 33203 Gijón, Spain

Received 15 September 2014; accepted in revised form 20 November 2014

Abstract. The ductile-brittle transition behaviour of organo modified montmorillonite-based Poly(lactic acid) films (PLA/o-MMT) was analysed using the Essential Work of Fracture (EWF) methodology, Small Punch Tests (SPT) and Enthalpy relaxation analysis. While the EWF methodology could only be applied successfully to de-aged samples, small punch test (SPT) was revealed as more effective for a mechanical characterization during the transient behaviour from ductile to brittle. According to differential scanning calorimetry (DSC) results, physical aging at 30°C of PLA/o-MMT samples exhibited slower enthalpy relaxation kinetics as compared to the pristine polymer. Although all samples exhibited an equivalent thermodynamic state after being stored one week at 30°C, significant differences were observed in the mechanical performances. These changes could be attributed to the toughening mechanisms promoted by o-MMT.

Keywords: nanocomposites, PLA, physical aging, fracture and fatigue

1. Introduction

Over the past ten years, Poly(lactic acid) (PLA) has gained much interest in commercial applications. The ring-opening polymerization of lactic acid is the current method to obtain PLA of high molecular weight [1]. It is a high strength and high modulus aliphatic thermoplastic biopolymer with mechanical properties ranging between those of Polystyrene (PS) and Poly(ethylene terephthalate) (PET) [2, 3]. However, some other properties such as its low melt stability throughout processing due to hydrolytic degradation reactions, low melt strength, low heat distortion temperature (HDT) and its high brittleness reduce its use to very limited applications [4]. As already established by numerous research groups, different strategies may be used to mitigate these

drawbacks. In this way, the addition of plasticizers, copolymerization, melt blending with other thermoplastics, reactive extrusion combined with multifunctional reactive agents and (nano)composites have demonstrated encouraging results [5–8].

PLA parts are usually found in their amorphous state due to the relatively fast cooling rates of industrial processes as compared to the crystallization rates of current commercial PLA grades [9]. As PLA parts are employed at temperatures below but close to T_g , these thermodynamically unstable glasses rapidly tend toward an equilibrium state through slow segmental rearrangements over time. This phenomenon is commonly referred to as ‘physical aging’, which promotes a ductile to brittle transition in mechanical and fracture behaviour. The resulting brittleness

*Corresponding author, e-mail: maria.lluisa.maspoch@upc.edu
© BME-PT

does not only affect the end use behaviour but also the handling and processing, leading to important limitations in large-scale production [10, 11].

Over the last years, numerous studies have reported the effect of the physical aging on the PLA properties. [12, 13]. Nevertheless, there are few works describing the effect of physical aging on the fracture behaviour of PLA using Fracture Mechanics approaches. It has been shown that the EWF methodology is a useful tool to investigate the effect of physical aging on PET and Glycol-modified Poly (ethylene terephthalate) (PETG) films [14–16]. In the case of PLA, which has faster physical aging than PET and PETG, the EWF analysis can only be successfully applied in the non-aged material. After 1 hour of de-aging treatment, a transient ductile-brittle situation is observed, and each tested sample shows a different behaviour [17, 18].

The EWF methodology is frequently placed at the forefront of the post-yielding fracture characterization. However, this technique is laborious and time consuming. The main difficulties arise from the preparation and the evaluation of a large number of notched specimens. Since PLA exhibits a fast physical aging, sample conditioning and experimentation should be performed quickly.

Recently, the small punch test (SPT) has seen significant developments as an alternative to conventional mechanical testing procedures. SPT method provides specific advantages as compared to the EWF procedure. For instance, both specimen sizes and test times are lower in SPT than in EWF methodology. Although this method has been largely used in the field of steels and some metallic alloys, only few works report the investigation of polymeric materials [19, 20]. Rodriguez *et al.* [21] reported a correlation between the mechanical (Elastic modulus, Yield stress) and SPT parameters normalized by sample thickness (t) for PLA films. Moreover, the authors intended to correlate the specific essential work of fracture (w_e) with the normalized mechanical work at break using SPT.

This work aims to evaluate the applicability of the SPT to study the ductile-brittle transition of PLA films with two different contents of organically modified montmorillonite (o-MMT) during the physical aging process. In addition, the effect of the o-MMT on the PLA physical aging kinetics was investigated.

2. Experimental

2.1. Materials and processing

A commercial PLA extrusion grade (Ingeo 2002D[®], NatureWorks, Arendonk, Belgium) characterized by a MFI (210°C/2.16 kg) of 5.8±0.2 dg/min and a nominal D-enantiomer lactide content of 4.25% mol. was used in this study. An organically modified montmorillonite (o-MMT) clay (Cloisite[®] 30B) purchased from Southern Clay Products (USA) in powder form was used as a filler. The clay was modified with a Methyl-tallow-bis-2-hydroxyethyl ammonium salt (MT2EtOH) and was characterized by a density of 1.98 g·cm⁻³, loss on ignition of about 30 wt% and an interlaminar distance d_{001} of 1.85 nm. Melt compounding of the o-MMT and PLA was performed in a twin-screw extruder 25 mm $L/D = 36$ (KNETER 25X24D, COLLIN, Ebersberg, Germany). The screw speed was set to 85 rpm and the temperature profile was established from 145°C in the feed section to 200°C in the die. Films with a nominal thickness (t) of 400 µm and 100 mm nominal width were calendered (Techline CR72T, COLLIN, Ebersberg, Germany).

Prior to processing, PLA was dried for 3 h at 80°C in a hopper-dryer (DSN 506HE, Piovan, Venice, Italy) with a dew point of -40°C and kept under the same conditions during the whole process. o-MMT was dried at 130°C for 22 hours using a convection oven (J. P. Selecta, S. A., Barcelona, Spain).

Using the above described processing parameters, two PLA/o-MMT films were obtained with a mean o-MMT concentration of 0.5±0.1 wt% (PLA-C0.5) and 2.5±0.1 wt% (PLA-C2.5). Using similar extrusion conditions, neat PLA (PLA) films were prepared. More details on films manufacturing can be found in [22].

Previous studies showed that under the used processing conditions, all films were amorphous, according to the differential scanning calorimetry (DSC) results obtained from the first heating cycle (30–200°C) at 10°C·min⁻¹. On the other hand, Transmission Electronic Microscopy (TEM) analysis exhibited a homogeneous distribution of o-MMT particles, irrespective of its contents (Figure 1a), with some intercalation and exfoliation (Figure 1b) which was verified by WAXS tests [22].

A ‘De-aging’ thermal treatment was applied to the films in order to release internal stresses and to avoid excessive defects during sample cutting due

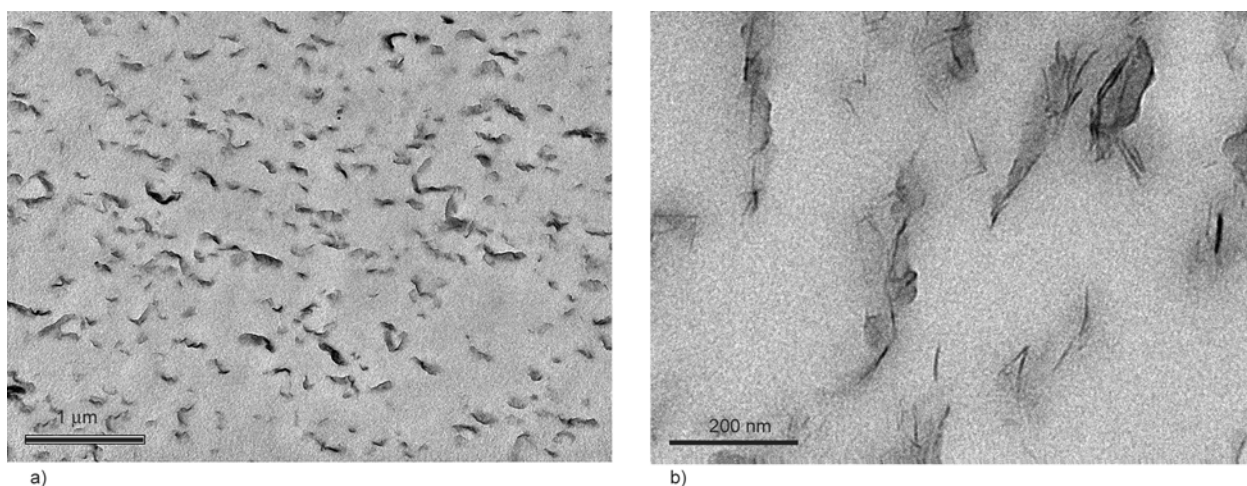


Figure 1. TEM micrograph of PLA films with 2.5 wt% of o-MMT (PLA-C2.5). a) general view ($\times 17\,000$) and b) higher magnification view ($\times 90\,000$).

to their pronounced brittleness. Films were heated to $60\pm 1^\circ\text{C}$ for 20 min in a convection oven (J. P. Selecta, S. A., Barcelona, Spain) and subsequently quenched in an ice water bath ($2\pm 2^\circ\text{C}$) for 5 min. After drying, specimens for the mechanical and fracture tests were immediately extracted from the centre of the films. Prior to testing, several sample sets were stored at room conditions ($23\pm 2^\circ\text{C}$, 50% RH) for different aging times (t_a) ranging from 10^4 to $2.6\cdot 10^5$ min.

Mechanical and fracture tests were carried out on samples aged for different t_a . ‘De-aged’ samples (referred to as D_a) were tested immediately after the end of the thermal treatment ($t_a = 0$ min). A period of 6 months ($t_a = 2.6\cdot 10^5$ min) was verified as sufficiently long to reach a mechanically stable aged state (*i.e.* regardless of t_a , all tested samples exhibited similar deformation behaviours and consistent mechanical parameters). This group of samples was referred to as ‘equilibrated aged’ samples.

2.2. Essential work of fracture (EWF) tests

The fracture characterisation was based on the Post-Yielding Fracture Mechanics through the Essential Work of Fracture (EWF) methodology. The theoretical basis, experimental procedure and data reduction have been extensively described in the previous works of Martinez *et al.* [23], Bárányi *et al.* [24] and the ESIS-TC4 test protocol [25]. The fracture parameters are obtained from linear fitting of the specific work of fracture (w_f) vs. ligament length (l). From the linear regression, the specific essential work of fracture (w_e) and the non-essential or ‘plastic’ term (βw_p) are obtained using Equation (1):

$$w_f = w_e + \beta w_p l \quad (1)$$

Three main preconditions have to be fulfilled in order to properly analyse the EWF results: (1) (l) of the specimens should be in a range that guarantees a full ligament yielding prior to the crack propagation onset; (2) a self-similarity of the load-displacement curves between each ligament length should be observed to ensure a similar fracture process between all samples; and (3) the process should take place in a pure plane-stress state condition for the whole range of l considered [23–25].

In this work, EWF analysis was performed using deeply double-edge notched tension (DDENT) specimens. Samples were extracted from the centre of the film, parallel to the MD direction and using the following dimensions: Length $L = 100$ mm, width $W = 50$ mm. The considered nominal ligament length (l_n) was in the range of 4 and 26 mm. Prior to testing, initial cracks were sharpened using a fresh razor blade.

Fracture tests were carried out on a universal testing machine (SUN 2500, GALDABINI, Cardano al Campo, Italy) equipped with a 5 kN load cell at a constant crosshead speed of 1 mm/min and at $23\pm 2^\circ\text{C}$ and 50% RH. The displacement was measured using a video extensometer (OS-65D CCD, Minstron, Taipei, Taiwan) coupled to a Windows-based software (Messphysik, Material Testing, Fürstenfeld, Austria), according to the procedure described in a previous work [26].

After testing, a binocular microscope (Carton, Pathumthani, Thailand) was used to determine the

accurate ligament lengths (l) and to observe the whole deformation and fracture process zone.

In order to make the self-similarity verification and selection of valid load (P)-displacement (d) traces from fracture tests, curves of nominal engineering stress (σ_N) (Equation (2)) against normalized displacement (d_N) (Equation (3)) for each group of samples were constructed. Those curves that did not overlap until the crack onset propagation region within a 5% confidence band or showed some unexpected cross in the propagation (tear) region were discarded.

$$\sigma_N = \frac{P}{l \cdot t_r} \quad (2)$$

$$d_N = \frac{d}{l} \quad (3)$$

Fracture surfaces of selected DDENT specimens were inspected using scanning electronic microscopy (SEM) JEOL JSM 5610 (Jeol, Tokyo, Japan) with an acceleration voltage of 10 kV. The fracture surfaces were sputter coated with a thin Au/Pd layer using a Bal-Tec SCD005 Sputter Coater (Bal-Tec, Liechtenstein).

2.3. Small punch tests

In Figure 2 is sketched the experimental SPT mechanism with the sample geometry and dimensions. The punch was connected to an universal testing machine (MTS Sinergy, Roissy-en-Brie, France) equipped with a 5 kN load cell. Samples are placed on the lower matrix, which has a 4 mm diameter hole with a 0.2 mm fillet radius. The specimen is firmly clamped by means of a threaded fixer and the load is applied by a 2.5 mm hemispherical diameter

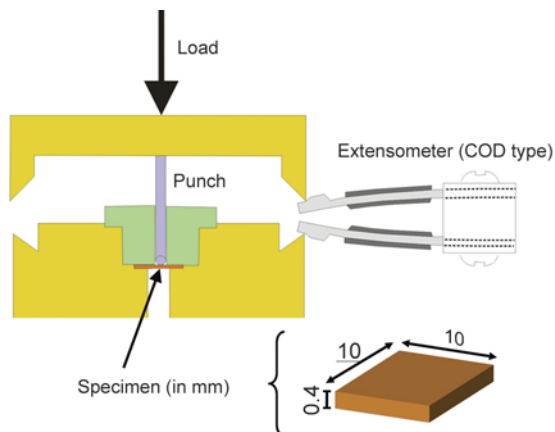


Figure 2. Sketch of the SPT device used and specimen dimensions

punch. A COD type extensometer is used to measure the punch displacement (d) [27, 28].

Tests were carried out at room conditions ($23 \pm 2^\circ\text{C}$ and 50% RH) and at constant crosshead speed of $0.2 \text{ mm} \cdot \text{min}^{-1}$. The specimens were tested at different physical aging times (t_a) as described in section 2.1. A minimum of ten samples were used to characterise each material at each t_a . The mechanical work at break (W_b) was calculated as the area up to the rupture point of the load-punch displacement curves. W_b was normalized by the squared of the specimen thickness (t), W_b/t^2 .

2.4. Thermal characterization

The effect of o-MMT on the rate of physical aging at 30°C was investigated using a differential scanning calorimeter (DSC) (Pyris 1 coupled to a 2P intracooler, Perkin Elmer, Waltham, MA, USA) under a dry nitrogen atmosphere. Temperatures as well as heat of transition were calibrated with lead and indium at $10^\circ\text{C}/\text{min}$.

About 5–6 mgs of each material were encapsulated in aluminium pans. A total of 8 thermal cycles as shown in Figure 3 was performed with the following t_a : 0, 10, 30, 70, 100, 300, 700 and 1000 min. The last heating scan (ramp c) was programmed to record the DSC trace of the aged sample. For an aging time of 10^4 min (7 days) the thermal treatment was performed using an encapsulated sample and stored in a controlled convection oven.

In order to improve accuracy and to minimize the errors brought by baseline fluctuations and calibrations, this procedure were repeated three times using fresh samples taken from different zones of the film.

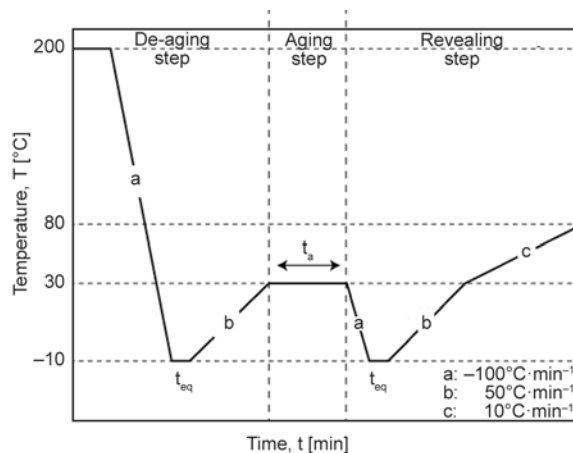


Figure 3. DSC thermal protocol used to investigate the rate of enthalpy relaxation at 30°C

The thermal fatigue degradation of samples was verified after completing the thermal protocol. Such verification was performed according to the procedure described in a previous work [17].

From the heating scan of ramp c, the enthalpy relaxation (or enthalpy recovery) (δ_H) for each aging time (t_a) was calculated as the difference in area between the heating scan of isothermally aged samples and the heating scan of the quenched reference sample. The overall enthalpy relaxation rate (β_H) of a bulk sample, which is a reasonable indicator of the aging kinetics, may be estimated from the slope of δ_H as a function of the $\log t_a$ according to Equation (4) [13, 29]:

$$\beta_H = \frac{d\delta_H}{d(\log t_a)} \quad (4)$$

As a result of the current aging temperature (30°C), a significant annealing time was required to reach a complete material structural equilibrium. Therefore, freshly de-aged samples were aged for 6 months at room temperature (23±2°C, 50% RH) and thereafter heated from 30 to 80°C at 10°C·min⁻¹ in order to reveal their aged state.

3. Results and discussion

Figure 4 shows typical engineering stress (σ_N) vs. normalized displacement (d_N) curves obtained from the EWF tests of de-aged ($t_a = 0$ min) and ‘equilibrated aged’ ($t_a = 6$ month) samples.

Using a Digital Image Correlation (DIC) analysis [17, 18], it was observed that for both groups of sample, the yielding process was initiated well before the maximum load was reached and from both sharpened cracks. As an example, the crack propagation onset was observed at the point indicated by the arrows as shown in Figure 4. Although ‘de-aged’ samples (Figure 4a) showed full ligament yielding before crack propagation, ‘equilibrated aged’ samples (Figure 4b) exhibited the crack propagation onset prior to the complete plastic collapse of the ligament.

According to Bárányi *et al.* [24], ‘the best EWF model material’ would show a curve similar to the one observed in Figure 4a. This is usually obtained from amorphous polymers which are prone to fail by shear yielding in the used test conditions. The last observation could invalidate the applicability of the EWF concept for the ‘equilibrated aged’ samples (Figure 4b).

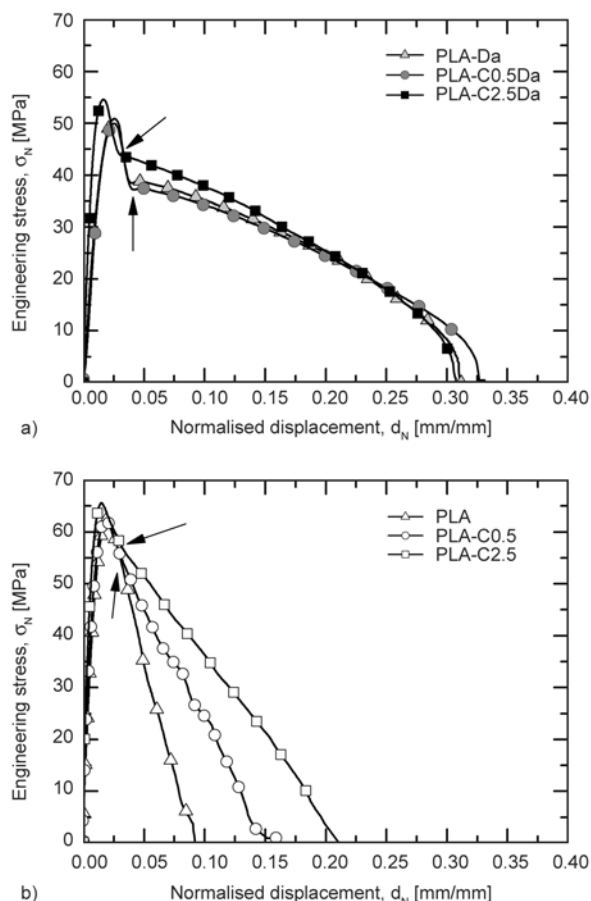


Figure 4. Typical engineering stress (σ_N) vs. normalized displacement curves (d_N) for (a) De-aged ($t_a = 0$ min) (Da) and (b) ‘equilibrated aged’ ($t_a = 6$ months) DDENT samples. $l_n = 15$ mm. Arrows indicate the onset of crack propagation.

Qualitatively, it can be seen that the largest differences are observed for ‘equilibrated aged’ samples, especially in the tearing stage (crack propagation). As shown in Figure 4b, PLA-C2.5 seems to show a greater tear resistance as compared to PLA and PLA-C0.5. For de-aged samples, these differences seem to be minimized due to the large similarity between all measurements. However, it is obvious that the stress level required to initiate the crack propagation was superior for PLA-C2.5Da samples.

Although ‘equilibrated aged’ samples did not fulfil all EWF analysis requirements, a comparative quantitative study of the performance of the composite films under these two thermodynamic conditions was performed using the EWF methodology.

As shown in Figure 5, both groups of samples showed a linear relationship between w_f and l , which allows the calculation of the parameters w_e and β_{w_p} (*c.f.* Equation (1)). Results are compiled in Table 1.

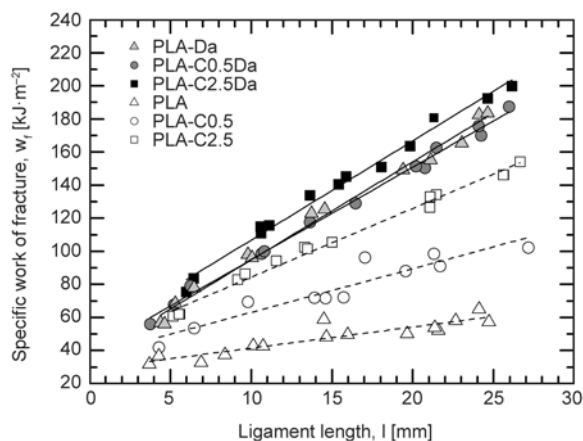


Figure 5. Specific work of fracture (w_f) vs. ligament length (l) for all investigated samples

Table 1. Fracture parameters obtained from the specific work of fracture analysis

Material	w_e [kJ·m ⁻²]	βw_p [MJ·m ⁻³]	R^2
‘De-aged’ (t_a: 0 min)			
PLA-Da	36±3	5.9±0.2	0.990
PLA-C0.5Da	39±2	5.6±0.1	0.995
PLA-C2.5Da	47±2	6.0±0.2	0.989
‘Equilibrated aged’ (t_a: 6 months)			
PLA	29±3	1.3±0.2	0.820
PLA-C0.5	37±5	2.6±0.3	0.885
PLA-C2.5	43±3	4.2±0.1	0.990

According to the correlation coefficient (R^2) values, de-aged samples exhibited the best linear fitting.

The obtained results confirm the previous observations made from the preliminary analysis of σ_N vs. d_N curves:

- Although slight differences were observed between all fracture parameters for ‘de-aged’ samples, PLA-C2.5Da exhibited the highest w_e value.
- A greater influence of the o-MMT particles on the fracture parameters was observed for ‘equilibrated aged’ samples. With increasing the o-MMT amount, the fracture parameters increased, which is apparently observed for the non-essential term (βw_p), commonly associated to the crack propagation resistance.

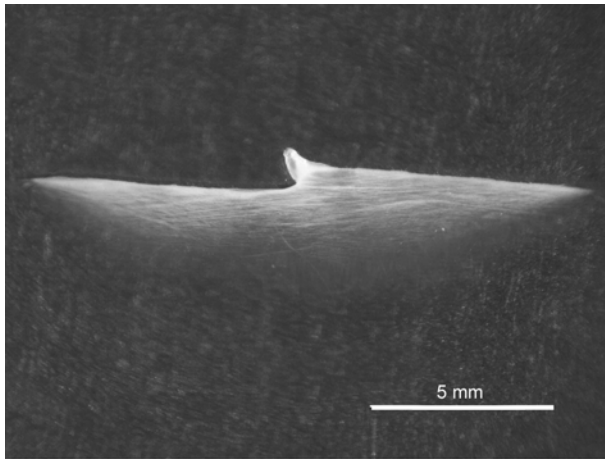
Regarding ‘equilibrated aged’ samples, a physical meaning can be correlated to the observed trend if the deformation process is considered. According to Karger-Kocsis and Czigány [30], shear banding via network stretching appeared to be the dominant deformation mechanism in the whole fracture and deformation process zone of amorphous thermoplastic polyesters. After being placed PLA and PLA-Da tested samples above T_g (60°C) for 10 min, this net-

work stretching mechanism was confirmed for both groups due to the complete recovery of the stretched region. However, when similar experiments were applied to the PLA-oMMT samples, partial recovery was observed which indicates that some true plastic or irreversible deformation micro-mechanism was operating.

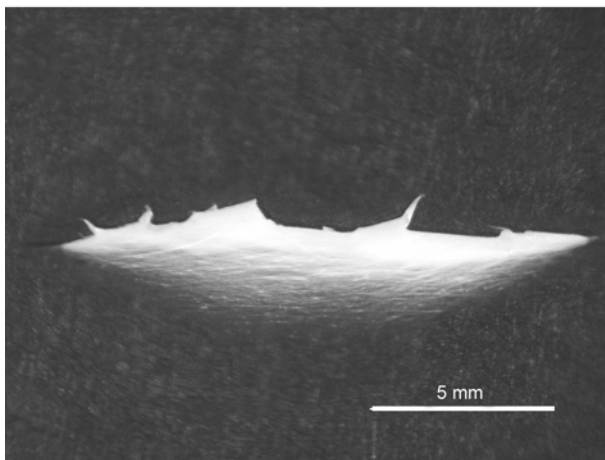
Figure 6 depicts optical micrographs of the fracture process zone of all ‘equilibrated aged’ samples. While PLA samples exhibited several long crazes surrounding the plane of crack propagation, this scenario substantially changed when o-MMT was added. By increasing the o-MMT content, the size of the whitening zone was enlarged. A larger proportion of shorter crazes was observed, which became thinner and better defined as the clay content increased (*c.f.* Figures 6b and 6c). This behaviour is frequently associated to an increasing content of irreversible deformation micro-mechanisms in the Outer ‘Plastic’ Deformation Zone (OPDZ).

The fractured surfaces of all ‘equilibrated aged’ samples were observed using SEM as shown in Figure 7. Ahead of the crack tip, PLA samples (Figure 7a) showed a typical brittle topography with a smooth surface. This aspect was due to the formation of long crazes as deformation micro-mechanism. Nevertheless, an increasing content of voiding and plastic deformation was observed with increasing o-MMT amount for PLA/o-MMT films. These observations suggest that the deformation process in the composite films results from a combination of matrix crazing and o-MMT/matrix debonding in form of voiding (cavitation) which releases the local triaxiality. For further loading, these voids and crazes grew with extensive fibrillation (shear yielding), which gives rise to the distortion and coalescence of the holes (*c.f.* Figure 7b and 7c) with ridge formation. Similar observations have been reported in Poly(propylene-block-ethylene) (EPBC) and PETG modified with several types of nanofillers, including the same o-MMT used in the current study [31]. All of these mechanisms led to the generation of a larger plastic deformation in the studied films which induced increasing βw_p values with o-MMT content.

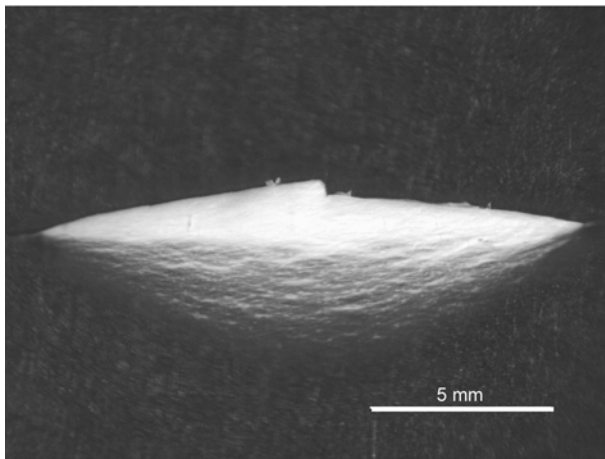
Although an obvious contribution of the o-MMT particles was observed in the increasing toughness of ‘equilibrated aged’ PLA samples, the effect of the o-MMT on the PLA physical aging kinetics should also be considered.



a)



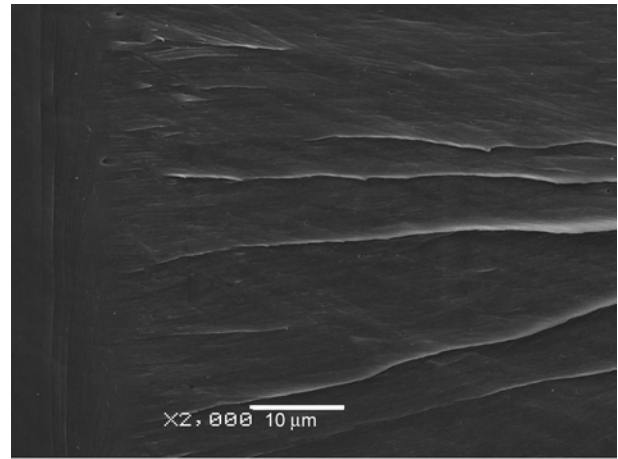
b)



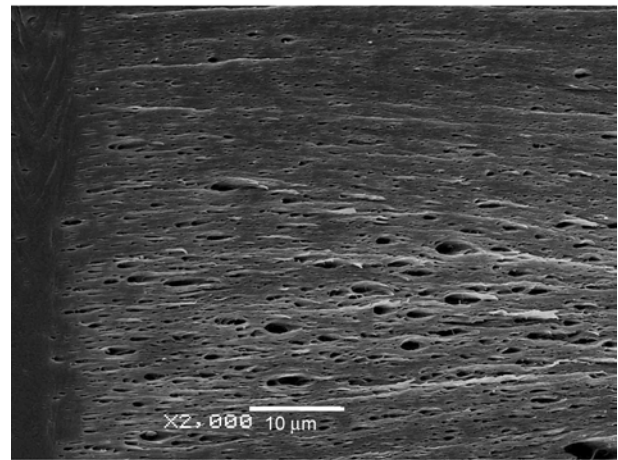
c)

Figure 6. Optical micrographs of the process zone after testing of a) PLA; b) PLA-C0.5; and c) PLA-C2.5

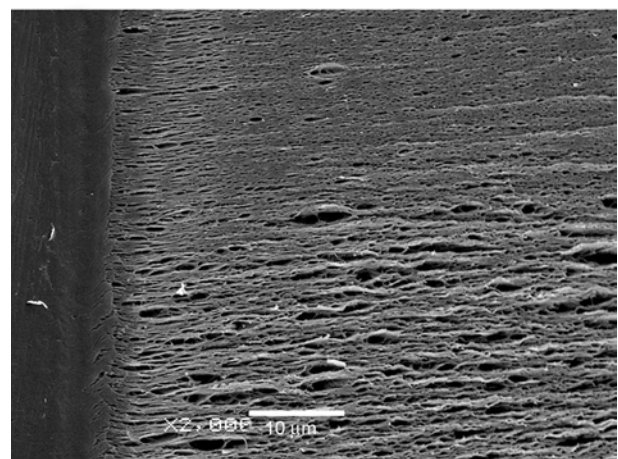
Regarding aged samples for different t_a (24, 48 h, 7 and 20 days), an attempt to perform an EWF analysis was done. However, non-consistent self-similar curves and erratic strain field distributions in the OPDZ and in the inner fracture process zone (IFPZ) were measured. This finding was attributed to the transient behaviour from ductile to brittle.



a)



b)



c)

Figure 7. SEM micrographs of the fracture surface of a) PLA; b) PLA-C0.5; and c) PLA-C2.5

As SPT experiments are less time consuming than EWF tests, the transient mechanical behaviour at a predetermined t_a may be monitored with more accuracy. Therefore, this work was complemented with SPT experiments in order to investigate the transient fracture behaviour.

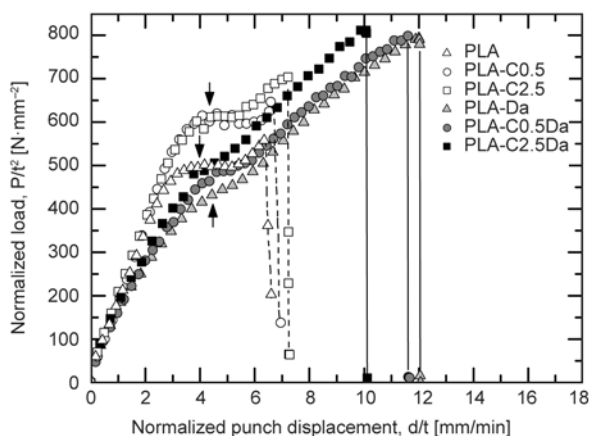


Figure 8. Typical SPT curves normalized by specimen thickness for ‘equilibrated aged’ and ‘de-aged’ materials. Arrows indicate the yielding region.

Figure 8 displays representative SPT load-punch displacement curves of all investigated samples. Regarding ‘equilibrated aged’ samples, the load increased and reached a first maximum value (P_y , indicated by an arrow) upon loading. Then, after a small load drop, a new increase in the load was registered until the final rupture of the sample. This last situation seems to indicate that a strain hardening process was taking place upon loading.

By comparing SPT curves to those of a conventional tensile test for these samples [32], a possible correlation may be established between the zone around P_y in SPT and the yield zones in the tensile tests.

The SPT load-punch displacement curves of ‘de-aged’ materials slightly differ from those of the ‘equilibrated aged’ samples. While de-aged samples exhibited a significant decrease in stiffness (slope in the initial zone of the curve), a considerable increase in ductility (displacement at break) was measured. The described behaviour is clearly appreciable for pristine samples. Moreover, the yielding zone is not easily observed due to a constant increase in the load with respect to the punch displacement upon loading. It is believed that yielding and strain hardening processes occurred simultaneously.

Figure 9 shows the variation of normalized work at break (W_b/t^2) with respect (t_a). Unlike EWF results, W_b/t^2 exhibited similar values during the first 17 h (0.7 days) for all samples. Then, pristine PLA samples showed a monotonous decrease of W_b/t^2 with t_a up to 42 days, where an equilibrated state seemed to be reached. A completely different scenario was observed for PLA/o-MMT samples. The presence

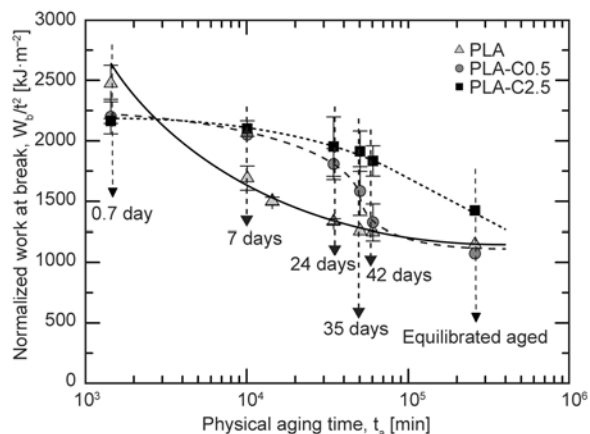


Figure 9. Variation of the normalised work at break (W_b/t^2) vs. aging time (t_a)

of o-MMT seems to decelerate the trend previously described; this was more noticeable for larger amounts of o-MMT. After 7 days, PLA-C2.5 has a loss of only 3% of the aforementioned parameter and 7% in the case of PLA-C0.5. At 35 days the PLA-C2.5 still exhibits a rather ductile behaviour with a loss of 12% in W_b/t^2 , while PLA-C0.5 has an intermediate behaviour, reporting a loss of 28%.

After 42 days ($6 \cdot 10^4$ min) the W_b/t^2 value of PLA-C0.5 converged to the one of unfilled PLA, while for PLA-C2.5 no such trend was observed. The ‘equilibrated aged’ group of samples (tested at $t_a = 6$ months), showed very similar values between PLA and PLA-C0.5 and still a larger value for PLA-C2.5, which is in line with the we trend previously reported (*cf.* Table 1).

Taking into account these results, three questions arise: Does o-MMT only change the failure mode, thereby influencing toughness?; 2) Does o-MMT affect the kinetics of physical aging?; or 3) Do both mechanisms operate simultaneously?

In order to answer these questions and to obtain more information about the physical aging process, the rate of enthalpy relaxation (β_H), associated to the aging kinetics, was determined using DSC measurements. Based on the heating scans of samples aged at 30°C during different and well controlled t_a , enthalpy relaxation (δ_H) was determined for each aged sample and plotted as a function of $\log t_a$ (Figure 10). From the slope of this linear representation the β_H value was determined [13, 17, 29].

As shown in Figure 10, only PLA samples exhibited a nearly linear relation in the whole range of t_a considered. Similar behaviour has been reported by Cailloux *et al.* [17] up to 6 months. However, this

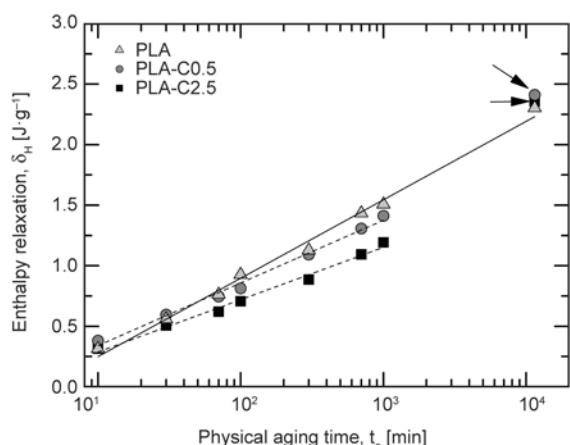


Figure 10. Determination of the rate of enthalpy relaxation (β_H) from the enthalpy relaxation (δ_H) versus $\log t_a$. For PLA-oMMT materials, values indicated by the arrow were not taken into the linear fitting. Relative errors of all δ_H measurement were lower than 5%.

behaviour changed substantially with the incorporation of o-MMT. For PLA/o-MMT films, the linear relationship between δ_H and $\log t_a$ remained solely valid up to 17 h (10^3 min). For longer t_a (10^4 min) the measured enthalpy relaxation converged to the values obtained for unfilled PLA (indicated by the arrows in Figure 10).

As compared to PLA samples, the non-linearity exhibited by all PLA/o-MMT samples suggest that the overall rate of enthalpy relaxation should be described by at least two values in the range of t_a analysed. Nevertheless, for comparative purposes, a linear fitting analysis was performed up to 10^3 min. Results are given in Table 2. The high correlation coefficient obtained suggests reliable data and the measured β_H value for PLA samples was in close agreement with previous works [17].

As shown in Table 2, the rate of enthalpy relaxation decreased with increasing o-MMT content. Although the calculated parameter should be considered only relative, the overall trend of the enthalpy relaxation (or enthalpy recovery) shown in Figure 10 indicates

Table 2. Enthalpy relaxation rate (β_H) at 30°C for all investigated samples

Material	β_H [J·g ⁻¹ per decade min]	R^2
PLA	0.65±0.02	0.992
PLA-C0.5	0.52±0.02	0.991
PLA-C2.5	0.43±0.02	0.989

that there is a broader distribution of relaxation times compared to pristine PLA.

This behaviour is in line with the domain relaxation model proposed by Lu and Nutt [33] in their study of epoxy-oMMT nanocomposites. Taking into account that the enthalpy relaxation during the physical aging process is related to the degree of chain segmental relaxation, the lower enthalpy relaxation of PLA/o-MMT composites can be ascribed to the slower relaxation rate of PLA chain segments arising from o-MMT restrictions in this range of t_a . According to this model, the rate of these relaxations is expected to vary with the distance from the nanoparticle surface, interaction degree between o-MMT-polymer, and the type of o-MMT dispersion (exfoliation or intercalation). In addition, the overall relaxation behaviour of nanocomposites is expected to depend on the ratio of restricted and unrestricted segment numbers which gives rise to a strong dependence on filler content.

As depicted in Figure 10, an equivalent thermodynamical state was measured for all samples aged for 7 days (10^4 min). Although not shown in this plot, this observation was also verified for longer t_a where a similar value of δ_H (3.4 ± 0.2 J·g⁻¹) was measured for samples aged for 6 months at 30°C and 50% RH. This behaviour suggests that for long annealing times (*i.e.* $t_a \geq 10^4$ min), the δ_H extend remains uninfluenced by the o-MMT particles but solely by the intrinsic aging kinetics of the PLA matrix.

Regarding mechanical performances, SPT results showed significant differences between pristine PLA and PLA/o-MMT materials aged for $t_a \geq 10^4$ min. As previously observed, these differences could be solely attributed to the toughening effect of the o-MMT and not to a change in the physical aging kinetics of the PLA matrix.

With respect to PLA-C0.5 samples, the toughening effect induced by the o-MMT appeared to be ineffective for $t_a \geq 42$ days. For higher o-MMT contents (PLA-C2.5), the toughening level was almost maintained (66% of the initial values) for samples aged up to 6 months. These observations suggest that the toughening micro-mechanisms promoted by the addition of o-MMT (contribution of cavitation/crazing/shear yielding) are insufficient to compensate or to alleviate the brittleness of PLA matrix due to the physical aging process.

4. Conclusions

The SPT appears to be an effective tool for the mechanical characterization of the ductile-brittle transition during the physical aging at $23\pm 2^\circ\text{C}$ of PLA/o-MMT films. It was possible to evaluate the transient ductile-to-brittle behaviour and the necessary time to complete the aforementioned transition.

During the first 17 h, the enthalpy relaxation analysis indicated that the rate of physical aging decreased with increasing o-MMT content. From a thermodynamical point of view, all systems were equivalent after being aged for 1 week. However, in terms of mechanical performance, significant differences were observed. These mechanical differences could not only be attributed to the change in the kinetics of the physical aging process, but also to the toughening mechanisms involved: o-MMT/matrix debonding or cavitation and simultaneous multiple crazing as well as shear yielding of the PLA matrix.

Acknowledgements

The authors would like to acknowledge the financial support from the Ministerio de Economía y Competitividad (Government of Spain) through the projects: MAT2010-19721-C02-01, MAT2011-28796-C03-03, MAT2013-40730-P.

References

- [1] Garlotta D.: A literature review of poly(lactic acid). *Journal of Polymers and the Environment*, **9**, 63–84 (2001).
DOI: [10.1023/A:1020200822435](https://doi.org/10.1023/A:1020200822435)
- [2] Auras R., Harte B., Selke S.: An overview of polylactides as packaging materials. *Macromolecular Bioscience*, **4**, 835–864 (2004).
DOI: [10.1002/mabi.200400043](https://doi.org/10.1002/mabi.200400043)
- [3] Briassoulis D.: An overview on the mechanical behaviour of biodegradable agricultural films. *Journal of Polymers and the Environment*, **12**, 65–81 (2004).
DOI: [10.1023/B:JOOE.000010052.86786.ef](https://doi.org/10.1023/B:JOOE.000010052.86786.ef)
- [4] Ogata N., Jimenez G., Kawai H., Ogihara T.: Structure and thermal/mechanical properties of poly(l-lactide)-clay blend. *Journal of Polymer Science Part B: Polymer Physics*, **35**, 389–396 (1997).
DOI: [10.1002/\(SICI\)1099-0488\(19970130\)35:2<389::AID-POLB14>3.0.CO;2-E](https://doi.org/10.1002/(SICI)1099-0488(19970130)35:2<389::AID-POLB14>3.0.CO;2-E)
- [5] Karger-Kocsis J., Kéki S.: Biodegradable polyester-based shape memory polymers: Concepts of (supra) molecular architecturing. *Express Polymer Letters*, **8**, 397–412 (2014).
DOI: [10.3144/expresspolymlett.2014.44](https://doi.org/10.3144/expresspolymlett.2014.44)
- [6] Imre B., Renner K., Pukánszky B.: Interactions, structure and properties in poly(lactic acid)/thermoplastic polymer blends. *Express Polymer Letters*, **8**, 2–14 (2014).
DOI: [10.3144/expresspolymlett.2014.2](https://doi.org/10.3144/expresspolymlett.2014.2)
- [7] Cailloux J., Santana O. O., Franco-Urquiza E., Bou J. J., Carrasco F., Gámez-Pérez J., MasPOCH M. L.: Sheets of branched poly(lactic acid) obtained by one step reactive extrusion calendaring process: Melt rheology analysis. *Express Polymer Letters*, **7**, 304–318 (2013).
DOI: [10.3144/expresspolymlett.2013.27](https://doi.org/10.3144/expresspolymlett.2013.27)
- [8] Raquez J-M., Habibi Y., Murariu M., Dubois P.: Polylactide (PLA)-based nanocomposites. *Progress in Polymer Science*, **38**, 1504–1542 (2013).
DOI: [10.1016/j.progpolymsci.2013.05.014](https://doi.org/10.1016/j.progpolymsci.2013.05.014)
- [9] Miyata T., Masuko T.: Crystallization behaviour of poly(L-lactide). *Polymer*, **39**, 5515–5521 (1998).
DOI: [10.1016/S0032-3861\(97\)10203-8](https://doi.org/10.1016/S0032-3861(97)10203-8)
- [10] Lim L-T., Cink K., Vanyo T.: Processing of poly(lactic acid). in ‘Poly(lactic acid): Synthesis, structures, properties, processing and applications’ (eds.: Auras R., Lim L. T., Selke S. E. M., Tsuji H.) Wiley, Hoboken, 189–215 (2010).
- [11] Lim L-T., Auras R., Rubino M.: Processing technologies for poly(lactic acid). *Progress in Polymer Science*, **33**, 820–852 (2008).
DOI: [10.1016/j.progpolymsci.2008.05.004](https://doi.org/10.1016/j.progpolymsci.2008.05.004)
- [12] Pluta M., Murariu M., Alexandre M., Galeski A., Dubois P.: Polylactide compositions. The influence of ageing on the structure, thermal and viscoelastic properties of PLA/calcium sulfate composites. *Polymer Degradation and Stability*, **93**, 925–931 (2008).
DOI: [10.1016/j.polymdegradstab.2008.02.001](https://doi.org/10.1016/j.polymdegradstab.2008.02.001)
- [13] Pan P., Zhu B., Inoue Y.: Enthalpy relaxation and embrittlement of poly(L-lactide) during physical aging. *Macromolecules*, **40**, 9664–9671 (2007).
DOI: [10.1021/ma071737c](https://doi.org/10.1021/ma071737c)
- [14] Karger-Kocsis J., Bárány T., Moskala E. J.: Plane stress fracture toughness of physically aged plasticized PETG as assessed by the essential work of fracture (EWF) method. *Polymer*, **44**, 5691–5699 (2003).
DOI: [10.1016/S0032-3861\(03\)00590-1](https://doi.org/10.1016/S0032-3861(03)00590-1)
- [15] Bárány T., Ronkay F., Karger-Kocsis J., Czigány T.: In-plane and out-of-plane fracture toughness of physically aged polyesters as assessed by the essential work of fracture (EWF) method. *International Journal of Fracture*, **135**, 251–265 (2005).
DOI: [10.1007/s10704-005-3947-2](https://doi.org/10.1007/s10704-005-3947-2)
- [16] Bárány T., Földes E., Czigány T.: Effect of thermal and hygrothermal aging on the plane stress fracture toughness of poly(ethylene terephthalate) sheets. *Express Polymer Letters*, **1**, 180–187 (2007).
DOI: [10.3144/expresspolymlett.2007.28](https://doi.org/10.3144/expresspolymlett.2007.28)

- [17] Cailloux J., Santana O. O., Franco-Urquiza E., Bou J. J., Carrasco F., Maspoch M. L.: Sheets of branched poly(lactic acid) obtained by one-step reactive extrusion–calendering process: Physical aging and fracture behavior. *Journal of Materials Science*, **49**, 4093–4107 (2014).
DOI: [10.1007/s10853-014-8101-y](https://doi.org/10.1007/s10853-014-8101-y)
- [18] Gamez-Pérez J., Velazquez-Infante J. C., Franco-Urquiza E., Pages P., Carrasco F., Santana O. O., Maspoch M. L.: Fracture behavior of quenched poly (lactic acid). *Express Polymer Letters*, **5**, 82–91 (2011).
DOI: [10.3144/expresspolymlett.2011.9](https://doi.org/10.3144/expresspolymlett.2011.9)
- [19] Giddings V. L., Kurtz S. M., Jewett C. W., Foulds J. R., Edidin A. A.: A small punch test technique for characterizing the elastic modulus and fracture behavior of PMMA bone cement used in total joint replacement. *Biomaterials*, **22**, 1875–1881 (2001).
DOI: [10.1016/S0142-9612\(00\)00372-0](https://doi.org/10.1016/S0142-9612(00)00372-0)
- [20] Jaekel D. J., MacDonald D. W., Kurtz S. M.: Characterization of PEEK biomaterials using the small punch test. *Journal of the Mechanical Behavior of Biomedical Materials*, **4**, 1275–1282 (2011).
DOI: [10.1016/j.jmbbm.2011.04.014](https://doi.org/10.1016/j.jmbbm.2011.04.014)
- [21] Rodríguez C., Arencón D., Belzunce J., Maspoch M. L.: Small punch test on the analysis of fracture behaviour of PLA-nanocomposite films. *Polymer Testing*, **33**, 21–29 (2014).
DOI: [10.1016/j.polymertesting.2013.10.013](https://doi.org/10.1016/j.polymertesting.2013.10.013)
- [22] Franco-Urquiza E. A., Cailloux J., Santana O., Maspoch M. L., Velazquez Infante J. C.: The influence of the clay particles on the mechanical properties and fracture behavior of PLA/o-MMT composite films. *Advances in Polymer Technology*, in press (2014).
DOI: [10.1002/adv.21470](https://doi.org/10.1002/adv.21470)
- [23] Martínez A. B., Gamez-Perez J., Sanchez-Soto M., Velasco J. I., Santana O. O., Maspoch M. L.: The essential work of fracture (EWF) method – Analyzing the post-yielding fracture mechanics of polymers. *Engineering Failure Analysis*, **16**, 2604–2617 (2009).
DOI: [10.1016/j.engfailanal.2009.04.027](https://doi.org/10.1016/j.engfailanal.2009.04.027)
- [24] Bárány T., Czigány T., Karger-Kocsis J.: Application of the essential work of fracture (EWF) concept for polymers, related blends and composites: A review. *Progress in Polymer Science*, **35**, 1257–1287 (2010).
DOI: [10.1016/j.progpolymsci.2010.07.001](https://doi.org/10.1016/j.progpolymsci.2010.07.001)
- [25] Clutton E. Q.: Essential work of fracture. in ‘Fracture mechanics testing methods for polymers, adhesive and composites’ (eds.: Moore D. R., Pavan A., Williams J. G.) Elsevier, Oxford, 177–202 (2001).
- [26] Gamez-Perez J., Santana O. O., Martínez A. B., Maspoch M. L.: Use of extensometers on essential work of fracture (EWF) tests. *Polymer Testing*, **27**, 491–497 (2008).
DOI: [10.1016/j.polymertesting.2008.02.002](https://doi.org/10.1016/j.polymertesting.2008.02.002)
- [27] Rodríguez C., Cárdenas E., Belzunce F. J., Betegón C.: Experimental determination of the fracture toughness of steels by means of the small punch test. *Experimental Mechanics*, **53**, 385–392 (2013).
DOI: [10.1007/s11340-012-9637-x](https://doi.org/10.1007/s11340-012-9637-x)
- [28] García T. E., Rodríguez C., Belzunce F. J., Suárez C.: Estimation of the mechanical properties of metallic materials by means of the small punch test. *Journal of Alloys and Compounds*, **582**, 708–717 (2014).
DOI: [10.1016/j.jallcom.2013.08.009](https://doi.org/10.1016/j.jallcom.2013.08.009)
- [29] Hutchinson J. M.: Physical aging of polymers. *Progress in Polymer Science*, **20**, 703–760 (1995).
DOI: [10.1016/0079-6700\(94\)00001-1](https://doi.org/10.1016/0079-6700(94)00001-1)
- [30] Karger-Kocsis J., Czigany T.: Strain rate dependence of the work of fracture response of an amorphous poly (ethylene-naphthalate) (PEN) film. *Polymer Engineering and Science*, **40**, 1809–1815 (2000).
DOI: [10.1002/Pen.11312](https://doi.org/10.1002/Pen.11312)
- [31] Karger-Kocsis J., Khumalo V. M., Bárány T., Mészáros L., Pegoretti A.: On the toughness of thermoplastic polymer nanocomposites as assessed by the essential work of fracture (EWF) approach. *Composite Interfaces*, **20**, 395–404 (2013).
DOI: [10.1080/15685543.2013.807145](https://doi.org/10.1080/15685543.2013.807145)
- [32] Santana O. O., Rodríguez C., Belzunce J., Gámez-Pérez J., Carrasco F., Maspoch M. L.: Fracture behaviour of de-aged poly(lactic acid) assessed by essential work of fracture and J-integral methods. *Polymer Testing*, **29**, 984–990 (2010).
DOI: [10.1016/j.polymertesting.2010.09.004](https://doi.org/10.1016/j.polymertesting.2010.09.004)
- [33] Lu H., Nutt S.: Restricted relaxation in polymer nanocomposites near the glass transition. *Macromolecules*, **36**, 4010–4016 (2003).
DOI: [10.1021/Ma034049b](https://doi.org/10.1021/Ma034049b)

Effect of the solvent type and polymerization conditions on the curing kinetics, thermal and viscoelastic performance of poly(amide-imide) resins

Z. Rasheva*, L. Sorochynska, S. Grishchuk, K. Friedrich

Institut für Verbundwerkstoffe GmbH (Institute for Composite Materials), Erwin-Schrödinger-Str. 58, 67663 Kaiserslautern, Germany

Received 26 September 2014; accepted in revised form 23 November 2014

Abstract. Isothermal and non-isothermal curing kinetics of both N-methyl-2-pyrrolidone (NMP) and N-methylimidazole (MI) based poly(amide-imide) (PAI) resins were investigated by DSC analysis using tightly closed high-pressure crucibles. Several exothermal peaks on the non-isothermal DSC-traces were observed and attributed to the reactions of different functional groups of PAI-resin. Furthermore the final conversion (polymerization degree) of PAI was determined under isothermal conditions, simulating three programs with the post-curing temperatures set as 215, 240 and 270°C. For the MI-PAI based resin, the conversion values were found to be much higher compared to those for the NMP-PAI system. Compared to NMP-based PAI-resin, a shift of the main exothermal peaks to the lower temperatures was observed in the non-isothermal kinetic investigations when MI was used as a solvent. This was accompanied with a reduction of activation energy (E_a) values, as up to a factor of 3 determined by the Flynn-Wall-Ozawa approach for all the main formation reactions. It indicates a catalytic effect of MI on the PAI polymerization.

In addition, conversion values were determined according to the Di Benedetto equation for both systems cured using open molds in the oven. Regardless the different post-curing temperatures, the conversion values were similar for all the samples. Thermal and viscoelastic properties as well as crosslink density (n_c) were also investigated for these systems. It was found that the MI-based samples demonstrate lower n_c values compared to the NMP-based ones at an almost two times higher storage modulus (E') at room temperature.

Keywords: thermosetting resins, curing kinetics, activation energy, crosslink density, storage modulus

1. Introduction

Poly(amide-imide) resins (PAI) are mostly aromatic polymers attractive for a variety of high-performance applications. They are characterized by high thermal stability combined with excellent mechanical properties and chemical resistance [1, 2]. Due to their outstanding sliding and abrasion behaviors they are used as a main polymer in various tribological coatings for sliding machine elements [1].

There are two main industrially applied routes of PAI synthesis: the trimellitic acid chloride (TMAC) and the isocyanate routes [3, 4]. By TMAC tech-

nique, PAI is obtained as a product of polycondensation reaction between an aromatic diamine and trimellitic acid chloride (TMAC). This reaction takes place in organic solvents such as N-methyl-2-pyrrolidone (NMP), dimethylacetamide (DMAC), dimethylformamide (DMF), etc. [5] with release of condensation products (hydrogen chloride (HCl) and water (H₂O)) [3]. Therefore, applicable PAI resins are usually oligomers with quite high conversion of reactive groups of initial monomers. Such pre-polymer route in combination with careful cure procedure guarantees obvious prevention of void

*Corresponding author, e-mail: zdravka.rasheva@gmail.com

formation due to strong reduction of amount of condensation byproducts.

N-methyl-2-pyrrolidone (NMP) has proven itself over the years as the most suitable solvent for PAI-resins. However, after the implementation of the 31st Directive of the Dangerous Substances Classification 67/548/EEC (EEC: European Economic Community) in 2010, there is a reclassification of NMP in Europe from Xi (irritating) to T (toxic). This fact makes an industrial use of NMP-containing PAI-resins complicate and therefore has activated a research on suitable alternative nontoxic solvents for PAI-resins.

The high solvent amount in PAI resins (ca. 60–80 wt%) brings difficulties for investigation of the curing kinetics of these resins by thermal analysis. Some authors report the determination of the curing kinetics of polyimides using FTIR or NMR analysis [6–9]. Detecting the increase of the imide bands intensity during the chemical reaction, the conversion can be determined with quite high accuracy. For this purpose, however, the proportion of starting monomers must be known, which often is not the case for industrially purchased resins.

Another technique widely used for investigation of curing kinetics is thermal analysis using DSC. Usually, for the convenient DSC-measurement, standard aluminium (Al)-crucibles are used, where the sample is not hermetically closed within the pans. However, in case of PAI-resin, the presence of high amount of solvent makes conventional DSC analysis inapplicable, since the exothermal curing reactions are overlapped with endothermal effects of solvent evaporation. On the other hand, the solvent is a media in which the PAI reactions occur. The post-curing reaction is extremely important for the final structure formation and occurs at elevated temperatures, when the solvent is evaporated [7, 10].

In the present study, effect of both curing conditions and solvent type on the polymerization kinetics and final properties of PAI resins was investigated. N-methyl-2-pyrrolidone (NMP) usually used in the standard commercial formulations was replaced with the N-methylimidazole (MI) used as less dangerous alternative solvent. The curing kinetics was investigated by DSC analysis using high-pressure crucibles (HPC). In this case solvent remains trapped in the reaction system and its amount remains constant during the experimental run. The reaction in HPC represents an ‘ideal’ case, since under real

conditions the solvent evaporates mostly during the initial stage of the curing. Although the HPC-measurements represent the ‘ideal’ case, they give an important insight into the curing behavior of PAI-resins. Based on these experiments some conclusions regarding the curing process in ‘real’ case could be drawn.

Further, a non-toxic PAI-resin formulation containing MI as an alternative solvent was developed. MI is a heterocyclic compound, which belongs to the group of the tertiary amines. It has an aromatic structure and is mainly used as a solvent in various chemical processes [11] or as a catalyst for the curing of epoxy resins and polyurethanes [12]. The PAI resins based on N-methylimidazole are more environmentally friendly and are very promising for development of a new generation of PAI systems. Apart from the curing kinetics, a particular attention was paid to the chemical structure, thermal behavior and viscoelastic properties of the cured final materials and results were compared to the state-of-the-art NMP-based PAI-systems.

2. Experimental

2.1. Chemicals used

In the present study an industrially produced PAI-resin based on NMP (Rhodethal 200 ES, Huntsmann Advanced Materials, Switzerland) was compared with a PAI-resin prepared in laboratory, based on MI. Both systems are manufactured following the TMAC technique [3, 13, 14].

To prepare the PAI resin in laboratory, PAI pre-polymer in powder form (Solvay Advanced Polymers, USA) was mixed with the solvent N-methylimidazole (Sigma Aldrich Chemie GmbH, Germany) in proportion 21 to 79 wt%. In the present work, a low viscosity version of PAI, referred to as ‘Torlon[®] 4000T-LV’ was used. Diamine component of Torlon[®] 4000T consists of 30% m-Phenylenediamine (m-PDA) and of 70% 4,4'-Oxydianiline (ODA) [3, 14].

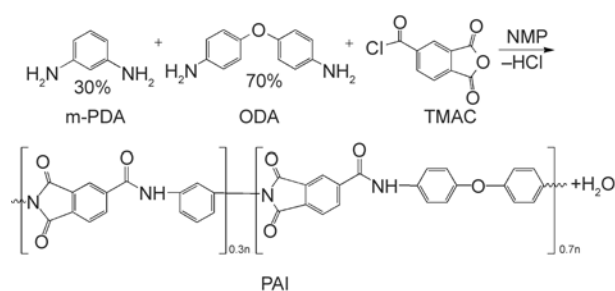


Figure 1. Synthesis of Torlon[®] 4000 T (TMAC route) [14, 13]

The chemical reaction of the PAI-formation of Torlon® 4000T is schematically presented in Figure 1. Polymerisation of the Rhodethal 200 ES follows similar route, however an exact chemical content of the amine components is unknown. Both of the used PAI pre-polymers are partly pre-imidized [5].

2.2. Samples preparation

Investigation of the curing kinetics and the weight loss during chemical reaction was performed for the fresh prepared reactive mixtures of Torlon® 4000T-LV and Rhodethal 200 ES further referred to as MI_TC(L) and NMP_TC(I), respectively. All further experiments (e.g. decomposition range, DMTA analysis viscoelastic properties and crosslink density) were performed using cured PAI-samples.

In order to study an effect of the post-curing conditions on the mechanical properties of PAI, several different curing programs were used for the manufacturing of the samples (Table 1). The list of the samples prepared is given in Table 2 where the post-curing temperature is mentioned in the sample name.

2.3. Testing methods

2.3.1. Fourier transform infrared spectroscopy (FTIR) measurements

FTIR measurements were performed on a Nicolet 510 spectrometer (Wisconsin, USA). Investigation of the PAI films was performed in ATR mode on ZnSe crystal in the transmission mode at 4 cm⁻¹ spectral

resolution in the wavelength range 4000–650 cm⁻¹. Prior to the tests both PAI samples were vacuum dried at 50°C until constant weight.

2.3.2. Thermogravimetric analysis (TGA)

For the investigation of the PAI thermal stability a thermogravimetric analyzer DTG60 (Shimadzu, Japan) was used. For reactive systems, weight loss during the iso-thermal curing conditions was determined. These samples were tested at respective thermal curing programs (c.f. Table 1) in nitrogen atmosphere. Decomposition range of the final cured PAI-samples was determined in a temperature range from 25 to 600°C at a heating rate of 10°C/min and a nitrogen flow of 30 mL/min. An initial samples weight was taken at about 10 mg.

2.3.3. Differential scanning calorimetry (DSC)

The investigations were carried out using DSC1 Mettler Toledo thermal analyzer (Giessen, Germany). Investigation of the curing kinetics of the reactive PAI mixtures by the conventional DSC method, when sample was placed in open Al-crucibles, is particularly difficult due to the high solvent content. In standard aluminum crucibles the reaction peak (exothermic) is overlapped by the peak of the solvent evaporation (endothermic). In order to avoid such effects, DSC measurements were carried out in 40 µL gold-plated steel high-pressure crucibles (HPC) (called as ‘ideal’ case). The samples

Table 1. Applied curing programs

Curing algorithm	Program 1	Program 2	Program 3	Program 4
Start temperature	70°C			
First heating step	20 min; from 70°C to 180°C			
First tempering step	20 min at 180°C			
Second heating step	20 min; from 180°C to 215°C	30 min; from 180°C to 240°C	30 min; from 180°C to 270°C	45 min; from 180°C to 290°C
Second tempering step	1 h at 215°C	1 h at 240°C	1 h at 270°C	20 h at 290°C

Table 2. An overview of the samples tested

Sample name	Solvent used	Resin origin (industrial or laboratory prepared)	Curing program used
NMP_TC(I)_215	N-methyl-2-pyrrolidone (NMP)	Industrial	1
NMP_TC(I)_240			2
NMP_TC(I)_270			3
NMP_TC(I)_290			4
MI_TC(L)_215	N-methyl imidazole (MI)	Laboratory	1
MI_TC(L)_240			2
MI_TC(L)_270			3
MI_TC(L)_290			4

were tested at iso-thermal conditions using the temperature programs, given in Table 1.

For the determination of the activation energy reaction, non-isothermal DSC tests of uncured PAI samples were done in the temperature range of 70–350°C at different heating rates (3, 5.5 and 7°C/min). Determination of the glass transition temperature (T_g) of cured PAI-resins is not an easy task due to the post-curing reactions occurring at high temperatures with elimination of the reaction by-products. From that reason, the cured pure PAI samples were tested by DSC with stochastic temperature modulation (TOPEM®) allowing distinguishing between the total, reversible and non-reversible signals. The total heat flow signal is equivalent to the conventional DSC and is divided for reversible (relaxation related) and non-reversible (kinetics related) signals. For DSC, the measurement temperature range was from 0 to 300°C (or to 350°C in some cases), using a heating rate of 2 K/min with a stochastic modulation of 0.5 K/s, in nitrogen atmosphere. The glass transition temperature (T_g) was determined as a heat capacity drop in the curves of the reversible signal.

2.3.4. Dynamic mechanical thermal analysis (DMTA)

The viscoelastic properties (storage modulus E' and the damping factor $\tan \delta$) of the cured PAI-samples were measured by mean of a dynamic mechanical thermal analyzer DMA Q800 TA Instruments (New Castle, USA). For these studies, samples of pure PAI-resins were prepared as thin films with dimensions of approx. 4 mm×12 mm×0.3 mm and tested in tension mode in the temperature range of 0–375°C, at a frequency of 10 Hz, amplitude of 20 μ m and a heating rate of 3°C/min.

3. Results and discussion

The analysis of the FTIR spectra of both powdered Torlon 4000T-LV and dried Rhodethal 200ES PAI-oligomers showed that both of the studied PAI-resins are quite identical by their chemical structure.

3.1. Non-isothermal curing

At a non-isothermal DSC analysis of PAI in standard aluminum crucibles the exothermic polymerization process is fully overlapped with several endothermic peaks, which correspond to the evaporation of the solvent (202°C for NMP and 198°C for MI

pure solvents), absorbed and reaction by-products. In order to avoid an evaporation of the volatile components and to preserve the constant weight during the DSC measurements, the high pressure crucibles (HPC) were applied for the investigation of the PAI cure kinetics.

Prior to these measurements, the pure solvents (e.g. NMP and MI) used for both reactive PAI-mixtures were also investigated by DSC in HPC (Figure 2). It is worthy to note that in contrary to NMP (Figure 2a) a small exothermal peak was observed for the pure MI (Figure 2b). It indicates a chemical reaction, which occurs, most probably, due to the oxidation reaction of MI in the presence of oxygen and water, absorbed from air [15]. This reaction is observed at relatively high temperatures (above 200°C, Figure 2b). However, at real curing conditions the solvent evaporates before these temperatures achieved suggesting negligible effect of the MI on the polymerization of the MI_TC(L) resin. Nevertheless, it can affect the chemical structure of the PAI in the initial stage of the polymerization process (as long as MI is still present in the reactive system).

The non-isothermal DSC traces of the PAI reaction in the presence of NMP and MI performed in HPC are shown in Figures 3a and 3b, respectively. In order to make a deeper analysis and to evaluate a contribution of the main reactions in the total polymerization process, the DSC curves were deconvoluted using a Gauss-function (dash lines in Figure 3). After deconvolution, five main reaction peaks at ~100, 150, 180, 250 and 300°C are evident for both

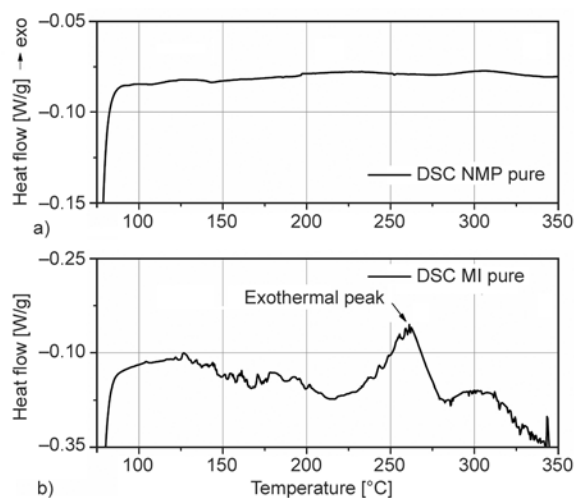


Figure 2. DSC (HPC) analysis of the pure solvents N-methyl-2-pyrrolidone (a) and N-methyl imidazole (b) recorded at 10°C/min heating rate

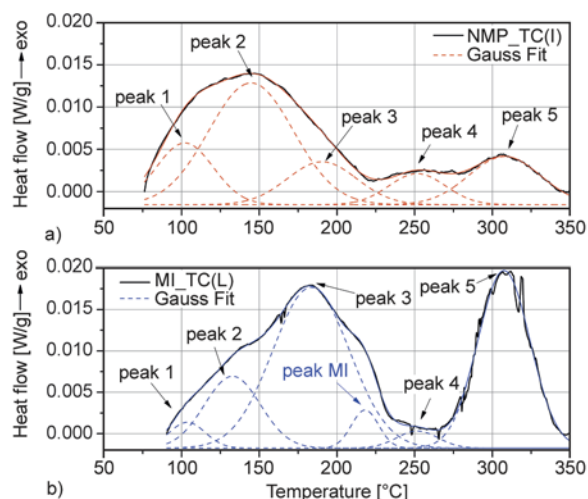


Figure 3. DSC traces of the NMP_TC(I) (a) and MI_TC(L) (b) PAI resins tested at 5.5°C/min heating rate in HPC and their Gauss deconvolutions. Note: All curves were normalized to the respective sample weight and shifted to the baseline for a better representation.

resins. They probably belong to the reactions of the different functional groups [16]. For the MI_TC(L) an additional reaction peak at ~220°C observed in Figure 3b can be very probably attributed to the reaction peak of the pure solvent of Figure 2b. The shift of this peak to the lower temperature in comparison to the pure solvent can be due to the presence of PAI resin.

As it is known, the imidization reaction occurs in several stages [16]. Addition of the dianhydride to a diamine (aminoacylation) in a dipolar aprotic solvent such as MI and NMP leads to the formation of the intermediate poly(amic acids) (PAAc) due to the nucleophilic attack of the aminogroup on the carbonyl carbon of the anhydride. This reaction of an anhydride ring opening is influenced by the solvent used [17]. According to Kreuz *et al.* [16] and Lauver [18], the polyamic acid is formed in form of two con-

formers with different steric structure, i.e. isophthalic (a) and terephthalic (b) shown in Figure 4. This reaction is fast and can occur even under relatively mild conditions. At the same time, the amidization reaction between amino groups of the Cl-anhydride and the diamine occurs. Both of these reactions can be related to the peak 1 and 2 and schematically are presented in Figure 4 as reactions 1 and 2.

The next stage of the polyimidization is the cyclization of the PAAc (intermediate products (a) and (b) in Figure 4) via dehydration.

The high-temperature peaks on the DSC-traces at ~180°C and ~260°C were assigned to the imidization reactions of the different conformers of PAAc (reactions 3 and 4 in Figure 4) [19]. The last high temperature exothermal peak (peak 5 in Figure 3) was assigned to the post-curing reactions of sterically hindered reactive centers.

3.2. Activation energy of polymerization

The non-isothermal integral Flynn-Wall-Ozawa method was applied to estimate the activation energy (E_a) of the PAI curing reactions [20, 21] (Equation (1)):

$$\ln\beta = \ln\frac{AE_a}{g(\alpha)R} - 5.333 - 1.052\frac{E_a}{R T} \quad (1)$$

where β is the heating rate [K/min], E_a is the temperature-dependent activation energy of the polymerization [J/mol], R is the universal gas constant $R = 8.314\text{J}/(\text{mol}\cdot\text{K})$, A is the pre-exponential factor [s^{-1}], $g(\alpha)$ is the integration function of conversion, and T is the peak temperature [K]. The temperatures of the individual peaks were taken from the Gauss deconvolution and the results are presented in Table 3.

As can be seen from the data, the activation energies of two first low temperature reactions, identified in

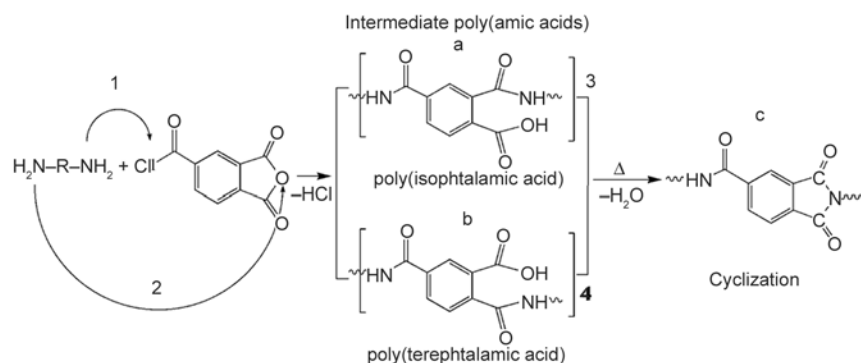


Figure 4. Scheme of the amidization (a, b) and imidization (e.g. cyclization of polyamic acid) reactions (c)

Table 3. Reaction peak temperatures (T_p) at different heating rates and activation energy (E_a) results. The peaks are referred to the reactions proposed in Figure 4.

NMP_TC(I)						
Peak	1	2	3	MI-reaction	4	5
Reaction	Cl-anhydride+ NH ₂	PAAc formation	Cyclisation of isophthalic conformer	MI related	Cyclisation of terephthalic conformer	High temperature post-curing
T_p at 3 C/min	106	140	188	–	249	287
T_p at 5.5 C/min	103	146	191	–	252	307
T_p at 7 C/min	115	163	193	–	264	310
E_a [kJ/mol]	42	46	292	–	102	89
MI_TC(L)						
T_p at 3 C/min	90	120	172	198	232	295
T_p at 5.5 C/min	104	135	183	218	252	308
T_p at 7 C/min	107	136	186	226	263	312
E_a [kJ/mol]	52	60	93	56	59	128

previous section as the amidization reaction of chloranhydride with diamine and formation of polyamic acid (1 and 2 in Figure 4), are slightly lower for the NMP-based resin than those for the MI-based one (42 and 46 kJ/mol in contrast to 52 and 60 kJ/mol, respectively). Accordingly, their peak intensities are also higher (Figure 3). However, an onset of the polymerization reaction in the presence of MI takes place at lower temperatures indicating an activating effect of MI on the reaction onset.

For the peaks 3 and 4, assigned to the cyclization reaction of the different conformers of the polyamic acid, the E_a values determined for MI-based resin is much lower (93 and 59 kJ/mol in contrast to 292 and 102 kJ/mol for the NMP-based resin). The lower activation energy in this case can be explained by the catalytic effect of MI for the PAAc-cyclisation. At the same time, this solvent is known for its catalytic effect among other nucleophilic reactions in acidic conditions [16, 22, 23]. In addition, there is a direct correlation between the basicity and the nucleophilicity: increase of the basicity increases the nucleophilicity [24] and, accordingly, the reaction rate [10, 25]. Taking into account the fact that MI has a higher pH value than NMP ($pH_{NMP} = 7.7-8$; $pH_{MI} = 9.5-10.5$) [26, 27] it can be supposed that MI could bring more benefits as media for the PAI reaction than NMP. The determined E_a value for the high-temperature reactions (peak 5 in Table 3) in MI-media is much higher than that for the NMP-based resin, however, both values are comparable with the data determined for the industrial resins being about 96 kJ/mol [16].

It is noteworthy, that the peak intensity of the isophthalic conformer for MI_TC(L) sample (peak 3 in

Figure 3) is much higher compared to the reaction peak of terephthalic one (assigned as peak 4), whereas for the NMP-based PAI resin these peaks demonstrate similar intensity. Reaction of both the conformers is strongly dependent on the media and they are different by their thermodynamic stability reacting at the different speed and temperature. Thus, Ning-Jo Chu etc. has found that terephthalic conformation is thermodynamically more stable than the isophthalic one due to the stronger ability to build the hydrogen bonds with NMP and, thereof, reacts at higher temperatures. Moreover, the ratio of tere- to isophthalic isomers in NMP solution is 3 to 1 found by NMR analysis whereas in dimethylacetamide (DMAc) this ratio was found to be lower (1 to 1) [28]. Since MI used as solvent in this work is hardly able to solvate PAAc through the hydrogen bonding, formation of the low-energy isophthalic-conformation is preferable and causes the lowering the reaction temperature and activation energy. Unfortunately, there is no literature known for authors studying the conformation of polyamic acid isomers in MI solvent. On the other hand, the NMP based PAI resin is commercial product, and its exact chemical structure is unknown and presence of some additives cannot be excluded.

The last high temperature reaction peak can be attributed to the post-curing (probably further imidization reactions). The activation energy of this chemical process is higher for the MI-PAI resin (128 kJ/mol compared to 89 kJ/mol for the NMP-based resin). Taking into account obviously higher enthalpy and much stronger intensity of this exothermal peak for the MI-resin against NMP-based one, it can be concluded that there are more functional groups react-

ing. However, the higher completeness of the previous reactions in presence of MI (discussed above) should cause stronger steric hindrances for the later stage of post-curing reactions. Therefore, different reaction types could probably take place during high-temperature post-curing of NMP and MI based PAI-resins. This is also partially confirmed by difference in the respective E_a values for both resins. It could be possible that reaction products of MI in the structure of PAI-network are responsible for this. However, it was not a topic of this work and should be investigated in depth in the future. Nevertheless, it is worthy to note that the reaction peak of low intensity observed at 200–250°C for the MI-based resin has no correspondent peak for NMP-based PAI. The estimated E_a value of this reaction is 56 kJ/mol. It should be mentioned that an exothermic peak was observed in the similar temperature range for the pure MI solvent with some shift to the lower temperature and was attributed therefore to the possible reactions of the MI itself. This observation indicates possible incorporation of the MI in the PAI-network structure. In general, it could be concluded that, in contrary to NMP, MI has a significant influence on the final properties of the cured PAI-resin.

3.3. Isothermal curing in ‘ideal’ (closed) conditions

The cure kinetics of thermosetting polymers is conveniently monitored by the DSC technique. Since the PAI cure reaction is an exothermal process, the heat flow measured by DSC is proportional to both the heat release and the cure rate. Thus, the polymerisation degree $\alpha(t)$ at the respective time interval can be determined by Equation (2):

$$\alpha(t) = \frac{\Delta H_t}{\Delta H_{total}} \quad (2)$$

where ΔH is the reaction enthalpy measured at given time t and ΔH_{total} is the total reaction enthalpy which can be determined as the area under the exothermal peaks from the non-isothermal DSC scans [29]. In this work, ΔH_t was taken from the isothermal segments of DSC curves by simulating the respective isothermal curing program (see Table 1), whereas ΔH_{total} was generated from the non-isothermal scans collected at 3°C/min. All isothermal tests were done in high pressure crucibles (so called ‘ideal case’), and the conversion for each resin system at

each curing program was plotted as a function of time.

The iso-thermal kinetics in terms of conversion curves as well as corresponding temperature profiles are shown in Figures 5a and 5b for NMP_TC(I) and MI_TC(L), respectively. The conversions achieved for both resin systems at respective post-curing temperatures are given in Table 4. As can be seen, the final conversion for the NMP_TC(I) is much lower compared to the MI_TC(L) for all the curing programs applied (22–41% compared to 73–99%, respectively). After the initial heating stage (70–180°C for 20 min, titled as non-isoI) and the first isothermal stage (20 min at 180°C, titled as isoI) the NMP_TC(I) system shows the conversion about 17%. In contrast, the conversion of the MI_TC(L) system at similar curing conditions reached about 52%. The second heating stage (non-isoII) changed the conversion of NMP based systems insignificantly (Figure 5a), whereas in MI-media the reaction occurs more intensively and for all MI-based systems reached about 60–70% (Figure 4b). After the last isothermal stage (isoII) at 215°C, MI_TC(L)_215 represents more than factor three higher conversion (~74%) compared to that of NMP_TC(I)_215 (~22%). After the post-curing at 240°C, the conversion for the MI_TC(L)_240 system is again almost three times higher (~87%) in comparison to respective NMP_TC(L)_240 resin (~29%). After the isothermal stage at 270°C, the MI_TC(L)_270 system shows a conversion value

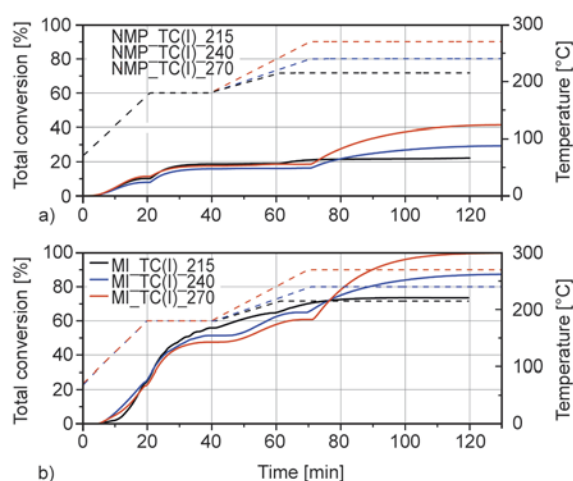


Figure 5. Isothermal curing kinetics of the NMP_TC(I) (a) and MI_TC(L) (b) resins with the respective temperature curing programs 1, 2 and 3 using HPC-DSC: conversion curves (solid lines) and their temperature programs (dashed-lines)

Table 4. Conversion values $\alpha_{\text{non-iso/iso}}$ at different stages of the respective curing programs

Sample	$\alpha_{\text{non-isoI}}$ [%]	α_{isoI} [%]	$\alpha_{\text{non-isoII}}$ [%]	α_{isoII} [%]
	non-isoI: 70-180°C	isoI: 20 min at 180°C	non-isoII: 180-215/240/270°C	isoII: 1 h at 215/240/270°C
NMP_TC(I)_215	8.8	18.4	18.9	22.2
NMP_TC(I)_240	7.0	15.6	16.3	29.3
NMP_TC(I)_270	9.6	17.4	18.5	41.3
MI_TC(L)_215	24.9	55.8	64.8	73.5
MI_TC(L)_240	25.8	51.3	65.3	87.3
MI_TC(L)_270	22.9	47.5	60.7	99.7

of ~99%, which is more than twice higher compared to the NMP_TC(I)_270 (~41%). As can be seen, the highest conversion for all the resins was achieved at the highest post-curing temperatures (isoII stage at 270°C). However, even though, the MI-based resin being post-cured at 215°C demonstrated higher conversion than that of NMP-based one at 270°C (73.5% compared to 41% respectively). The data observed are in good agreement with the results described in the previous section in terms of activation energies and non-isothermal reaction profiles.

Information taken from non-isothermal kinetics could be also used indirectly for possible explanations of reactions during isothermal curing. For example, up to 20 min of non-isothermal curing, when high conversion values are already achieved, the temperature reached 180°C. The main reaction occurring in this temperature interval was identified as the reaction of poly(amic acid) formation (isophthalic conformer, peak 3 in Figure 3 and respective reaction 3 in Figure 4 and Table 3). Therefore, an assumption could be made that this reaction is dominant by heating up to 180°C and following isothermal curing stage at this temperature. In NMP solvent, the activation energy E_a of this reaction was found to be 292 kJ/mol, whereas for the same reaction in MI media the E_a was 93 kJ/mol. In addition, the enthalpy and intensity of the corresponding exothermal peak in DSC-curves was much more intensive in MI solvent than that observed for NMP (cf. Figure 3). This indicates some possible catalytic effect of MI on the polymerization of PAI-resin at the initial stages of the reaction. Taking into account possible build in of MI in the PAI network structure also, much higher final conversion of PAI in MI media could be explained. Apart from that, one of the very important factors is possible conformational changes of PAI resin in MI media. However, it should be more carefully investigated. Based on the data observed, it

can be concluded that the initial stage of the PAI curing plays a dominant role in the formation of the final resin structure.

3.4. Isothermal curing in ‘real’ (open) conditions

Under real conditions, the PAI resins are cured under air atmosphere in thin films. Under such ‘open’ conditions, the solvent used as resin media evaporates at the beginning of a curing process in the first isothermal reaction step. After that the samples weight changes insignificantly and it occurs due to the evaporation of by-products of the cyclization reaction. The weight of the final samples can slightly differ depending on the final curing temperatures and is connected to the final conversion. As result, it can have an important influence on the final properties of the PAI thin films.

3.4.1. Thermal stability of the cured PAI-films

TGA-curves and their differential representations (DTG) vs. temperature of NMP- and MI-based PAI are presented in Figures 6a and 6b for the PAI samples cured in open conditions using temperature programs 1 and 3, respectively.

As can be seen, mass loss of the PAI samples is a multistage process. Peaks of the low intensity in the temperature range up to 150°C correspond to the evaporation of absorbed moisture. The first intensive peak in the range of 200–400°C represents the evaporation of the post-polymerization byproducts (e.g. HCl, H₂O). It is noteworthy that this peak (peak 1 in Figure 6) demonstrates significantly reduced intensity when the PAI films are cured using program 3 with a post-curing temperature of 270°C. It confirms that the higher conversion/imidization degree of the PAI at higher cure-temperatures increases its thermal stability. At the same time, the MI-based PAI samples demonstrated notable shift of the Peak1 (reaction byproducts elim-

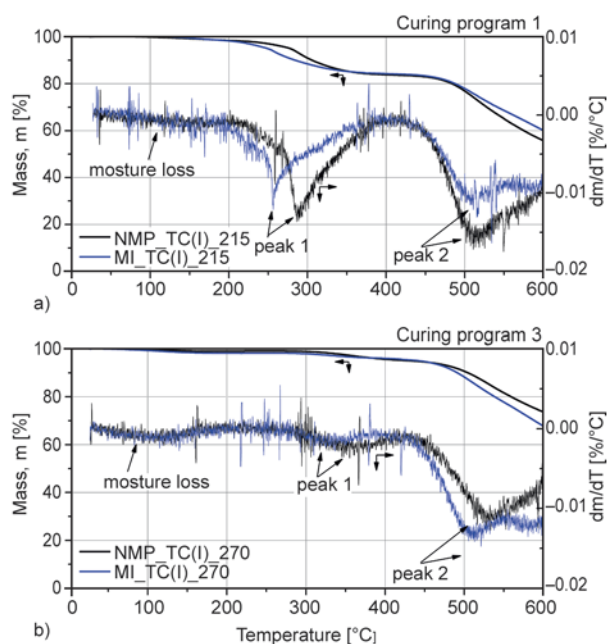


Figure 6. TGA- (left axes) and DTG- (right axes) curves vs. temperature for NMP_TC(I) and MI_TC(L) cured using programs 1 (a) 3 (b), respectively

ination) to the lower temperatures (up to 30°C) in comparison to the NMP based ones, independently on the post-curing temperature applied. It confirms a catalytic effect of MI on the PAI-curing reaction, which was also observed in the curing kinetics and activation energy values discussed above.

The second intensive peak was observed in the high-temperature range (~400–600°C). It corresponds to the thermal degradation of the PAI resins with onsets at ~430°C for NMP_TC(I) and ~420°C for MI_TC(L), which is in agreement with results of other authors for polyimide-systems [30]. As can be concluded, the thermostability of cured PAI films is marginally influenced by the solvent used.

3.4.2. Conversion of the PAI films cured under ‘real’ conditions

Due to the strong endothermal effect of the solvent evaporation in reactive PAI resins under ‘open’ conditions, determination of their final conversion values using DSC technique is not possible. However, according to the Di Benedetto’s equation, the final conversion can be calculated from the information on the glass transition temperature of the finally cured resin (T_g). For that, $T_{g, \min}$ and $T_{g, \max}$ after “complete” curing ($T_{g, \max}$) should be known [31].

In order to estimate the conversion values of the PAI films cured under real conditions according to

the Di Benedetto equation, the samples with the highest polymerization degree were obtained using post-cure for 20 hours at 290°C (program 4 – Table 1) followed by repeated heating up to 375°C (thermal stability limit obtained from TGA data) until a shift of the glass transition temperature (T_g) was less than 1°C (Figure 6). After that the last heating scan was run up to 450°C to find out the range of rubber-elasticity plateau.

Although the complete network formation for PAI resins is hardly possible and strongly depends on the curing conditions, the network obtained in such manner was assumed as the fully crosslinked (‘ideal’ network) and its T_g and storage modulus (E') values were used for further calculations of conversion and cross-link density.

For the NMP_TC(I), T_g displacement less than 1°C was observed after the 20th repeat-scanning till 375°C (Figure 7a, 7b). The 21st scan was run up to 450°C to determine the plateau. The value of respective $T_{g, \max}$ was found at ~241°C red at maximum range of $\tan \delta$ and used for conversion determination by Di Benedetto equation (Table 5). The estimated values of T_{plateau} (~430°C) and E'_{plateau} (~673 MPa) were used for the calculation of the ‘idealized’ crosslink density and are given in Table 6.

For the MI_TC(L) only 12 heating DMA-scans were performed (see Figure 7c, 7d). The test samples always broke after the 12th heating suggesting its higher brittleness. For this reason, the E'_{plateau} value and the corresponding rubbery plateau temperature onset (T_{plateau}) were calculated using an approximation approach described below.

In order to estimate, if the acquired DMTA values are able to provide an adequate approximation model, the values of storage modulus at the glass transition temperature were plotted as an exponential function of glass transition temperature determined as the peak temperature on the $\tan \delta$ curves (Figure 8). As can be seen, the glass transition temperature T_g slowly reaches an equilibrium which allows performing such modeling. Similar to that, the temperatures of the plateau onset (T_{plateau}) from the E' curves were plotted versus T_g and the found extrapolated value of the T_{plateau} of the 12th DMTA run is ~388°C. In similar manner the E'_{plateau} was determined and was found as ~18 MPa.

The conversion α ($0 \leq \alpha \leq 1$) at ‘real’ conditions was calculated from Di Benedetto’s equation (Equation (3)) [31]:

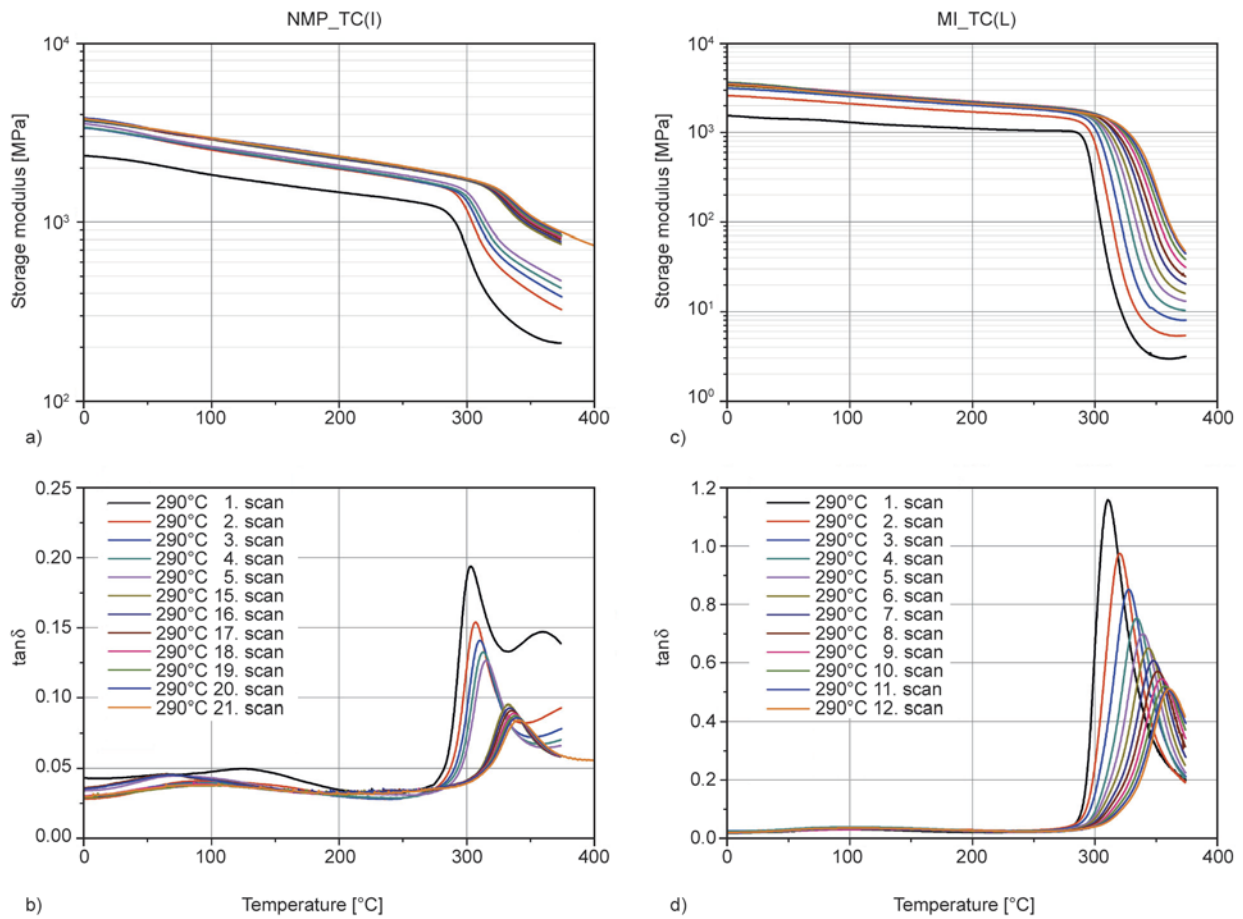


Figure 7. Storage modulus E' (a, c) and loss factor $\tan \delta$ (b, d) as a function of temperature for the systems NMP_TC(I) (left) and MI_TC(L) (right) cured with program 4 at repeated scanning on the same test specimens. Final post-curing temperature and number of the scans are given in the legend; legend in (b) and (d) also belongs to (a) and (c).

$$\frac{T_g - T_{g, \min}}{T_{g, \max} - T_{g, \min}} = \frac{\lambda \alpha}{1 - (1 - \lambda) \alpha} \quad (3)$$

where λ is determined by Equation (4) [32, 33]:

$$\lambda = \frac{T_{g, \min}}{T_{g, \max}} \quad (4)$$

here $T_{g, \min}$ was determined by DSC using stochastically thermo-modulated method (TOPEM®). The glass transition temperature of the ‘fully’ cross-linked system $T_{g, \max}$ was estimated from the multi-cycled DMTA testing. The conversions calculated

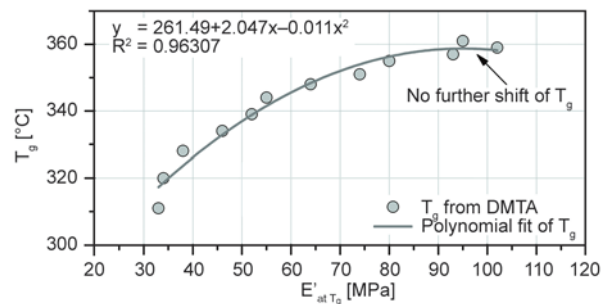


Figure 8. Determination of the $T_{g, \max}$ approximation approach. Similar approximations were done for T_{plateau} and E'_{plateau} . Explanations are given in text.

Table 5. Conversions in real conditions determined according to Di Benedetto

Sample name	$T_{g, \min}$ [°C]	$T_{g, \max}$ [°C]	Tg [°C]	λ	Total conversion α [%]
NMP_TC(I)_215	-101	341	169	0.28	85
NMP_TC(I)_240			207		89
NMP_TC(I)_270			225		91
MI_TC(L)_215	-121	361	193	0.24	89
MI_TC(L)_240			222		91
MI_TC(L)_270			225		91

via the Di Benedetto’s equation for both resin systems are listed in Table 5.

The calculated total conversions at real conditions for both MI and NMP based systems, have been found to be similar and they all are in the range of 85–93% with marginal tendency to increase at rise of the final post-cure temperature (215, 240 or 270°C). Thus, in order to make further statements on the final properties of the investigated resins, the viscoelastic properties and their crosslink densities were carefully investigated.

3.4.3. Viscoelastic behavior and crosslink density

The DMA results (temperature dependencies of storage modulus E' and loss factor $\tan\delta$) for the cured samples NMP_TC(I) and MI_TC(L) are presented in Figure 9. As can be seen, all PAI-systems post-cured at 215, 240 and 270°C demonstrate complicate storage modulus profile and several peaks on $\tan\delta$ traces. For NMP based samples at increase of

the post-curing temperature the E' values at room temperature and in the rubbery state increase indicating improvement of mechanical stiffness of the PAI films cured at higher temperatures. Increase of the E' in the rubbery state was determined for all samples regardless the post-curing temperature. This indicates further post-curing effects. The $\tan\delta$ curves clearly demonstrate a shift of the first α -relaxation peak to the right with increase of the post-curing temperature. This shift of T_g indicates that for NMP-based PAI systems the curing program with the post-curing temperature at 215°C is too low which result in incomplete cure. These data play in fact with the conversion determined by Di Benedetto approach, where the calculated conversion of NMP_TC(I)_215 (see Table 5) was ~85% and for the NMP_TC(I)_270 it slightly increases up to ~91%.

At the same time the second peak of $\tan\delta$ corresponds to the T_g of the post-cured system and is not changed with increase of the final curing tempera-

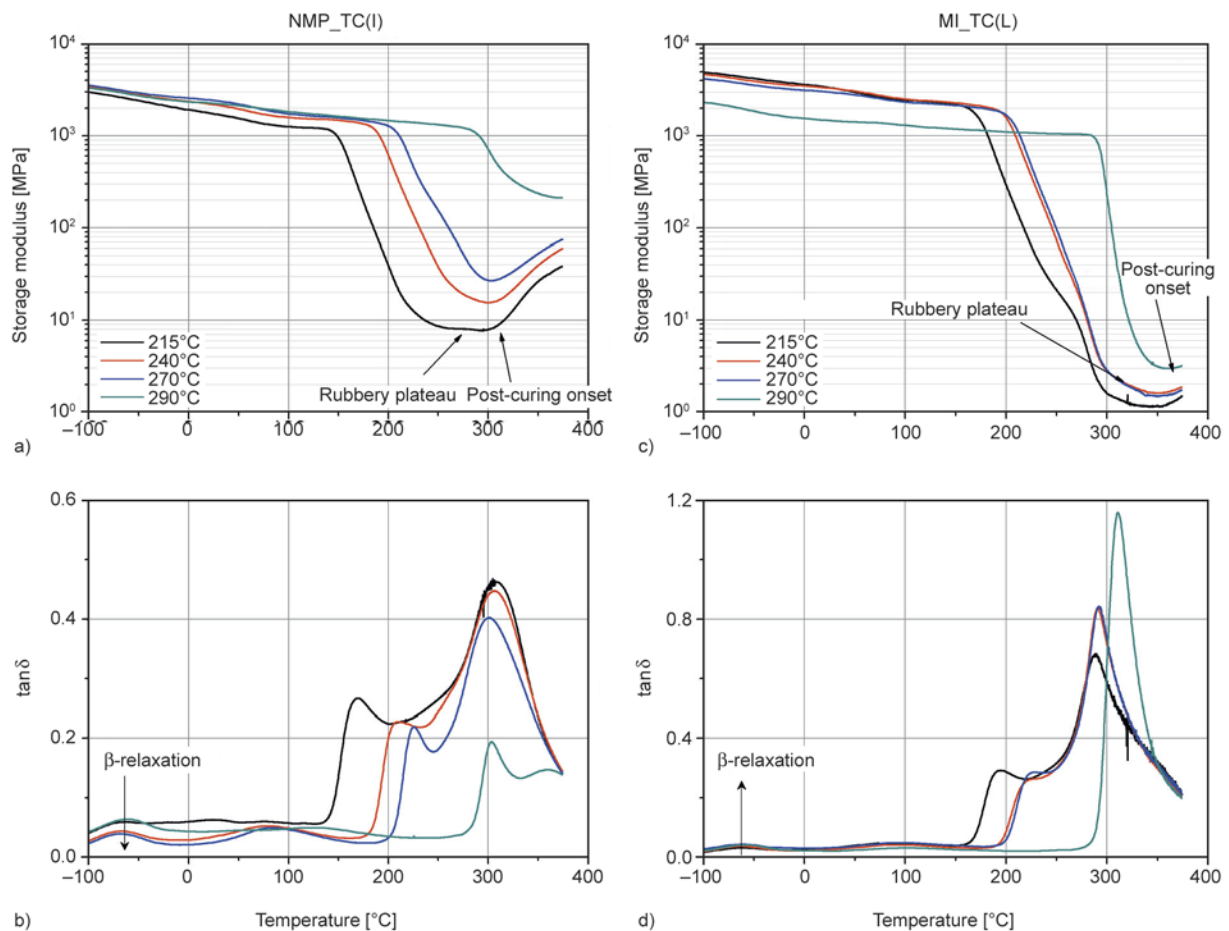


Figure 9. Storage modulus E' (a, c) and loss factor $\tan\delta$ (b, d) as a function of temperature for the NMP_TC(I) (left) and MI_TC(L) (right) systems cured at different curing programs (their final post-curing temperatures are given in the legend); legend in (a) and (c) also belongs to (b) and (d)

ture. It indicates that for all these systems similar post-reaction processes take place. When the samples were post-cured at 290°C, the first T_g disappeared and only the high-temperature $\tan \delta$ peak was observed.

Similar tendency of T_g increase with rise of post-curing temperature was also found for the MI-PAI system. At the same time, the samples post cured at 240 and 270°C demonstrate similar behavior. It indicates that increase of the post-curing temperature up to 270°C has marginal effect on the viscoelastic properties of the MI-PAI-resin and the lower temperatures can be applied with similar efficiency. It has to be noted that the T_g shift at increase of the post-curing temperature is not so pronounced as for NMP-based resin which is in good agreement with the conversion values of these systems (c.f. Table 5).

One can see that the E' values of the NMP-based PAI resins in rubbery state are higher than those of MI-based ones, which can indicate the difference in their crosslink density.

For the crosslinked polymers, mechanical properties in the viscoelastic state are related to the network structure. Then, their crosslink density can be determined from Equation (5) [34, 35], which was also used by other authors for the determination of the crosslink density for highly crosslinked imide-compounds [8] (Equation (5)):

$$n_c = \frac{E'_{\text{plateau}}}{3RT_{\text{plateau}}} \quad (5)$$

where n_c is the crosslink density (molar concentration of junction points per volume unit) [mol/cm³]; E'_{plateau} is the storage modulus in rubbery region; R is the gas constant [MPa·cm³/(mol·K)]; T_{plateau} is the absolute temperature of E'_{plateau} taken [K].

Since the E' rises at the glass transition due to the post-curing effects, the values of the E'_{plateau} were taken as the lowest points of the E' in the rubbery region before the obvious post-curing occurs. The values of the E' determined at 30°C ($E'_{30^\circ\text{C}}$), the T_g determined from the first $\tan \delta$ peak, temperature of the rubbery plateau (T_{plateau}) and corresponding modulus value (E'_{plateau}) as well as the results of the crosslink densities of both tested PAI systems are summarized in Table 6.

An increase of the final curing temperature has a significant effect on the final network formation. It is noteworthy that at increase of the final curing temperature from 215 to 240°C and from 240 to 270°C,

the crosslink density of the NMP_TC(I) system increases almost twice. For the ‘perfectly’ cross-linked network (determined after 21 DMA-scans as described above) the n_c value is several times higher and is 41 194 mol/m³ (see Table 6). Simultaneous to n_c increase of the T_g and E' at room temperature indicates the formation of more rigid and denser PAI network at higher post-curing temperature.

Surprisingly, the MI based PAI resin showed different behavior. For this system the crosslink density and T_g values rise insignificantly with the post-curing temperature, whereas E' at room temperature slightly decreases or stays constant in case of the ‘perfectly’ cured network (after 12 DMA-scans: c.f. Table 6). Moreover, the n_c values of MI_TC(L) systems are significantly lower than those of respective NMP-based ones. At the same time, the storage moduli in glassy state (before T_g) for MI-PAI systems are higher compared to NMP-based ones. It is noteworthy that, in contrast to the NMP-based systems, at increase of the last curing temperature step from 215 to 270°C intensity of the β -relaxation peak in $\tan \delta$ curves rises (see Figure 9b and 9c, effect of the temperature increase on the β -relaxation intensity is showed with arrows). Similar behavior was found for the internally antiplasticized epoxy systems. Thus, internal antiplasticization effects were observed for the epoxy resins (EP) hybridized with benzoxazines at increase of EP functionality [36]. In our case, increase of free volume at lower crosslink density of the MI based PAI polymer system promotes associations of small moieties and pendant groups causing an improved antiplasticization effect at lower post-curing temperature. This is confirmed by rise of storage modulus in the glassy state, decrease of the β -transition intensity, and tendency to reduction of T_g value by decreasing post-curing temperature.

Obviously, a catalytic effect of N-methylimidazole increases the reaction efficiency on the stage of the macromolecule growth and imidization. The latter is also confirmed by the results of the non-isothermal curing kinetics with preferable formation of longer fully imidized linear chain fragments at high conversion degree where E_a values of the corresponding reactions (titled as 3 and 4 in Table 3 and Figure 4) are much lower than those for the NMP-based determined from the isothermal curing kinetics tested at ‘ideal’ conditions. The higher values of the glass transition temperature for the MI-based PAI compared to the NMP-based ones can be explained by possi-

Table 6. Overview of the values acquired by DMA-measurements and of the calculated crosslinking density (n_c) for both investigated PAI resins

Resin system	Curing program (post-curing temperature)	$E'_{30^\circ\text{C}}$ [MPa]	T_g [°C]	Onset T_{plateau} [°C]	E'_{plateau} [MPa]	n_c [mol/m ³]
NMP_TC(I)	Program 1 (215°C)	1697	169	258	8	604
	Program 2 (240°C)	2149	207	296	16	1 092
	Program 3 (270°C)	2411	225	302	27	1 883
	Program 4 21. scan(290°C)	3550	342	430	673	41 194
MI_TC(L)	Program 1 (215°C)	3647	193	360	3	188
	Program 2 (240°C)	3514	222	367	5	335
	Program 3 (270°C)	3161	225	371	8	498
	Program 4 12. scan(290°C)	3503	361	388*	18*	1 065

*the values are found using the approximation approach. Note: all systems of program 4 were subjected to multiple DMA-tests cycling until fracture (e.g. 21 scans for NMP-PAI, whereas 12 scans for MI-PAI).

ble incorporation of the MI units into the aromatic structure of PAI network increasing the stiffness of the system in addition to better realization of the polyimidization/polycyclization reactions [37].

4. Conclusions

N-methylimidazole is a material, not used so far as a solvent for the manufacturing of polyamide-imide resins. However, it provides several benefits and positive effects on the PAI curing process and the final material properties. In this work, use of the high-pressure DSC-crucibles allowed investigations of the PAI curing kinetics preserving the reactive media constant and avoiding its influence on the exothermal reaction. In such conditions, several reaction peaks were recognized.

Analyzing the final properties of the PAI resins cured under ‘real’ conditions and the data of the non-isothermal curing kinetics in ‘ideal’ (closed) conditions the following conclusions can be drawn. The imidization reactions of the iso- and terephthalic conformers of the PAI resin in MI media have much lower activation energy than in the NMP one. It indicates that MI-media is more preferable for the curing of PAI-resin and catalyzes the PAI polymerization reaction shifting the ‘low-temperature’ reactions to the lower temperatures. At the same time, MI has no obvious effect on the ‘high-temperature’ post-curing reaction. Investigation of the PAI reaction at isothermal conditions simulating the real curing, the final completeness of the conversion was significantly higher for the MI-based resins, compared to the conventional NMP-based ones for all the curing programs applied. It confirms again the results observed at the non-isothermal investigations.

From their viscoelastic properties, it was determined that MI-based PAI-system shows two times higher storage modulus at 30°C ($E'_{30^\circ\text{C}}$) in comparison to the conventional NMP-PAI resin when the lowest final curing temperature was used. For the MI-based resins, simultaneously to the lowering of the $E'_{30^\circ\text{C}}$, the crosslink density n_c slightly increased at rise of the post-curing temperature, whereas for the NMP-PAI samples the $E'_{30^\circ\text{C}}$ rises together with the n_c values. Such untypical behavior of the MI-PAI was explained with possible internal antiplasticization effect and build in of aromatic MI-units in the structure of PAI-network. The latter was assumed from the reaction peak observed on the DSC traces of the neat MI-solvent.

Summarized, the observed results make N-methylimidazole very promising for the use as a PAI-resin solvent. Further, due to its lower toxicity, it is extremely attractive for the production of PAI systems with outstanding and tunable properties.

Acknowledgements

The authors are thankful to Prof. Dr. h.c. József Karger-Kocsis for the helpful discussions and to Mettler Toledo GmbH (Giessen, Germany), especially to Mr. Peter Bamfaste, for the kind support and technical cooperation.

References

- [1] Gebhard A., Hauptert F., Schlarb A. K.: Development of nanostructured slide-coatings for automotive components. in ‘Tribology of polymeric nanocomposites’ (eds.: Friedrich K., Schlarb A. K.) Elsevier, Oxford, Vol 55, 619–648 (2008). DOI: [10.1016/B978-0-444-59455-6.00018-0](https://doi.org/10.1016/B978-0-444-59455-6.00018-0)
- [2] Fink J. K.: Poly(amide-imide)s in ‘High performance polymers’ (ed.: Ebnesajjad S.) Elsevier, New York, 321–366 (2014).

- [3] Murray T.: Poly(amide-imides): Wire enamels with excellent thermal and chemical properties. *Macromolecular Materials and Engineering*, **293**, 350–360 (2008). DOI: [10.1002/mame.200700365](https://doi.org/10.1002/mame.200700365)
- [4] Hong Y-T., Jin M. Y., Suh D. H., Lee J-H., Choi K-Y.: New preparation method of poly(amide-imide)s using direct polycondensation with thionyl chloride and their characterization. *Die Angewandte Makromolekulare Chemie*, **248**, 105–122 (1997). DOI: [10.1002/apmc.1997.052480107](https://doi.org/10.1002/apmc.1997.052480107)
- [5] Underwood G.: Polyamide-imide (PAI). in ‘Engineering plastics handbook’ (ed.: Margolis J. M.) McGraw-Hill, Montreal, 257–285 (2006). DOI: [10.1036/0071457674](https://doi.org/10.1036/0071457674)
- [6] Russell J. D., Kardos J. L.: Modeling the imidization kinetics of AFR700B polyimide. *Polymer Composites*, **18**, 64–78 (1997). DOI: [10.1002/pc.10262](https://doi.org/10.1002/pc.10262)
- [7] Kim Y. J., Glass T. E., Lyle G. D., McGrath J. E.: Kinetic and mechanistic investigations of the formation of polyimides under homogeneous conditions. *Macromolecules*, **26**, 1344–1358 (1993). DOI: [10.1021/ma00058a024](https://doi.org/10.1021/ma00058a024)
- [8] Kimura H., Ohtsuka K., Matsumoto A., Fukuoka H., Oishi Y.: Synthesis and characterization of phenylethynylcarbonyl terminated novel thermosetting imide compound. *Express Polymer Letters*, **7**, 161–171 (2013). DOI: [10.3144/expresspolymlett.2013.15](https://doi.org/10.3144/expresspolymlett.2013.15)
- [9] Chang K. C., Hsu C. H., Lu I. H., Ji W. F., Chang C. H., Li W. Y., Chuang T. L., Yeh J. M., Liu W. R., Tsai M. H.: Advanced anticorrosive coatings prepared from electroactive polyimide/graphene nanocomposites with synergistic effects of redox catalytic capability and gas barrier properties. *Express Polymer Letters*, **8**, 243–255 (2014). DOI: [10.3144/expresspolymlett.2014.28](https://doi.org/10.3144/expresspolymlett.2014.28)
- [10] Harris F. W.: Synthesis of aromatic polyimides from dianhydrides and diamines. in ‘Polyimides’ (eds: Wilson D., Stenenberger H. D., Hergenrother P. M.) Springer Netherlands, 1–37 (1990).
- [11] Eckert C. A., Knutson B. L., Debenedett P. G.: Supercritical fluids as solvents for chemical and materials processing. *Nature*, **383**, 313–318 (1996). DOI: [10.1038/383313a0](https://doi.org/10.1038/383313a0)
- [12] Chen K-L., Shen Y-H., Yeh M-Y., Wong F. F.: Complexes of imidazole with poly(ethylene glycol)s as the thermal latency catalysts for epoxy–phenolic resins. *Journal of the Taiwan Institute of Chemical Engineers*, **43**, 306–312 (2012). DOI: [10.1016/j.jtice.2011.08.007](https://doi.org/10.1016/j.jtice.2011.08.007)
- [13] Chafin R. W. II: Torlon® and silicalite mixed matrix membranes for xylene isomer purification. PhD thesis, Georgia Institute of Technology, Atlanta (2007).
- [14] Robertson G., Guiver D. M., Yoshikawa M., Brownstein S.: Structural determination of Torlon® 4000T polyamide–imide by NMR spectroscopy. *Polymer*, **45**, 1111–1117 (2004). DOI: [10.1016/j.polymer.2003.12.029](https://doi.org/10.1016/j.polymer.2003.12.029)
- [15] Lin Y-S., Liu C-W., Tsai T. Y. R.: 1-methylimidazole 3-*N*-oxide as a new promoter for the Morita–Baylis–Hillman reaction. *Tetrahedron Letters*, **46**, 1859–1861 (2005). DOI: [10.1016/j.tetlet.2005.01.099](https://doi.org/10.1016/j.tetlet.2005.01.099)
- [16] Kreuz J. A., Endrey A. L., Gay F. P., Sroog C. E.: Studies of thermal cyclizations of polyamic acids and tertiary amine salts. *Journal of Polymer Science Part A-1: Polymer Chemistry*, **4**, 2607–2616 (1966). DOI: [10.1002/pol.1966.150041023](https://doi.org/10.1002/pol.1966.150041023)
- [17] Yang C-P.: Synthesis of polymers containing pyromellitimide and benzimidazole or pyrrolobenzimidazole moieties and of their corresponding model compounds. *Die Makromolekulare Chemie*, **187**, 2509–2523 (1986). DOI: [10.1002/macp.1986.021871101](https://doi.org/10.1002/macp.1986.021871101)
- [18] Lauver R. W.: Kinetics of imidization and crosslinking in PMR polyimide resin. *Journal of Polymer Science: Polymer Chemistry Edition*, **17**, 2529–2539 (1979). DOI: [10.1002/pol.1979.170170825](https://doi.org/10.1002/pol.1979.170170825)
- [19] Chu N-J., Huang J-W.: Reactivity of poly(amic acid) isomers in thermal imidization. *Polymer Journal*, **22**, 725–732 (1990). DOI: [10.1295/polymj.22.725](https://doi.org/10.1295/polymj.22.725)
- [20] Barral L., Cano J., López J., López-Bueno I., Nogueira P., Abad M. J., Ramírez C.: Kinetic studies of the effect of ABS on the curing of an epoxy/cycloaliphatic amine resin. *Journal of Polymer Science Part B: Polymer Physics*, **38**, 351–361 (2000). DOI: [10.1002/\(SICI\)1099-0488\(20000201\)38:3<351::AID-POLB1>3.0.CO;2-C](https://doi.org/10.1002/(SICI)1099-0488(20000201)38:3<351::AID-POLB1>3.0.CO;2-C)
- [21] Núñez L., Fraga F., Núñez M. R., Villanueva M.: Thermogravimetric study of the decomposition process of the system BADGE ($n=0$)/1,2 DCH. *Polymer*, **41**, 4635–4641 (2000). DOI: [10.1016/S0032-3861\(99\)00687-4](https://doi.org/10.1016/S0032-3861(99)00687-4)
- [22] Gagliano R. A. Jr., Knowlton R. C., Byers L. D.: Methylimidazole-catalyzed ester hydrolysis: Nonlinear kinetics. *Journal of Organic Chemistry*, **54**, 5247–5250 (1989). DOI: [10.1021/jo00283a015](https://doi.org/10.1021/jo00283a015)
- [23] Wang H-L., O’Malley M., Fernandez J. E.: Electrochemical and chemical polymerization of imidazole and some of its derivatives. *Macromolecules*, **27**, 893–901 (1994). DOI: [10.1021/ma00082a003](https://doi.org/10.1021/ma00082a003)
- [24] Peter K., Vollhardt C., Schore N. E., Butenschön H.: *Organische chemie*. Wiley, Weinheim (2011).
- [25] Takekoshi T.: Synthesis of polyimides. in ‘Polyimides: Fundamentals and applications’ (eds: Ghosh M. K., Mittal K. L.) Marcel Dekker, New York, 7–48 (1996).
- [26] Hofmann K.: *Chemistry of heterocyclic compounds: Imidazole and its derivatives, Part I*. Wiley, New York (1953). DOI: [10.1002/9780470186541](https://doi.org/10.1002/9780470186541)

- [27] Harreus A. L., Backes R., Eichler J.-O., Feuerhake R., Jäkel C., Mahn U., Pinkos R., Vogelsang R.: 2-Pyrrolidone. in 'Ullmann's encyclopedia of industrial chemistry' Wiley, Weinheim (2002).
DOI: [10.1002/14356007.a22_457.pub2](https://doi.org/10.1002/14356007.a22_457.pub2)
- [28] Chu N.-J., Huang J.-W., Chang C. H., Whang W. T.: Solvent effects on chain structure and conformation of poly (amic acids) and their crystallosolvate formation. *Die Makromolekulare Chemie*, **190**, 1799–1808 (1989).
DOI: [10.1002/macp.1989.021900805](https://doi.org/10.1002/macp.1989.021900805)
- [29] Liang G., Chandarashekhara K.: Cure kinetics and rheology characterization of soy-based epoxy resin system. *Journal of Applied Polymer Science*, **102**, 3168–3180 (2006).
DOI: [10.1002/app.24369](https://doi.org/10.1002/app.24369)
- [30] Uğur M. H., Toker R. D., Kayaman-Apohan N., Güngör A.: Preparation and characterization of novel thermoset polyimide and polyimide-peo doped with LiCF₃SO₃. *Express Polymer Letters*, **8**, 123–132 (2014).
DOI: [10.3144/expresspolymlett.2014.15](https://doi.org/10.3144/expresspolymlett.2014.15)
- [31] Di Benedetto A. T.: Prediction of the glass transition temperature of polymers: A model based on the principle of corresponding states. *Journal of Polymer Science Part B: Polymer Physics*, **25**, 1949–1969 (1987).
DOI: [10.1002/polb.1987.090250914](https://doi.org/10.1002/polb.1987.090250914)
- [32] Pascault J. P., Williams R. J. J.: Relationships between glass transition temperature and conversion. *Polymer Bulletin*, **24**, 115–121 (1990).
DOI: [10.1007/BF00298330](https://doi.org/10.1007/BF00298330)
- [33] Pascault J. P., Williams R. J. J.: Glass transition temperature versus conversion relationships for thermosetting polymers. *Journal of Polymer Science Part B: Polymer Physics*, **28**, 85–95 (1990).
DOI: [10.1002/polb.1990.090280107](https://doi.org/10.1002/polb.1990.090280107)
- [34] Hofmann K., Glasser W. G.: Cure monitoring of an epoxy-amine system by dynamic mechanical thermal analysis (DMTA). *Thermochimica Acta*, **166**, 169–184 (1990).
DOI: [10.1016/0040-6031\(90\)80179-3](https://doi.org/10.1016/0040-6031(90)80179-3)
- [35] Gent A. N.: Rubber elasticity: Basic concepts and behavior. in 'Science and technology of rubber' (eds: Mark J. E., Erman B., Eirich F. R.) Elsevier, Amsterdam, 1–27 (2005).
DOI: [10.1016/B978-012464786-2/50004-3](https://doi.org/10.1016/B978-012464786-2/50004-3)
- [36] Grishchuk S., Schmitt S., Vorster O. C., Karger-Kocsis J.: Structure and properties of amine-hardened epoxy/benzoxazine hybrids: Effect of epoxy resin functionality. *Journal of Applied Polymer Science*, **124**, 2824–2837 (2012).
DOI: [10.1002/app.35302](https://doi.org/10.1002/app.35302)
- [37] Connors K. A., Pandit N. K.: N-methylimidazole as a catalyst for analytical acetylations of hydroxy compounds. *Analytical Chemistry*, **50**, 542–544 (1978).
DOI: [10.1021/ac50033a038](https://doi.org/10.1021/ac50033a038)

Polyamide blend-based nanocomposites: A review

W. S. Chow^{1,2}, Z. A. Mohd Ishak^{1,2*}

¹School of Materials and Mineral Resources Engineering, Engineering Campus, Universiti Sains Malaysia, Nibong Tebal 14300 Penang, Malaysia

²Cluster for Polymer Composites, Science and Engineering Research Centre, Engineering Campus, Universiti Sains Malaysia, Nibong Tebal 14300 Penang, Malaysia

Received 24 September 2014; accepted in revised form 26 November 2014

Abstract. Polymer blend nanocomposites have been considered as a stimulating route for creating a new type of high performance material that combines the advantages of polymer blends and the merits of polymer nanocomposites. In nanocomposites with multiphase matrices, the concept of using nanofillers to improve select properties (e.g., mechanical, thermal, chemical, etc) of a polymer blend, as well as to modify and stabilize the blend morphology has received a great deal of interest. This review reports recent advances in the field of polyamide (PA) blend-based nanocomposites. Emphasis is placed on the PA-rich blends produced by blending with other thermoplastics in the presence of nanofillers. The processing and properties of PA blend-based nanocomposites with nanofillers are discussed. In addition, the mechanical properties and morphology changes of PA blends with the incorporation of nanofillers are described. The issues of compatibility and toughening of PA blend nanocomposites are discussed, and current challenges are highlighted.

Keywords: polymer blends and alloys, nanocomposites, polymer composites

1. Introduction

1.1 Background of polyamide blend-based nanocomposites

Polyamide (PA) is well known as an engineering thermoplastic material that is widely used in industrial applications (e.g., fibers, films, textiles and various molding products) for its remarkable mechanical and thermal properties. However, these advantages are accompanied by limitations such as moisture absorption, notch sensitivity, relatively low impact strength and poor dimensional stability. Thus, modification of PA to improve its physical properties and to introduce new properties has drawn much attention [1–4]. Polymer nanocomposites offer new technological and economical benefits. The incorporation of nanometer-scale reinforcement may dramatically improve select properties of PA. These nanocomposites exhibit superior properties

such as enhanced mechanical properties, reduced permeability, increased electrical conductivity and improved flame retardancy [5–9].

Recently, there has been increasing interest in blending a second polymeric component into PA nanocomposites with the addition of a nanofiller (e.g., nanoclay, nanotube). Blends of PA with polyolefins are particularly attractive because it is theoretically possible to couple the excellent mechanical properties of the PA and the good processability and toughness of the polyolefin. Nanocomposites based on polymer blends of PA and polyolefins are widely reported in the scientific literatures. For example, blending of polyamide 6 (PA6) and polypropylene (PP) has been attempted to achieve improvement in mechanical properties, paintability and barrier properties. PA6 contributes mechanical and thermal properties, whereas PP ensures good processability and

*Corresponding author, e-mail: zarifin@usm.my
© BME-PT

insensitivity to moisture. Polymer blend nanocomposites may lead to a new type of high performance material that combines the advantages of polymer blends and the merits of polymer nanocomposites [10, 11].

Consequently, two types of PA blend-based nanocomposite have been studied by numerous researchers, i.e., PA nanocomposites prepared by thermoplastic-thermoplastic blending and rubber (both functionalized and un-functionalized) modification approaches:

- (a) PA nanocomposites with a matrix composed of a blend of two thermoplastics (for example, PA6/PP/nanoclay [1, 12–18], PA6/polyimide/organoclay [19]; PA6/thermotropic liquid crystalline polymer (TLCP)/organoclay [20]; Nylon 66/Nylon 6/organoclay [21]; PA6/acrylonitrile-butadiene-styrene (ABS)/multi-walled carbon nanotube (MWNT) [4, 22]; PA6/low density polyethylene (LDPE)/nanoclay [23]; PA6/LDPE/organoclay [24]; polyamide 12 (PA12)/PP/boehmite alumina nanoparticles [25]; PA6/polymethyl methacrylate (PMMA)/functionalized single-walled carbon nanotube (SWCNT) [26]; PA6/polystyrene (PS)/nanoclay [27]; PA6/PS/nanosilica [28])
- (b) PA nanocomposites toughened by a rubber or rubber-modified PA6 nanocomposites (for example, PA6/maleated styrene-ethylene butylstyrene (SEBS-*g*-MA)/montmorillonite [29]; PA6/maleinized ethylene-propylene-rubber (mEPR)/nanoclay [30]; PA6/ethylene-*co*-propylene maleated rubber/organoclay [31]; PA6/silicone rubber/clay [32]; PA66/SEBS-*g*-MA/organoclay [33]; PA6/metallocene ethylene-propylene-diene copolymer/maleated ethylene-propylene-diene copolymer (EPDM-*g*-MA)/nanoclay [34]; PA6/maleinized ethylene propylene-diene monomer (mEPDM)/nanoclay [35]; PA6/maleinized styrene-ethylene-butylstyrene (mSEBS)/nanoclay [36–38]; PA6/maleated ethylene-propylene-diene rubber (EPDM-*g*-MA)/organoclay [39]; PA6/ethylene-*co*-butyl acrylate elastomer/nanoclay [40]; amorphous PA/ethylene-1-octene (EOR)/organoclay [41]; PA6/maleated styrene-hydrogenated butadiene-styrene (mSEBS) elastomer/nanosilica [42]; PA6/SEBS-*g*-MA/silicon carbide nanoparticles [43]; PA6/acrylonitrile butadiene rubber (NBR)/nanoclay [44]; PA6/ethylene-

propylene-diene metallocene terpolymer (EPDM)/sepiolite [45]; PA6/reactive acrylonitrile-butadiene-styrene core-shell rubber (ABS-*g*-MA)/organoclay [46]).

The first approach can be used to tailor select properties of the PA6 nanocomposites, such as the mechanical, thermal, and water barrier properties, by blending with other types of thermoplastics. The latter approach offers the potential to overcome the tendency for notch sensitivity and low notched-fracture toughness of PA nanocomposites by means of rubber modification. Table 1 lists examples of PA blend-based nanocomposites.

Polymer blends have been described as a well recognized class of materials with a set of properties targeted towards specific applications, and they have received a great deal of academic and technological interest. The properties of the blends are strongly influenced by the constituent blend components, the interface and the morphology developed during processing [22, 47]. Blending of existing polymers has become a widely accepted practice for obtaining new materials with desirable properties. Although some polymer blends are completely or partially miscible, most polymer blends are immiscible and exhibit multiple phase morphologies [48].

Nesterov and Lipatov [49] showed that solid fillers can act as stabilizers for immiscible polymer mixtures. The introduction of a specific filler in binary polymer mixtures was demonstrated to increase the thermodynamic stability of the ternary system. The compatibilizing effect of the filler depends on the change in the free energy of mixing between the two polymers, and the effect is more pronounced for immiscible systems. Specifically, when the fillers localize at the interface between two immiscible polymers, they act as a compatibilizer. Most frequently, the presence of solid fillers at the interface of a blend induces a reduction of the size distribution of the dispersed phase. This concept has been used to control the morphological of polymer blend-based nanocomposites. One of the feasible methods to improve the performance of a polymer blend is by introducing a nanofiller. According to the interaction between the nanofiller (e.g., nanoclay) and the two polymers, three basic structures exist: (1) the nanofiller is dispersed in one phase, (2) the nanofiller is dispersed in both polymer phases and (3) the nanofiller is located at the interface [50,

51]. Concurrently, at least three different morphology changes of polymer blend-based nanocomposites have been observed due to the addition of nanoparticles. In the first type of morphology change, a reduction of the domain size of the dispersed phase is observed, namely, nanoparticles act as a compatibilizer. The second type of morphology change is the alteration from a sea-island to a *co*-continuous morphology. The third type of morphology change is phase inversion, which is characterized by the transition from a sea-island to a *co*-continuous and back to a sea-island morphology with the aid of a high shear rate [48].

When nanoparticles are combined with an immiscible polymer blend, they often distribute heterogeneously. The heterogeneous distribution of nanoparticles has been reported to minimize and stabilize the polymer domain size, and in many cases, it broadens the composition range for *co*-continuity of the polymer blends. This property of nanoparticle/polymer mixtures attracts great interest because it not only provides a low-cost method for enhancing the function of these nanocomposites but also allows for the modification of their morphologies to optimize their mechanical properties [52]. The addition of nanoparticles to a polymer system with an existing phase-separated morphology, such as a polymer blend, represents an innovative approach to controlling the microstructure and, therefore, the macroscopic properties of the material [53]. Due to the high specific surface area of nanoparticles, the anchoring of the polymer components on the solid nanoparticles is believed to thermodynamically stabilize nano-filled polymer blend systems [54].

Phase continuity development and *co*-continuous morphologies are highly affected by the nature of the interface in immiscible polymer blends [55]. In general, the mechanical and optical properties of immiscible polymers depend on the disperse phase morphology. During shear flow, the droplet size is a direct result of droplet breakup and coalescence processes [56]. Among the existing polymer morphologies, *co*-continuous structures are promising because they can combine in unique and synergistic ways the advantages of various polymer components. Polymer materials with *co*-continuous structures of sub-micrometer size are interesting for many applications such as solar cell panels or separation and catalytic membranes [57]. Additionally, selective filling of conducting fillers in *co*-continuous, binary,

immiscible blends has been exploited for many potential applications such as antistatic devices, electromagnetic interference (EMI) shielding materials, etc. The selective localization of conducting fillers in either of the phases or at the interface of a *co*-continuous, binary, immiscible polymer blend is a conceptual approach (termed as double percolation) for achieving conducting blends that utilize a very low concentration of conducting fillers [22].

Numerous reports have shown that nanofillers (e.g., nanoclay) can dramatically reduce the size of the dispersed phase in a polymer blend [41]. This change may result from a barrier effect that limits the coalescence of the dispersed phases. The compatibilizing effect and resulting properties are determined by the clay localization and degree of dispersion, which is strongly influenced by the clay-polymer affinity. A marked effect of clay on the refinement of the dispersed phase was found when the clay was present in the matrix phase and at the interface, limiting coalescence due to an active interfacial role of the clay [58]. The observed morphology refinement could be due to the modification of the viscosity ratio between both polymers in the blend [28]. Accordingly, the morphological changes could affect the mechanical properties of the polymer blend nanocomposites.

Adding small amounts of nanoparticles could affect the microstructure of immiscible polymer blends, either causing a drastic size reduction of the minor phase or by promoting the formation of *co*-continuous morphologies. In other words, nanofiller can be used to promote morphology refinement and *co*-continuity of a polymer blend. In general the mechanical properties of a polymer blend based nanocomposite can be controlled by the nanofiller induced *co*-continuous morphology. It is believed that stable *co*-continuity can form provided that the interfacial tension between the filled and the unfilled polymer phase is balanced by the stress bearing ability of the nanoparticle network [59–62].

In most of the research studies, the degree of the diameter decrease of the dispersed phase was demonstrated to be dependent on the content and type of the polymeric (organic) compatibilizer (e.g., maleic anhydride-grafted compatibilizer). Accordingly, compatibilizers and nanoclays were simultaneously introduced into immiscible polymer blends to achieve a new type of material. Using a maleic anhydride-based compatibilizer and a nanoclay, a high performance PA6 blend that combines the advantages of compat-

Table 1. Current research on PA6 (rich) blend based-nanocomposites

	PA6 blend based-nanocomposites system	Dispersed phase in PA matrix and its function	Nanofiller	Processing technique	Authors
1	PA6/PP/MAH-g-PP/ Organoclay	PP: ensures good processability and insensitivity to moisture; MAH-g-PP: compatibilizer	Organoclay (4 wt%)	Melt compounding	[1, 12]
2	PA6/PP/EPR-g-MA/ Organoclay	PP: ensures good processability and insensitivity to moisture; EPR-g-MA: compatibilizer and impact modifier	Organoclay (4 wt%)	Melt compounding	[13]
3	PA6/PP/SEBS-g-MAH/ Modified MMT	PP: ensures good processability and insensitivity to moisture; SEBS-g-MAH: impact modifier	Modified MMT (4 wt%)	Melt compounding	[16, 17]
4	PA6/PP/MAPP/Organoclay	PP: ensures good processability and insensitivity to moisture; MAPP: compatibilizer	Organoclay (3.7 phr)	Melt compounding (different mixing protocols)	[69]
5	PA6/HDPE/Organoclay	HDPE: insensitivity to moisture	Organoclay (3 wt%)	Melt compounding	[2]
6	PA6/HDPE/Organoclay	HDPE: offer high toughness and cost effective	Organoclay (5 wt%)	Melt compounding (different mixing protocols)	[72]
7	PA6/HDPE/Organo-bentonite	HDPE: insensitivity to moisture	Organo-bentonite clay (1.2–2.4 wt%)	Melt compounding	[82]
8	Nylon 6/HDPE/ PE-g-MA/Nanoclay	HDPE: offers low permeability to water vapor; PE-g-MA: compatibilizer	Nanoclay (0.5–3 phr)	Melt compounding	[83]
9	Nylon 6/HDPE/ PE-g-MA/Modified clay	HDPE: offer high toughness and cost effective; PE-g-MA: compatibilizer	Modified clay (0.5–2.5 phr)	Melt compounding	[99]
10	PA6/LDPE/Organoclay	LDPE: offers low permeability to oxygen and water	Organoclay (0.5–4 phr)	Melt compounding	[24]
11	PA6/LDPE/PE-g-MA/Clay	LDPE: offers low permeability to oxygen and water; PE-g-MA: compatibilizer	Clay (3 phr)	Melt compounding	[23]
12	PA6/PS/Organophilized clays	PS: offers stiffness	Organophilized clays (5 wt%)	Melt compounding	[58]
13	PA6/PS/Organoclay	PS: offers stiffness	Organoclay (2–7 wt%)	In situ bulk polymerization followed by melt compounding	[74]
14	PA6/Polyimide/Organoclay	Polyimide: offers high-temperature, high-performance applications	Organoclay (3 wt%)	Melt compounding	[19]
15	PA6/Thermotropic liquid crystalline polymer (TLCP)/MAPP/Clay	TLCP: possess excellent mechanical and thermal properties and good anti-wear properties; MAPP: compatibilizer	Clay (4 wt%)	Melt compounding	[20]
16	PA6/poly(epichlorohydrin-co-ethylene oxide) (ECO)/Organoclay	ECO: enhances ductility and impact strength	Organoclay (6 wt%)	Two-step melt blending process	[3]
17	PA6/ABS/Styrene-maleic anhydride copolymer (SMA)/Modified montmorillonite	ABS: offers high impact strength SMA: compatibilizer	Modified montmorillonite (5 wt%)	Melt compounding (different mixing protocols)	[71]
18	PA6/ABS/Ethylene-n butyl acrylate-carbon monoxide-maleic anhydride (EnBACO-MAH)/Nanoclay	ABS: offers high impact strength EnBACO-MAH: compatibilizer	Nanoclay (2–4 wt%)	Melt compounding	[85]
19	PA6/PP/MPP/Multiwalled carbon nanotubes (MWNT)	PP: provide a good resistance against moisture and ensure good processability; MPP: compatibilizer	MWNT (0.4, 1, 2 phr)	Melt compounding	[96]
20	PA6/ABS/MWNT	ABS: offers high impact strength, high water resistance and low mold shrinkage	MWNT (1–4 wt%)	Melt compounding	[22]
21	PA6/ABS/MWNTs	ABS: offers high impact strength, high water resistance and low mold shrinkage	MWNTs (0.1–1 wt%)	Master-batch (via solution-mixing) and melt compounding	[4]
22	PA6/ABS/Styrene maleic anhydride copolymer (SMA)/MWNTs	ABS: offers high impact strength SMA: reactive compatibilizer	MWNTs (2 and 5 wt%)	Melt compounding	[100]
23	PA6/PS/MWNTs	PS: offers stiffness	MWNTs (0.5–1.5 wt%)	Successive in-situ polymerization	[66]
24	PA6/PMMA/carboxylic acid functionalized single walled carbon nanotubes (SWCNTs-COOH)	PMMA: improve mixing and miscibility with PA6	SWCNTs-COOH (1 wt%)	Melt mixing	[26]

ibilized polymer blends and the merits of polymer nanocomposites can be prepared. The coalescence of the dispersed minor phase in the PA6 matrix was restricted by the clay, and the interfacial adhesion was improved due to the compatibilizer [63]. In the most ideal model, the clay functions first, decreasing the average diameters of the dispersed particles and stabilizing the morphologies of the blends, and the compatibilizer functions successively, strengthening the interfacial adhesion between the dispersed particles and the matrix.

1.2. Processing of PA blend-based nanocomposites

Several processing methods have been employed for the production of thermoplastic nanocomposites such as melt mixing, in situ polymerization, and solution processing. Among these methods, melt mixing of nanofillers with PA blends using conventional processing techniques is particularly desirable because the process is fast, simple, solvent-free and available in the plastic industry. Most of the PA blend-based nanocomposites are prepared by melt compounding, whereas few studies used the combination of in situ polymerization followed by melt mixing. In this review, some processing topics are highlighted, such as the master-batch approach, the effects of mixing conditions and protocols, reactive blending, multiple reprocessing cycles, and the thermal stability (or decomposition) of nanofillers during melt mixing, as well as the innovation in extrusion and molding techniques for PA blend-based nanocomposites.

The master-batch concept has been applied in the processing of PA blend-based nanocomposites. In this way, preformed, largely dispersed master-batches (usually containing 10–20 wt% nanofiller) are produced. This is an advantageous processing method because hazardous contact with the nano-sized inclusions is reduced to a minimum and the dispersion is close to the optimum [64].

Bose *et al.* [65] prepared a series of multi-component polymer blends involving PA6, PP, ABS and high-density polyethylene (HDPE) with MWNT [pretreated with either a sodium salt of 6-amino-hexanoic acid (Na-AHA) or octadecyl tri-phenyl phosphonium bromide (OTPB)] by melt mixing. The MWNT were either compounded directly or by employing a master-batch dilution approach in binary (PA6/ABS), ternary (PA6/PP/ABS) and quaternary

(PA6/PP/ABS/HDPE) blends. The master batch dilution approach resulted in the selective localization of the pretreated MWNT in the PA6 phase of the multi-component blends, leading to an improvement in the AC electrical conductivity compared with blends prepared by direct addition.

In a study by Liu *et al.* [4], MWNTs were introduced into PA6/ABS blends without a compatibilizer using melt mixing. To obtain a good dispersion of MWNTs in the blends, a PA6/MWNT master-batch with a relatively high MWNT content was pre-made via solution-mixing with the aid of ultrasonication, and then the master-batch was diluted during the melt mixing. SEM observation showed a good dispersion of MWNTs both in the master-batch and in the blends and revealed that the PA6/ABS (70/30 wt) blends show a sea-island morphology, whereas the PA6/ABS (50/50 wt) blends show a *co*-continuous morphology. By incorporating MWNTs, the selective distribution of MWNTs in the PA6 phase altered the viscosity ratio of the two phases and led to a stabilization of the interface.

Périé *et al.* [57] demonstrated that combining master-batch and reactive mixing is a safe and simple method to yield polymer blend nanocomposites. They obtained fine and homogeneous dispersions of carbon nanotubes by mixing master-batches of low molecular-weight amino-terminated PA6 containing 10 or 17 wt% of MWNT with maleic anhydride-functionalized polyethylene at temperatures above melting of PA6. The use of PA6-MWNT master-batches permits the production of conductive nanocomposites with various compositions and a wide range of high performance mechanical properties.

Yan and Yang [66] prepared MWNTs-filled PA6/PS blends by in situ successive polymerization. The interface-localized MWNTs can act as a compatibilizer in PA6/PS blends and resulted in both decreased size of the PS domains and increased phase inversion concentration. For the PA6/PS (70/30) blends, the PA6/PS interface was continuous. The interface-localized MWNTs could be connected with each other in the continuous interface. Thus, a conductive MWNTs pathway was created, which was effective in decreasing the volume resistivity.

Siengchin and Karger-Kocsis [67] produced ternary composites composed of PA6, hydrogenated nitrile rubber (HNBR) and sodium fluorohectorite (FH) or boehmite alumina (BA) by melt blending with latex pre-compounding. The related master-batch was

produced by mixing the HNBR latex with water dispersible BA or water swellable FH. The PA6/HNBR/FH composites produced by the master-batch technique outperformed the PA6/HNBR/BA systems with respect to most of the mechanical and viscoelastic characteristics. This result was attributed to the preferred localization of the FH in the PA6 matrix and to its higher aspect ratio compared with BA.

One of the factors affecting the structure and properties of polymer blend nanocomposites is the processing route. During melt mixing of the constituents, the particles migrate toward specific regions of the material and are driven by more favorable thermodynamic interactions. However, kinetic effects related to the high viscosity of the polymer melts may lead to non-equilibrium morphologies. This makes the mixing procedure crucial for controlling the space distribution of the nanofiller and, thus, the microstructure of the blend and its final properties [53]. Specifically, the compounding sequence often plays an important role in determining the phase morphology [68]. For melt blending, there are two generally feasible approaches: (1) a one-step process (direct melt blending) in which the polymer and nanofiller are simultaneously loaded and (2) a two-step process that often involves master-batch preparation, e.g., blending the nanofillers with one polymer and adding the second polymer during a second extrusion step.

Filippone and Acierno [53] investigated the effect of the addition sequence of the constituents in blends of PA6 and PS with an organoclay prepared by melt compounding. In the single-step procedure, the filler and the polymers were simultaneously loaded into the mixing apparatus, whereas in the two-step procedure, a homopolymer-based PA6 nanocomposite was first prepared then mixed with the PS. Morphological analyses showed that the filler mainly enriched the more polar PA6 phase, regardless of the mixing procedure. The presence of the filler added via the single-step procedure widened the range of *co*-continuity and, thus, enhanced the mechanical strength at high temperatures due to the continuity of the PA6 phase.

Wang *et al.* [69] prepared organoclay-filled PA6/PP/maleic anhydride-grafted PP (MAPP) blends using four types of compounding sequences (e.g., direct mixing, one-step mixing, a master-batch approach, or a pre-blending approach). The PA6/organoclay

master-batch approach resulted in the smallest average domain size because it had the best organoclay dispersion, the highest amounts of PA6 grafted to MAPP, and localization of the organoclay at the interface, which efficiently stabilized the droplets and prevented droplet coalescence. Nevertheless, the use of organoclay in the preparation of PA6/PP/MAPP blends increased the dynamic storage modulus, regardless of the compounding sequence.

Naderi *et al.* [70] prepared PA-based nanocomposites in a laboratory mixer using PA6, polyepichlorohydrin-*co*-ethylene oxide (ECO), and an organoclay by a two-step melt mixing process. First, the PA6 was melt blended with the organoclay and then mixed with ECO rubber. Further intercalation and exfoliation were achieved due to the shear stress developed during the mixing process with ECO, which was due to the increased viscosity. In the PA nanocomposites prepared with 20, 30, and 40 wt% of ECO, almost complete exfoliation and a random distribution of clay in the thermoplastic phase was observed by X-ray diffraction (XRD) and transmission electron microscopy (TEM) analysis.

Oliveira *et al.* [71] studied the effects of the mixing protocol on the performance of nanocomposites based on PA6/ABS/OMMT with a styrene-maleic anhydride copolymer (SMA) as a compatibilizer. For all of the blend systems, the OMMT was preferentially located in the PA6 phase and showed an exfoliated structure. The rigidity improvement was greater when the organoclay was located in the phase that had a larger concentration. In contrast, increased toughness in some cases appeared to be greatest when the organoclay was located in the phase that had the minor concentration. In the mixing sequence of (PA6 + OMMT + SMA) + ABS (i.e., a pre-mixture of PA6, OMMT, and SMA was made, and then the PA6/SMA/OMMT nanocomposite was blended with the ABS in a second extrusion), a greater toughness was observed compared with the other sequences, and there were more uniform ABS domains in the PA6 matrix.

Zhang *et al.* [72] prepared various PA6-HDPE-clay nanocomposites by a two-step extrusion process. The processing sequence played a key role in the clay dispersion and phase morphology of the PA6-HDPE-clay nanocomposites. When PA6 was extruded with clay and even in the presence of HDPE in the first extrusion, the resultant PA6-HDPE-clay nanocomposites had a continuous PA6 phase domain

with exfoliated clay platelets and fine HDPE droplets dispersed in the continuous phase.

According to Dasari *et al.* [73] it is beneficial in terms of impact strength to have the maximum amount of the exfoliated organoclay in the nylon 66 matrix. Thus blending nylon 66 and organoclay initially and later mixing with SEBS-*g*-MA is the preferred blending sequence to maximize the impact strength. However, if the organoclay is located in the SEBS-*g*-MA phase (as organoclay is blended with SEBS-*g*-MA first) it could reduce the cavitation ability of SEBS-*g*-MA particle, and thus resulting in reduced toughening efficiency.

Although some researchers found that the mixing sequences resulted in significant morphology evolution and resultant changes in the mechanical properties, Wang *et al.* [35] found that the blending sequence did not exert a large influence on the mechanical properties. They found that a one step blending sequence satisfied their desired balanced mechanical properties for PA6/EPDM-*g*-MA/organoclay ternary nanocomposites.

Compounding procedure represents a versatile parameter for the control of the phase morphology in PA blend-based nanocomposites. In general, different melt blending sequences will give different initial distribution and dispersion states of nanofiller, and subsequently affecting the droplets deformation, breakup and coalescence through viscosity changes and barrier effects of nanofillers. In the presence of compatibilizer it will further influences morphology evolution by reducing interfacial tension and suppressing droplets coalescence. It was found that in most of the cases adding organoclay to the preblend of PA6/the second polymer/maleinized polymer gives the smallest particle size, because the reaction between PA6 and the maleinized polymer can be maximized if organoclay is added after preblending [69].

In general, the microstructure in PA blend-based nanocomposites was significantly influenced by the blending sequence, which affecting their mechanical properties. The changes in mechanical properties (i.e., stiffness, toughness) are largely attributed to the location, dispersion and distribution of the nanofillers in the polymer blends. Thus some of the factors need to be considered for the mixing protocols strategy, for example, priority of select mechanical properties (e.g., stiffness, strength or toughness); materials formulation (e.g., types of PA blends, com-

positions [PA-rich or vice versa], nanofiller, compatibilizer, toughener); affinity and preferential location of the nanofiller (e.g., nanoclay selectively located in PA phase rather than non polar polymer phase); rheology behavior (e.g., viscosity changes, shear stress, shear rate) and morphology evolution (e.g., droplets, *co*-continuous).

Yang *et al.* [74] synthesized PS/organoclay nanocomposites via in situ bulk polymerization and blended it with PA6 to obtain a ternary nanocomposite. Blending the PS/organoclay nanocomposite previously synthesized via in situ bulk polymerization with PA6 enabled full exfoliation of the organoclay in the final ternary nanocomposite, whereas an intercalated structure was achieved by directly blending the three components. The distribution of the organoclay in the polymer pairs was mainly determined by the surface properties of the clay layers.

The increased shear in melt processing is expected to promote the exfoliation of the clay, i.e., the shearing of the clay platelets from the stacks. Ozkoc *et al.* [75] prepared PA6/ABS/organo-montmorillonite clay using a twin-screw micro-extruder. The operating conditions of the micro-extruder were screw speeds of 100 and 200 rpm and a barrel temperature profile of 235°C. Doubling the screw speed reduced the dimensions of the dispersed phase and the phases in *co*-continuous blends. Most of the clays were selectively exfoliated in the PA6 phase.

An additional issue that should be considered is the thermal decomposition of the nanofiller during the melt compounding of PA blend-based nanocomposites. It is well known that the thermal instability of some nanofillers (e.g., ammonium ion-modified clay) is a major limitation for the melt compounding of polymer nanocomposites. The most often used alkyl ammonium surfactants are known to begin degrading at temperatures between 180 and 200°C, which is within the processing temperature range for most commodity plastics. To obtain nanocomposites without thermal degradation of the organic-modified nanofiller (e.g., organoclay) during processing at higher temperatures (i.e., the PA6 processing temperature of >230°C), a nanofiller that is thermally stable at temperatures higher than the processing temperatures must be used. Because polymer nanocomposites are also attractive for use in industrial applications, concerns are beginning to be raised about the behavior of such systems. These concerns are related to possible degradation occurring during

processing and reprocessing, particularly when multiple reprocessing cycles are performed [76]. Scafaro *et al.* [77] found that re-extrusion slightly improves the morphology of PA 6/PE blend-clay nanocomposites most likely due to the supplementary stresses induced on the blend in the second processing step, allowing further dispersion of the nanofiller with a consequently higher intercalation level.

1.3. Properties of PA blend-based nanocomposites

1.3.1. Nanoclay-reinforced PA blend-based nanocomposites

The preparation of polymer/clay nanocomposites has been an important approach to tailor the properties of polymeric materials because of their excellent properties and potential industrial applications. Polymer/layered silicate nanocomposites have attracted recent attention due to the report by the Toyota research group on the improved properties of PA6 nanocomposites, as well as due to the observation by Giannelis and co-workers that their preparation is possible by simple melt mixing of the polymer with the layered silicate [78–80]. In this review, the properties, such as mechanical, thermal, morphological, rheological, water barrier, flame retardancy, and wear resistance, of PA blend-based nanocomposites are highlighted.

In our previous work, we prepared PA6/PP (70/30) nanocomposites using direct melt compounding. The tensile modulus of the PA6/PP increased with increasing OMMT content. The modulus enhancement is attributed to the exfoliation- and reinforcing-ability of OMMT layered silicates. The highest strength values were observed with an organoclay content of 4 wt% in the blends. The flexural strength was twice the tensile strength, which was attributed to the effect of the injection molding-induced skin-core structure and the alignment of the exfoliated/agglomerated organoclay [12]. Because pristine clay is not compatible with most polymers due to its hydrophilic nature, it must be chemically modified to render its surface more hydrophobic. The most popular surface treatment is ion exchange of the clay with organic ammonium cations, which not only renders its surface more hydrophobic but also expands the spaces between the silicate layers [17, 81]. Modification of clay using various different types of organic modifiers plays an important role

for the enhancement of stiffness and strength. Kusmono *et al.* [17] investigated four different types of OMMT (i.e., dodecylamine-modified MMT (D-MMT), 12-aminolauric acid-modified MMT (A-MMT), stearylamine-modified MMT (S-MMT), and commercial organo-MMT (C-MMT)) on the properties of PA6/PP blends. The best reinforcement effect was observed for stearylamine modified MMT (S-MMT) due to its longest alkyl chains, largest basal spacing, and better exfoliation in the PA6/PP matrix. Kelnar *et al.* [58] reported the effect of montmorillonite modification on the behavior of PA/PS blends. The results indicated that nanosilicates can effectively influence the structure of PA/PS blends. The simultaneous reinforcement of both polymer constituents by clay enhanced their stiffness over the entire range of concentrations, whereas strength and toughness were only enhanced for low PS contents. Although the clay was found at the interface in this system, in the case of two rigid polymers (with inclusions even more rigid than the matrix), the core-shell structure did not lead to a toughness enhancement.

In our earlier work, we established that the organoclay is well dispersed (exfoliated) and preferentially embedded in the PA6 phase for a PA6/PP/organoclay nanocomposite [12, 18]. Figure 1 shows the TEM images of PA6/PP/OMMT/PP-g-MA nanocomposites. It can be seen that the OMMT silicate layers are exfoliated and selectively located in the PA6 matrix. Fang *et al.* [82] prepared PA6/HDPE/organobentonite clay and PA6/HDPE-grafted-acrylic acid (PEAA)/organobentonite clay nanocomposites via melt compounding. The majority of the organoclay platelets were concentrated in the PA6 phase and in the interfacial region between PA6 and HDPE. The organoclay platelets acted as a coupling agent between the two polymers, increasing the interaction of the two phases to a certain extent. These results were confirmed using Fourier Transform Infrared (FTIR) and positron annihilation lifetime spectroscopy. The coarse dispersion of HDPE became markedly finer due to the apparent compatibilization effect of the organoclay. Mallick and Khatua [83] studied the effect of a nanoclay on the morphology of PA6/HDPE (70/30) blends. A reduction in the average domain sizes (D) of the dispersed HDPE phase was observed; therefore, improved mixing was observed compared with the blend without nanoclay. XRD and TEM studies revealed that

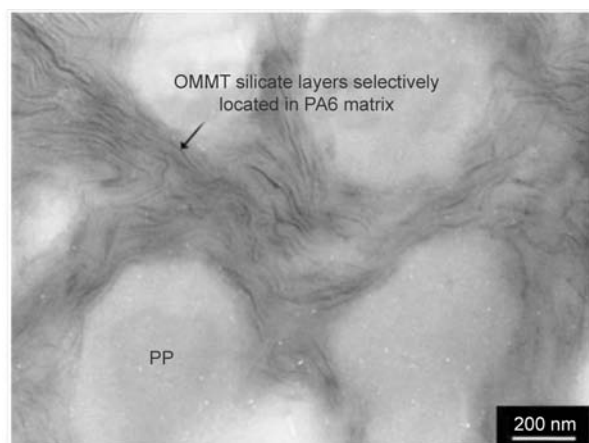


Figure 1. TEM images of PA6/PP/OMMT/PP-g-MA nanocomposites [18]. Reproduced from Kusmono, Mohd Ishak, Chow, Takeichi and Rochmadi by permission of Express Polymer Letters, Budapest University of Technology and Economics, Department of Polymer Engineering, Hungary, Budapest.

the nanoclay layers were mostly located in the PA6 matrix. Taghizadeh *et al.* [3] reported that the organoclay silicate layers were partially exfoliated in both the PA6 and poly(epichlorohydrin-*co*-ethylene oxide) phases in ternary blends of PA6/ECO/organoclay nanocomposites. A higher level of exfoliation was achieved by increasing the ECO content as a result of the higher shear stress applied to the matrix. Khoshkava *et al.* [24] found that the LDPE particle size in PA6/LDPE/organoclay nanocomposites was smaller than that in a PA6/LDPE blend. This result could be explained in terms of a reduction in the PE droplet coalescence, enhancement of the interfacial interactions, and improved thermodynamic compatibility between the blend components, all caused by high aspect ratio organoclay platelets.

The rheological behavior of PA6/PP/organoclay (70/30/4) nanocomposites with and without compatibilizers (PP-g-MAH and EPR-g-MA) was determined by various methods, such as melt flow index (MFI), capillary and plate/plate rheological measurements. Attempts were made to trace the rheological parameters that reliably reflect the observed changes in the clay dispersion. Some parameters in the viscoelastic range were found to be derived from the frequency sweep measurements using a plate/plate rheometer and are suitable indicators for changes in the clay dispersion. Considering the TEM results of the clay dispersions in the nanocomposites, the following rheological parameters in the

viscoelastic range at low frequency may be considered as suitable indicators: the storage modulus (G') and its slope and the complex viscosity (η^*) and its slope. The higher G' and the smaller the related slope, as well as the higher η^* and its higher related slope, the better the clay dispersion is [84]. Mojarrad *et al.* [85] studied the influence of a nanoclay on the rheological properties of PA6/ABS nanocomposites (with ethylene-*n* butyl acrylate-carbon monoxide-maleic anhydride as a compatibilizer). The incorporation of nanoclay (2–6%) and ABS (15–35%) causes increased relaxation times and zero-shear viscosities for all of the blends.

According to Kusmono *et al.* [86] the initial thermal stability of a PA6/PP blend was improved with the incorporation of both Na-MMT and OMMT. Dynamic Mechanical Analysis (DMA) and heat distortion temperature (HDT) results confirmed the higher values in both the storage modulus and the HDT in the PA6/PP/4Na-MMT and PA6/PP/4OMMT nanocomposites. This result may be attributed to the presence of strong hydrogen bonds between the polymer matrix and clay surface. Varley *et al.* [19] prepared PA6/low-molecular-weight polyetherimide/organoclay using a twin-screw extruder. The addition of small quantities of a commercial polyimide substantially improved the HDT and the glass transition temperatures of PA6/clay nanocomposites.

The water absorption and hygrothermal aging behavior of PA6/PP/organoclay/MAH-g-PP nanocomposites was studied at three different temperatures (30, 60, and 90°C). The equilibrium moisture content and the diffusion coefficient were dependent on the OMMT loading, MAH-g-PP concentration, and immersion temperatures. At any immersion temperature, the MAH-g-PP-compatibilized PA6/PP/OMMT nanocomposites showed excellent retention ability and recovery properties. The presence of MAH-g-PP not only enhanced the resistance of the nanocomposites against direct water immersion but also improved the resistance of the composites against hygrothermal attack [87].

Lu *et al.* [27] utilized ammonium polyphosphate (APP) and clay to improve the flame resistance of PA6/PS blends. In the blends with a continuous PA6 phase and a dispersion of clay at interface, the aggregation of clay platelets at the interface benefited the formation of a compact residue char on outer surface and a loose and large porosity on inner surface.

This morphology was more effective at delaying thermal degradation, resulting in improved thermal stability.

Dayma *et al.* [88] reported that the incorporation of nanoclay into a PA6/PP-g-MA binary blend matrix caused an enhancement in the wear resistance. The wear surface morphology studies indicated a transition in the wear failure mechanism from matrix-dominated plastic-flow to shear-induced low-intensity ductile-chipping with the increase in nanoclay content, which plays a determining role in controlling the sliding wear performance.

1.3.2. CNT-reinforced PA blend-based nanocomposites

Carbon nanotube (CNT)-modified polymer blends have attracted a large amount of attention in recent years. Most researchers reported that CNT-filled immiscible polymer blends with *co*-continuous morphologies usually exhibit excellent electrical conductivity due to the selective distribution of the CNTs in one phase even if the CNT content is very low. In addition, altering the morphology of immiscible polymer blends is possible by adding CNTs [48, 89]. CNTs have emerged as potential conducting fillers due to their exceptional electrical properties and high aspect ratio (L/D). Thus, a very high conductivity in the polymer/CNT nanocomposites can be achieved with very low CNT concentrations [90]. However, due to strong inter-tube van der Waals forces and the lack of interfacial interactions with the polymer matrix, CNTs tend to agglomerate to form clusters (or insufficient de-agglomeration) and often manifest a higher electrical percolation threshold with a lower effective L/D . Hence, an effective L/D is a key factor in achieving a low electrical percolation threshold in the polymer matrix. In addition, adequate interfacial interaction between the CNTs and the polymer matrix is another prerequisite for obtaining enhanced dispersions of CNTs. To this end, functionalization of CNTs is one of the strategies employed to enhance their phase adhesion with the polymer matrix [22]. Most of the research regarding CNT-reinforced PA blend-based nanocomposites is focused on the morphological evolution and electrical properties.

Bose *et al.* [22] prepared *co*-continuous blends of PA6 and ABS containing multiwall carbon nanotubes (MWNT) using a conical twin-screw microcompounder. The electrical and rheological percola-

tion thresholds in PA6/ABS blends were 3–4 and 1–2 wt% MWNT, respectively. A unique reactive modifier (sodium salt of 6-amino hexanoic acid, Na-AHA) was employed to facilitate the network-like structure of the MWNT and to confine them in a specific phase. This morphology was achieved by establishing specific interactions with the delocalized ' π -electron' clouds of the MWNT and the melt-interfacial reaction during melt mixing. A significant refinement in the *co*-continuous structure was observed in the blends in presence of Na-AHA-modified MWNT. TEM investigations revealed a uniform dispersion and the selective localization of the MWNT in the PA6 phase of the blends in the presence of Na-AHA. A similar observation was reported by Zhang *et al.* [91] for PA6/PP/MWNTs nanocomposites and Liu *et al.* [4] for PA6/ABS/MWNTs nanocomposites.

According to Zhang *et al.* [91], the MWNTs preferentially located in the PA6 phase, and a small amount of the MWNTs bridged the PA6 and PP phases. Liu *et al.* [4] observed a homogeneous and selective dispersion of MWNTs in the PA6 phase, a significant morphology refinement with reduced sizes of the ABS domains, and a stabilized interface.

Xiang *et al.* [48] investigated the effect of functionalized multiwall carbon nanotubes (FMWCNTs) on the phase morphology of immiscible PA6/HDPE blends. Adding small amounts of FMWCNTs (<2.0 wt%) did not exert a profound influence on the sea-island morphology of the nanocomposites. However, a typical *co*-continuous morphology was detected with moderate content of FMWCNTs (2.0 and 5.0 wt%). Further increasing the FMWCNT content (10.0 wt%) induced phase inversion.

Madhukar *et al.* [26] demonstrated that uniform PMMA dispersion is achieved by the addition of carboxylic acid-functionalized single walled carbon nanotubes (SWCNTs-COOH) in PA6/PMMA. The SWCNTs-COOH acted as a compatibilizer of PA6/PMMA by inducing hydrogen bonding between PA6 and PMMA.

1.3.3. Effects of polymeric compatibilizer on the PA blend-based nanocomposites

Blending commercial polymers to produce new materials with targeted properties is a popular and attractive topic. The final aim is to promote synergism among the immiscible polymer pairs to form blends with enhanced or new, tailored properties

with respect to the parent components. Normally, a compatibilization step is needed to improve the otherwise weak interfacial adhesion and to reduce the morphological instability of the straight blends [81]. A compatibilizer is usually added into immiscible polymer blends to intensify the interfacial strength because it has similar chain structures to the two components of the polymer blend or it reacts with one component via the functional groups (sometimes forming hydrogen bonds). Furthermore, the addition of a compatibilizer also reduces the diameters of the dispersed minor polymer phase by reducing the interfacial tension within the blend [63].

The achievement of compatibilization, whether by the addition of a third component (i.e., a compatibilizer) or by an in situ chemical reaction between the blend components (reactive blending), has played an important role in the development of polymer blends. Physical and reactive compatibilizations are used to reduce the interfacial tension between the two phases and to improve their interfacial adhesion. Block and graft copolymers with covalently connected immiscible blocks have demonstrated effective compatibilization in immiscible blends [92].

In our previous work, we have shown the peculiar clay dispersion in PA6/PP blends with and without compatibilizer. The major results of this work were that the exfoliated/intercalated clay layers were exclusively located in the more polar PA6 phase in the uncompatibilized blends and that adding a maleated compatibilizer results in a finer dispersion of the organoclay (octadecylamine-intercalated montmorillonite). Furthermore, the clay layers were preferentially embedded in a PA6-grafted polyolefin phase, formed via chemical reactions between the primary and secondary amines of the PA6 and the anhydride groups of the maleated polypropylene (MAH-g-PP) and ethylene/propylene rubber (EPR-g-MA), respectively. The melt viscosity of the compatibilizer (EPR-g-MA \gg MAH-g-PP) was suggested to also affect the dispersion state of the organoclay [84].

The strength and stiffness of the PA6/PP nanocomposites were significantly improved in the presence of MAH-g-PP. This result was attributed to the synergistic effect of the organoclay and MAH-g-PP. The MAH-g-PP-compatibilized PA6/PP nanocomposites showed a homogeneous morphology, supporting the compatibility improvement between PA6, PP and the organoclay [1]. Adding EPR-g-MA to the PA6/PP (70/30) blends resulted in a finer dis-

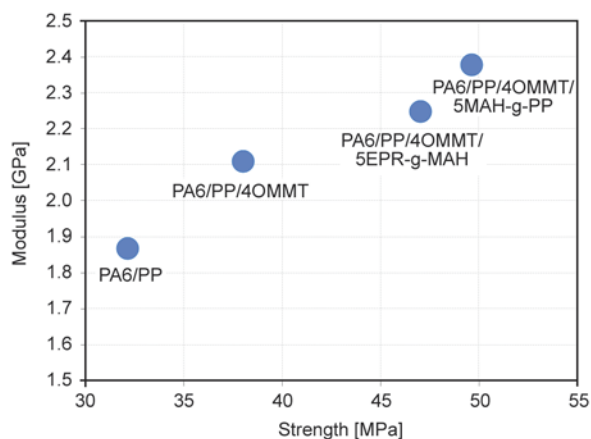


Figure 2. Effects of compatibilizer (MAH-g-PP and EPR-g-MA) and OMMT on the modulus and strength improvement of the PA6/PP blends

persion of the PP phase. The storage (G') and loss moduli (G'') assessed using plate/plate rheometry of the PA6/PP blends increased with the incorporation of EPR-g-MA and organoclay. Furthermore, the apparent shear viscosity of the PA6/PP blend significantly increased for the EPR-g-MA-compatibilized PA6/PP/organoclay nanocomposite. This result was traced to the formation of an interphase between PA6 and PP (via PA6-g-EPR) and effective intercalation/exfoliation of the organoclay [13]. Figure 2 shows the effects of compatibilizer (MAH-g-PP and EPR-g-MA) and OMMT on the modulus and strength improvement of the PA6/PP. It can be seen that the modulus/strength of PA6/PP/4OMMT/5MAH-g-PP > PA6/PP/4OMMT/5EPR-g-MAH > PA6/PP/4OMMT > PA6/PP.

The phase structure and clay dispersion in PA6/PP/organoclay (70/30/4) systems with and without an additional 5 parts of maleated polypropylene (MAH-g-PP) as a compatibilizer were studied using atomic force microscopy (AFM). AFM scans were taken from the polished surface of specimens that were chemically and physically etched with formic acid and argon ion bombardment (technique adopted from Karger-Kocsis *et al.* [93]), respectively. The latter technique was found to be very sensitive to the blend morphology; PP was far more resistant to ion bombardment than PA6. The organoclay was located in the PA6 phase in the uncompatibilized blends, whereas it was embedded in the PA6-g-PP phase in the PA6/PP blends compatibilized with MAH-g-PP. This information was deduced from the AFM scans performed on physically etched samples. The preferential location of the clay in the PA6-g-

PP phase was traced to possible chemical interactions between the PA6 and the organic intercalant of the clay [94].

According to Kusmono *et al.* [18], the presence of PP-g-MA in the PA6/PP/dodecylamine-modified MMT (OMMT) nanocomposite enhanced the properties such as stiffness, strength, ductility, impact strength, and HDT. This result was attributed to the compatibilizing effect of PP-g-MA, which improved the interfacial adhesion between the OMMT and the PA6/PP matrix and also promoted the exfoliation of silicate layers in the PA6/PP matrix [18]. The OMMT selectively localized in the PA6 matrix. A similar observation was also reported by Covas *et al.* [95] on the PA/PP/alkyl ammonium-modified montmorillonite nanoclay.

Ozkoc *et al.* [75] reported that addition of carbon monoxide-modified ethylene-n-butyl acrylate-maleic anhydride (EnBACO-MAH) as a compatibilizer resulted in a decrease in the dispersed phase morphology for a compatibilized PA6/acrylonitrile-butadiene-styrene (ABS)/organoclay system. TEM micrographs showed that the clays were selectively dispersed in the PA6 phase.

Zhang *et al.* [96] used maleated polypropylene (MPP) as a compatibilizer for multiwall carbon nanotube (MWNTs)-reinforced PA6/PP (70/30) composites. The MPP and MWNTs had a synergistic effect on the improvement of the thermal stability. Adding MPP (5 phr) significantly increased the tensile, flexural and impact strength of PA6/PP/MWNTs nanocomposites (70/30/0.4) approximately 5.3, 8.6 and 70.4%, respectively.

Zhang *et al.* [20] prepared two hybrid nanocomposites by melt blending a thermotropic liquid crystalline polymer (TLCP) and a well-dispersed PA6/clay nanocomposite (with and without the incorporation of maleic anhydride grafted polypropylene (MAPP) as a compatibilizer). The addition of MAPP improved the compatibility between TLCP and the matrix and thus enhanced the fibrillation of the dispersed TLCP phase. The wear resistance of the MAPP-compatible hybrid nanocomposite was effectively improved, as indicated by the low values of the specific wear rate and the frictional coefficient, especially under high-normal load (i.e., 80 N). For the compatibilized PA6/TLCP/OMMT/MAPP nanocomposite, the debris formed a compact and uniform transfer film on the counter surface.

Malmir *et al.* [23] studied the rheology and morphology of PA/PE/clay hybrid nanocomposites. The rheological measurements indicated that the loading of clay into a PA/PE blend dramatically increased its viscosity and elasticity compared with that of pure PE and PA, especially in the presence of a maleic anhydride-grafted polyethylene (PE-g-MA) compatibilizer. The PA/PE nanocomposite with PE-g-MA compatibilizer exhibited higher melt viscosity and storage modulus than the nanocomposite without compatibilizer, which was related to improved dispersion and polymer-silicate interactions.

In recent years, new compatibilization strategies have been explored, such as using inorganic nanofillers. Finer dispersion of the minor phase and a more stable phase morphology of the polymer blends were achieved by incorporating nanofillers [97]. The most crucial factor in the enhancement of properties in nanocomposites is the extent of interaction between the nanofiller and the polymer matrix, which leads to the selective localization of the nanofiller in multiphase systems. In this context, the addition of a compatibilizer to a nanofiller-containing multiphase system can contribute towards nanofiller positioning and its state of dispersion due to the induced changes in the thermodynamic system [98].

Mallick *et al.* [99] reported the synergistic effect of nanoclay and maleic anhydride-grafted polyethylene (PE-g-MA) on the morphology and properties of nylon 6/high density polyethylene (HDPE) blends. The size of phase separated domains decreased considerably with increasing nanoclay content and PE-g-MA. The addition of PE-g-MA in the blend-clay nanocomposites enhanced the exfoliation of the clays in the PA6 matrix, especially at the interface. Simultaneously, PE-g-MA improved the adhesion between the phases at the interface.

Jogi *et al.* [100] investigated the effect of simultaneous addition of multiwall carbon nanotubes (MWNTs) and a reactive compatibilizer (styrene maleic anhydride copolymer, SMA) during melt mixing on the phase morphology of a PA6/ABS (80/20) blend. Fourier transform infrared spectroscopic (FTIR) analysis indicated the formation of imide bonds during melt mixing. The SMA copolymer acted as a reactive compatibilizer, reduced the interfacial tension and lowered the rate of coalescence; therefore, it stabilized the phase morphology of the blends and led to higher storage modulus.

Table 2. Mechanical properties of compatibilized PA6-blend based nanocomposites

	PA6-blend based nanocomposites system	Nanofiller types and loading	Compatibilizer types and loading	Tensile strength [MPa]	Tensile modulus [GPa]	EB [%]	Ref.
1	PA6/PP (70/30) – control	–	–	32.1	1.87	22.8	[1]
	PA6/PP/organoclay (70/30/4)	Organoclay intercalated by octadecylamine/4 phr	–	38.0 [+17.4%]	2.11 [+12.8%]	4.2 [–81.5%]	
	PA6/PP/MAH-g-PP/organoclay (70/30/5/4)	Organoclay intercalated by octadecylamine/4 phr	MAH-g-PP with 1.2 wt% of maleic anhydride (MA)/5 phr	49.6 [+54.5%]	2.38 [+27.3%]	4.8 [–78.9%]	
2	PA6/PP (70/30) – control	–	–	32.1	1.87	22.8	[13]
	PA6/PP/organoclay (70/30/4)	Organoclay intercalated by octadecylamine/4 phr	–	38.0 [+17.4%]	2.11 [+12.8%]	4.2 [–81.5%]	
	PA6/PP/EPR-g-MA/organoclay (70/30/5/4)	Organoclay intercalated by octadecylamine/4 phr	EPR-g-MA containing 1 wt% MA/5 phr	47.0 [+46.4%]	2.25 [+20.3%]	6.7 [–70.6%]	
3	PA6/PP (70/30) – control	–	–	44.0	–	–	[96]
	PA6/PP/MWNT (70/30/0.4)	Multiwalled carbon nanotube/0.4 phr	–	57.1 [+29.8%]	–	–	
	PA6/PP/MPP/MWNT (70/30/5/0.4)	Multiwalled carbon nanotube/0.4 phr	Maleated polypropylene (MPP)/5 phr	60.1 [+36.6%]	–	–	
4	PA6/HDPE (80/20) – control	–	–	24.5	2.26	13.4	[99]
	PA6/HDPE/Nanoclay (80/20/0.5)	Nanoclay/0.5 phr	–	29.6 [+20.8%]	2.82 [+24.8%]	11.8 [–11.9%]	
	PA6/HDPE/PE-g-MA/Nanoclay (80/20/0.5/0.5)	Nanoclay/0.5 phr	PE-g-MA/0.5 phr	32.8 [+33.9%]	2.98 [+31.8%]	13.6 [+1.49%]	

Note: Value in [] indicates the percentage of properties changes compare to control sample (i.e., PA6 blends).

Table 2 shows the mechanical property changes of compatibilized PA6-blend based nanocomposites. The mechanical properties (modulus, strength, and elongation at break) are highly governed by the nanofillers and compatibilizers. In general, the effectiveness of compatibilization is dependent on several factors: (1) the nature and types of PA6 blends (e.g., their continuous and dispersed phases, *co*-continuous morphology), (2) the type and loading of nanofillers (e.g., surface modified or unmodified), and (3) the type and loading of the compatibilizer (e.g., grafting percentage of MA, content of reactive groups).

1.3.4. Toughening strategies for PA blend-based nanocomposites

To improve the toughness of PA nanocomposites, many investigations regarding blends with styrene-ethylene/butylene-styrene triblock copolymer (SEBS), ethylene-propylene random copolymer (EPR), ethylene/1-octene copolymer (EOR), ethylene-polypropylene-diene copolymer (EPDM), and metallocene EPDM/maleated EPDM copolymer (mEPDM/EPDM-g-MA) have been reported. Toughness is usually achieved at the expense of strength

and stiffness. Many investigations have been directed towards improving the toughness-to-stiffness balance in PA. The stiffness of rubber-toughened PA can be restored by the addition of inorganic fillers [34]. In contrast, the toughness of PA nanocomposites can be improved by the addition of a suitable impact modifier. In this review, we mainly emphasize the toughness improvement of PA blend (thermoplastic-thermoplastic)-based nanocomposites (for example, PA6/PP/nanofiller, PA6/HDPE/nanofiller, and PA6/PS/nanofiller).

The addition of a nanofiller into a PA6 blend system, for example, in the case of PA6/PP/organoclay nanocomposites, drastically decreased the impact strength. The reduction in impact strength could be attributed to the immobilization of the macromolecular chains by the clay particles, which limited their ability to adapt to deformation and resulted in a more brittle material. In addition, each silicate layer (especially aggregates of silicate layers) was the site of stress concentration and could act as a micro crack initiator.

Among the already studied toughened PA6/PP nanocomposites, we can include PA6/PP/organoclay/maleated ethylene-propylene rubber (EPR-g-MA)

[13], PA6/PP/organoclay/polyethylene octane elastomer (POE) [14], PA6/PP/clay/maleic anhydride polyethylene octane elastomer (POE-g-MA) [15], and PA6/PP/modified clay/maleated styrene-ethylene-butylene-styrene (SEBS-g-MA) [16, 17]. Chow *et al.* [13] and Wahit *et al.* [14] demonstrated that the ductility and toughness of PA6/PP/organoclay nanocomposites improved by the addition of EPR-g-MA and POE, respectively.

According to Kusmono *et al.* [16] the incorporation of maleated styrene-ethylene-butylene-styrene (SEBS-g-MA) increased the fracture toughness (assessed by single edge notched three point bending tests) of PA6/PP/organoclay (70/30/4) nanocomposites. The increase in ductility and fracture toughness at high testing speeds could be attributed to the thermal blunting mechanism in front of the crack tip [16]. The rubber particles dispersed within a neat PA6 matrix increased the toughness via cavitation, which relieves the triaxial stress state ahead of the advancing crack tip and allows the PA6 matrix to shear yield, thereby dissipating more energy and enhancing the toughness [17]. A similar finding was reported by Attari *et al.* [101] for PA6/HDPE/SEBS-g-MA/modified clay nanocomposites. The presence of SEBS-g-MA improved the toughness and thermal properties of PA6/HDPE/modified clay nanocomposites. In another work by Kusmono *et al.* [102], a SEBS-g-MA compatibilizer was more efficient in improving the fracture toughness of PA6/PP/OMMT nanocomposites than a PP-g-MA compatibilizer at high testing speeds (i.e., tensile testing speed of 500 mm/min).

Chen *et al.* [21] prepared PA66/PA6/organoclay ternary nanocomposites by mixing PA6 and OMMT as a master-batch and then blending it with PA66 and different elastomers in a twin-screw extruder. The incorporation of POE-g-MA markedly toughened the nanocomposites. A PA66-co-POE-g-MA copolymer formed in situ during the melt extrusion of PA66 and POE-g-MA improved the compatibility between PA66 and POE-g-MA by lowering the interfacial tension and thus decreasing the sizes of the POE-g-MA particles. The smaller POE-g-MAH domains are hypothesized to toughen the blends.

The application of elastomeric tougheners in nanocomposites usually leads to an increase in toughness at the expense of stiffness and strength. In contrast, when applying the compatibilization reinforcement concept to an elastomer-toughened PA6

nanocomposite, Kelnar *et al.* [103] found a significant size reduction and modification of the dispersed phase morphology. TEM showed the formation of core-shell particles (rubber surrounded by stacks of clay platelets) enhancing the toughening effect of the elastomer. As a result, the simultaneous enhancement of the strength, toughness and stiffness was achieved. Additionally, taking into account the potential of clay-compatibilization, which leads to a dispersed core/shell rubber phase with enhanced toughening ability, Kelnar *et al.* [104] studied the PA6/PS/ethylene propylene elastomer (EPR)/nanoclay system (i.e., nanocomposite with ternary matrix consisting of PA6 with dispersed rubbery and rigid polymer phases). The addition of nanoclay to the PA6/PS/EPR matrix led to a decrease in the particle size. However, the presence of the nanoclay in a ternary matrix caused predominantly opposite changes in mechanical behavior compared with binary blends. The differences include a decrease in toughness with increasing clay content and a less effective toughening effect of the core-shell (elastomer/clay) particles. Thus, a proper combination of rigid and elastomeric inclusions should be selected to achieve nanocomposites with balanced mechanical behavior.

Future challenges and conclusion remarks

As illustrated within this review, nanofillers represent an interesting method to extend and to improve the properties of PA blends to prepare high-performance PA blend-based nanocomposites. The properties of PA blend-based nanocomposites are influenced by various factors such as the compositions, morphologies, interfacial interactions, nanofillers and processing methods (see Figure 3). The superior properties derived through the combination of PA blends and nanofiller appear to be relevant in the development of materials for various applications. However, there are some challenges of particular note. These include:

- (1). Nanofillers tend to agglomerate, which can influence the dispersibility and interfacial interaction with the polymer; thus, the incorporation of nanofiller in a PA blend matrix must overcome processing and dispersion challenges. A new route of PA blend based nanocomposites processing, for example, water injection-assisted melt compounding (see contribution works from Siengchin and Karger-Kocsis

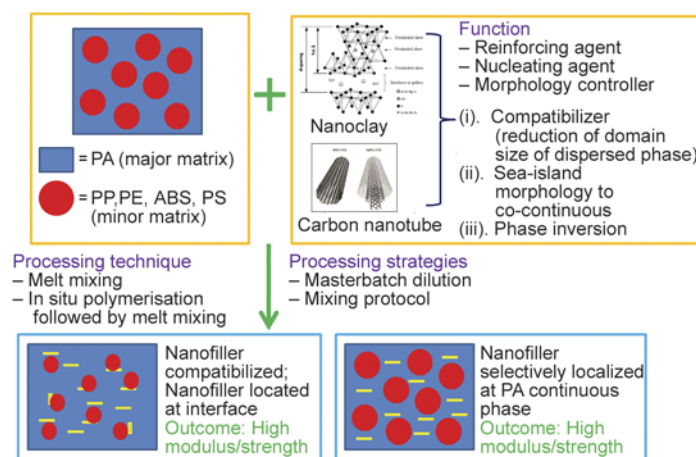


Figure 3. Structure-properties-processing relationship of PA blend-based nanocomposites

[105]) and ultrasound assisted melt compounding is potential and feasible.

- (2). The surface chemistry of the nanofiller has a dramatic influence on their localization in the PA blend and hence on the possible compatibilizing role and on the final properties. In most cases, the localization of nanofiller at the interface is not often accurate and the size and surface chemistry are not well-controlled parameters; thus, nanofillers with desired surface properties with controllable localization and dispersion in PA blends should be further developed. This is of great importance for nanoparticle-induced morphology control.
- (3). The interfacial strength of PA blends and nanofiller is always a challenge in the development of a high performance nanocomposites; thus, suitable surface modification of nanofiller and compatibilization technique must be selected in order to maximize the properties of PA blend-based nanocomposites. In this aspect, the research work carried out by Karger-Kocsis's group is worth mention. With the presence of a selected compatibilizer and appropriate mixing protocol, well-functionalized nanoparticles can be located at the interface and thus stabilize the morphology of a polymer blend. Thus, the compatibilization mechanisms contribute to a finer morphology of polymer-blend based nanocomposites. In addition, the interaction of compatibilizer (e.g., maleic-anhydride based) and nanofiller is essential to control the preferential state of the nanofillers in the selected polymer phase [68, 97].
- (4). Nanofillers such as halloysite nanotubes (HNTs) make it possible, in contrast to other nano-

fillers, to significantly reduce the ductility loss upon addition in a polymer matrix (e.g., PP, PA6 and linear low density polyethylene (LLDPE) – as reported in ref [106–108]). We believe that adding HNT into PA6 blends could be a feasible approach to prepare nanocomposites with a good balance in strength, stiffness and toughness because HNT works well with both PA and polyolefin (e.g., PP, LLDPE). In addition, graphene, a new generation carbonaceous-layered material has shown considerable potential as a reinforcing material in polymer nanocomposites. It has a very large surface area and tunable surface properties [109–114]. Graphene is a good candidate that can be used to improve the mechanical (e.g., modulus, strength, creep resistance) and electrical properties of PA blend-based nanocomposites and hence widen the multi-functionality needed for electronic applications (e.g., electrical energy storages, actuators, flexible electronics, electromagnetic interference shielding and sensors) and corrosion resistance and gas barrier properties.

List of abbreviation

ABS:	acrylonitrile–butadiene–styrene
ABS-g-MA:	acrylonitrile–butadiene–styrene core-shell rubber
A-MMT:	12-aminolauric acid modified montmorillonite
APP:	ammonium polyphosphate
AFM:	atomic force microscopy
BA:	boehmite alumina
C-MMT:	commercial organo-montmorillonite
CNT:	carbon nanotube
D-MMT:	dodecylamine modified montmorillonite

DPIM:	dynamic packing injection molding	SEBS:	styrene-ethylene/butylenes-styrene tri-block copolymers
ECO:	polyepichlorohydrin-co-ethylene oxide	SEBS-g-MA:	maleated styrene-ethylene butylenes-styrene
EMI:	electromagnetic interference	SMA:	styrene-maleic anhydride copolymer
EnBACOMAH:	carbon monoxide-modified ethylene-n-butyl acrylate-maleic anhydride	S-MMT:	stearylamine modified MMT (S-MMT)
EOR:	ethylene-1-octene	SWCNT:	single-walled carbon nanotube
EPDM:	ethylene-propylene-diene metallocene terpolymer	SWCNTs-COOH:	carboxylic acid functionalized single walled carbon nanotubes
EPDM-g-MA :	maleated ethylene-polypropylene-diene copolymer	TEM:	transmission electron microscopy
EPR:	ethylene-propylene random copolymer	TLCP:	thermotropic liquid crystalline polymer
EPR-g-MA:	maleated ethylene/propylene rubber	XRD:	X-ray diffraction
FH:	sodium fluorohectorite		
FMWCNT:	functionalized multiwall carbon nanotubes		
FTIR:	fourier transform infrared spectroscopic		
HDPE:	high density polyethylene		
HDT:	heat distortion temperature		
HNBR:	hydrogenated nitrile rubber		
HNT:	halloysite nanotubes		
LDPE:	low density polyethylene		
LLDPE:	linear low density polyethylene		
MA:	maleic anhydride		
MAH-g-PP:	maleated polypropylene		
MAPP:	maleic anhydride grafted PP		
MAV:	maleic anhydride intercalated vermiculite		
mEPDM:	metallocene ethylene-polypropylene-diene copolymer		
mEPR:	maleinized ethylene-propylene-rubber		
MFI:	melt flow index		
MMT:	montmorillonite		
MPP:	maleated polypropylene		
mSEBS:	maleinized styrene-ethylene-butylene-styrene		
MWNT:	multi-walled carbon nanotube		
Na-AHA:	sodium salt of 6-aminohexanoic acid		
Na-MMT:	sodium montmorillonite		
NBR:	acrylonitrile butadiene rubber		
OMMT:	organo-montmorillonite		
OTPB:	octadecyl tri-phenyl phosphonium bromide		
PA:	polyamide		
PA6:	polyamide 6		
PA66:	polyamide 66		
PA12:	polyamide 12		
PE:	polyethylene		
PEAA:	high density polyethylene-grafted-acrylic acid		
PE-g-MA:	maleic anhydride grafted polyethylene		
PMMA:	poly(methyl methacrylate)		
POE-g-MA:	maleic anhydride polyethylene octane elastomer		
PP:	polypropylene		
PP-g-MAH:	maleic anhydride grafted polypropylene		
PPO:	poly(phenylene oxide)		
PS:	polystyrene		

Acknowledgements

The authors would like to thank the Universiti Sains Malaysia for the Research University Grant (grant number: 814070, 814199, 814132) and Ministry of Higher Education (Malaysia) for the FRGS Grant (grant number: 6071260) and ERGS grant (grant number: 6730084). We sincerely thank Professor Karger-Kocsis for his professional advice and knowledge sharing in the research and development of polymer blend nanocomposites. We also thank Prof. Azman Hassan, Professor Takeichi, Dr. Mat Uzir, Dr. Kusmono for their valuable research collaboration works and contributions.

References

- [1] Chow W. S., Mohd Ishak Z. A., Karger-Kocsis J., Apostolov A. A., Ishiaku U. S.: Compatibilizing effect of maleated polypropylene on the mechanical properties and morphology of injection molded polyamide 6/polypropylene/organoclay nanocomposites. *Polymer*, **44**, 7427–7440 (2003). DOI: [10.1016/j.polymer.2003.09.006](https://doi.org/10.1016/j.polymer.2003.09.006)
- [2] Erdmann E., Dias M. L., Pita V. J. R. R., Destéfanis H., Monasterio F., Acosta D.: Characterization of HDPE/polyamide 6/nanocomposites using scanning and transmission electron microscopy. *Macromolecular Symposia*, **258**, 82–89 (2007). DOI: [10.1002/masy.200751209](https://doi.org/10.1002/masy.200751209)
- [3] Taghizadeh E., Naderi G., Razavi-Nouri M.: Effects of organoclay on the mechanical properties and microstructure of PA6/ECO blend. *Polymer Testing*, **30**, 327–334 (2011). DOI: [10.1016/j.polymertesting.2011.01.007](https://doi.org/10.1016/j.polymertesting.2011.01.007)
- [4] Liu X-Q., Yang W., Xie B-H., Yang M-B.: Influence of multiwall carbon nanotubes on the morphology, melting, crystallization and mechanical properties of polyamide 6/acrylonitrile-butadiene-styrene blends. *Materials and Design*, **34**, 355–362 (2012). DOI: [10.1016/j.matdes.2011.08.028](https://doi.org/10.1016/j.matdes.2011.08.028)
- [5] Ray S. S., Okamoto M.: Polymer/layered silicate nanocomposites: A review from preparation to processing. *Progress in Polymer Science*, **28**, 1539–1641 (2003). DOI: [10.1016/j.progpolymsci.2003.08.002](https://doi.org/10.1016/j.progpolymsci.2003.08.002)

- [6] Chow W. S., Mohd Ishak Z. A.: Mechanical, morphological and rheological properties of polyamide 6/ organo-montmorillonite nanocomposites. *Express Polymer Letters*, **1**, 77–83 (2007). DOI: [10.3144/expresspolymlett.2007.14](https://doi.org/10.3144/expresspolymlett.2007.14)
- [7] Kim G-M., Lee D-H., Hoffmann B., Kressler J., Stöpelmann G.: Influence of nanofillers on the deformation process in layered silicate/polyamide-12 nanocomposites. *Polymer*, **42**, 1095–1100 (2001). DOI: [10.1016/S0032-3861\(00\)00468-7](https://doi.org/10.1016/S0032-3861(00)00468-7)
- [8] Liu X., Wu Q., Berglund L. A.: Polymorphism in polyamide 66/clay nanocomposites. *Polymer*, **43**, 4967–4972 (2002). DOI: [10.1016/S0032-3861\(02\)00331-2](https://doi.org/10.1016/S0032-3861(02)00331-2)
- [9] Lonjon A., Caffrey I., Carponcin D., Dantras E., Lacabanne C.: High electrically conductive composites of Polyamide 11 filled with silver nanowires: Nanocomposites processing, mechanical and electrical analysis. *Journal of Non-Crystalline Solids*, **376**, 199–204 (2013). DOI: [10.1016/j.jnoncrysol.2013.05.020](https://doi.org/10.1016/j.jnoncrysol.2013.05.020)
- [10] Li Y., Shimizu H.: Co-continuous polyamide 6 (PA6)/ acrylonitrile-butadiene-styrene (ABS) nanocomposites. *Macromolecular Rapid Communications*, **26**, 710–715 (2005). DOI: [10.1002/marc.200400654](https://doi.org/10.1002/marc.200400654)
- [11] Dayma N., Satapathy B. K.: Microstructural correlations to micromechanical properties of polyamide-6/ low density polyethylene-grafted-maleic anhydride/ nanoclay ternary nanocomposites. *Materials and Design*, **33**, 510–522 (2012). DOI: [10.1016/j.matdes.2011.04.057](https://doi.org/10.1016/j.matdes.2011.04.057)
- [12] Chow W. S., Mohd Ishak Z. A., Ishiaku U. S., Karger-Kocsis J., Apostolov A. A.: The effect of organoclay on the mechanical properties and morphology of injection-molded polyamide 6/polypropylene nanocomposites. *Journal of Applied Polymer Science*, **91**, 175–189 (2004). DOI: [10.1002/app.13244](https://doi.org/10.1002/app.13244)
- [13] Chow W. S., Abu Bakar A., Mohd Ishak Z. A., Karger-Kocsis J., Ishiaku U. S.: Effect of maleic anhydride-grafted ethylene-propylene rubber on the mechanical, rheological and morphological properties of organoclay reinforced polyamide 6/polypropylene nanocomposites. *European Polymer Journal*, **41**, 687–696 (2005). DOI: [10.1016/j.eurpolymj.2004.10.041](https://doi.org/10.1016/j.eurpolymj.2004.10.041)
- [14] Wahit M. U., Hassan A., Mohd Ishak Z. A., Abu Bakar A.: The effect of polyethylene-octene elastomer on the morphological and mechanical properties of polyamide 6/polypropylene nanocomposites. *Polymer and Polymer Composites*, **13**, 795–805 (2005).
- [15] Hassan A., Othman N., Wahit M. U., Wei L. J., Rachmat A. R., Mohd Ishak Z. A.: Maleic anhydride polyethylene octene elastomer toughened polyamide 6/ polypropylene nanocomposites: Mechanical and morphological properties. *Macromolecular Symposia*, **239**, 182–191 (2006). DOI: [10.1002/masy.200690095](https://doi.org/10.1002/masy.200690095)
- [16] Kusmono, Mohd Ishak Z. A., Chow W. S., Takeichi T., Rochmadi: Influence of SEBS-g-MA on morphology, mechanical, and thermal properties of PA6/PP/organoclay nanocomposites. *European Polymer Journal*, **44**, 1023–1039 (2008). DOI: [10.1016/j.eurpolymj.2008.01.019](https://doi.org/10.1016/j.eurpolymj.2008.01.019)
- [17] Kusmono, Mohd Ishak Z. A., Chow W. S., Takeichi T., Rochmadi: Compatibilizing effect of SEBS-g-MA on the mechanical properties of different types of OMMT filled polyamide 6/polypropylene nanocomposites. *Composites Part A: Applied Science and Manufacturing*, **39**, 1802–1814 (2008). DOI: [10.1016/j.compositesa.2008.08.009](https://doi.org/10.1016/j.compositesa.2008.08.009)
- [18] Kusmono, Mohd Ishak Z. A., Chow W. S., Takeichi T., Rochmadi: Enhancement of properties of PA6/PP nanocomposites via organic modification and compatibilization. *Express Polymer Letters*, **2**, 655–664 (2008). DOI: [10.3144/expresspolymlett.2008.78](https://doi.org/10.3144/expresspolymlett.2008.78)
- [19] Varley R. J., Groth A. M., Leong K. H.: Preparation and characterisation of polyamide-polyimide organoclay nanocomposites. *Polymer International*, **57**, 618–625 (2008). DOI: [10.1002/pi.2385](https://doi.org/10.1002/pi.2385)
- [20] Zhang B., Wong J. S-P., Yam R. C-M., Li R. K-Y.: Enhanced wear performance of nylon 6/organoclay nanocomposite by blending with a thermotropic liquid crystalline polymer. *Polymer Engineering and Science*, **50**, 900–910 (2010). DOI: [10.1002/pen.21607](https://doi.org/10.1002/pen.21607)
- [21] Chen J., Wu W., Chen C., He S.: Toughened nylon66/ nylon6 ternary nanocomposites by elastomers. *Journal of Applied Polymer Science*, **115**, 588–598 (2010). DOI: [10.1002/app.30989](https://doi.org/10.1002/app.30989)
- [22] Bose S., Bhattacharyya A. R., Kulkarni A. R., Pötschke P.: Electrical, rheological and morphological studies in co-continuous blends of polyamide 6 and acrylonitrile-butadiene-styrene with multiwall carbon nanotubes prepared by melt blending. *Composites Science and Technology*, **69**, 365–372 (2009). DOI: [10.1016/j.compscitech.2008.10.024](https://doi.org/10.1016/j.compscitech.2008.10.024)
- [23] Malmir S., Razavi Aghjeh M. K., Hemmati M., Ahmadi Tehrani R.: Relationship between morphology and rheology of PA/PE/clay blend nanocomposites. I. PA matrix. *Journal of Applied Polymer Science*, **125**, E503–E514 (2012). DOI: [10.1002/app.36439](https://doi.org/10.1002/app.36439)
- [24] Khoshkava V., Dini M., Nazockdast H.: Study on morphology and microstructure development of PA6/LDPE/ organoclay nanocomposites. *Journal of Applied Polymer Science*, **125**, E197–E203 (2012). DOI: [10.1002/app.33970](https://doi.org/10.1002/app.33970)
- [25] Ogunniran E. S., Sadiku R., Ray S. S., Luruli N.: Morphology and thermal properties of compatibilized PA12/ PP blends with boehmite alumina nanofiller inclusions. *Macromolecular Materials and Engineering*, **297**, 627–638 (2012). DOI: [10.1002/mame.201100254](https://doi.org/10.1002/mame.201100254)

- [26] Madhukar K., Sainath A. V. S., Sanjeeva Rao B., Suresh Kumar D., Bikshamaiah N., Srinivas Y., Mohan Babu N., Ashok B.: Role of carboxylic acid functionalized single walled carbon nanotubes in polyamide 6/poly (methyl methacrylate) blend. *Polymer Engineering and Science*, **53**, 397–402 (2013).
DOI: [10.1002/pen.23272](https://doi.org/10.1002/pen.23272)
- [27] Lu C., Gao X-P., Yang D., Cao Q-Q., Huang X-H., Liu J-C., Zhang Y-Q.: Flame retardancy of polystyrene/nylon-6 blends with dispersion of clay at the interface. *Polymer Degradation and Stability*, **107**, 10–20 (2014).
DOI: [10.1016/j.polyimdegradstab.2014.04.028](https://doi.org/10.1016/j.polyimdegradstab.2014.04.028)
- [28] Parpaite T., Otazaghine B., Taguet A., Sonnier R., Caro A. S., Lopez-Cuesta J. M.: Incorporation of modified Stöber silica nanoparticles in polystyrene/polyamide-6 blends: Coalescence inhibition and modification of the thermal degradation via controlled dispersion at the interface. *Polymer*, **55**, 2704–2715 (2014).
DOI: [10.1016/j.polymer.2014.04.016](https://doi.org/10.1016/j.polymer.2014.04.016)
- [29] Tjong S. C., Bao S. P.: Impact fracture toughness of polyamide-6/montmorillonite nanocomposites toughened with a maleated styrene/ethylene butylene/styrene elastomer. *Journal of Polymer Science Part B: Polymer Physics*, **43**, 585–595 (2005).
DOI: [10.1002/polb.20360](https://doi.org/10.1002/polb.20360)
- [30] Ahn Y-C., Paul D. R.: Rubber toughening of nylon 6 nanocomposites. *Polymer*, **47**, 2830–2838 (2006).
DOI: [10.1016/j.polymer.2006.02.074](https://doi.org/10.1016/j.polymer.2006.02.074)
- [31] Baldi F., Bignotti F., Tieghi G., Riccò T.: Rubber toughening of polyamide 6/organoclay nanocomposites obtained by melt blending. *Journal of Applied Polymer Science*, **99**, 3406–3416 (2006).
DOI: [10.1002/app.22955](https://doi.org/10.1002/app.22955)
- [32] Dong W., Zhang X., Liu Y., Wang Q., Gui H., Gao J., Song Z., Lai J., Huang F., Qiao J.: Flame retardant nanocomposites of polyamide 6/clay/silicone rubber with high toughness and good flowability. *Polymer*, **47**, 6874–6879 (2006).
DOI: [10.1016/j.polymer.2006.07.038](https://doi.org/10.1016/j.polymer.2006.07.038)
- [33] Farahani R. D., Ahmad Ramazani S. A.: Melt preparation and investigation of properties of toughened polyamide 66 with SEBS-g-MA and their nanocomposites. *Materials and Design*, **29**, 105–111 (2008).
DOI: [10.1016/j.matdes.2006.11.018](https://doi.org/10.1016/j.matdes.2006.11.018)
- [34] García-López D., López-Quintana S., Gobernado-Mitre I., Merino J. C., Pastor J. M.: Study of melt compounding conditions and characterization of polyamide 6/ metallocene ethylene-polypropylene-diene copolymer/maleated ethylene-polypropylene-diene copolymer blends reinforced with layered silicates. *Polymer Engineering and Science*, **47**, 1033–1039 (2007).
DOI: [10.1002/pen.20782](https://doi.org/10.1002/pen.20782)
- [35] Wang K., Wang C., Li J., Su J., Zhang Q., Du R., Fu Q.: Effects of clay on phase morphology and mechanical properties in polyamide 6/EPDM-g-MA/organoclay ternary nanocomposites. *Polymer*, **48**, 2144–2154 (2007).
DOI: [10.1016/j.polymer.2007.01.070](https://doi.org/10.1016/j.polymer.2007.01.070)
- [36] González I., Eguiazábal J. I., Nazábal J.: Compatibilization level effects on the structure and mechanical properties of rubber-modified polyamide-6/clay nanocomposites. *Journal of Polymer Science Part B: Polymer Physics*, **43**, 3611–3620 (2005).
DOI: [10.1002/polb.20663](https://doi.org/10.1002/polb.20663)
- [37] González I., Eguiazábal J. I., Nazábal J.: Rubber-toughened polyamide 6/clay nanocomposites. *Composites Science and Technology*, **66**, 1833–1843 (2006).
DOI: [10.1016/j.compscitech.2005.10.008](https://doi.org/10.1016/j.compscitech.2005.10.008)
- [38] González I., Eguiazábal J. I., Nazábal J.: Effects of the processing sequence and critical interparticle distance in PA6-clay/mSEBS nanocomposites. *European Polymer Journal*, **44**, 287–299 (2008).
DOI: [10.1016/j.eurpolymj.2007.11.027](https://doi.org/10.1016/j.eurpolymj.2007.11.027)
- [39] Zhang L., Wan C., Zhang Y.: Investigation on morphology and mechanical properties of polyamide 6/ maleated ethylene-propylene-diene rubber/organoclay composites. *Polymer Engineering and Science*, **49**, 209–216 (2009).
DOI: [10.1002/pen.21201](https://doi.org/10.1002/pen.21201)
- [40] Prasath Balamurugan G., Maiti S. N.: Effects of nanotalc inclusion on mechanical, microstructural, melt shear rheological, and crystallization behavior of polyamide 6-based binary and ternary nanocomposites. *Polymer Engineering and Science*, **50**, 1978–1993 (2010).
DOI: [10.1002/pen.21724](https://doi.org/10.1002/pen.21724)
- [41] Yoo Y., Tiwari R. R., Yoo Y-T., Paul D. R.: Effect of organoclay structure and mixing protocol on the toughening of amorphous polyamide/elastomer blends. *Polymer*, **51**, 4907–4915 (2010).
DOI: [10.1016/j.polymer.2010.08.036](https://doi.org/10.1016/j.polymer.2010.08.036)
- [42] Zhang B., Wong J. S-P., Shi D., Yam R. C-M., Li R. K-Y.: Investigation on the mechanical performances of ternary nylon 6/SEBS elastomer/nano-SiO₂ hybrid composites with controlled morphology. *Journal of Applied Polymer Science*, **115**, 469–479 (2010).
DOI: [10.1002/app.30185](https://doi.org/10.1002/app.30185)
- [43] Liao C. Z., Tjong S. C.: Mechanical and thermal behaviour of polyamide 6/silicon carbide nanocomposites toughened with maleated styrene–ethylene–butylene–styrene elastomer. *Fatigue and Fracture of Engineering Materials and Structures*, **35**, 56–63 (2011).
DOI: [10.1111/j.1460-2695.2011.01561.x](https://doi.org/10.1111/j.1460-2695.2011.01561.x)
- [44] Jahromi A. E., Arefazar A., Jazani O. M., Sari M. G., Saeb M. R., Salehil M.: Taguchi-based analysis of polyamide 6/acrylonitrile–butadiene rubber/nanoclay nanocomposites: The role of processing variables. *Journal of Applied Polymer Science*, **130**, 820–828 (2013).
DOI: [10.1002/app.39191](https://doi.org/10.1002/app.39191)
- [45] Gallego R., García-López D., Merino J. C., Pastor J. M.: How do the shape of clay and type of modifier affect properties of polymer blends? *Journal of Applied Polymer Science*, **127**, 3009–3016 (2013).
DOI: [10.1002/app.37979](https://doi.org/10.1002/app.37979)

- [46] Zhou L., Wan Y., Chen X., Sun S., Zhou C.: Toughening of PA6 nanocomposites by reactive acrylonitrile–butadiene–styrene core–shell rubber particles. *Polymer Composites*, **35**, 864–871 (2014).
DOI: [10.1002/pc.22730](https://doi.org/10.1002/pc.22730)
- [47] Rhim J-W., Park H-M., Ha C-S.: Bio-nanocomposites for food packaging applications. *Progress in Polymer Science*, **38**, 1629–1652 (2013).
DOI: [10.1016/j.progpolymsci.2013.05.008](https://doi.org/10.1016/j.progpolymsci.2013.05.008)
- [48] Xiang F., Shi Y., Li X., Huang T., Chen C., Peng Y., Wang Y.: Cocontinuous morphology of immiscible high density polyethylene/polyamide 6 blend induced by multiwalled carbon nanotubes network. *European Polymer Journal*, **48**, 350–361 (2012).
DOI: [10.1016/j.eurpolymj.2011.11.013](https://doi.org/10.1016/j.eurpolymj.2011.11.013)
- [49] Nesterov A. E., Lipatov Y. S.: Compatibilizing effect of a filler in binary polymer mixtures. *Polymer*, **40**, 1347–1349 (1999).
DOI: [10.1016/S0032-3861\(98\)00277-8](https://doi.org/10.1016/S0032-3861(98)00277-8)
- [50] Zou H., Zhang Q., Tan H., Wang K., Du R., Fu Q.: Clay locked phase morphology in the PPS/PA66/clay blends during compounding in an internal mixer. *Polymer*, **47**, 6–11 (2006).
DOI: [10.1016/j.polymer.2005.11.031](https://doi.org/10.1016/j.polymer.2005.11.031)
- [51] Zou H., Wang K., Zhang Q., Fu Q.: A change of phase morphology in poly(*p*-phenylene sulfide)/polyamide 66 blends induced by adding multi-walled carbon nanotubes. *Polymer*, **47**, 7821–7826 (2006).
DOI: [10.1016/j.polymer.2006.09.008](https://doi.org/10.1016/j.polymer.2006.09.008)
- [52] Cai X., Li B., Pan Y., Wu G.: Morphology evolution of immiscible polymer blends as directed by nanoparticle self-agglomeration. *Polymer*, **53**, 259–266 (2012).
DOI: [10.1016/j.polymer.2011.11.032](https://doi.org/10.1016/j.polymer.2011.11.032)
- [53] Filippone G., Acierno D.: Altering the onset of *co*-continuity in nanocomposite immiscible blends by acting on the melt-compounding procedure. *Journal of Applied Polymer Science*, **122**, 3712–3719 (2011).
DOI: [10.1002/app.34785](https://doi.org/10.1002/app.34785)
- [54] Entezam M., Khonakdar H. A., Yousefi A. A., Jafari S. H., Wagenknecht U., Heinrich G.: Dynamic and transient shear start-up flow experiments for analyzing nanoclay localization in PP/PET blends: Correlation with microstructure. *Macromolecular Materials and Engineering*, **298**, 113–126 (2013).
DOI: [10.1002/mame.201100435](https://doi.org/10.1002/mame.201100435)
- [55] Bhadane P. A., Champagne M. F., Huneault M. A., Tofan F., Favis B. D.: Continuity development in polymer blends of very low interfacial tension. *Polymer*, **47**, 2760–2771 (2006).
DOI: [10.1016/j.polymer.2006.01.065](https://doi.org/10.1016/j.polymer.2006.01.065)
- [56] Ramic A. J., Hudson S. D., Jamieson A. M., Manas-Zloczower I.: Temporary droplet-size hysteresis in immiscible polymer blends. *Polymer*, **41**, 6263–6270 (2000).
DOI: [10.1016/S0032-3861\(99\)00845-9](https://doi.org/10.1016/S0032-3861(99)00845-9)
- [57] Périé T., Brosse A-C., Tencé-Girault S., Leibler L.: Co-continuous nanostructured nanocomposites by reactive blending of carbon nanotube masterbatches. *Polymer*, **53**, 984–992 (2012).
DOI: [10.1016/j.polymer.2012.01.007](https://doi.org/10.1016/j.polymer.2012.01.007)
- [58] Kelnar I., Rotrekl J., Kotek J., Kaprálková L.: Effect of montmorillonite modification on the behaviour of polyamide/polystyrene blends. *Polymer International*, **57**, 1281–1286 (2008).
DOI: [10.1002/pi.2475](https://doi.org/10.1002/pi.2475)
- [59] Filippone G., Dintcheva N. Tz., Acierno D., La Mantia F. P.: The role of organoclay in promoting *co*-continuous morphology in high-density poly(ethylene)/poly(amide) 6 blends. *Polymer*, **49**, 1312–1322 (2008).
DOI: [10.1016/j.polymer.2008.01.045](https://doi.org/10.1016/j.polymer.2008.01.045)
- [60] Filippone G., Dintcheva N. Tz., La Mantia F. P., Acierno D.: Using organoclay to promote morphology refinement and *co*-continuity in high-density polyethylene/polyamide 6 blends – Effect of filler content and polymer matrix composition. *Polymer*, **51**, 3956–3965 (2010).
DOI: [10.1016/j.polymer.2010.06.044](https://doi.org/10.1016/j.polymer.2010.06.044)
- [61] Nuzzo A., Bilotti E., Peijs T., Acierno D., Filippone G.: Nanoparticle-induced *co*-continuity in immiscible polymer blends – A comparative study on bio-based PLA-PA11 blends filled with organoclay, sepiolite, and carbon nanotubes. *Polymer*, **55**, 4908–4919 (2014).
DOI: [10.1016/j.polymer.2014.07.036](https://doi.org/10.1016/j.polymer.2014.07.036)
- [62] Nuzzo A., Coiai S., Carroccio S. C., Dintcheva N. Tz., Gambarotti C., Filippone G.: Heat-resistant fully bio-based nanocomposite blends based on poly(lactic acid). *Macromolecular Materials and Engineering*, **299**, 31–40 (2014).
DOI: [10.1002/mame.201300051](https://doi.org/10.1002/mame.201300051)
- [63] Chen J., Chen J-W., Chen H-M., Yang J-H., Chen C., Wang Y.: Effect of compatibilizer and clay on morphology and fracture resistance of immiscible high density polyethylene/polyamide 6 blend. *Composites Part B*, **54**, 422–430 (2013).
DOI: [10.1016/j.compositesb.2013.06.014](https://doi.org/10.1016/j.compositesb.2013.06.014)
- [64] González I., Eguiazabal J. I., Nazabal J.: Attaining high electrical conductivity and toughness in PA6 by combined addition of MWCNT and rubber. *Composites Part A: Applied Science and Manufacturing*, **43**, 1482–1489 (2012).
DOI: [10.1016/j.compositesa.2012.03.013](https://doi.org/10.1016/j.compositesa.2012.03.013)
- [65] Bose S., Bhattacharyya A. R., Khare R. A., Kamath S. S., Kulkarni A. R.: The role of specific interaction and selective localization of multiwall carbon nanotubes on the electrical conductivity and phase morphology of multicomponent polymer blends. *Polymer Engineering and Science*, **51**, 1987–2000 (2011).
DOI: [10.1002/pen.21998](https://doi.org/10.1002/pen.21998)

- [66] Yan D. G., Yang G. S.: Effect of multiwalled carbon nanotubes on the morphology and electrical properties of polyamide 6/polystyrene blends prepared via successive polymerization. *Journal of Applied Polymer Science*, **125**, E167–E174 (2012).
DOI: [10.1002/app.35680](https://doi.org/10.1002/app.35680)
- [67] Siengchin S., Karger-Kocsis J.: Structure and creep response of toughened and nanoreinforced polyamides produced *via* the latex route: Effect of nanofiller type. *Composites Science and Technology*, **69**, 677–683 (2009).
DOI: [10.1016/j.compscitech.2009.01.003](https://doi.org/10.1016/j.compscitech.2009.01.003)
- [68] Li W., Karger-Kocsis J., Schlarb A. K.: Dispersion of TiO₂ particles in PET/PP/TiO₂ and PET/PP/PP-g-MA/TiO₂ composites prepared with different blending procedures. *Macromolecular Materials and Engineering*, **294**, 582–589 (2009).
DOI: [10.1002/mame.200900123](https://doi.org/10.1002/mame.200900123)
- [69] Wang L., Guo Z.-X., Yu J.: Effect of compounding sequence on the morphology of organoclay-filled PA6/PP/MAPP blends. *Journal of Applied Polymer Science*, **120**, 2261–2270 (2011).
DOI: [10.1002/app.33450](https://doi.org/10.1002/app.33450)
- [70] Naderi G., Razavi-Nouri M., Taghizadeh E., Lafleur P. G., Dubois C.: Preparation of thermoplastic elastomer nanocomposites based on polyamide-6/polyepichlorohydrin-co-ethylene oxide. *Polymer Engineering and Science*, **51**, 278–284 (2011).
DOI: [10.1002/pen.21824](https://doi.org/10.1002/pen.21824)
- [71] Oliveira A. D., Larocca N. M., Paul D. R., Pessan L. A.: Effects of mixing protocol on the performance of nanocomposites based on polyamide 6/acrylonitrile-butadiene-styrene blends. *Polymer Engineering and Science*, **52**, 1909–1919 (2012).
DOI: [10.1002/pen.23152](https://doi.org/10.1002/pen.23152)
- [72] Zhang M., Lin B., Sundararaj U.: Effects of processing sequence on clay dispersion, phase morphology, and thermal and rheological behaviors of PA6-HDPE-clay nanocomposites. *Journal of Applied Polymer Science*, **125**, E714–E724 (2012).
DOI: [10.1002/app.36692](https://doi.org/10.1002/app.36692)
- [73] Dasari A., Yu Z.-Z., Mai Y.-W.: Effect of blending sequence on microstructure of ternary nanocomposites. *Polymer*, **46**, 5986–5991 (2005).
DOI: [10.1016/j.polymer.2005.05.145](https://doi.org/10.1016/j.polymer.2005.05.145)
- [74] Yang J., Sun L., Xiang S., He J., Gu L., Zhong M.: Influence of organoclay and preparation technique on the morphology of polyamide 6/polystyrene/organoclay nanocomposites. *Journal of Applied Polymer Science*, **110**, 276–282 (2008).
DOI: [10.1002/app.28178](https://doi.org/10.1002/app.28178)
- [75] Ozkoc G., Bayram G., Tiesnitsch J.: Microcompounding of organoclay–ABS/PA6 blend-based nanocomposites. *Polymer Composites*, **29**, 345–356 (2008).
DOI: [10.1002/pc.20392](https://doi.org/10.1002/pc.20392)
- [76] Chow W. S.: Cyclic extrusion of poly(butylene terephthalate)/organo-montmorillonite nanocomposites: Thermal and mechanical retention properties. *Journal of Applied Polymer Science*, **110**, 1642–1648 (2008).
DOI: [10.1002/app.28804](https://doi.org/10.1002/app.28804)
- [77] Scaffaro R., Botta L., Mistretta M. C., La Mantia F. P.: Processing – morphology – property relationships of polyamide 6/polyethylene blend–clay nanocomposites. *Express Polymer Letters*, **7**, 873–884 (2013).
DOI: [10.3144/expresspolymlett.2013.84](https://doi.org/10.3144/expresspolymlett.2013.84)
- [78] Vaia R. A., Ishii H., Giannelis E. P.: Synthesis and properties of two-dimensional nanostructures by direct intercalation of polymer melts in layered silicates. *Chemistry of Materials*, **5**, 1694–1696 (1993).
DOI: [10.1021/cm00036a004](https://doi.org/10.1021/cm00036a004)
- [79] Giannelis E. P.: Polymer layered silicate nanocomposites. *Advanced Materials*, **8**, 29–35 (1996).
DOI: [10.1002/adma.19960080104](https://doi.org/10.1002/adma.19960080104)
- [80] Usuki A., Kojima Y., Kawasumi M., Okada A., Fukushima Y., Kurauchi T., Kamigaito O.: Synthesis of nylon 6-clay hybrid. *Journal of Materials Research*, **8**, 1179–1184 (1993).
DOI: [10.1557/JMR.1993.1179](https://doi.org/10.1557/JMR.1993.1179)
- [81] Scaffaro R., Mistretta M. C., La Mantia F. P.: Compatibilized polyamide 6/polyethylene blend–clay nanocomposites: Effect of the degradation and stabilization of the clay modifier. *Polymer Degradation and Stability*, **93**, 1267–1274 (2008).
DOI: [10.1016/j.polymdegradstab.2008.04.008](https://doi.org/10.1016/j.polymdegradstab.2008.04.008)
- [82] Fang Z., Xu Y., Tong L.: Effect of clay on the morphology of binary blends of polyamide 6 with high density polyethylene and HDPE-*graft*-acrylic acid. *Polymer Engineering and Science*, **47**, 551–559 (2007).
DOI: [10.1002/pen.20675](https://doi.org/10.1002/pen.20675)
- [83] Mallick S., Khatua B. B.: Morphology and properties of nylon6 and high density polyethylene blends in absence and presence of nanoclay. *Journal of Applied Polymer Science*, **121**, 359–368 (2011).
DOI: [10.1002/app.33580](https://doi.org/10.1002/app.33580)
- [84] Chow W. S., Mohd Ishak Z. A., Karger-Kocsis J.: Morphological and rheological properties of polyamide 6/poly(propylene)/organoclay nanocomposites. *Macromolecular Materials and Engineering*, **290**, 122–127 (2005).
DOI: [10.1002/mame.200400269](https://doi.org/10.1002/mame.200400269)
- [85] Mojarrad A., Jahani Y., Barikani M.: Influence of nanoclay on the rheological properties of polyamide 6/acrylonitrile butadiene styrene nanocomposites. *Journal of Applied Polymer Science*, **125**, E571–E582 (2012).
DOI: [10.1002/app.34092](https://doi.org/10.1002/app.34092)
- [86] Kusmono, Mohd Ishak Z. A., Chow W. S., Takeichi T., Rochmadi: Effect of clay modification on the morphological, mechanical, and thermal properties of polyamide 6/polypropylene/montmorillonite nanocomposites. *Polymer Composites*, **31**, 1156–1167 (2010).
DOI: [10.1002/pc.20902](https://doi.org/10.1002/pc.20902)

- [87] Chow W. S., Abu Bakar A., Mohd Ishak Z. A.: Water absorption and hygrothermal aging study on organo-montmorillonite reinforced polyamide 6/polypropylene nanocomposites. *Journal of Applied Polymer Science*, **98**, 780–790 (2005).
DOI: [10.1002/app.22172](https://doi.org/10.1002/app.22172)
- [88] Dayma N., Satapathya B. K., Patnaik A.: Structural correlations to sliding wear performance of PA-6/PP-g-MA/nanoclay ternary nanocomposites. *Wear*, **271**, 827–836 (2011).
DOI: [10.1016/j.wear.2011.03.008](https://doi.org/10.1016/j.wear.2011.03.008)
- [89] Hassani A. J., Mohd Ishak Z. A., Mohamed A. R.: Preparation and characterization of polyamide 6 nanocomposites using MWCNTs based on bimetallic Co-Mo/MgO catalyst. *Express Polymer Letters*, **8**, 177–186 (2014).
DOI: [10.3144/expresspolymlett.2014.21](https://doi.org/10.3144/expresspolymlett.2014.21)
- [90] Shrivastava N. K., Maiti S., Suin S., Khatua B. B.: Influence of selective dispersion of MWCNT on electrical percolation of in-situ polymerized high-impact polystyrene/MWCNT nanocomposites. *Express Polymer Letters*, **8**, 15–29 (2014).
DOI: [10.3144/expresspolymlett.2014.3](https://doi.org/10.3144/expresspolymlett.2014.3)
- [91] Zhang L., Wan C., Zhang Y.: Morphology and electrical properties of polyamide 6/polypropylene/multi-walled carbon nanotubes composites. *Composites Science and Technology*, **69**, 2212–2217 (2009).
DOI: [10.1016/j.compscitech.2009.06.005](https://doi.org/10.1016/j.compscitech.2009.06.005)
- [92] Ou B., Li D., Liu Y.: Compatibilizing effect of maleated polypropylene on the mechanical properties of injection molded polypropylene/polyamide 6/functionalized-TiO₂ nanocomposites. *Composites Science and Technology*, **69**, 421–426 (2009).
DOI: [10.1016/j.compscitech.2008.11.010](https://doi.org/10.1016/j.compscitech.2008.11.010)
- [93] Karger-Kocsis J., Gryshchuk O., Fröhlich J., Mülhaupt R.: Interpenetrating vinyl ester/epoxy resins modified with organophilic layered silicates. *Composites Science and Technology*, **63**, 2045–2054 (2003).
DOI: [10.1016/S0266-3538\(03\)00110-6](https://doi.org/10.1016/S0266-3538(03)00110-6)
- [94] Chow W. S., Mohd Ishak Z. A., Karger-Kocsis J.: Atomic force microscopy study on blend morphology and clay dispersion in polyamide-6/polypropylene/organoclay systems. *Journal of Polymer Science Part B: Polymer Physics*, **43**, 1198–1204 (2005).
DOI: [10.1002/polb.20408](https://doi.org/10.1002/polb.20408)
- [95] Covas J. A., Almeida M. F., Machado A. V., Larocca N. M., Pessan L. A.: Nanoclays dispersion in a PA6/PP blend by twin screw compounding. *Macromolecular Symposia*, **301**, 55–62 (2011).
DOI: [10.1002/masy.201150308](https://doi.org/10.1002/masy.201150308)
- [96] Zhang L., Wan C., Zhang Y.: Investigation on the multi-walled carbon nanotubes reinforced polyamide 6/polypropylene composites. *Polymer Engineering and Science*, **49**, 1909–1917 (2009).
DOI: [10.1002/pen.21428](https://doi.org/10.1002/pen.21428)
- [97] Li W., Karger-Kocsis J., Thomann R.: Compatibilization effect of TiO₂ nanoparticles on the phase structure of PET/PP/TiO₂ nanocomposites. *Journal of Polymer Science Part B: Polymer Physics*, **47**, 1616–1624 (2009).
DOI: [10.1002/polb.21752](https://doi.org/10.1002/polb.21752)
- [98] As'habi L., Jafari S. H., Khonakdar H. A., Boldt R., Wagenknecht U., Heinrich G.: Tuning the processability, morphology and biodegradability of clay incorporated PLA/LLDPE blends via selective localization of nanoclay induced by melt mixing sequence. *Express Polymer Letters*, **7**, 21–39 (2013).
DOI: [10.3144/expresspolymlett.2013.3](https://doi.org/10.3144/expresspolymlett.2013.3)
- [99] Mallick S., Kar P., Khatua B. B.: Morphology and properties of nylon 6 and high density polyethylene blends in presence of nanoclay and PE-g-MA. *Journal of Applied Polymer Science*, **123**, 1801–1811 (2012).
DOI: [10.1002/app.34648](https://doi.org/10.1002/app.34648)
- [100] Jogi B. F., Bhattacharyya A. R., Poyekar A. V., Pötschke P., Simon G. P., Kumar S.: The simultaneous addition of styrene maleic anhydride copolymer and multiwall carbon nanotubes during melt-mixing on the morphology of binary blends of polyamide 6 and acrylonitrile butadiene styrene copolymer. *Polymer Engineering and Science*, in press (2015).
DOI: [10.1002/pen.23905](https://doi.org/10.1002/pen.23905)
- [101] Attari M., Arefazar A., Bakhshandeh G.: Mechanical and thermal properties of toughened PA6/HDPE/SEBS-g-MA/clay nanocomposite. *Polymer Engineering and Science*, in press (2015).
DOI: [10.1002/pen.23866](https://doi.org/10.1002/pen.23866)
- [102] Kusmono, Mohd Ishak Z. A., Chow W. S., Takeichi T., Rochmadi: Effects of compatibilizers and testing speeds on the mechanical properties of organophilic montmorillonite filled polyamide 6/polypropylene nanocomposites. *Polymer Engineering and Science*, **50**, 1493–1504 (2010).
DOI: [10.1002/pen.21622](https://doi.org/10.1002/pen.21622)
- [103] Kelnar I., Khunová V., Kotek J., Kaprálková L.: Effect of clay treatment on structure and mechanical behavior of elastomer-containing polyamide 6 nanocomposite. *Polymer*, **48**, 5332–5339 (2007).
DOI: [10.1016/j.polymer.2007.06.062](https://doi.org/10.1016/j.polymer.2007.06.062)
- [104] Kelnar I., Rotrekl J., Kotek J., Kaprálková L., Hromádková J.: Effect of montmorillonite on structure and properties of nanocomposite with PA6/PS/elastomer matrix. *European Polymer Journal*, **45**, 2760–2766 (2009).
DOI: [10.1016/j.eurpolymj.2009.06.024](https://doi.org/10.1016/j.eurpolymj.2009.06.024)
- [105] Siengchin S., Karger-Kocsis J.: Mechanical and stress relaxation behavior of Santoprene® thermoplastic elastomer/boehmite alumina nanocomposites produced by water-mediated and direct melt compounding. *Composites Part A: Applied Science and Manufacturing*, **41**, 768–773 (2010).
DOI: [10.1016/j.compositesa.2010.02.009](https://doi.org/10.1016/j.compositesa.2010.02.009)

- [106] Prashantha K., Lacrampe M. F., Krawczak P.: Processing and characterization of halloysite nanotubes filled polypropylene nanocomposites based on a masterbatch route: Effect of halloysites treatment on structural and mechanical properties. *Express Polymer Letters*, **5**, 295–307 (2011).
DOI: [10.3144/expresspolymlett.2011.30](https://doi.org/10.3144/expresspolymlett.2011.30)
- [107] Prashantha K., Schmitt H., Lacrampe M. F., Krawczak P.: Mechanical behaviour and essential work of fracture of halloysite nanotubes filled polyamide 6 nanocomposites. *Composites Science and Technology*, **71**, 1859–1866 (2011).
DOI: [10.1016/j.compscitech.2011.08.019](https://doi.org/10.1016/j.compscitech.2011.08.019)
- [108] Pedrazzoli D., Pegoretti A., Thomann R., Kristóf J., Karger-Kocsis J.: Toughening linear low-density polyethylene with halloysite nanotubes. *Polymer Composites*, in press (2015).
DOI: [10.1002/pc.23006](https://doi.org/10.1002/pc.23006)
- [109] Sridhar V., Lee I., Chun H. H., Park H.: Graphene reinforced biodegradable poly(3-hydroxybutyrate-co-4-hydroxybutyrate) nano-composites. *Express Polymer Letters*, **7**, 320–328 (2013).
DOI: [10.3144/expresspolymlett.2013.29](https://doi.org/10.3144/expresspolymlett.2013.29)
- [110] Gopiraman M., Fujimori K., Zeeshan K., Kim B. S., Kim I. S.: Structural and mechanical properties of cellulose acetate/graphene hybrid nanofibers: Spectroscopic investigations. *Express Polymer Letters*, **7**, 554–563 (2013).
DOI: [10.3144/expresspolymlett.2013.52](https://doi.org/10.3144/expresspolymlett.2013.52)
- [111] Bhattacharyya A., Chen S., Zhu M.: Graphene reinforced ultra high molecular weight polyethylene with improved tensile strength and creep resistance properties. *Express Polymer Letters*, **8**, 74–84 (2014).
DOI: [10.3144/expresspolymlett.2014.10](https://doi.org/10.3144/expresspolymlett.2014.10)
- [112] Chang K. C., Hsu C. H., Lu H. I., Ji W. F., Chang C. H., Li W. Y., Chuang T. L., Yeh J. M., Liu W. R., Tsai M. H.: Advanced anticorrosive coatings prepared from electroactive polyimide/graphene nanocomposites with synergistic effects of redox catalytic capability and gas barrier properties. *Express Polymer Letters*, **8**, 243–255 (2014).
DOI: [10.3144/expresspolymlett.2014.28](https://doi.org/10.3144/expresspolymlett.2014.28)
- [113] Wu C. M., Yu S. A., Lin S. L.: Graphene modified electrospun poly(vinyl alcohol) nanofibrous membranes for glucose oxidase immobilization. *Express Polymer Letters*, **8**, 565–573 (2014).
DOI: [10.3144/expresspolymlett.2014.60](https://doi.org/10.3144/expresspolymlett.2014.60)
- [114] Seppälä J., Luong N. D.: Chemical modification of graphene for functional polymer nanocomposites. *Express Polymer Letters*, **8**, 373 (2014).
DOI: [10.3144/expresspolymlett.2014.41](https://doi.org/10.3144/expresspolymlett.2014.41)

The influence of chain defects on the crystallisation behaviour of isotactic polypropylene

D. W. van der Meer^{1,2}, J. Varga^{3*}, G. J. Vancso¹

¹Department of Materials Science and Technology of Polymers and MESA+ Research Institute for Nanotechnology, University of Twente, P.O.Box 217, 7500 AE Enschede, The Netherlands

²Dutch Polymer Institute, P.O.Box 217, 7500 AE Enschede, The Netherlands

³Department of Physical Chemistry and Materials Science, Laboratory of Plastics and Rubber Technology, Budapest University of Technology and Economics, H-1111 Budapest, Műegyetem rkp. 3., Hungary

Received 29 September 2014; accepted in revised form 27 November 2014

Abstract. The crystallization characteristics of the α -, β - and γ -phases of isotactic polypropylene were studied for well-defined and fully characterized polymers with varying amounts of stereo- and regio-defects. The specimens enabled us to study separately the influence of the type of chain defect and the concentration of defects on the parameters of interest. A combined defect fraction (CDF) was introduced to describe arbitrary iPP samples with a varying amount of stereo- and regio-defects and a combination thereof. Crystal growth rates were found to decrease linearly with the defect fraction and were substantially stronger influenced by regio-defects as compared with stereo-defects. The deceleration of the growth rate of the β -phase is higher compared to the α -phase with increasing defect fraction. We also found a critical defect fraction, (X_{crit}) for which the growth rates of the α - and β -phases are equal. Analysis of the crystallization was performed using the model of Sanchez and Eby. Results of the analysis are in good agreement with the results found for the samples with a variation in the number of stereo-defects. The excess free energy for incorporating a stereo-defect into the trigonal crystal lattice of the β -phase is lower as compared with the α -phase. The theory correctly predicts the critical defect fraction, for which the growth rate of the α - and β -phase is equal.

Keywords: polymer blends and alloys, isotactic polypropylene, beta-nucleation, stereo- and regio-defects, thermal properties

1. Introduction

The various forms of the crystalline morphology of polymers can be directly derived from the mechanisms and kinetics of crystallization, which – in turn – depend on the primary chemical structure and chain topology of macromolecules [1]. Therefore, it is of great importance to understand the influence of the primary structure on the different aspects of crystallization and on the resulting morphology. Variations in the morphology due to incorporation of defects in the chain take place on the secondary and higher levels of the morphological hierarchy, i.e. on the lamellar level and on the spherulitic level

[2, 3]. Several studies addressed the effects of chain architecture on the various levels of the morphology and crystallization behaviour of isotactic polypropylene (iPP) [2–5]. Yet as the availability of PP chains with well-defined primary structure has been limited, no seminal conclusions regarding morphology-structure behaviour have been reached.

In iPP, which exhibits polymorphism, the relative amounts of the different crystal phases (α , β , and γ) may change as function of chain regularity. Especially in metallocene catalysed polymers, an enhancement in the formation of the γ -phase can be seen [4, 6]. This was ascribed to a decrease in crystallisable

*Corresponding author, e-mail: Jvarga@mail.bme.hu
© BME-PT

sequence length as a consequence of an increase in the fraction stereo- and regio-defects [7], or morphological effects that render the chain folding in lamellae more difficult [8]. Morphology changes on the spherulitic level for iPP involve variations in the crosshatched structure of the α -phase and the frequency of branching in the β -phase [5, 9]. Naturally, changes in the morphology on the spherulitic level take place due to variations in the relative amounts of the β - and γ -phases compared to the commonly existing α -phase.

The influence of chain architecture on the crystallization behaviour of the β -phase has not been extensively studied; certainly not at the extent as it has been performed for the α -phase. We have been particularly interested in the β -phase as this structure has better impact properties than the typical α -phase [10, 11]. Thus the influence of one property shortcoming of PP, i.e. mediocre toughness, can in principle be improved by increasing the amount of the β -polymorph. Varga and Schulek-Tóth [12] found that the formation of the β -phase was strongly restricted in copolymers of propylene and ethylene. Growth rates of the β -phase in these copolymers were found to be lower for all temperatures studied [13] as compared to pure homopolymers. In these studies selective nucleating agents were used to induce the nucleation of the β -phase. Formation of the β -phase can also be enhanced by shearing the melt prior to crystallization. Shear stress generated for example by pulling a fibre through an undercooled melt produces row nuclei consisting of the α -phase, inducing the growth of a cylindrical growth front consisting of the β -phase. Several studies [14–19] were dealing with parameters that influence the formation of such β -cylindrites, like the temperature of pulling (T_{pull}), crystallization temperature (T_c), time of pulling (t_{pull}), speed of fibre pull (v_{pull}), etc. The conclusion from these studies was that samples rich in β -phase are formed when $T_{\alpha\beta} < T_c \leq T_{\text{pull}} < T_{\beta\alpha}$, where $T_{\alpha\beta}$ and $T_{\beta\alpha}$ are the lower and upper critical crystallisation temperatures for the formation of the β -phase, respectively [19]. As described in reference [20], a lowering of the upper critical temperature ($T_{\beta\alpha}$) due to the presence of chain defects is predicted. In this study we will investigate the influence of chain defects on $T_{\beta\alpha}$ and on the formation of β -cylindrites.

In order to perform rigorous analyses of (chain) structure-property relationships, well defined and well

characterized samples are needed. Most of the aforementioned studies lack a complete characterization of the chain microstructure of the polymer specimen used and the studies are usually restricted to providing the percentage *m*-pentads (% [*mmmm*]). Moreover, in most cases the polymers used were polypropylenes produced with Ziegler-Natta (ZN) catalysts. As polymers obtained by ZN stereospecific polymerizations exhibit heterogeneous chemical and stereo-chemical distributions within one batch and within a single polymer chain, these macromolecules are not very well suitable for structure-property studies.

With the advent and widespread availability of iPPs obtained by metallocene polymerizations (m-iPPs) it is now possible to perform rigorous scientific chain architecture – polymer morphology studies. Metallocene catalysts are essentially composed of a single type of catalytic active centres, which produce rather uniform homo- and copolymers. Structural uniformity in these polymers is far superior compared with ZN catalysed chains [5, 21]. Possible defects are distributed homogeneously in the chain and all chains possess a practically equal number and distribution of defects [21]. In addition to the conventional ZN catalysed iPPs, which contain only stereo-defects, metallocene catalysed iPPs include also regio-defects. Furthermore, the length (molar mass) distribution of polymers obtained by metallocene catalysis is much narrower as compared with ZN catalysed polymers.

In this study we collected a number of iPPs obtained by metallocene catalysis from different manufacturers, made by using various catalysts. The samples were fully characterized by ^{13}C nuclear magnetic resonance (^{13}C -NMR). In this study two distinguishable groups of polymer samples are used. The first group exhibits a variation in the number of regio-defects, however with a constant amount of stereo-defects. The second group possesses a varying amount of stereo-defects but virtually no regio-defects. Especially the latter group is interesting, as these m-iPPs without regio-defects are not widely available. This collection of polymers provides us with the possibility to investigate independently the influence of regio- and stereo-defects on the crystallization behaviour and morphology of iPP. Such comprehensive and comparative studies, to our knowledge, have not been presented.

In the present paper we discuss the crystallization behaviour of the α -, β -, and γ -phases as a function of stereo- and regio-defects in the polymer chain. An elaborate description of the samples used is given. Spherulitic growth rates are measured for the different polymorphs of iPP by a combined use of polarised light microscopy (PLM) and hot-stage (thermo-optical method). We systematically investigate the influence of the amount and type of defects on the nucleation and crystallization behaviour of the β -phase using a highly selective nucleating agent and the fibre-pull technique. A discussion about the origin of the growth rate difference between the α - and β -phase as function of defect fraction is provided. Results obtained from the crystallization experiments are analyzed with the theory of Sanchez and Eby [22, 23].

2. Experimental

2.1. Samples

A collection of samples including one ZN catalysed polymer, 15 different metallocene-catalysed polymers (M_x), and 5 blends (BL_x) were used in this study. Table 1 gives the relevant characteristics of the individual polymers. The blends (BL_x) were made by solution blending of M6 and ZN. Solutions of M6

and ZN in tetrachloro-ethene were prepared (10 wt%) at the solvent boiling point (121.1°C) and stabilized with 0.1 wt% 2,6-di-tert.-butyl-4-methylphenol 99% antioxidant (Aldrich). The hot solutions were mixed in the desired ratios. After 10 min stirring, the polymer solution was quenched in ice-water, filtered over a glass-filter, and subsequently washed with ethanol. After drying for 48 hours in a vacuum oven the blends were ready for use.

In order to determine the tacticity of the samples, ^{13}C -NMR measurements were performed. The samples were prepared and measured according to the procedure described in the literature [24, 25]. The assignment of the peaks was done using the results described in reference [26].

Number average and weight average molar masses (\bar{M}_n and \bar{M}_w) and polydispersity index values (\bar{M}_w/\bar{M}_n) were determined by using gel permeation chromatography (GPC) measurements using a Waters-GPC set-up equipped with a differential refractometer (Water model 410) detection system. Narrow polystyrene standards were used for calibration. Prior to the measurements, samples were dissolved in trichloro-benzene (TCB) at 130°C and stabilized with 0.1 wt% 2,6-di-tert.-butyl-4-methylphenol 99% (Aldrich) [25].

Table 1. Molecular characteristics of samples with varying amounts of stereo defects (ZN/BL0-M5), approximately constant amount of stereo defects (M6/BL100-BL15) and varying amounts of regio- and stereo defects (BL20-M15)

Polymer sample	$\bar{M}_n \cdot 10^{-4}$ [g/mol]	$\bar{M}_w \cdot 10^{-4}$ [g/mol]	\bar{M}_w/\bar{M}_n [-]	Percentage [mmmm] [%]	Fraction regio defects [-]	Fraction stereo defects [r] [-]
¹ ZN/BL0	–	–	–	98.0	<0.0001	0.0020
² M1	1.80	3.80	2.11	83.1	<0.0001	0.1390
² M2	4.00	8.10	2.03	84.2	<0.0001	0.1460
² M3	9.90	20.0	2.02	97.6	<0.0001	0.0222
² M4	6.80	20.0	2.94	97.6	<0.0001	0.0223
² M5	2.90	8.30	2.86	97.4	<0.0001	0.0234
³ M6/BL100	–	15.0	–	98.5	0.0034	0.0200
³ M7	–	–	–	98.0	0.0034	0.0200
² M8	28.0	83.0	2.96	97.3	0.0055	0.0010
² M9	7.50	26.0	3.47	97.3	0.0055	0.0010
² M10	–	–	–	97.3	0.0055	0.0010
² BL15	–	–	–	98.0	0.0011	0.0026
BL20	–	–	–	98.0	0.0018	0.0036
BL30	–	–	–	98.0	0.0026	0.0054
BL50	–	–	–	98.0	0.0030	0.0092
BL70	–	–	–	98.0	0.0032	0.0128
² M11	2.00	3.90	1.95	84.6	0.0065	0.0920
³ M12	6.00	12.0	2.00	95.8	0.0027	0.0500
³ M13	–	18.0	–	95.0	0.0027	0.0500
³ M14	10.0	23.0	2.30	95.0	0.0027	0.0500
³ M15	–	–	–	–	–	–

¹DSM, Geleen, The Netherlands; ²Basell, Ferrara, Italy; ³Fina Research, Feluy, Belgium.

2.2. Morphology studies

Wide angle X-ray scattering (WAXS) measurements were performed on the beam-line ID2 at the European Synchrotron Radiation Facility (ESRF). In the WAXS experiments the wavelength of the X-ray radiation was 1 \AA ($\lambda = 1 \text{ \AA}$). Air-scattering and detector-response were subtracted from the two-dimensional (2D) diffraction pattern. Integration over the azimuthal angle yielded the one-dimensional (1D) plot of intensity (I) versus scattering vector (2θ). The background, taken as a straight line, was subtracted from the 1D WAXS patterns.

The relative amount of the γ -phase compared with the α -phase was determined by WAXS. The fraction of the γ -phase (ω_γ) is best expressed using the intensity ratio of the reflections $(130)_\alpha$ ($2\theta \approx 12.0^\circ$) and $(117)_\gamma$ ($2\theta \approx 13.1^\circ$), respectively [27]. The areas from the $(130)_\alpha$ reflection (A_α) and $(117)_\gamma$ reflection (A_γ) are used in the calculation for ω_γ . Non-overlapping areas are taken as overlapping reflections may introduce extra uncertainties in the determination of the mass γ -fraction. The mass fraction of the γ -phase was then calculated by the empirical Equation (1) [28]:

$$\omega_\gamma = \frac{A_\gamma}{A_\alpha + A_\gamma} \quad (1)$$

In the rest of the paper we will denote mass fractions of the γ -phase simply as fraction.

2.3. Crystallization studies

Crystallization was followed using a light microscope (Olympus BX60) equipped with a CCD camera (Sony HyperHAD) and computer and polarisers. Micrographs were captured automatically by a commercially available software (Image SXM, Scion Corp.) and kept for subsequent image processing. Growth rates were determined by measuring the length of the crystalline structures (i.e. a growth front of a spherulite) with time using the captured micrographs. From the slope of the length vs. time plot growth rate values were determined. In order to reduce the statistical error, growth rate experiments were repeated at least two times and per experiment at least 5 structures were measured.

The corresponding crystallization rates of both the α - and β -phases were studied. Crystallization of the α -phase was observed in non-nucleated samples. To induce the β -phase, a selective β -nucleating agent, the calcium salt of suberic acid [29] of 1000 ppm,

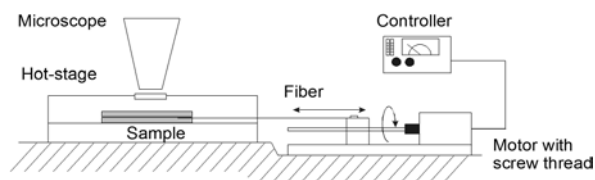


Figure 1. Schematic drawing of the fibre pull device employed for shear induced crystallization experiments

was used. The nucleant was manually dispersed into the melt. Although the β -phase could be easily distinguished from the α -phase in most cases, the presence of β -phase crystals was always confirmed by selective melting of the β -phase prior to analyzing measured growth rates. For a typical crystallization experiment, the polymer was pressed between two glass cover-slides in a thermally controlled microscope hot stage (Mettler FP82). The polymer was kept at 220°C for 5 min to remove the thermal-rheological history and then cooled to the temperature of crystallization (130°C) within approximately 1 min. Subsequently, the polymer was cooled down to 110°C and heated up from 110 to 180°C with $10^\circ\text{C}/\text{min}$ in order to study the aforementioned selective melting of the β -phase.

Shear-induced crystallization experiments were performed with the help of a fibre pull device (Figure 1). In this device a fibre was pulled at a controlled rate (v_{pull}) for a predetermined time (t_{pull}). The fibre was sandwiched between two thin solid polymer films. The two polymer films together with the fibre are placed between two cover-slides and melted. As in normal quiescent crystallization experiments, the polymer was kept at 220°C for 5 min to remove the thermal-rheological history and then cooled to the temperature of crystallization ($T_c = 130^\circ\text{C}$) within approximately 1 min. Upon reaching T_c the fibre was pulled. The temperature of pulling (T_{pull}) was set to be equal to T_c . The course of crystallization was followed by PLM as in the case of quiescent crystallization.

3. Results

In this section the results of this research are arranged as follows. The section starts with a short description of the samples. We show the possible defect structures present in the samples and characterize the amount of defects by defect-fractions. Next, we describe the dependence of the amount of the various polymorphs on the amount and type of

the defects. The section proceeds with the presentation of the results obtained from crystallization experiments. A description of the growth rates of both the α -phase and β -phase as a function of the number and type of defects is given. The section ends with a discussion of the results regarding the formation of the β -phase under shear.

3.1. Description of defects

Table 1 shows the main characteristics of the samples used in this research. The polymer samples show a large diversity in chain regularity. The regularity or the configuration of successive stereo centres (chiral carbon atoms) in the isotactic iPP chain determines the overall order (tacticity) of the polymer. Theoretical predictions were essentially made for polymers with randomly distributed defects. Therefore it is important to make use of polymers with only randomly distributed defects. The samples mentioned in Table 1 are predominantly metallocene catalysed iPPs with different chain-architectures in which the defects are distributed evenly and randomly in the chains. Identification and quantification of the defects are necessary in order to investigate the influence of chain architecture on the melting and crystallization of the polymer. With help of ^{13}C -NMR the sequence length on the pentad level [21] was determined. Since we are interested in the fraction of stereo-defects, denoted as the racemic diad $[r]$, we need to calculate $[r]$ from the measured pentad fractions. This was done according to the method described in literature [30]. The results are given in Table 1. We assume a similar influence of the many possible stereo sequence defects on crystallization behaviour of iPP, therefore we decided to take the fraction *racemic* $[r]$ additions as a measure for the number of stereo-defects. The fraction of stereo-defects presented in Table 1, is thus a collection of all the possible stereo errors, no discrimination was made for the possible variations of stereo-sequences in the chain. We believe, that although this may be an oversimplification, it is a very powerful way of dealing with all given polymer samples in a combined fashion. In addition to the stereo-defects, the polymer chain may also contain regio-defects. Regio-defects are defined as a mis-insertion of the propylene unit in the chain [30], usually denoted as a 2,1 addition. The results of the quantification of the regio-defect fraction as measured by ^{13}C -NMR are also given in Table 1.

In order to facilitate the analyses, the samples in Table 1 were sorted in three groups. The first group of samples (Group 1) contains polymers with only stereo-defects (ZN, M1–M5). No regio-defects are present in these samples. The second group (Group 2) contains polymers with a low amount of stereo-defects, but with a strong varying amount of regio-defects (M3–M10). The third group (Group 3) contains polymers with both significant amounts of stereo- and regio-defects (BL15–M15). By dividing the polymers in these 3 groups it is possible to *separately* investigate the influence of stereo- and regio-defects on the crystallization behaviour and morphology.

3.2. Polymorphic composition of the samples as observed by WAXS

As mentioned above, the formation of the γ -phase is enhanced with the incorporation of defects within the chain. Especially in metallocene catalysed iPPs an increase in the amount of the γ -phase can be found. In order to investigate the influence of stereo- and regio-defects on the formation of the γ -phase, WAXS experiments were performed. Each sample was crystallized isothermally at 130°C and rapidly cooled to room temperature. The WAXS measurements were performed at room temperature.

To qualitatively show the influence of chain defects on the formation of the γ -phase, WAXS diffractograms (Figure 2) are given for a given number of polymers with increasing defect fraction (ZN, BL70, BL30, BL15, and M11), see Table 1. Included in the figure are the most (M11) and least (ZN) defected polymers (upper and lower curves, respectively).

For all polymers the characteristic $(117)_\gamma$ reflection is present, including the ZN catalysed iPP with the least defects, although for the latter with very weak intensity. As expected, the intensity of the $(117)_\gamma$ reflection strongly increases with defect fraction, while the intensity of the $(130)_\alpha$ reflection decreases. The increase in the amount of the γ -phase can also be seen in the increasing intensity of the small $(113)_\gamma$ peak indicated by the arrow.

The amount of the γ -phase (ω_γ) is quantified by the ratio of the relative areas of the $(117)_\gamma$ and $(130)_\alpha$ reflections. The percentage of crystals exhibiting the γ -phase (ω_γ) is plotted as a function of defect fraction, in Figure 3. The different specimens were grouped and plotted according to the specific defect

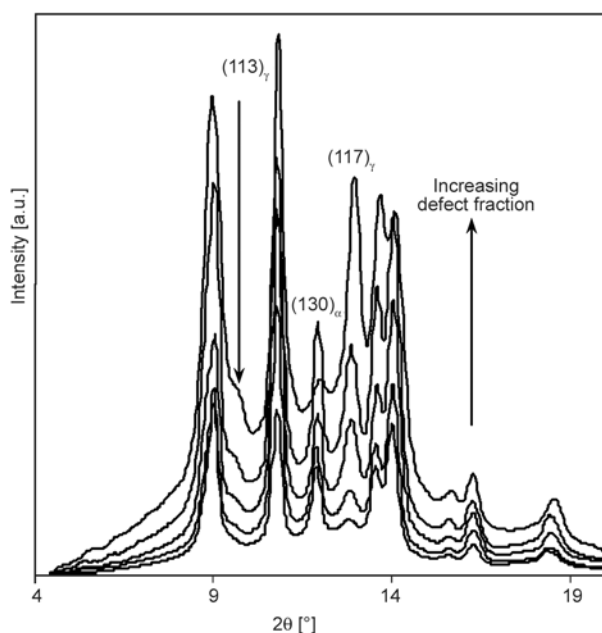


Figure 2. WAXS diffractograms of several iPP polymers (α/γ -phase) with increasing defect fraction (from bottom to top) obtained after complete crystallization. Explanation of peaks indicated can be found in the text.

type as function of the type of the given defect fraction, i.e. the amount of the γ -phase of the polymers:

- (1) with only stereo-defects (ZN, M1-M5) (\blacktriangle) is plotted as function of the fraction stereo-defects (Group 1);
- (2) with varying fraction of regio-defects (M3–M10) (\blacksquare) but with approximately the same fraction of stereo-defects is plotted as function of fraction regio-defects (Group 2);
- (3) with both stereo- and regio-defects (BL15–M15) (\circ) is plotted as function of fraction stereo-defects [31] (Group 3).

We saw already qualitatively that the fraction of the γ -phase increases with increasing number of defects. Data from Figure 3 quantifies this result. As Figure 3 shows a much stronger increase of the γ -phase as a function of increasing regio-defect fraction as compared to the amount of stereo-defects. This conclusion is in disagreement with an earlier published result that the two types of defects (regio/ stereo) have the same influence on the formation of the γ -polymorphic form of iPP [32].

Under the crystallization conditions employed, the γ -phase percentage increases up to $93 \pm 5\%$ [33] for the polymer with the highest fraction of defects. The polymer with the lowest fraction of defects, i.e. the polymer synthesized by a ZN, contains approximately $7 \pm 5\%$ [33] γ -phase, which is still consider-

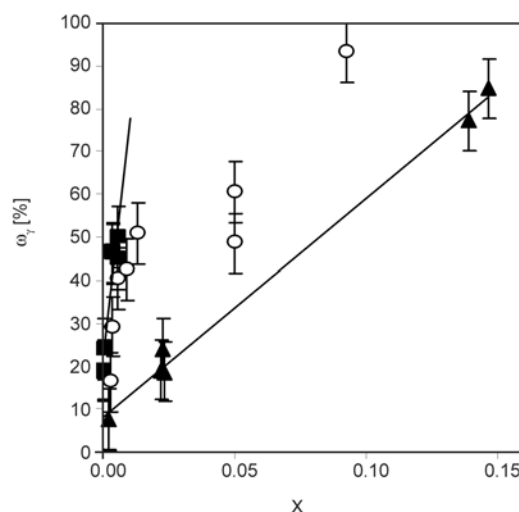


Figure 3. Fraction of the γ -phase of the polymer sample studied as a function of defect fraction. Assignments of the symbols are given in the text. The error bars are estimated errors of 5%.

able. As one can see, Figure 3 shows two approximately linear dependences on the number of regio- and stereo-defects, respectively. The observed relationships between the percentage of the γ -phase as a function of the two different types of defects (regio/ stereo) were fitted with a linear relationship using a standard least-squares fit procedure. The following numerical equations were obtained (Equation (2) and (3)):

$$(\omega_{\gamma,s})_{X_r=0} = (8.3 \pm 1.6) + (5.1 \pm 0.2) \cdot 10^2 X_s \quad (2)$$

$$(\omega_{\gamma,r})_{X_s \approx 0} = (22.2 \pm 3.0) + (5.3 \pm 0.9) \cdot 10^2 X_r \quad (3)$$

where $(\omega_{\gamma,s})_{X_r=0}$ corresponds to the percentage of the γ -phase as function of stereo-defects, while the fraction of the regio-defects was kept zero. $X_s \approx 0$ in the subscript of Equation (3) refers to approximately zero fraction of stereo-defects for the equation fitted with the amount of regio-defect fraction used as independent variable (Equation (3)). A linear combination of Equation (2) and (3) yields the Equations (4) and (5):

$$\omega_{\gamma,s/r} = (8.3 \pm 1.6) + (5.1 \pm 0.2) \cdot 10^2 \tilde{X} \quad (4)$$

$$\text{where } \tilde{X} = X_s + (10.3 \pm 1.5) X_r \quad (5)$$

The combined defect fraction (\tilde{X}) is the sum of the number of stereo-defects and the number of regio-defects multiplied by a given weighting factor with a value of 10.3. Equation (4) and (5) predicts a linear relationship between the amount of the γ -phase

with the combined defect fraction (\tilde{X}). Figure 4 shows the percentage γ -phase as a function of \tilde{X} for all polymers mentioned in Table 1. We see that the formation of the γ -phase is approximately linear with the combined defect fraction (\tilde{X}). Equations (4) and (5) predict that the percentage of the γ -phase will be 100% at a combined defect fraction of $\tilde{X} \approx 0.17$. Equations (2)–(5) are strictly valid for values of $\tilde{X} < 0.17$ or for $\omega_{\gamma,s} < 100\%$.

Although a linear fit is used to describe the observed percentage of the γ -phase as function of the combined defect fraction, a higher order (e.g. a second order) polynomial would fit the trend more accurately (see the dashed trend line in Figure 4). In the calculation of Equation (4) and (5) we assumed a linear dependence of the amount of the γ -phase for both the regio- and stereo-defects. Probably this assumption is not entirely valid and a higher-order dependence describing the relationship between the fraction of regio-defects (or stereo-defects) and the percentage of the γ -phase would yield a better fit with the observed data. Nevertheless, the data presented in Figure 4 clearly show that the amount of the γ -phase strongly depends on the amount of regio- and stereo-defects, exhibiting a stronger function on the fraction of regio-defects.

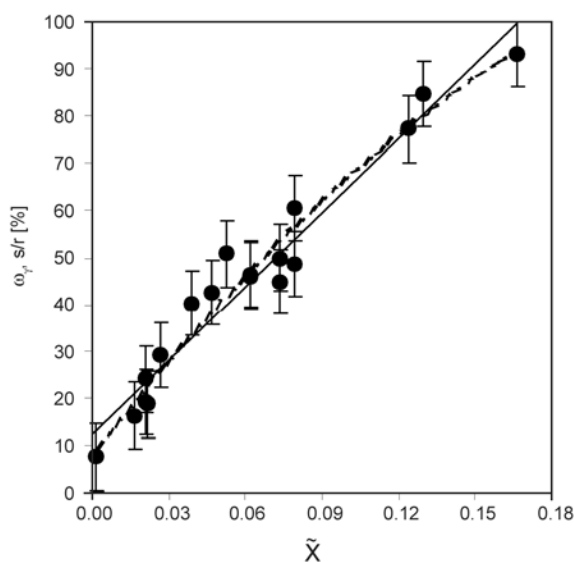


Figure 4. Fractions of the γ -phase of the used polymers as a function of combined defect fraction. Assignments of the symbols are given in the text. Error bars correspond to estimated errors of 5%.

3.3. Polymorphism and chain architecture (β -phase)

From the literature it is known that only negligible amounts of the β -phase forms in random (ethylene/propylene) copolymers with low (1.8–2.5%) ethylene content [12]. Based on these observations, it was suggested that the tendency to β -crystallization is suppressed by the disturbance of the chain regularity [13, 34]. As we have access to a large set of PP samples with various types and amounts of chain defects, the opportunity arose to perform a comprehensive structure-property study on the formation of the β -phase and its dependence on the chain architecture.

To demonstrate the decrease in the tendency for β -crystallization with the incorporation of defects in the chain, WAXS measurements were performed. Two peaks in the WAXS diffractograms of iPP are characteristic for the β -phase, i.e. $(300)_\beta$ at $2\theta = 10.4^\circ$ and $(311)_\beta$ at $2\theta = 13.8^\circ$ diffraction angle, respectively. Figure 5 shows the WAXS diffractograms for a selective number of polymers with increasing defect fraction (ZN, BL70, BL30, BL15, M12). The arrows in Figure 5 show the strong decrease in intensity of the characteristic peaks. Thus, the amount of

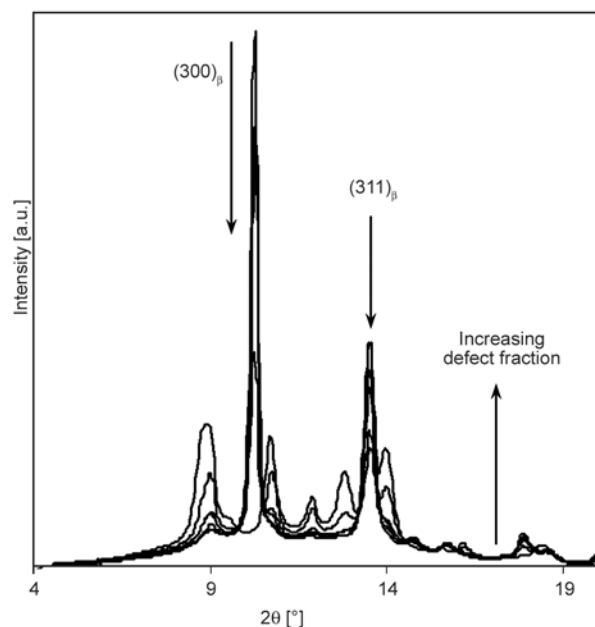


Figure 5. WAXS diagrams of several iPP polymers (characteristic reflections for the β -phase are labelled) with increasing defect fraction obtained after complete crystallization. Explanation of the peaks indicated can be found in the text.

the β -phase strongly decreases with increasing fraction of defects. The β -phase was present in relative high amounts only in polymers with relatively low amounts of defects (ZN, M1-M4, and BL15-BL30). In the next section we will see that separate peaks from SAXS can be detected only for the polymers with considerable β -phase formation.

Several reasons exist why the amount of the β -phase strongly decreases with increasing concentration of defects. The amount of the β -phase is kinetically determined and depends on the relative growth rates of the α -phase and the β -phase (G_α and G_β), respectively. At the crystallization temperature of 130°C, G_α/G_β is smaller than unity for conventional ZN catalysed iPPs [35]. However, this ratio increases rapidly with increasing fraction of defects and becomes even larger than unity above some critical defect concentration. Once nucleated, the β -phase is easily overgrown by the α -phase if the growth rate of the α -phase is higher ($G_\alpha > G_\beta$). Consequently, the growth of the β -phase is increasingly restricted with increasing defect fraction.

Another factor determining the fraction of the β -phase originates from the use of a β -nucleating agent. Assuming that the β -phase epitaxially nucleates [36] on the surface of the nucleant, it is expected that epitaxial nucleation will be disturbed by the presence of defects. An increase in the amount of defects, therefore, reduces the efficiency of the nucleant.

3.4. Growth rate measurements by PLM

In this section we describe the isothermal growth kinetics of the samples used. The growth rate of crystallization (G) was monitored by measuring the increase of the spherulitic diameter in the radial direction as a function of time. The spherulite size increased linearly with time and remained linear over the measured time. The growth rates of both α - and β -phases of the ZN sample (indicated by 1, Figure 6) are larger compared with the growth rates (α - and β -phases) measured for the more defected sample M9 (indicated by 2). We see that the growth rate of the β -phase clearly exceeds the growth rate of the α -phase for the ZN-sample. Furthermore, for the sample M9 the growth rates of the β - and α -phases are approximately the same. These results indicate that the absolute growth rates depend on the number (and type) of defects and that the β -phase shows a stronger dependence on the number (and type) of defects than the α -phase.

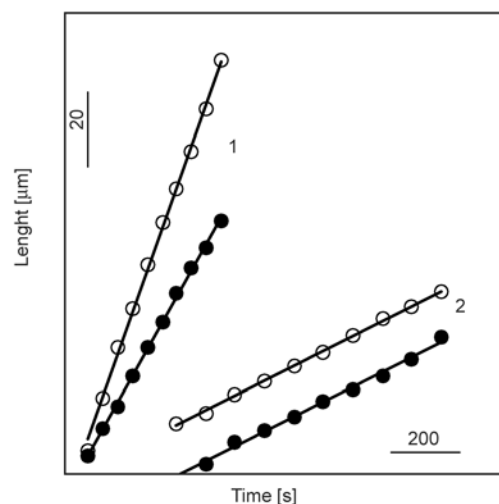


Figure 6. The spherulitic diameter as a function of time for the samples ZN (1) and M9 (2) at the crystallization temperature of 130°C. Open circles (○) represent the β -phase, closed circles (●) originate from the α -phase.

No influence of the molar mass on the spherulitic growth rate could be detected for the molar mass range studied here. For example, the polymers M9 and M10 with similar chain characteristics but different molar masses ($8.25 \cdot 10^5$ and $2.55 \cdot 10^5$ g/mol, respectively) show very similar growth rates (0.037 and 0.035 $\mu\text{m/s}$, respectively).

3.5. Growth rates of the α - and β -phases

Growth rates (G) were determined for all samples mentioned in Table 1 at the crystallization temperature of 130°C. Linear growth rates with time were found for all polymers. Figure 7 shows the values of $\ln G$ of iPP (α -phase) as a function of defect fraction. In principle, we measured the growth rates of spherulites consisting of the α -phase, but at the same time an increase in the amount of γ -phase was detected in samples with increasing defect fraction. As the formation of the γ -phase is related to the presence of the α -phase, it was not possible to separately measure the growth rates of the α - and γ -phases. Therefore, in the rest of this section we denote the growth rate of spherulites exhibiting both the α - and γ -phases as G_α .

The $\ln G$ of specimen with the different types of dominating defects (regio- or stereo-defects) were plotted according to a specific defect type as function of that defect fraction. The growth rates of the polymers:

- (1) with only *stereo*-defects (ZN, M1-M5) (▲) are plotted as function of the fraction *stereo*-defects (Group 1);

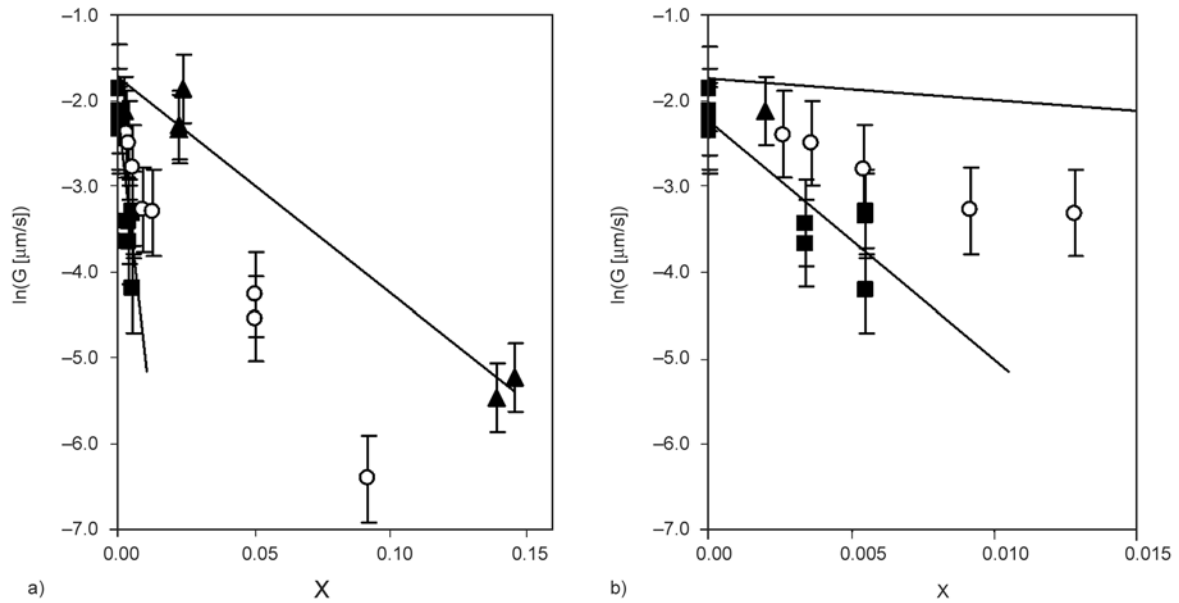


Figure 7. (a) Growth rates of the α -phase as a function of the defect fraction. (b) Magnification of a section showed in (a) for low defect fractions. The solid lines are fitted lines using a least squares fit through the data points. Assignments of symbols are given in the text.

- (2) which show a variation in the fraction *regio*-defects (M3–M10) (■) but exhibit approximately the same fraction of stereo-defects are plotted as function of fraction *regio*-defects (Group 2);
- (3) with both *stereo*- and *regio*-defects (BL15–M15) (○) are plotted as function of fraction stereo-defects (Group 3).

Figure 7 shows a decrease in growth rate for all samples with increasing defect fraction. The growth rates of samples with a varying amount of *regio*-defects but constant amount of stereo-defects (Group 2) show a much stronger dependence on the number of defects than the growth rates of the samples with only a varying amount of stereo-defects.

As can be seen in Figure 7, two trend lines are given. One trend line shows the linear dependence of the growth rate as function of stereo-defects, while the other shows the linear dependence of the growth rate as function of *regio*-defects, respectively. The two trend lines can be presented as two linear equations (Equation (6) and (7)):

$$\ln(G_{\alpha,s})_{X_r=0} = -(2.5 \pm 0.2) \cdot 10^1 \cdot X_s - (1.74 \pm 0.22) \quad (6)$$

$$\ln(G_{\alpha,r})_{X_s=0} = -(2.8 \pm 0.5) \cdot 10^2 \cdot X_r - (2.23 \pm 0.19) \quad (7)$$

where $\ln(G_{\alpha,s})_{X_r=0}$ corresponds to the logarithm of the growth rate of the α -phase as function of stereo-defects with zero fraction of *regio*-defects.

In order to describe also the group of polymers that exhibit a variation in both stereo- and *regio*-defects (○) a linear combination of Equations (6) and (7) was made. The linear combination results in the Equation (8):

$$\ln G_{\alpha,s/r} = -(2.5 \pm 0.2) \cdot 10^1 \cdot X_s - (2.8 \pm 0.5) \cdot 10^2 \cdot X_r - (1.74 \pm 0.22) \quad (8)$$

which can be further simplified to Equation (9) and (10):

$$\ln G_{\alpha,s/r} = -(2.5 \pm 0.2) \cdot 10^1 \cdot \tilde{X} - (1.74 \pm 0.22) \quad (9)$$

$$\text{where } \tilde{X} = X_s + (11.1 \pm 3.1) X_r \quad (10)$$

As described earlier, a combined defect fraction (\tilde{X}) is introduced. \tilde{X} is the sum of the number of stereo-defects and the number of *regio*-defects multiplied by a given *regio*-error coefficient with a certain value. The value of *regio*-error coefficient (11.1 ± 3.1) was calculated using an error propagation estimation. The combined defect fraction provides us with the possibility to describe any sample with an arbitrary amount of stereo- and *regio*-defects with a single parameter. The *regio*-error coefficient is a measure for the (stronger) influence of *regio*-defects on the rate of crystallization.

The growth rate of the β -phase (G_β) as function of the number and type of defects was measured, as well. Similar to Figure 7 for the α -phase Figure 8

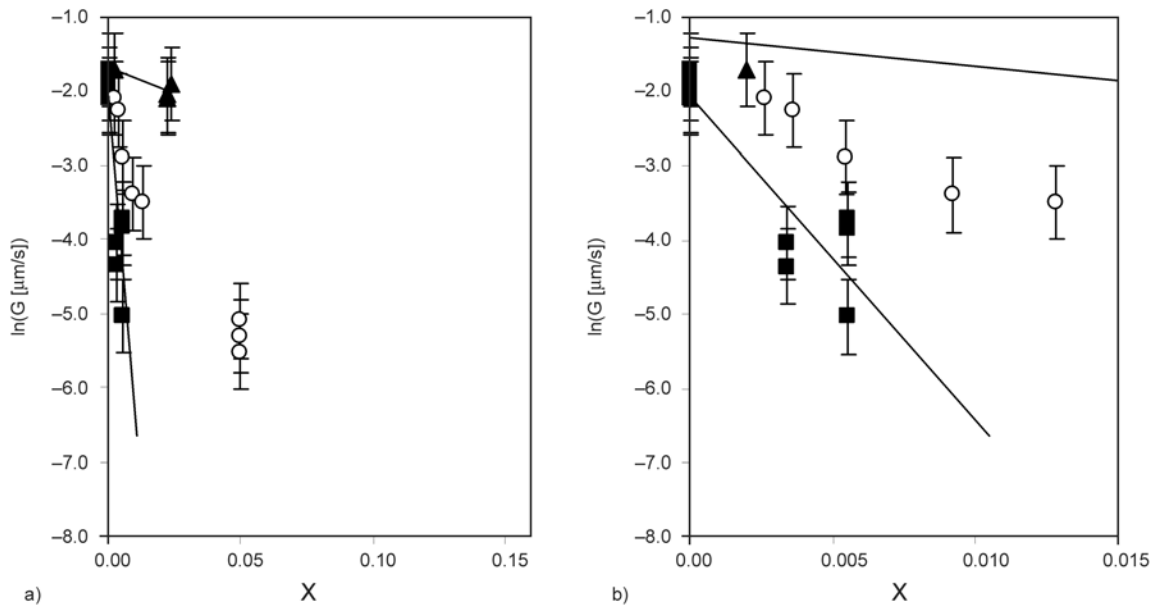


Figure 8. (a) $\ln G$ of the β -phase for various samples as a function of the fraction of defects. The figure to the right (b) shows the dependence of the defect fractions with enlarged x-scale. The solid lines are fitted through the data points. Assignments of symbols are given in the text.

gives the natural logarithm of the growth rate of the β -phase ($\ln G_\beta$) as a function of defect fraction. The polymers with different types of defects were grouped as it was done for the α -phase.

The linear dependence of $\ln G_\beta$ on the amount of regio-defects can be written in the following form (Equation (11)):

$$\ln(G_{\beta,r})_{X_s \approx 0} = -(4.4 \pm 0.8) \cdot 10^2 \cdot X_r - (2.1 \pm 0.3) \quad (11)$$

As one can see from Equation (7) and Equation (11), the values of the slopes are $-2.8 \cdot 10^2$ and $-4.4 \cdot 10^2$ for the α - and β -phase, respectively. In addition to the general larger influence of the regio-defects on the growth rate, the influence of regio-defects on the growth rate of the β -phase is much larger as compared with the growth rate of the α -phase.

Unfortunately, the growth rates of the polymers with the highest defect concentrations could not be determined at the crystallization temperature of 130°C. The lowest growth rate for the β -phase, which was possible to directly measure, was approximately 0.0039 $\mu\text{m/s}$. For the samples with the highest defect fractions the relative growth rate of the α -phase compared with the β -phase was much higher. Therefore, a growing β -phase crystal was readily surrounded and overgrown by α -phase crystals. Moreover, the nucleating ability of the β -nucleants to induce the β -phase decreased with an increasing amount of defects, which resulted in a practically

undetectable amounts of the β -phase for these samples. Therefore the determination of the β -phase growth rate at 130°C for samples with the highest defect concentrations (M1) was done indirectly. The indirect method involved the measurement of the crystal growth rates of the β -phase at lower crystallization temperatures ($105^\circ\text{C} < T_c < 120^\circ\text{C}$) followed by an extrapolation to the crystallization temperature of 130°C. Figure 9a shows the results of the growth rates as function of various crystallization temperatures. The line through the measurement points is extrapolated to 130°C and gives the value of $\ln G = -6.6$ at 130°C. This value of the growth rate is plotted in Figure 9b. In the figure the solid line is fitted using the data points, and exhibits a slope of $3.8 \cdot 10^1$.

We assume that $\ln G_\beta$ has a linear dependence on X_s ; thus we can write Equation (12):

$$\ln(G_{\beta,s})_{X_r = 0} = -(3.8 \pm 0.2) \cdot 10^1 \cdot X_s - (1.28 \pm 0.16) \quad (12)$$

Since we know the dependence of $\ln G_\beta$ on the amount of regio-defects (Equation (11)) and stereo-defects (Equation (12)), it is possible to combine these equations as was done for the α -phase (see Equation (9) and (10)) resulting in Equation (13) and (14):

$$\ln G_{\beta,s/r} = -(3.8 \pm 0.2) \cdot 10^1 \cdot \tilde{X} - (1.28 \pm 0.16) \quad (13)$$

$$\text{where } \tilde{X} = X_s + (11.6 \pm 2.8) X_r \quad (14)$$

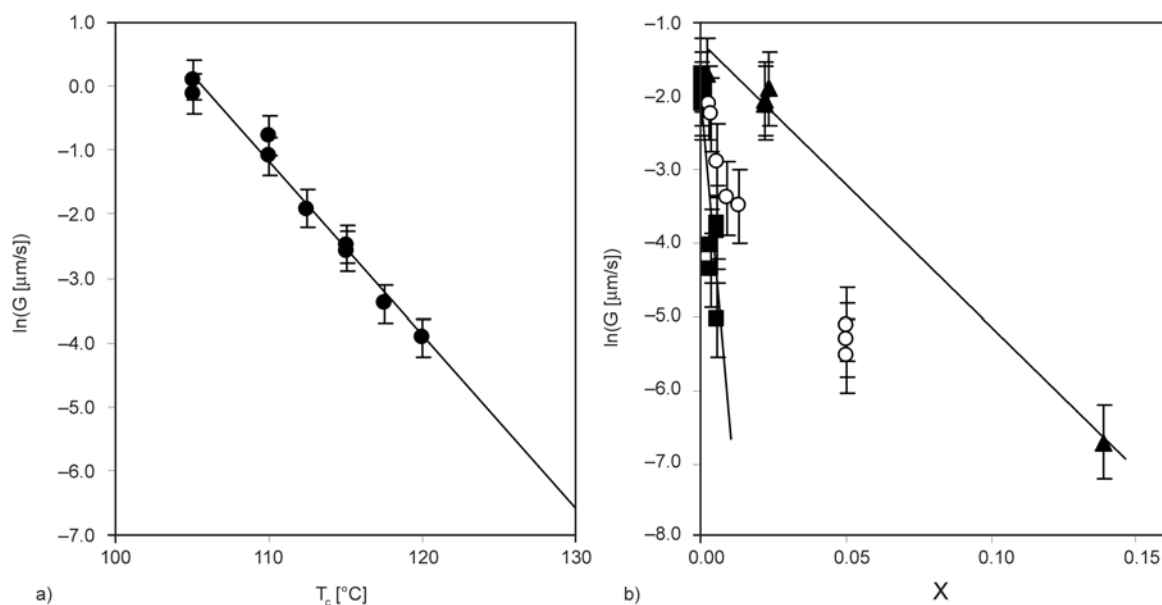


Figure 9. (a) $\ln G$ of the β -phase for sample M1 as a function of crystallization temperature (T_c). The figure to the right (b) shows $\ln G$ of the β -phase for various samples as a function of the fraction of defects (= Figure 8a). The solid lines are fitted through the data points. Assignments of symbols are given in the text.

The *regio-error coefficients* of the α - and β -phases show a remarkable resemblance. In both equations the influence of the regio-defects on the growth rate is approximately 11–12 times higher than for the stereo-defects. Comparing Equation (9) and (13) we can draw the conclusion that the influence of stereo-defects on the growth rate of the β -phase is larger as compared to the influence of stereo-defects on the α -phase. We already drew the conclusion that the influence of regio-defects on the growth rate of the β -phase is larger as compared to the influence of regio-defects on the α -phase.

Although regio-defects have a *larger* influence on the crystallization rate of β -phase as compared to the α -phase, regio-defects *compared* with stereo-defects exert a *similar* influence on the growth rate of the α - and β -phases, respectively. In other words, the influence of the number of (stereo- and regio-) defects on the growth rate of the β -phase is a constant factor larger as compared with the α -phase.

The use of the combined defect fraction (\tilde{X}) provides us with the possibility to describe any sample with an arbitrary amount of stereo- and regio-defects. Utilizing this possibility the growth rate data of all samples mentioned in Table 1 (for both the α - and β -phases) was plotted as function of the combined defect fraction. This procedure resulted in Figure 10. Clearly, G_β is higher than G_α at zero combined defect fraction, however, with increasing defect fraction G_β decreases stronger than G_α as a function of \tilde{X} . At

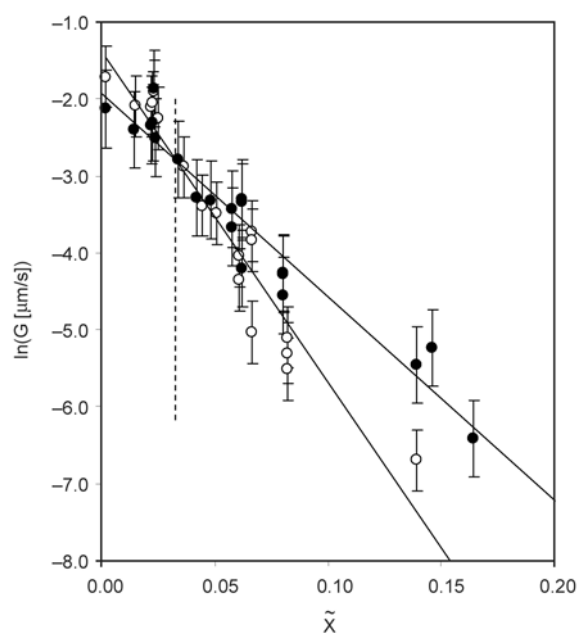


Figure 10. Growth rates as a function of the combined defect fraction. Open symbols (\circ): growth data for the β -phase. Closed symbols (\bullet): growth data for the α -phase.

approximately $\tilde{X} = 0.03$ a cross-over takes place, which is characterized by an equal growth rate of the α - and β -phase ($G_\beta = G_\alpha$). According to the literature, equal growth rates for both phases take place at a critical $\beta\alpha$ -crystallization temperature ($T_{\beta\alpha}$) of 140°C for virtually defect-free samples [13, 35]. This critical temperature was determined using highly isotactic (ZN catalysed) iPP samples. At a

crystallization temperature $T_c = 130^\circ\text{C}$ and at a combined defect fraction of 0.03 the growth rates for the α - and β -phases are equal. Consequently, for samples exhibiting a combined defect fraction of 0.03 the $T_{\beta\alpha}$ is lowered from 140 to 130°C .

3.6. The shear induced formation of the β -phase

The relative growth rates of the α - and β -phases are important for the formation of the β -phase. A lowering of the $T_{\beta\alpha}$ has a profound influence on the formation of the β -phase under shear. In the previous section we saw that at the crystallization temperature of 130°C the ratio of G_β/G_α decreases with increasing defect fraction and above $\tilde{X} \approx 0.03$, $G_\beta < G_\alpha$. In this section we study the consequences of the decreasing $\beta\alpha$ -recrystallisation temperature ($T_{\beta\alpha}$) on the formation of the β -phase under shear conditions.

A cylindritic morphology is formed by crystallization of a melt under mechanical load (shear, elongation). The mechanical load can be introduced by pulling a fibre through an undercooled melt at a certain temperature T_{pull} . The shear stress generated by fibre pulling produces row nuclei consisting of the α -phase that induce the growth of a cylindritic growth front [13–19, 37]. These row nuclei surround the fibre in a cylindritic fashion thus the growth front is cylindrical and proceeds in the radial direction. The row nuclei likely consist of extended chain crystals [13, 19, 38] which act as nucleants for the β -phase. On these structures, if $G_\beta > G_\alpha$, β -phase crystallites can nucleate (although at a lower nucleation density as compared with the nucleation density of the α -phase). Figure 11 gives a schematic representation of such a cylindritic morphology.

In typical shear-induced crystallization experiments performed in this research, a fibre was pulled at a controlled rate (v_{pull}) for a predetermined time (t_{pull}).

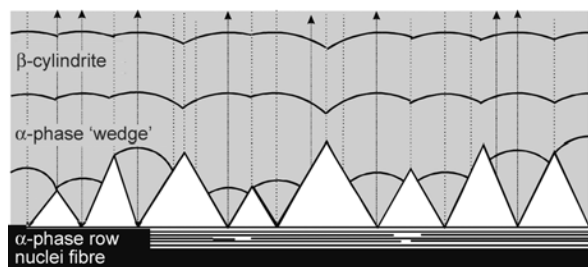


Figure 11. Schematic representation of the cylindritic morphology according to the Varga-Karger Kocsis model [19, 38]. The arrows indicate the direction of growth front.

The polymer was kept at 220°C for 5 min to remove the thermal-rheological history and then cooled to the temperature of crystallization ($T_c = 130^\circ\text{C}$) within approximately 1 min. The temperature of pulling (T_{pull}) was set to be equal to T_c . The formation of the cylindritic morphology was followed with PLM. Figure 12 shows typical microstructures as revealed by PLM of two fibre-pull experiments in which the time of pulling (t_{pull}) was varied (1 and 8 s, respectively). The β -cylindritic structure as schematically presented in Figure 11. can be clearly seen in Figure 12b. An α -phase ‘wedge’ is indicated with a white arrow. Due to the variation in t_{pull} , the morphology shows several differences, which can be best seen at the upper side of the fibre. The number of β -nuclei (N_β) is much lower after a shorter shear time (1 sec). The α -phase grows much longer unperturbed as can be seen by the larger ‘wedges’ (arrow in Figure 12b). In case of higher shearing times (t_{pull}) more β -nuclei (N_β) are generated, and as a consequence the α -phase ‘wedges’ are smaller.

From the PLM-micrographs we could quantify the number of β -nuclei (N_β). This was done by counting the number of ‘wedges’ for a certain length of the fibre. The length of the fibre for which the number of nuclei was counted was chosen such that adding further length to the already counted length did not further change the mean value of nuclei per unit length. As the number of nuclei (N_β) strongly increases with t_{pull} and v_{pull} , the distance between the nuclei becomes less and as a result the determination of nuclei becomes more difficult. This will increase the absolute error in the number of counted nuclei and limits the range of experimentally accessible values of t_{pull} and v_{pull} .

The number of β -nuclei (N_β) was found to increase strongly with increasing v_{pull} , as seen in Figure 13 (note the logarithmic scale). The solid line in the figure is the most probable fit through the data points. Figure 13 gives an indication of a minimum shear rate for β -nucleus formation for the experimental conditions used (see the dashed line). The N_β per length will not reach zero because of the presence of sporadic nucleation of the β -phase in the crystallization of iPP. The limit is approximated by a line at $v_{\text{pull}} \approx 1$ mm/s.

The growth rate of the cylindrites was determined for various samples mentioned in Table 1. Growth rates of the cylindrites were determined by measuring the increase of the diameter perpendicular to the

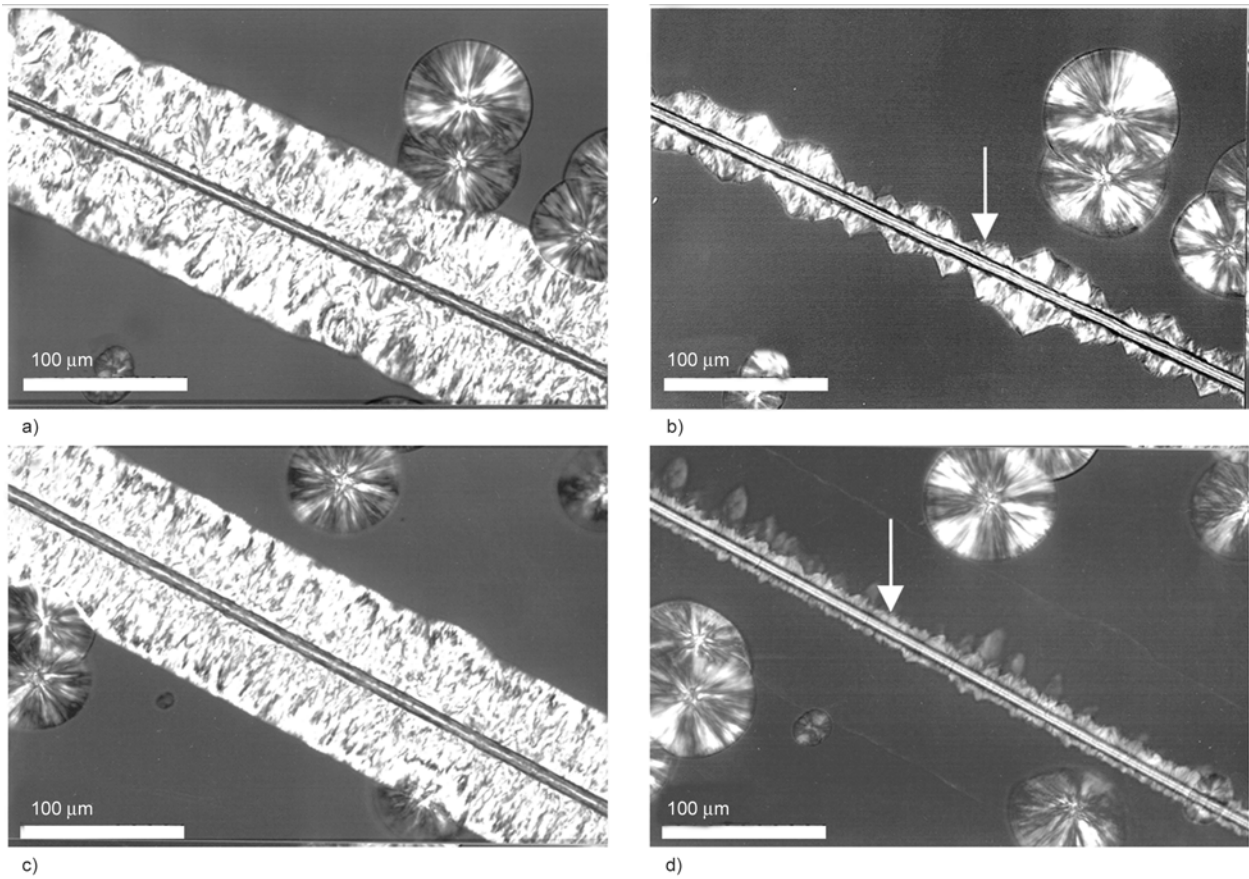


Figure 12. PLM micrographs of cylindritic morphologies formed in typical shear experiments with $t_{\text{pull}} = 1$ s (a) and $t_{\text{pull}} = 8$ s (c). Micrographs (b) and (d) show the morphology after selective melting of the β -phase.

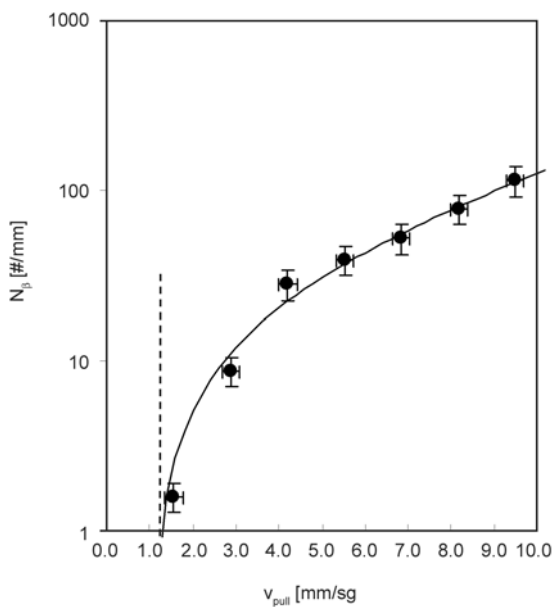


Figure 13. Number of β -nuclei as function of fibre pull speed (v_{pull})

fibre direction as function of time (see the arrows in Figure 11). The size of the cylindrites increased linearly with time and remained linear over the measured time.

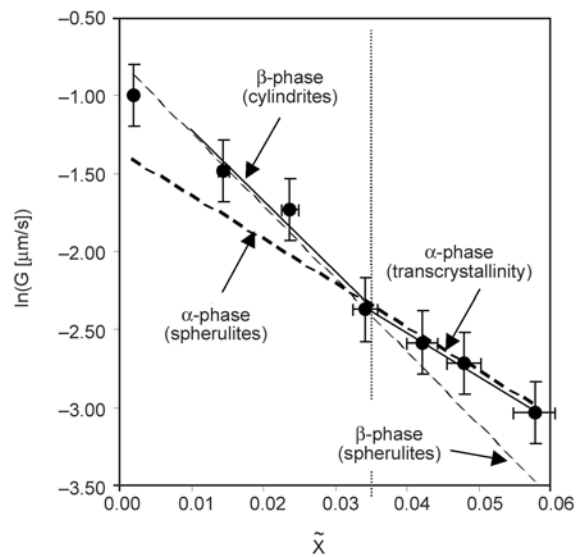


Figure 14. Growth rates of cylindrites after shearing as function of combined defect fraction. Indicated dashed lines are the trend-lines of the growth data from Figure 10 i.e. the growth data measured on spherulites.

Figure 14 shows the growth rates of the cylindritic structures as function of the combined defect fraction (\tilde{X}). In this graph only samples with $\tilde{X} < 0.06$

are plotted. The growth rate of the cylindrites is linearly decreasing with increasing \tilde{X} . At $\tilde{X} \approx 0.03$, a distinct change in the slope can be seen. At this point the growth rates of the α -phase equals that of the β -phase ($G_\alpha = G_\beta$). As the upper crystallization temperature ($T_{\beta\alpha}$) is defined by the condition of equal growth rates, we can state the condition ($T_{\alpha\beta} < T_{\text{pull}} = T_c < T_{\beta\alpha}$) for the formation of β -cylindrites under shear is no longer fulfilled for samples containing more than $\tilde{X} < 0.03$ defects (for $\tilde{X} < 0.03$, $T_{\beta\alpha} < T_c$). From PLM observation we could determine that a β -cylindritic morphology was formed after shear in the samples with $\tilde{X} < 0.03$. However, samples containing more than $\tilde{X} \approx 0.03$ defect fraction showed simple α -transcrystallisation. The growth rates of the β - and α -cylindrites were found the same as the growth rates of the β - and α -spherulites, respectively (see Figure 10). The growth rates of the spherulites (α - and β -phase) are indicated as dashed lines in Figure 14. An obvious question arises whether the transition at $\tilde{X} \approx 0.03$ depends on the speed of the fibre or on the shearing time. We found the transition independent of both parameters, which implies that the condition $T_{\alpha\beta} < T_c < T_{\beta\alpha}$ is a necessary condition to be fulfilled for the formation of the β -phase under shear.

4. Discussion

During the course of crystallization, defects will be partitioned among the amorphous and crystalline phases. It is not possible to establish *a priori* by theory the actual ratio of the amount of defects incorporated in the two phases, but two extreme cases can be distinguished: complete exclusion and uniform inclusion of defects in the crystal phase [39]. In case of inclusion, the defect can either enter the lattice as an equilibrium requirement, or be located within the lattice as a non-equilibrium defect [39].

Several types of crystal defects can be distinguished [40] such as dislocations, chain disorder, and amorphous defects. Dislocations occur when the periodicity of the crystal is interrupted along a certain direction. Chain disorder is specified as a point defect. It includes chain ends, kinks, and chain torsion. Amorphous defects can be described as an inclusion of a disordered region within the crystal. Obviously, the boundaries between the different types of crystal defects are not sharp and they vary in the energy, which is needed to incorporate such defects into the crystal, i.e. a point like chain disorder

defect may result in an amorphous defect when the chain disorder is high enough. We saw from growth rate measurements that the regio-defects have a more pronounced influence on the crystallization rate as compared to the stereo-defects. In order to obtain a better understanding of the influence of the amount and different types of defects on the growth rate we analysed our data with a theory originally developed by Lauritzen and Hoffman (LH-theory) [41, 42], and later modified by Sanchez and Eby [22, 23]. Although the LH-theory served as the basis for the derivation the theory, the final result will be independent of the exact molecular mechanisms (and thus the molecular background for the theory) involved for the particular case studied.

4.1. Crystallization of homo-polymers

In the LH-polymer crystallization theory the spherulitic growth rate (G) at a given undercooling $\Delta T = (T_m^0 - T)$ is given by Equation (15):

$$G = G_0 \exp\left(-\frac{U^*}{R(T - T_\infty)}\right) \exp\left(-\frac{K_g}{T \cdot \Delta T}\right) \text{ or} \\ \ln G = \ln G_0 - \frac{U^*}{R(T - T_\infty)} - \frac{K_g}{T \cdot \Delta T} \quad (15)$$

where U^* is the (material independent) activation energy for polymer diffusion across the phase boundary. For U^* the value of 6.28 kJ/mol was suggested by Hoffman *et al.* [42]. R is the universal gas constant; K_g is called the secondary nucleation constant for a given regime; T_∞ is the temperature below which diffusion of polymer segments is negligible ($T_\infty = T_g - 30$ K); T is the crystallization temperature and T_m^0 is the equilibrium melting temperature for the completely defect-free homopolymer with infinite lamellar thickness and molar mass. The term G_0 is a pre-exponential factor, which may depend slightly on temperature. However, its contribution to the temperature dependence of G is negligible relative to that of the transport term $\{U^*/[R(T - T_\infty)]\}$ and the nucleation free energy term $\{K_g/(T \cdot \Delta T)\}$, respectively [42]. The expression for the secondary nucleation constant is the following Equation (16):

$$K_g = \frac{n\sigma_u\sigma_e b_0 T_m^0}{R \cdot \Delta H^0} \quad (16)$$

In this equation σ_u and σ_e are the interfacial lateral free energy and the interfacial surface free energy, respectively. The interfacial free energies defined

here are related to nucleation (like all other terms) and cannot a priori be identified with characteristics of the mature crystallites that subsequently develop. In Equation (16) the term b_0 is the layer thickness; n is a coefficient which depends on the growth regime: $n = 4$ in regimes I and III and $n = 2$ in regime II. For a description of the various regimes we refer to the literature [43]. Inserting Equation (16) into Equation (10) yields the following Equation (17) for the secondary nucleation rate of homo-polymers (regime III) [44]:

$$\ln G = \ln G_0 - \frac{U^*}{R(T - T_\infty)} - \frac{4\sigma_u \sigma_e b_0 T_m^0}{R\Delta H^0 T \Delta T} \quad (17)$$

As one can see, the growth rate depends exponentially on $T_m^0/(T \Delta T)$, according to Equation (17). The spherulitic growth rate (G) strongly depends on molar mass. At a given temperature, the rate decreases when the molar mass increases up to a value where the growth is not affected by the length of the polymer chain, any further. If the kinetic nucleation theory is used in the infinite molecular mass approximation, the free energy of nucleation is given by Equation (16) and this will be used in further analyses.

4.2. Crystallization of copolymers

Crystallization kinetics is influenced by the molar mass and chemical structure of the macromolecules, pressure, strain, and by changes in chain architecture. Modifications of the sequence distribution and tacticity of the polymer chains lead to different crystallization kinetics and thus lead to different properties of the resulting crystallites. As far as crystallization kinetics is concerned, isomerism, stereo irregularities, and branching impart a co-polymeric character to the chain. The theory for copolymer crystallization (and melting) therefore can be applied for regio- and stereo- irregular systems, as well. Increasing concentration of the chain defects in the polymer chain reduces both the spherulitic growth rate and the overall crystallization rate. Sanchez and Eby [23] derived a general expression for the spherulitic growth rate G (assuming a coherent surface nucleus and regime III growth) (see Equation (18)):

$$\ln G = \ln G_0 - \frac{U^*}{R(T - T_\infty)} - \frac{2\sigma_u b_0 J_{c,i}^0 [1 + f(X, T)]}{RT} \quad (18)$$

It is possible to express the nucleation rate of the copolymer in terms of the homo-polymer nucleation rate plus a term that contains the comonomer concentration if the following function is defined (Equation (19)):

$$f(X, T) \equiv \frac{\Delta G^0}{\Delta G^*} - 1 \quad (19)$$

The term ΔG^0 is the bulk free energy difference for the complete defect-free (homo) polymer with infinite lamellar thickness and molar mass compared to the defect containing ‘real’ lamella of finite thickness and is usually approximated by Equation (20):

$$\Delta G^0 = \Delta H^0 \left(1 - \frac{T}{T_m^0} \right) \quad (20)$$

For ΔG^0 it is assumed that at moderate undercooling the heat of fusion (ΔH^0) and entropy of fusion (ΔS^0) are temperature independent [45]. From the nucleation theory [45] follows Equation (21):

$$l_{c,i} = \frac{2\sigma_c}{\Delta G^0} + \delta l_c \quad (21)$$

where $l_{c,i}$ is the initial crystal thickness and σ_c is the surface free energy. δl_c is the extra thickness a crystal needs to be stable above the crystallization temperature. The minimum crystal thickness at the particular crystallization temperature is given by $2\sigma_c/\Delta G^0$. Under the assumption that $\delta l_c = 0$, we get for crystallized polymers with finite lamellar thicknesses: $l_{c,i}^0 = 2\sigma_c/\Delta G^0$. The term ΔG^* is the bulk free energy difference between a crystal with partially included defects with concentration X_c and the melt with a concentration of defects equal to the overall defect composition X . ΔG^* is given by Equation (22) [39]:

$$\Delta G^* = \Delta G^0 - RT \left(\frac{\varepsilon X_c}{RT} + (1 - X_c) \cdot \ln \frac{1 - X_c}{1 - X} + X_c \cdot \ln \frac{X_c}{X} \right) \quad (22)$$

The excess free energy of the defect, created by incorporating a defect in the crystalline lattice is labelled by ε .

The tendency to enter the lattice depends on the excess free energy of the defect (ε). It was shown [39] that under equilibrium conditions the fraction of defects, which enter the crystal lattice with a penalty ε can be calculated using Equation (23) [46]:

$$X_c^{\text{eq}} = \frac{Xe^{-\varepsilon/RT}}{(1-X) + Xe^{-\varepsilon/RT}} \quad (23)$$

The parameter X_c^{eq} is the equilibrium fraction of defects in the crystal and X is the global defect fraction of the melt prior to crystallization. Insertion of Equation (23) into Equation (22) yields the free energy of crystals with an equilibrium defect concentration given by Equation (24) [39]:

$$\Delta G^* = \Delta G^0 + RT \cdot \ln(1 - X + Xe^{-\varepsilon/RT}) \quad (24)$$

When the concentration of defects is negligible ($X_c = 0$) then Equation (22) is reduced to the exclusion limit:

$$\Delta G^* = \Delta G^0 + RT \cdot \ln(1 - X) \quad (25)$$

Equation (25) can also be obtained from Equation (24) by increasing ε to infinity ($\varepsilon \rightarrow \infty$). Using the equations for the bulk free energy difference between a crystal with partially included defects and the copolymer melt (ΔG^*) in conjunction with Equation (19) we obtain Equation (26) for the parameter $f(X, T)$:

$$\begin{aligned} f(X, T) &= \frac{-RT \cdot \ln(1 - X + Xe^{-\varepsilon/RT})}{\Delta G^0 + RT \cdot \ln(1 - X + Xe^{-\varepsilon/RT})} = \\ &= \lim_{X \rightarrow 0} \frac{RT \cdot X}{\Delta G^0} (1 - e^{-\varepsilon/RT}) \end{aligned} \quad (26)$$

and Equation (27)

$$f(X, T) = \frac{-RT \cdot \ln(1 - X)}{\Delta G^0 + RT \cdot \ln(1 - X)} = \lim_{X \rightarrow 0} \frac{RT \cdot X}{\Delta G^0} \quad (27)$$

for the equilibrium and total exclusion limit, respectively.

Since the expressions for $f(X, T)$ are given for the different cases, we can continue with the general expression for the spherulitic growth rate G (Equation (18)). As $f(X, T)$ incorporates the influence of the defects on the crystallization, it is possible to separate the terms referring to the copolymer and the homopolymer, respectively. Under the assumption that the transport term is independent of the copolymer composition for low defect fractions ($X < 0.15$), the separation of terms results in the Equation (28) for $\ln G$:

$$\ln G = \ln G^0 - \frac{2\sigma_u b_0^j f(X, T)}{RT} \text{ or}$$

$$\ln G = \ln G^0 - \frac{4\sigma_u \sigma_e b_0 T_m^0 f(X, T)}{RT \cdot \Delta H^0 \cdot \Delta T} \quad (28)$$

where G^0 is the growth rate of the homopolymer (not the preexponential factor G_0). Inserting the expressions for $f(X, T)$ (i.e. Equation (26) or (27)) into Equation (28) yield the growth rate in case of equilibrium inclusion of defects into the crystal (Equation (29)):

$$\begin{aligned} \ln G = \ln G^0 - \\ - \frac{4\sigma_u \sigma_e b_0 T_m^0 \cdot RT \cdot \ln(1 - X + Xe^{-\varepsilon/RT})}{R \cdot \Delta H^0 \cdot T \cdot \Delta T \cdot (\Delta G^0 + RT \cdot \ln(1 - X + Xe^{-\varepsilon/RT}))} \end{aligned} \quad (29)$$

and the growth rate in the case of total exclusion of defect is given by Equation (30):

$$\ln G = \ln G^0 - \frac{4\sigma_u \sigma_e b_0 T_m^0 \cdot RT \cdot \ln(1 - X)}{R \cdot \Delta H^0 \cdot T \cdot \Delta T \cdot (\Delta G^0 + RT \cdot \ln(1 - X))} \quad (30)$$

Equation (30) is the same expression for the copolymer crystallization as described by Alamo and Mandelkern [1] and Helfand and Lauritzen [46]. In case $X = 0$ Equation (29) and Equation (30) reduce to the homo-polymer case as described above.

4.3. Analysis of the crystallization behaviour of the α - and β -phases of iPP

In this section we analyze the results of the dependence of the growth rates on the fraction of defects with the theory described in the sections above. At the crystallization temperature used in the experiments, iPP crystallizes in regime III [43], which makes it possible to use Equation (29) or (30) given in the previous analysis. In the Equation (29) or (30) the expression for ΔG^0 is given by Equation (20) and the remaining parameters can be found in literature [2, 3, 47]. However, the reported values, especially for σ_u and σ_e , widely scatter [13] and limit a useful calculation of K_g and ΔG^0 . Therefore, the parameters were determined independently using the growth rate expression for the homopolymer, see Equation (17). As a representative for a homopolymer we took the polymer with the least amount of defects (M4).

The growth rate of this polymer as function of temperature was determined. From a plot of

In $G + U^*/(R(T - T_\infty))$ against $1/(T \cdot \Delta T)$ we obtain from Equation (17) the following term from the slope (Equation (31)):

$$\frac{4\sigma_u\sigma_e b_0 T_m^0}{R \cdot \Delta H^0} = K_g \quad (31)$$

which contains all the necessary parameters (including σ_u and σ_e) for the calculation of $\ln G$, see Equation (28). The growth rates were measured for temperatures between 396 and 408 K. Figure 15 shows the result. From the slope we obtain the following values for the α -phase: $K_g = 3.68 \cdot 10^5 \text{ K}^2$ and β -phase: $K_g = 2.46 \cdot 10^5 \text{ K}^2$, respectively.

The only unknown parameter, which is left for the calculation of $\ln G$ as function of X is the excess free energy (ε) needed to incorporate a stereo defect into a crystal lattice. This parameter is used as a fitting parameter. The fitting of $\ln G$ as function of X using Equation (29) and Equation (30) was performed for the α - as well as for the β -phase.

Figure 16 shows both the fitted as the measured $\ln G$ as function of X , respectively. An excellent agreement is found between the calculated growth rates using the equilibrium inclusion of defects and the observed growth rate data for samples containing only a variation in the amount of stereo-defects (Figure 17). It is found that the growth rates of the defected polymer samples are decreased compared to the homopolymer samples. The model correctly predicts a critical defect fraction for which $G_\alpha = G_\beta$. In the fitting, we assumed a value of the excess free energy value for including a stereo-defect into an α -phase crystal of $\varepsilon = 1.6 \text{ kJ} \cdot \text{mol}^{-1}$. The value for the excess energy for including a stereo-defect into the

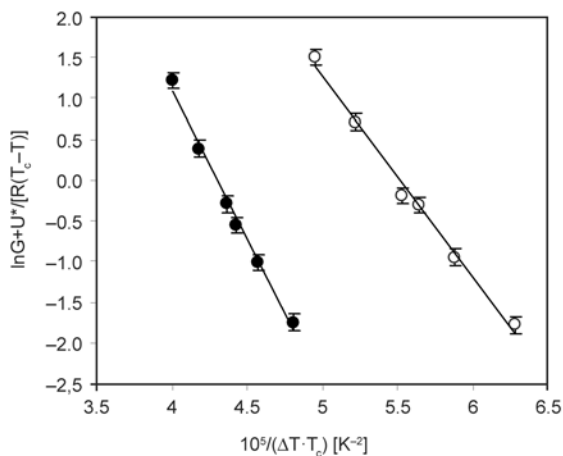


Figure 15. Plot of $\ln G + U^*/(R(T - T_\infty))$ against $1/(T \cdot \Delta T)$. Closed symbols (\bullet) represent the α -phase, open symbols (\circ) indicate the β -phase.

β -phase lattice is $\varepsilon = 1.2 \text{ kJ} \cdot \text{mol}^{-1}$. The excess free energy is thus lower for the trigonal crystal as compared to the monoclinic crystal.

For the fitting of the samples with regio-defects we maximized the excess defect free energy ($\varepsilon \rightarrow \infty$), which means that under equilibrium conditions virtually no regio-defects are included in the crystal (conform with Equation (30)). The growth rate data of the samples with a varying amount of regio-defects could be less satisfactorily fitted with the model. The model accounts for the much larger decrease in the growth rate due to the expelling of defects from the lattice. The model also rightly predicts the growth rate of the β -phase relative to the α -phase, i.e. the model shows a lower growth rate for the β -phase instead of the α -phase.

As the total exclusion of defects cannot account for the strong deceleration of the spherulitic growth rate in polymers exhibiting regio-defects, we can conclude that a certain amount of the total fraction of regio-defect will be included into the crystal as non-equilibrium defects, provided that the theory we used can be applied. The fraction of regio-defects incorporated into the crystal phase will be lower as compared to the fraction of stereo-defect, as the excess free energy of regio-defects is much higher.

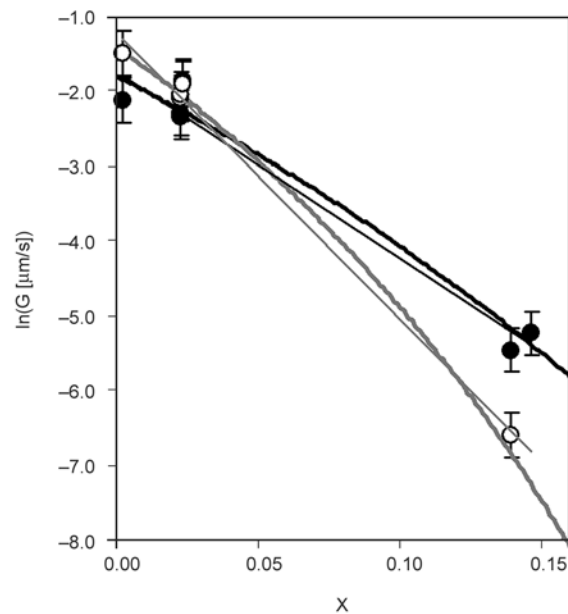


Figure 16. Calculated and measured growth rates of the α - and β -phases in the case of equilibrium inclusion of defects. The thick black-lines (—) and thick grey-lines (—) label the results for the α -phase and β -phase, respectively. Indicated are the measured growth rate data (and trend lines) for the stereo-defected samples (group 1); (\circ) = β -phase; (\bullet) = α -phase.

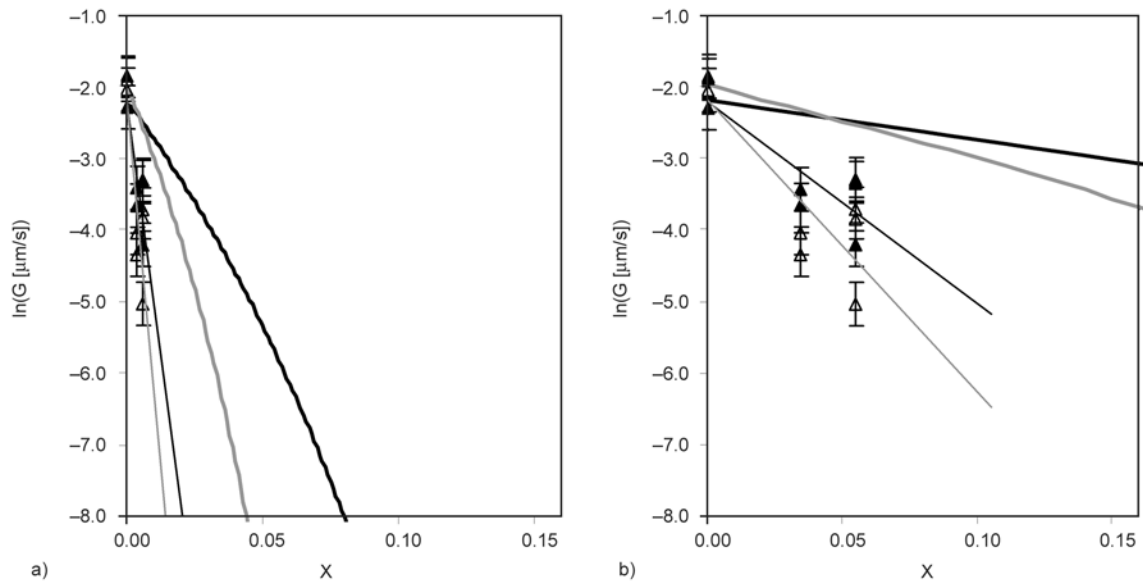


Figure 17. (a) Calculated and measured growth rates of the α - and β -phases in the case of total exclusion of defects; (b) Magnification of a section showed in (a) for low defect fractions. The thick black-lines (\blacksquare) and thick grey-lines (\blacksquare) label the results for the α -phase and β -phase, respectively. Indicated are the measured growth rate data (and trend lines) for the regio-defected samples (group 2); (\blacktriangle) = β -phase; (\triangle) = α -phase.

From the analysis developed above we find that the growth rate dependence on X is determined by the product of K_g with $f(X,T)$. From Figure 16 it was concluded that the value of K_g for the β -phase is smaller as compared to the α -phase, which would mean that the growth rate of α -phase is stronger influence by the incorporation of defects in the chain as compared to the β -phase. However, from Figure 10 we saw that the growth rate of the β -phase is a stronger function of X . As a consequence we may conclude that $f(X,T)$ predominantly determines the growth rate dependence on X compared with the effect of K_g . To visualize this influence, the parameter $f(X,T)$ was calculated separately for both total exclusion of defects and uniform inclusion (for the α - as well as for β -phases). The results of the calculations of $f(X,T)$ are graphically presented in Figure 18.

As expected, $f(X,T)$ increases with increasing defect fraction. Figure 18 shows that for small X the parameter $f(X,T)$ is approximately a linear function of the fraction of defects. However, $f(X,T)$ diverts from linearity for larger defect fraction. Obviously this has consequences for the prediction of the growth rate depression (see Figure 17). In the original derivation for $f(X,T)$ by Sanchez and Eby [23], the expressions for $f(X,T)$ were expanded in a power series under the assumption of small X ($X < 0.1$). Although mathematically correct, the expansion in power series is not required and in this paper use was made of the

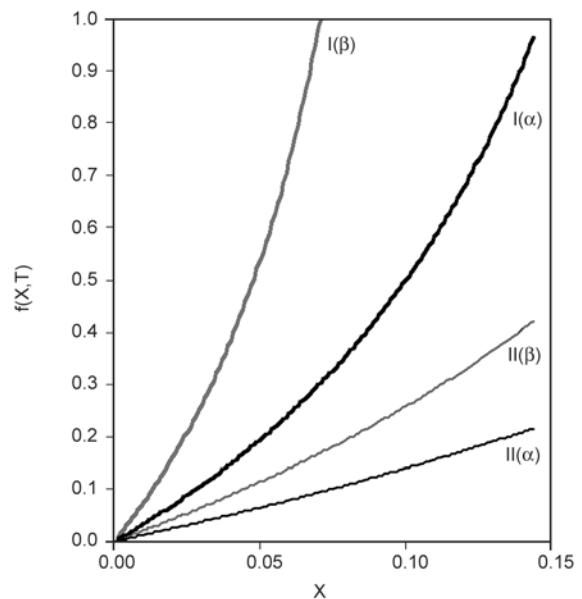


Figure 18. The parameter $f(X,T)$ as function of X for the α - and β -phases, respectively. I) $f(X,T)$ in case of total exclusion (Equation (27)), II) $f(X,T)$ in the case of equilibrium inclusion (Equation (26)).

basic expressions of $f(X,T)$ for copolymers. The trend of $f(X,T)$ with X (especially for small X) is very sensitive on the value of the bulk free energy of the homo-polymer (ΔG^0), see Equations (26) and (27). It also follows from the theory that the excess free energy of the homopolymer largely determines the magnitude of the growth rate dependence on X . The higher the value of ϵ the larger the dependence of the

growth rate on the number of defects. The influence of X on the growth rate is maximum when the energy of inclusion is infinite. A higher value of ε would result in a lower content of defects in the lattice. Under non-equilibrium conditions some of the defects will be introduced into the lattice. Energetically the inclusion of such defects is very unfavourable and therefore will retard, or even cease, the crystallization at that point. In principle, the distribution of defects between the amorphous and crystalline regions might depend on both the crystallization kinetics and on the crystal characteristics. It is not possible to establish a priori by theory the actual ratio of the amount of defects among the two phases [39]. Alamo *et al.* [48, 49] made large progress in determining the partitioning of several types of defects experimentally for stereo- and regio-defects of iPP (α -phase) using ^{13}C -NMR. They demonstrated that the partitioning of the defects does not depend on the kinetics of crystallization, which implies that the partitioning is ‘predetermined’ for a certain polymer chain. Whether this is the case for our systems needs further investigation.

In the section Results we defined the following function (Equation (9) and (10)) for the growth rate of the α -phase (Equation (32) and (33)):

$$\ln G_{\alpha,s/r} = - (2.5 \pm 0.2) \cdot 10^1 \tilde{X} - (1.74 \pm 0.22) \quad (32)$$

$$\text{where } \tilde{X} = X_s + (11.1 \pm 3.1) X_r \quad (33)$$

A combined defect fraction (\tilde{X}) was introduced and defined as the sum of the number of stereo-defects and the number of *regio-defects* multiplied by a given regio-error coefficient with a certain value $t(11.1 \pm 3.1)$. With the current copolymer crystallization theory an expression for the regio-error coefficient can be found. Similarly as done earlier we construct a linear combination of the expression describing the (theoretically found) growth rates of samples containing stereo- and regio-defects (Equation (34)):

$$\begin{aligned} \ln G_{\alpha,s/r} = & - \frac{2\sigma_u\sigma_e b_0}{R \cdot \Delta H^0 \cdot T \cdot \Delta T} f(X_r, T) - \\ & - \frac{2\sigma_u\sigma_e b_0}{R \cdot \Delta H^0 \cdot T \cdot \Delta T} f(X_s, T) - \ln G^0 \quad (34) \end{aligned}$$

We can introduce Equation (35):

$$f(X_r, T) \equiv f'(X_r, T) \cdot X_r \text{ and } f(X_s, T) \equiv f'(X_s, T) \cdot X_s \quad (35)$$

By inserting Equation (35) in Equation (34) the following result can be obtained:

$$\ln G_{\alpha,s/r} = - \left(\frac{2\sigma_u\sigma_e b_0}{R \cdot \Delta H^0 \cdot T \cdot \Delta T} f'(X_s, T) \right) \cdot \tilde{X} \quad (36)$$

$$\text{with } \tilde{X} = X_s + \frac{f'(X_r, T)}{f'(X_s, T)} \cdot X_r \quad (37)$$

Equations (36) and (37) are mathematically similar to Equations (9) and (10) or (32) and (33) when $f'(X_s, T)$ is not a strong function of X and thus can be approximated by a constant. In principle this is only valid for small X_s . However, since $f(X_s, T)$ is approximately a linear function of X_s (as was for example shown in Figure 18 by the curves $\text{II}\alpha$ and $\text{II}\beta$) we may assume that $f'(X_s, T)$ is approximately constant for larger X_s , as well. Equation (36) and (37) give an expression for the combined defect fraction and regio-error coefficient. The regio-error coefficient is given by: $f'(X_r, T)/f'(X_s, T)$. A similar analysis can be done for the β -phase and will yield a similar result. Equation (36) and (37) provides us with the opportunity to describe any sample exhibiting both stereo- and regio-defects.

5. Conclusions

For the research described in this paper we collected an unprecedented group of polypropylene polymers with a wide variety of stereo- and regio-defects. The characteristics of the samples were such that we could independently investigate the influence of the type of defect on the crystallization rates of the α -, β -, and γ -phases, respectively.

Growth rates of the α -, and β -polymorphs were measured under isothermal crystallization conditions as a function of the amount and type of defects. The growth rate dependence of the β -phase on the number of defects was much larger as compared with the α/γ -phases. As the growth rate of the β -phase is higher for pure iPP, but lower for more defected iPPs, a critical defect fraction was found for which the growth rates of both phases are the same. For samples having this specific critical defect fraction the upper critical crystallization temperature of iPP is lowered to 130°C.

A combined defect fraction (CDF) was introduced to uniformly and uniquely describe all samples with a random arbitrary amount and type of defects. The CDF is the sum of the number of stereo-defects and the number of regio-defects multiplied by a certain regio error coefficient. This coefficient showed that the influence on crystallization of regio-defects compared with stereo-defects is much larger.

Crystallization rates were analyzed according to the theory of Sanchez and Eby. The theory rightly predicts the stronger dependence of the growth rate of the β -phase on the defect fraction as compared with α -phase. The theory also predicts the critical defect fraction for which the growth rates of the α - and β -phases are equal. The equilibrium conditions for which the theory initially has been developed provides the boundaries for the non-equilibrium crystallization of copolymers. Finally, the theory gives an analytical expression for the CDF and the corresponding weighting factor.

In conclusion, we may state that iPP is a polymorphic polymer that provides us with a unique opportunity to study the influence of the chain architecture (regio-defects independently of stereo-defects) on the crystallization and thus on the three crystalline-phases existing in iPP.

Acknowledgements

The authors thank Dr. A. Demain (Fina Research, Feloy, Belgium), Dr. I. Mingozi (Basell, Ferrara, Italy), Dr. J. Chadwick and Dr. F. van der Burght (Technical University of Eindhoven, The Netherlands) for the polymer samples. The authors also greatly acknowledge Dr. S. Rastogi (Technical University of Eindhoven, Eindhoven, The Netherlands) for providing the opportunity to perform the SAXS and WAXS measurements and Dr. G. van den Velde for the NMR-measurements and useful discussions. This research was financially supported by the Dutch Polymer Institute and the MESA+ Institute for Nanotechnology of the University of Twente.

References

- [1] Alamo R. G., Mandelkern L.: Crystallization kinetics of random ethylene copolymers. *Macromolecules*, **24**, 6480–6493 (1991).
DOI: [10.1021/ma00024a018](https://doi.org/10.1021/ma00024a018)
- [2] Cheng S. Z. D., Janimak J. J., Zhang A., Zhang A., Hsieh E. T.: Isotacticity effect on crystallization and melting in polypropylene fractions: 1. Crystalline structures and thermodynamic property changes. *Polymer*, **32**, 648–655 (1991).
DOI: [10.1016/0032-3861\(91\)90477-Z](https://doi.org/10.1016/0032-3861(91)90477-Z)
- [3] Janimak J. J., Cheng S. Z. D., Giusti P. A., Hsieh E. T.: Isotacticity effect on crystallization and melting in polypropylene fractions. II. Linear crystal growth rate and morphology study. *Macromolecules*, **24**, 2253–2260 (1991).
DOI: [10.1021/ma00009a020](https://doi.org/10.1021/ma00009a020)
- [4] Fischer D., Mülhaupt R.: The influence of regio- and stereoirregularities on the crystallization behaviour of isotactic poly(propylene)s prepared with homogeneous group IVa metallocene/methylaluminoxane Ziegler-Natta catalysts. *Macromolecular Chemistry and Physics*, **195**, 1433–1441 (1994).
DOI: [10.1002/macp.1994.021950426](https://doi.org/10.1002/macp.1994.021950426)
- [5] De Rosa C., Auriemma F., Paolillo M., Resconi L., Camurati I: Crystallization behavior and mechanical properties of regiodefective, highly stereoregular isotactic polypropylene: Effect of regiodefects versus stereodeflects and influence of the molecular mass. *Macromolecules*, **38**, 9143–9154 (2005).
DOI: [10.1021/ma051004x](https://doi.org/10.1021/ma051004x)
- [6] Suhm J., Heinemann J., Thomann Y., Thomann R., Maier R-D., Schleis T., Okuda J., Kressler J., Mülhaupt R.: New molecular and supermolecular polymer architectures via transition metal catalysed alkene polymerization. *Journal of Materials Chemistry*, **8**, 553–563 (1998).
DOI: [10.1039/A706451I](https://doi.org/10.1039/A706451I)
- [7] Thomann R., Wang C., Kressler J., Mülhaupt R.: On the γ -phase of isotactic polypropylene. *Macromolecules*, **29**, 8425–8434 (1996).
DOI: [10.1021/ma951885f](https://doi.org/10.1021/ma951885f)
- [8] Thomann R., Semke H., Maier R-D., Thomann Y., Scherble J., Mülhaupt R., Kressler J.: Influence of stereoirregularities on the formation of the γ -phase in isotactic polypropylene. *Polymer*, **42**, 4597–4603 (2001).
DOI: [10.1016/S0032-3861\(00\)00675-3](https://doi.org/10.1016/S0032-3861(00)00675-3)
- [9] Radhakrishnan J., Ichikawa K., Yamada K., Toda A., Hikosaka M.: Nearly pure α_2 form crystals obtained by melt crystallization of high tacticity isotactic polypropylene. *Polymer*, **39**, 2995–2997 (1998).
DOI: [10.1016/S0032-3861\(97\)00617-4](https://doi.org/10.1016/S0032-3861(97)00617-4)
- [10] Karger-Kocsis J., Varga J., Ehrenstein G. W.: Comparison of the fracture and failure behavior of injection-molded α - and β -polypropylene in high-speed three-point bending tests. *Journal of Applied Polymer Science*, **64**, 2057–2066 (1997).
DOI: [10.1002/\(SICI\)1097-4628\(19970613\)64:11<2057::AID-APP1>3.0.CO;2-I](https://doi.org/10.1002/(SICI)1097-4628(19970613)64:11<2057::AID-APP1>3.0.CO;2-I)
- [11] Varga J.: β -modification of isotactic polypropylene: Preparation, structure, processing, properties, and application. *Journal of Macromolecular Science Part B: Physics*, **41**, 1121–1171 (2002).
DOI: [10.1081/MB-120013089](https://doi.org/10.1081/MB-120013089)
- [12] Varga J., Schulek-Tóth F.: Crystallization, melting and spherulitic structure of β -nucleated random propylene copolymers. *Journal of Thermal Analysis*, **47**, 941–955 (1996).
DOI: [10.1007/BF01979441](https://doi.org/10.1007/BF01979441)

- [13] Varga J.: Crystallization, melting and supermolecular structure of isotactic polypropylene. in 'Polypropylene: Structure, blends and composites' (ed.: Karger-Kocsis J.) Chapman and Hall, London, Vol 1, 56–115 (1995).
- [14] Devaux E., Chabert B.: Nature and origin of the transcrystalline interphase of polypropylene glass fibre composites after a shear stress. *Polymer Communications*, **32** 464–468 (1991).
- [15] Varga J., Karger-Kocsis J.: Direct evidence of row-nucleated cylindrical crystallization in glass fiber-reinforced polypropylene composites. *Polymer Bulletin*, **30**, 105–110 (1993).
DOI: [10.1007/BF00296241](https://doi.org/10.1007/BF00296241)
- [16] Thomason J. L., van Rooyen A. A.: Transcrystallized interphase in thermoplastic composites. *Journal of Materials Science*, **27**, 897–907 (1992).
DOI: [10.1007/BF01197639](https://doi.org/10.1007/BF01197639)
- [17] Alfonso G. C., Scardigli P.: Melt memory effects in polymer crystallization. *Macromolecular Symposia*, **118**, 323–328 (1997).
DOI: [10.1002/masy.19971180143](https://doi.org/10.1002/masy.19971180143)
- [18] Tribout C., Monasse B., Haudin J. M.: Experimental study of shear-induced crystallization of an impact polypropylene copolymer. *Colloid and Polymer Science*, **274**, 197–208 (1996).
DOI: [10.1007/BF00665636](https://doi.org/10.1007/BF00665636)
- [19] Varga J., Karger-Kocsis J.: Rules of supermolecular structure formation in sheared isotactic polypropylene melts. *Journal of Polymer Science Part B: Polymer Physics*, **34**, 657–670 (1996).
DOI: [10.1002/\(SICI\)1099-0488\(199603\)34:4<657::AID-POLB6>3.0.CO;2-N](https://doi.org/10.1002/(SICI)1099-0488(199603)34:4<657::AID-POLB6>3.0.CO;2-N)
- [20] Karger-Kocsis J., Varga J., Drummer D.: Instrumented falling weight impact of coinjection-molded multipolypropylene sandwich plaques containing β -phase polypropylene core. *Journal of Macromolecular Science Part B*, **41**, 881–889 (2002).
DOI: [10.1081/MB-120013071](https://doi.org/10.1081/MB-120013071)
- [21] Paukkeri R., Väänänen T., Lehtinen A.: Microstructural analysis of polypropylenes produced with heterogeneous Ziegler-Natta catalysts. *Polymer*, **34**, 2488–2494 (1993).
DOI: [10.1016/0032-3861\(93\)90577-W](https://doi.org/10.1016/0032-3861(93)90577-W)
- [22] Sanchez I. C., Eby R. K.: Crystallization of random copolymers. *Journal of Research of the National Bureau of Standards A: Physics and Chemistry*, **77**, 353–358 (1973).
DOI: [10.6028/jres.077A.023](https://doi.org/10.6028/jres.077A.023)
- [23] Sanchez I. C., Eby R. K.: Thermodynamics and crystallization of random copolymers. *Macromolecules*, **8**, 638–641 (1975).
DOI: [10.1021/ma60047a012](https://doi.org/10.1021/ma60047a012)
- [24] Randall J. C.: Carbon-13 nuclear magnetic resonance quantitative measurements of average sequence lengths of like stereochemical additions in polypropylene and polystyrene. *Journal of Polymer Science: Polymer Physics Edition*, **14**, 2083–2094 (1976).
DOI: [10.1002/pol.1976.180141113](https://doi.org/10.1002/pol.1976.180141113)
- [25] Resconi L., Balboni D., Baruzzi G., Fiori C., Guidotti S., Mercandelli P., Sironi A.: rac-[methylene(3-*tert*-butyl-1-indenyl)₂]ZrCl₂: A simple, high-performance zirconocene catalyst for isotactic polypropene. *Organometallics*, **19**, 420–429 (2000).
DOI: [10.1021/om990487o](https://doi.org/10.1021/om990487o)
- [26] Busico V., Cipullo R., Monaco G., Vacatello M., Segre A. L.: Full assignment of the ¹³C NMR spectra of regioregular polypropylenes: Methyl and methylene region. *Macromolecules*, **30**, 6251–6263 (1997).
DOI: [10.1021/ma970466a](https://doi.org/10.1021/ma970466a)
- [27] Turner-Jones A., Aizlewood J. M., Beckett D. R.: Crystalline forms of isotactic polypropylene. *Die Makromolekulare Chemie*, **75**, 134–158 (1964).
DOI: [10.1002/macp.1964.020750113](https://doi.org/10.1002/macp.1964.020750113)
- [28] Hauser G., Schmidtk J., Strobl G.: The role of co-units in polymer crystallization and melting: New insights from studies on syndiotactic poly(propene-co-octene). *Macromolecules*, **31**, 6250–6258 (1998).
DOI: [10.1021/ma980453c](https://doi.org/10.1021/ma980453c)
- [29] Varga J., Mudra I., Ehrenstein G. W.: Highly active thermally stable β -nucleating agents for isotactic polypropylene. *Journal of Applied Polymer Science*, **74**, 2357–2368 (1999).
DOI: [10.1002/\(SICI\)1097-4628\(19991205\)74:10<2357::AID-APP3>3.0.CO;2-2](https://doi.org/10.1002/(SICI)1097-4628(19991205)74:10<2357::AID-APP3>3.0.CO;2-2)
- [30] Busico V., Cipullo R.: Microstructure of polypropylene. *Progress in Polymer Science*, **26**, 443–533 (2001).
DOI: [10.1016/S0079-6700\(00\)00046-0](https://doi.org/10.1016/S0079-6700(00)00046-0)
- [31] Krache R., Benavente R., López-Majada J. M., Pereña J. M., Cerrada M. L., Pérez E.: Competition between α , β , and γ polymorphs in a β -nucleated metallocenic isotactic polypropylene. *Macromolecules*, **40**, 6871–6878 (2007).
DOI: [10.1021/ma0710636](https://doi.org/10.1021/ma0710636)
- [32] Alamo R. G., Kim M-H., Galante M. J., Isasi J. R., Mandelkern L.: Structural and kinetic factors governing the formation of the γ polymorph of isotactic polypropylene. *Macromolecules*, **32**, 4050–4064 (1999).
DOI: [10.1021/ma981849r](https://doi.org/10.1021/ma981849r)
- [33] Obadal M., Čermák R., Stoklasa K.: Tailoring of three-phase crystalline systems in isotactic poly(propylene). *Macromolecular Rapid Communications*, **26**, 1253–1257 (2005).
DOI: [10.1002/marc.200500272](https://doi.org/10.1002/marc.200500272)
- [34] Varga J., Garzó G., Ille A.: Kristallisation, umkristallisation und schmelzen der β -modifikation des polypropylens. *Die Angewandte Makromolekulare Chemie*, **142**, 171–181 (1986).
DOI: [10.1002/apmc.1986.051420115](https://doi.org/10.1002/apmc.1986.051420115)
- [35] Varga J.: Supermolecular structure of isotactic polypropylene. *Journal of Materials Science*, **27**, 2557–2579 (1992).
DOI: [10.1007/BF00540671](https://doi.org/10.1007/BF00540671)
- [36] Mathieu C., Thierry A., Wittmann J. C., Lotz B.: 'Multiple' nucleation of the (010) contact face of isotactic polypropylene, α phase. *Polymer*, **41**, 7241–7253 (2000).
DOI: [10.1016/S0032-3861\(00\)00062-8](https://doi.org/10.1016/S0032-3861(00)00062-8)

- [37] Wu C-M., Chen M., Karger-Kocsis J.: The role of metastability in the micromorphologic features of sheared isotactic polypropylene melts. *Polymer*, **40**, 4195–4203 (1999).
DOI: [10.1016/S0032-3861\(98\)00682-X](https://doi.org/10.1016/S0032-3861(98)00682-X)
- [38] Vancso G. J., Liu G., Karger-Kocsis J., Varga J.: AFM imaging of interfacial morphologies in carbon-fiber reinforced isotactic polypropylene. *Colloid and Polymer Science*, **275**, 181–186 (1997).
DOI: [10.1007/s003960050069](https://doi.org/10.1007/s003960050069)
- [39] Mandelkern L.: Crystallization and melting. in ‘Comprehensive polymer science’ (eds.: Booth C., Price C.) Pergamon Press, Oxford, Vol 2, 363–414 (1989).
- [40] Wunderlich B.: *Macromolecular physics*. Academic Press, New York (1973).
- [41] Lauritzen J. I., Hoffman J. D.: Extension of theory of growth of chain-folded polymer crystals to large undercoolings. *Journal of Applied Physics*, **44**, 4340–4352 (1973).
DOI: [10.1063/1.1661962](https://doi.org/10.1063/1.1661962)
- [42] Hoffman J. D., Davis G. T., Lauritzen J. L.: The rate of crystallization of linear polymers. in ‘Treatise on Solid State Chemistry’ (ed.: Hannay N. B.) Plenum Press, New York, Vol. 3, 497–614 (1976).
- [43] Clark E. J., Hoffman J. D.: Regime III crystallization in polypropylene. *Macromolecules*, **17**, 878–885 (1984).
DOI: [10.1021/ma00134a058](https://doi.org/10.1021/ma00134a058)
- [44] Hoffman J. D.: Regime III crystallization in melt-crystallized polymers: The variable cluster model of chain folding. *Polymer*, **24**, 3–26 (1997).
DOI: [10.1016/0032-3861\(83\)90074-5](https://doi.org/10.1016/0032-3861(83)90074-5)
- [45] Flory P. J.: *Principles of polymer chemistry*. Cornell University Press, Ithaca (1953).
- [46] Helfand E., Lauritzen J. I.: Theory of copolymer crystallization. *Macromolecules*, **6**, 631–638 (1973).
DOI: [10.1021/ma60034a031](https://doi.org/10.1021/ma60034a031)
- [47] Xu J., Srinivas S., Marand H., Agarwal P.: Equilibrium melting temperature and undercooling dependence of the spherulitic growth rate of isotactic polypropylene. *Macromolecules*, **31**, 8230–8242 (1998).
DOI: [10.1021/ma980748q](https://doi.org/10.1021/ma980748q)
- [48] VanderHart D. L., Alamo R. G., Nyden M. R., Kim M-H., Mandelkern L.: Observation of resonances associated with stereo and regio defects in the crystalline regions of isotactic polypropylene: Toward a determination of morphological partitioning. *Macromolecules*, **33**, 6078–6093 (2000).
DOI: [10.1021/ma992041p](https://doi.org/10.1021/ma992041p)
- [49] Alamo R. G., VanderHart D. L., Nyden M. R., Mandelkern L.: Morphological partitioning of ethylene defects in random propylene–ethylene copolymers. *Macromolecules*, **33**, 6094–6105 (2000).
DOI: [10.1021/ma000267i](https://doi.org/10.1021/ma000267i)

Shape-memory behavior of cross-linked semi-crystalline polymers and their blends

I. Kolesov, O. Dolynchuk, H.-J. Radusch*

Martin Luther University Halle-Wittenberg, Center of Engineering Sciences, D-06099 Halle, Germany

Received 30 September 2014; accepted in revised form 29 November 2014

Abstract. The present study deals with thermally induced one-way and invertible two-way shape-memory effect (SME) in covalent networks on the basis of crystallizable (co)polymers and their blends and is an attempt to generalize the results of own investigation received by the authors in the last ten years. The main focus of work clearly lies on research of covalently cross-linked binary and ternary blends having two and three crystalline phases with different thermal stability, respectively. The existence of two or three crystalline phases possessing different melting and crystallization temperatures in heterogeneous polymer networks can lead to triple-shape or even quadruple-shape behavior of such networks. However, the performed investigations point to crucial effect of phase morphology of crosslinked polymer blends on multiplicity of their shape-memory behavior beside the influence of blend content, crystallinity and cross-link density of blend phases as well as of processing conditions. For instance, triple-shape memory behavior in binary blends can be realized only if the continuous phase has a lower melting temperature than the dispersed phase. Cross-linked polymer blends are a facile alternative to expensive and complex synthesis of interpenetrating or block-copolymer networks used for shape memory polymers. In addition to findings of experimental investigation of SME in crystallizable covalent polymer networks, the results of modeling their shape-memory behavior on the basis of self-developed physically reasonable model have been briefly described and discussed. Thereby, good accordance between results of theory and experiment was achieved with physically justified fitting parameters.

Keywords: smart polymers, shape-memory effect, polymer blends, crystallizable polymer networks, cross-linking

1. Introduction

The aim of present mini-review is an attempt to perform the comparative description and analysis of results of our experimental investigation and of physically justified modeling of unconstrained one-way shape-memory effect (SME) and invertible two-way SME under load in crystallizable covalent polymer networks. Besides the dual SME in cross-linked homopolymers, the one- and two-way multi-shape behavior in heterogeneous networks on the basis of binary and ternary blends will be discussed. The special focus in present work is directed on the key role of phase morphology of cross-linked polymer blends varied by blend composition on the performances of multiple SM behavior.

1.1. Brief overview of various types of SME in polymeric materials

In the last decades the SME in polymeric materials was the research object of hundreds of original papers and many reviews (see for instance [1–8]). There are four main types of stimuli, which are able to trigger a shape change of polymeric materials: temperature variation, chemical reactions, light, and mechanical forces [2–7]. Correspondingly, among polymeric materials the thermo-, chemo-, photo-, and mechano-responsive material groups can be classified. In majority of publications, which consider SM behavior of polymer systems, the subject of investigation are thermo-responsive polymeric materials. According to the existence of ordered

*Corresponding author, e-mail: hans-joachim.radusch@iw.uni-halle.de
© BME-PT

nano-structure, the availability of thermal transitions in relevant temperature ranges, and of stable netpoints or entanglements within thermo-responsive polymeric materials, they can be divided into following pairs – amorphous and crystallizable polymer systems, polymer systems in which glass transition or melting/crystallization is responsible for switching mechanism, as well as covalent and physical polymer networks, respectively. Our research activities in the field of SM polymeric materials are focused on uniform and heterogeneous covalent networks on the basis of crystallizable polymers, because such crystallizable polymer networks besides irreversible one-way SME enable to create also invertible two-way SME in contrast to amorphous physical polymer networks where glass transition is used as switching mechanism.

1.2. One-way SME in polymeric materials

One-way SME arises predominantly from thermal triggering of recovery of pre-deformed SM polymeric material occurred at a temperature in the range

of such a thermal phenomenon as melting or glass transition, i.e. being a thermally induced SME. The remarkable appearance of thermally induced *one-way* SME is realizable for polymeric materials, which possess either a stable covalent or a physical network (entanglements or block-copolymer domains) and reveal at least one of mentioned thermal transitions. The initial (*permanent*) shape can be transferred to the *temporary* shape by means of deformation (e.g. stretching) of specimen at temperature above melting or glass transition temperature depending on SM polymer type.

Formation of crystalline structure or vitrification during the subsequent cooling under constant load fixes this *temporary* shape so well, that it remains nearly unchanged also after unloading of a sample at low (room) temperature. The entropy-elastic and viscoelastic forces originating from deformation in rubber-elastic state are stored inside the *temporary* shaped sample during its cooling to temperature below crystallization or glass transition point. Described procedure is referred to as programming

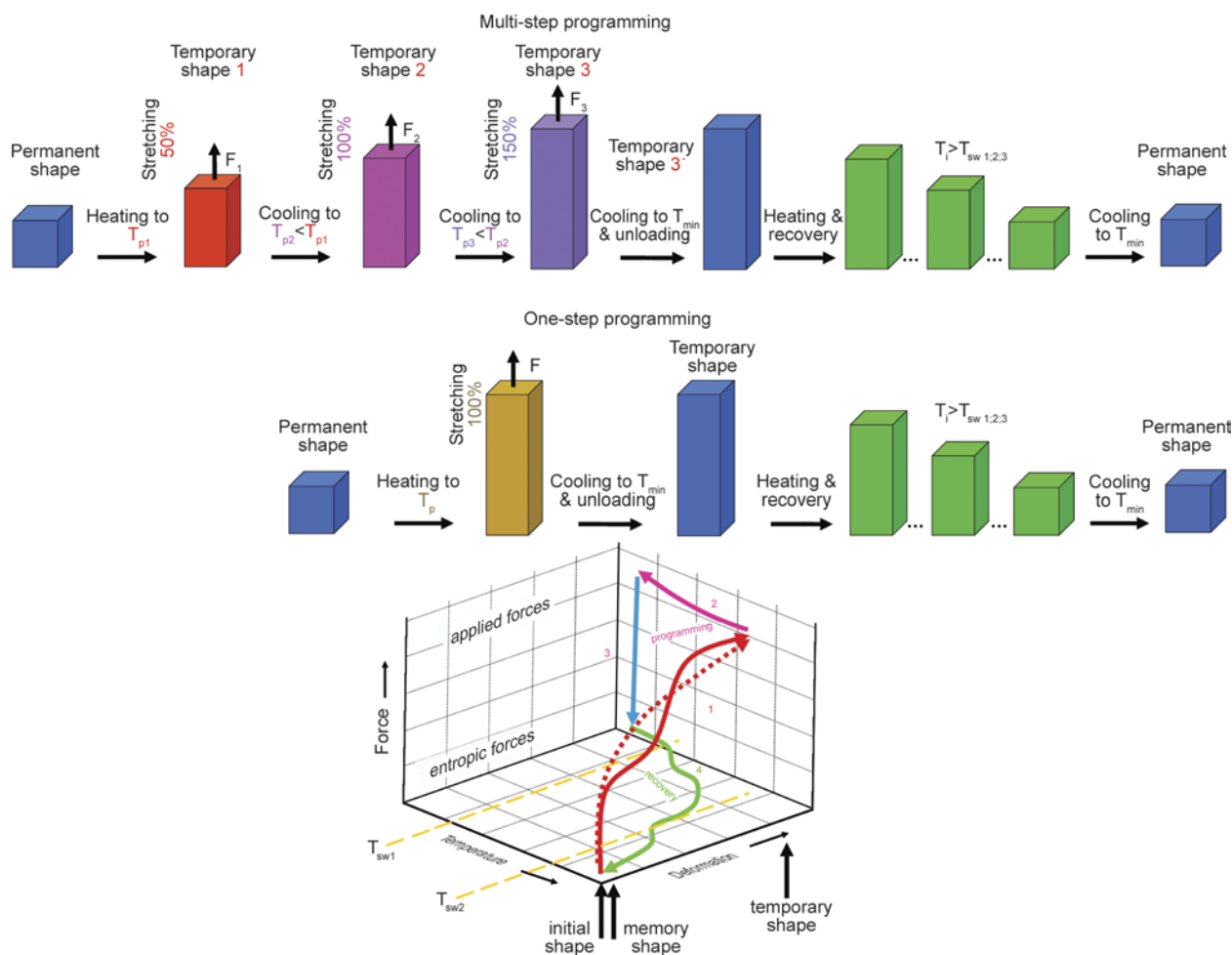


Figure 1. General shape memory behavior of thermally triggered polymer material

and is necessary for observation of *one-way* SME. *Programming* can be performed either at constant strain or at constant loading force. Programmed samples can be stored below their crystallization and melting temperatures (T_c and T_m), which are usually higher than room temperature [1–6].

At heating of programmed samples the stored entropic and viscoelastic forces serve as the driving force of recovery of *temporary* shape back to *permanent* (initial) shape, whereas the melting or glass transition fulfills the function of triggering or switching mechanism [1–6] as shown schematically in Figure 1.

Polymer networks possessing several crystalline phases with different crystallization/melting temperatures enable to observe not only *singular* but also *multiple* SM behavior. Multiple switchable SM polymer materials, which evince triple-shape behavior, have been developed some time ago as presented by Bellin *et al.* [9]. The main disadvantage of such SM polymers is a need for the application of special *multi-step* programming (MSP) process in order to produce the appearance of more or less considerable SM recovery steps during heating at two or more different temperatures [9]. Later it was demonstrated by Behl *et al.* [10] that complex multiphase AB copolymer networks created on the basis of poly(ϵ -caprolactone) and poly(cyclohexyl methacrylate) with suitable compositions show a pronounced triple-shape behavior with good SM characteristics after simple *one-step* programming (OSP) process.

Disadvantages of MSP compared to OSP process are technical complexity, diffuse indistinct steps and peaks of SM recovery strain and rate, respectively, as well as relatively low values of strain fixing (R_f) and strain recovery (R_r) ratios. This undesirable effect during MSP has to be expected as a consequence of the drastic increase of irreversible deformation part caused by plastic deformation of already crystallized phase in the second and third programming steps. Polymer materials, which reveal multiple SME, are highly innovative smart materials, which permit a number of novel engineering, medical, and pharmaceutical applications [9, 10]. Because of great importance of aforementioned applications, SM polymer materials with relatively low switching temperatures (T_{sw}), which are nearly equal to melting temperatures of their crystalline phases, are a matter of particular interest.

As an alternative to an expensive synthesis of complex interpenetrating networks and copolymers the multiple SM effects can be also achieved in covalent networks on the basis of polymer blends, if suitable phase morphology can be generated [11–13].

The distinct occurrence of triple-shape effect in polymer composites on the basis of electrospun PCL fibers embedded in an epoxy-based copolymer thermoset system was reported by Luo and Mather [11]. The temperature dependence of SM recovery strain obtained for this system both after two-step programming as well as after one-step programming (OSP) exhibit two well observable steps/decrements in temperature ranges of glass transition of epoxy-matrix and of PCL melting.

For blends of linear and short-chain branched polyethylenes cross-linked by peroxide an appreciable multiple SM behavior with relatively low characteristics could be achieved only by MSP process [12]. It is assumed that this is caused by the high affinity of blend components in molten state and correspondingly by insufficiently segregated crystalline phases of different thermal stability, also indicated by results of DSC investigations [12]. Also, heterogeneous blends of polyethylenes (PEs) and thermodynamically incompatible trans-polyoctenamer (TOR) with suitable compositions cross-linked via high energy electrons (HEE) show pronounced triple-shape behavior with high performance and even weakly pronounced quadruple-shape behavior after simple OSP process [13].

Similarly, the pronounced triple-shape behavior in bending mode was described independently from us in the same year by Cuevas *et al.* [14] in blend of TOR and linear medium polyethylene (20 wt% TOR/20 wt% PE) cross-linked by 1–3 wt% dicumyl peroxide.

Note that initially the binary uncross-linked melt-miscible [2, 8] and melt-immiscible polymer blends [15] were used in order to obtain SM polymeric materials with relatively stable physical network. In these blends the crystalline domains with higher thermal stability play a role of physical cross-links, whereas the domains of amorphous or less stable crystalline phase serve as switching segments. The blends of poly(vinyl acetate) (PVAc) with poly(lactic acid) (PLA) and PVAc or PMMA with poly(vinylidene fluoride) (PVDF) are indicative of melt-miscible polymer blends [2, 8]. Blends of maleated

PE with nylon/polyamide 6 as disperse phase can be cited as an example of melt-immiscible polymer blends [15].

Shape-memory effects depicted by Xie [16] as multiple SM effects cannot be considered as a true multiple SM behavior because of the use of special temperature program consisted of temperature soak (isothermal) segments in addition to temperature ramps during SM recovery measurements. Number and location of these isothermal segments and steps in SM recovery curves show an explicit correlation, which points to the kinetic nature of mentioned steps. The similar drawbacks are contained in some recently published papers [17, 18]. One-way ‘triple’-shape behavior of crystallizable covalent networks on the basis of PE/polypropylene (PP) blends with co-continuous phase morphology and on the basis of PCL grafted by 0.5–2.0 wt% of polydopamin (PDA) was evaluated as ‘pronounced’ and ‘good’, respectively, using temperature dependencies of SM recovery of these networks after their two-step programming [17, 18]. However, this interpretation cannot be accepted because the used temperature-time program contained the isothermal segment between two temperature ramps just within temperature range where the first step of SM recovery strain arises.

Because of the application of SMPs in medicine and pharmacology as intended e.g. by Lendlein and coworkers [3, 4, 19] and Mather and coworkers [2, 6] the biodegradable polyester-based shape-memory polymers have been a matter of particular interest [20]. On the other hand, as mentioned by Karger-Kocsis and coworkers [20, 21], potential applications for SMP exist in nearly every area of daily life: from self-repairing car bodies to kitchen utensils, from switches to sensors, from intelligent packing to tools.

1.3. Two-way SME in polymeric materials

The main focus of our investigation has been directed to the creation of two-way SM polymers on the basis of crystallizable covalently cross-linked polymers and their blends. Invertible thermally induced two-way SME in tensile mode can be initiated only in crystallizable covalent polymer networks loaded by suitable constant force. This two-way SME can be observed for preloaded strips of polymer networks in repeating thermal cycles ‘cooling-heating’. At cooling of initially stretched strip the oriented crystallization of network leads to an anomalous elongation (creep) of specimen. The subsequent melting

of crystalline phase triggers the shrinkage of specimen, which results in mechanical work carried out against an external force.

The recent findings have shown that cross-linked semi-crystalline polymers also possess an invertible so-called *two-way* SME that has been observed for covalent networks on the basis of polycyclooctene/trans-polyoctenamer (PCO/TOR) and of poly(ϵ -caprolactone) (PCL) [22–24]. The physical background of two-way SME is on the one hand the *anomalous* elongation of a sample, which is initiated by the non-isothermal crystallization during cooling under load (at a constant force) and accompanied by an increase of storage modulus, and on the other hand the expected contraction of a sample during heating under the same load triggered by melting of the oriented crystalline phase and by release of the entropic network forces. In contrast to irreversible one-way SME, invertible two-way SME can be reproduced repeatedly as long as a sample is loaded and temperature change is enough to cause consecutive crystallization and melting of the sample.

The performance of SME in cross-linked crystallizable polymers strongly depends on the properties of crystalline structure and of covalent polymer network, which has to be generated in the material. In the first instance, these are T_m value and crystallinity as a function of the temperature, which are dependent on crystal size and perfection, as well as crosslink density and related mechanical properties of the network, such as storage modulus, strain at break, and unrecoverable residual strain [25, 26].

Recently, the two-way SME with marked triple-shape behavior under suitable load was demonstrated for polymer networks based on crystallizable segments of poly(ω -pentadecalactone) and poly(ϵ -caprolactone) by Zotzmann *et al.* [27]. Both crystallization and melting of specified segment types occur at two different temperatures and are responsible for two increments and two decrements of strain at corresponding temperatures.

The two-way SME in PCL-PDA graft polymer network was reported by Bai *et al.* [18]. However, these networks demonstrated only negligible values of increment and decrement of SM creep and recovery strain, respectively, which amount merely few percents (3–4%) in spite of relatively large load of 1.3–2.0 MPa [18]. Therefore the practical application of these polymer networks as actuators or sensors should be hardly realizable.

Some current papers [28–33] containing results on two-way SME of layered polymer composites consider two other types of thermally induced two-way SME based on quite different physical principles as described above. So, the thermally induced reversible bending of active asymmetric layered polymer composites-laminates reported by Basit *et al.* [28] and Imai [29] occurs similarly to the well-known bimetallic strip effect in unconstrained as well as constrained state and under load [28, 29]. Westbrook *et al.* [30] described the reversible deformation of free-standing cross-linked polymer system in bending mode, while Behl and coworkers [31, 32] as well as Wu *et al.* [33] reported on reversible deformation of free-standing cross-linked polymer systems in tensile mode caused by internal stresses stored at least in one semi-crystalline phase of the polymer system during its preparation.

1.4. Modeling of one- and two-way SME in polymeric materials

The rapid development and discovery of novel manifestations of SM behavior in polymeric materials require precise and adequate physically grounded modeling of SM phenomena. However, a small number of scientific publications deals with theoretical description of SME, [34–45] especially in cross-linked semi-crystalline polymers [35, 36, 43, 46]. Majority of authors consider predominantly amorphous SM polymers with the glass transition as a switching mechanism and entangled macromolecules as a network [34, 37–42, 44, 45]. Only several scientific groups have tried their theoretical modeling of one-way SM behavior for cross-linked semi-crystalline polymers in case of the deformation about 100% and more [43, 46]. Nevertheless, some circumstances, like insufficient physical substantiation of used assumptions and meaningless of introduced fitting parameters, complicate description of SM recovery on the basis of these approaches. Note that only modeling based on the deep understanding of fundamental physical mechanisms and of main peculiar-

ities of a material can serve as a reliable tool for the prediction and creation of SM polymers with predetermined properties. Furthermore, it should be emphasized that a simulation on the basis of well-defined model provides the fitting parameters having quite concrete physical meaning and giving new information about SME.

Up to now only one publication is known dealing with modeling of two-way SME in cross-linked semi-crystalline polymers [46]. However, the authors used constitutive mechanical or engineering modeling and the most specific manifestation of two-way SME, the anomalous elongation under constant load during non-isothermal crystallization, was not physically explained as well as proposed assumptions remained unclear.

2. Preparation of SM polymer networks

All polymers used in our investigations are commercially available products. The blends have been prepared on the basis of polyethylenes from Dow Chemical (Germany) and predominantly of high-density polyethylene HDPE (KS 10100 UE), but partly also of metallocene-catalyzed homogeneous ethylene-octene copolymer (EOC) with approx. 30 or 60 hexyl branches per 1000 C (AFFINITY™), respectively. Poly(ϵ -caprolactone) (PCL) is biodegradable, high molecular weight linear polyester with trade name CAPA 6800 (Solvay, United Kingdom), which is derived from ϵ -caprolactone monomer via ring opening polymerization using catalyst. As another blend partner, which is thermodynamically incompatible with polyethylenes, polycyclooctene containing trans-polyoctenamer (TOR) with trade name VESTENAMER 8012 (Evonik Degussa, Germany) was employed. Few relevant parameters of these materials are given in Table 1.

The HDPE, PCL, EOC and binary HDPE/PCL and EOC/TOR blends containing cross-linking agent, namely 2,5-bis(t-butylperoxy)-2,5-dimethylhexane (DHBP) (Evonik, Germany) with different mass ratios of components (see Table 2) were prepared by

Table 1. Designations as well as some physical and molecular parameters of the used polymers

Designation	T_m [°C]	Density [kg/m ³]	Melt-Flow Index (MFI) [dg/min]		Mass-average molecular mass [kg/mol]	Polydispersity \bar{M}_w/\bar{M}_n
			190°C/2.16 kg	190°C/5.0 kg		
HDPE	132	955	3.0	10.1	99±2	4.3
EOC30/60	96/59	900/870	5.0/4.4	17.7/15.9	64±5/87±8	2.3/2.5
PCL	61	1145	7.29	–	120±2	1.74
TOR	54	910	16.40	45.5	90/120	7.3/9.7

Table 2. Designations and compositions of semi-crystalline binary and ternary blends as well as their components

Sample•		Composition				
		HDPE [%]	EOC30 [%]	EOC60 [%]	TOR [%]	PCL [%]
100HDPE	p, e	100	–	–	–	–
100EOC30	p, e	–	100	–	–	–
100EOC60	p	–	–	100	–	–
TOR	e	–	–	–	100	–
PCL	p	–	–	–	–	100
50HDPE/50EOC30	p, e	50	50	–	–	–
50HDPE/50TOR	p, e	50	–	–	50	–
30HDPE/70TOR	p, e	30	–	–	70	–
50EOC30/50EOC60	p	–	50	50	–	–
25EOC30/75EOC60	p	–	25	75	–	–
50EOC30/50TOR	p, e	–	50	–	50	–
33HDPE/33EOC30/34EOC60	p	33	33	34	–	–
10HDPE/45EOC30/45EOC60	p	10	45	45	–	–
10HDPE/23EOC30/67EOC60	p	10	23	67	–	–
20HDPE/40EOC30/40TOR	e	20	40	–	40	–
70HDPE/30PCL	p	70	–	–	–	30
50HDPE/50PCL	p	50	–	–	–	50
30HDPE/70PCL	p	30	–	–	–	70

p – cross-linking by peroxide

e – cross-linking by HEE

melt mixing in laboratory kneader (Brabender Plastimeter) for 5 min at 140°C. Films of TOR, EOC and HDPE as well as their blends with thickness of 0.5 and 1.0 mm were compression molded at 140°C and immediately afterwards cross-linked in press at 190°C.

Binary HDPE/TOR and EOC30/TOR as well as ternary HDPE/EOC30/TOR blends and their components without cross-linking agent were prepared by melt mixing and compression molding under the same conditions. These samples were either slowly cooled (*sc*) or quenched (*q*) from the molten state and subsequently cross-linked via high energy electrons (HEE) with a radiation dose of 200 kGy as described previously [13]. Such a preparation allows receiving two series of heterogeneous networks having different thermal history (TH) and correspondingly different phase morphology and crystalline properties.

Crosslink density of obtained covalent networks was evaluated on the basis of stress relaxation measurements performed during 3 hours at a constant temperature above melting temperature of all polymers under study. The crosslink density was calculated using Equation (1):

$$\nu_c = \frac{2 \cdot \sigma_\infty}{RT \cdot (\lambda - \lambda^{-2})} \quad (1)$$

Table 3. Crosslink density (ν_c) of HDPE, PCL, EOC, TOR, as well as nominal ν_c values of 50EOC/50TOR and 30HDPE/70TOR blends

Sample	Cross-linking method		Crosslink density, ν_c [mol/m ³]
	Electron irradiation dose [kGy]	Peroxide DHBP [wt%]	
HDPE	–	2.0	110
EOC30	–	2.0	270
PCL	–	1.3	139
	–	2.0	252
50EOC30/50TOR	–	2.0	318
HDPE	200	–	140
EOC30	200	–	148
TOR	200	–	360
30HDPE/70TOR	200	–	260

where σ_∞ is terminal stress (stress at infinitely long time), R is gas constant, T is absolute temperature of sample, and $\lambda \approx 2$ is draw ratio.

The terminal stress σ_∞ is obtained as fitting parameter as described previously [13, 26, 47]. The crosslink density values of cross-linked HDPE, EOC30, PCL and TOR as well as 30HDPE/70PCL and 30HDPE/70TOR blend are listed in Table 3.

3. Phase morphology of heterogeneous SM polymer networks

The strong correlation between phase morphology of the blends and multiple SM behavior was demon-

strated by means of visualization of the phase morphology by scanning electron microscopy (SEM) investigation. The blends under study were etched in order to expose phase morphology. SEM images of 30HDPE/70TOR and 50EOC30/50TOR blends, which show very discrete melting and crystallization

peaks for both components on DSC thermograms (see next section), reveal incompatibility between HDPE and TOR (Figure 2) as well as between EOC30 and TOR. Droplet-like or extended particles (Figure 2a–2c) with varying size from 1 to 50 μm , which are identified to be HDPE, indicate the dis-

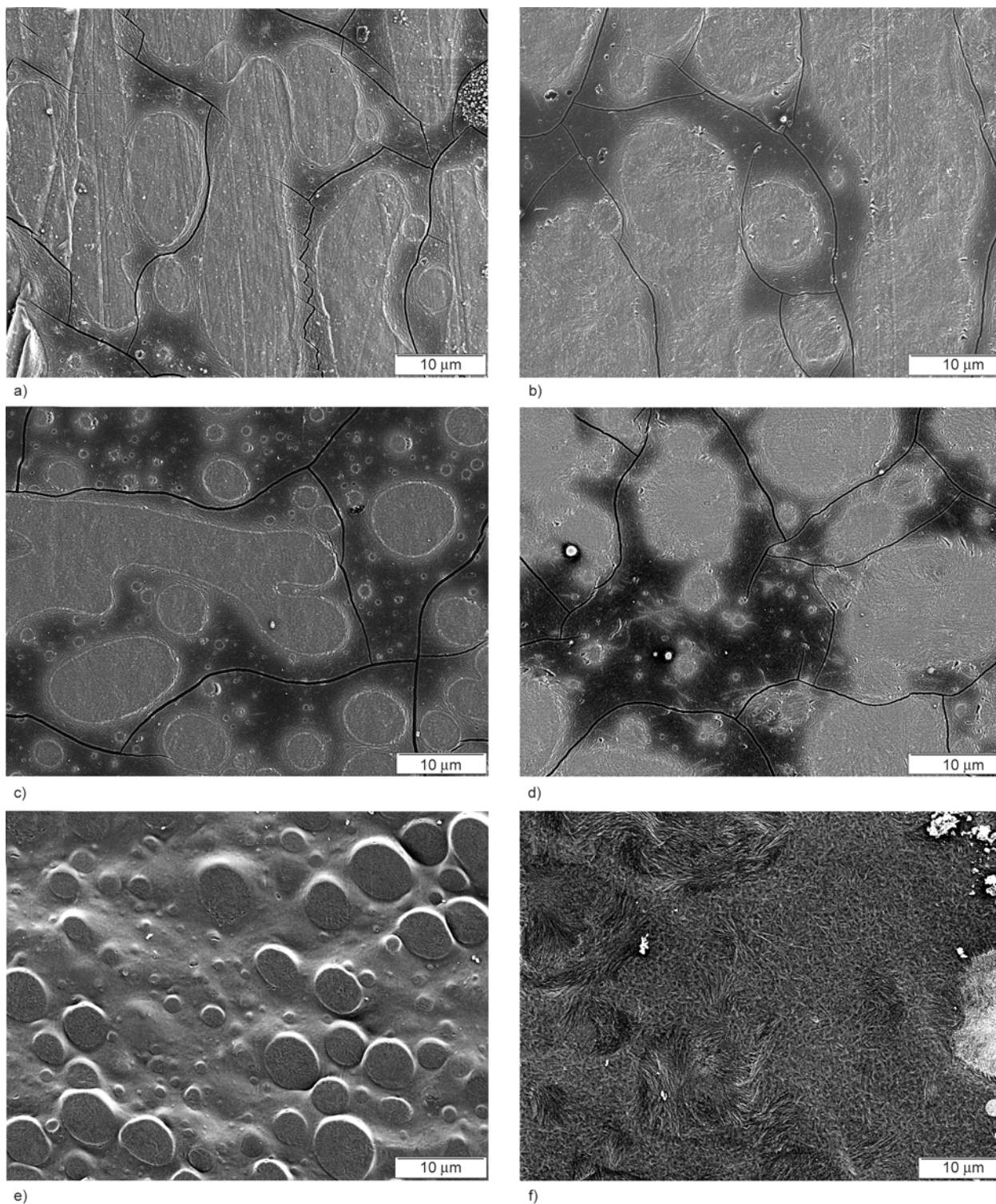


Figure 2. SEM images of stained cryo sections of 50TOR/50HDPE (a, b) and 70TOR/30HDPE (c–f) blends, which were quenched (a, c, and e) or slowly cooled (b, d, and f) from the melt before cross-linking. SEM images were obtained before (a–d) and after (e, f) removal of thin slices from surface of stained cryo sections [13].

persion of HDPE in TOR continuous phase, because the entire area of disperse phase of 50TOR/50HDPE blend is markedly larger in comparison to 70TOR/30HDPE blend.

It could be concluded that the HDPE disperse phase is segregated from the TOR continuous phase (matrix) as a result of their thermodynamic incompatibility.

In contrast, in the 50EOC30/50HDPE blend the separate phase was not able to be revealed by SEM. The SEM images of the 50EOC30/50HDPE blend with higher magnification (Figure 3a and 3b) demonstrate a poor supermolecular structure, which can be interpreted as distorted chaotically oriented lamellae caused by crystallization of both HDPE and EOC30. The SEM image of the 20HDPE/40EOC30/40TOR blend (Figure 3c and 3d) supports the assumption of thermodynamic incompatibility between TOR and EOC30/HDPE as there are only two contrasts for three components of blend in micrograph. The par-

tial compatibility of HDPE and EOC is already pointed out in Figure 3c and 3d, therefore, HDPE and EOC30 are seen in the same contrast in the 20HDPE/40EOC30/40TOR micrograph.

Figure 2e and 2f as well as Figure 3a and 3b illustrate that blends quenched before cross-linking (*q* preparation) show finer distribution of disperse phase and finer supermolecular structure of all phases in comparison to blends slowly cooled from the melt before cross-linking (*sc* preparation).

SEM images of cross-linked HDPE/PCL blends with three different proportions of components and the 50EOC30/50TOR blend are presented in Figure 4. Blends containing 70% HDPE and 30% PCL as well as 30% HDPE and 70% PCL exhibit relatively raw but well segregated disperse phase of PCL and HDPE, respectively, in matrix of the second component as a result of their thermodynamic incompatibility. The size of particles of dispersed phase shows a broad distribution between approx. 2 and 10 μm .

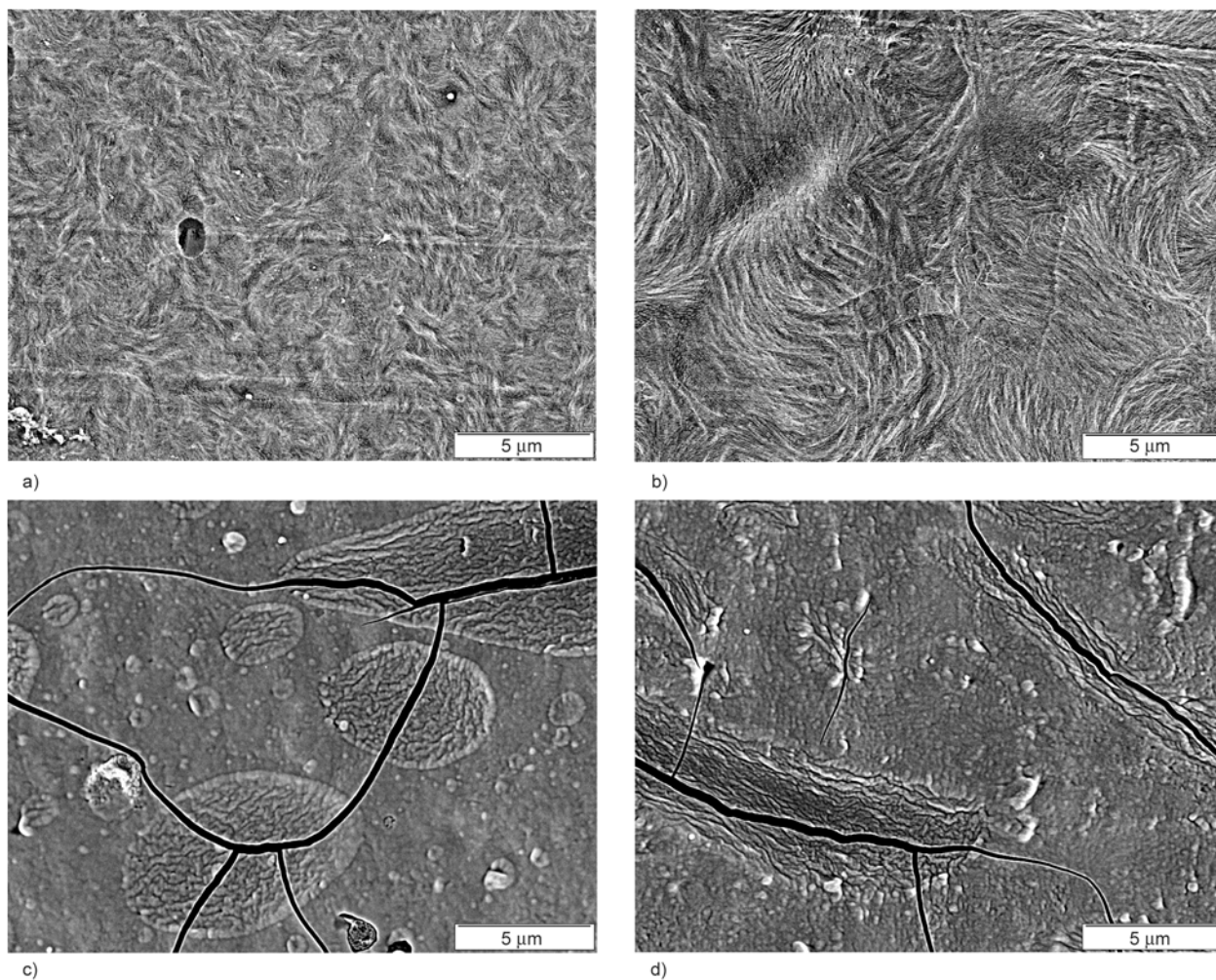


Figure 3. SEM images of stained cryo sections of 50HDPE/50EOC30 (a, b) and 20HDPE/40EOC30/40TOR (c, d) blends quenched (a, c) or slowly cooled (b, d) from the melt before cross-linking. SEM images obtained before (c, d) and after (a, b) removal of thin slices from surface of stained cryo sections [13].

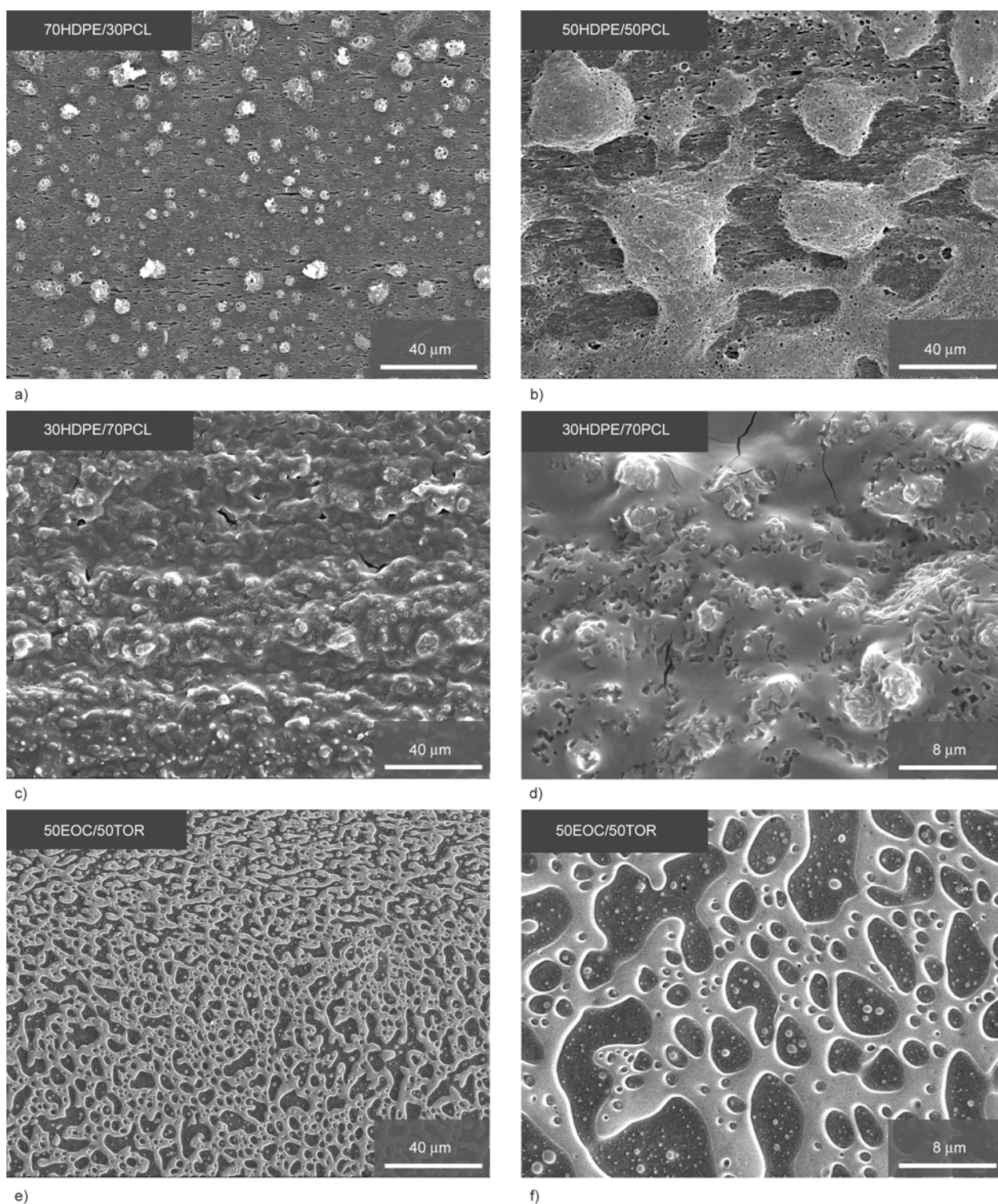


Figure 4. SEM images of HDPE/PCL blends (a–d) cross-linked by 1.3 wt% DHBP and of 50EOC30/50TOR blend (e, f) cross-linked by 2.0 wt% DHBP [48]

The SEM image of the 50HDPE/50PCL blend (see image top/right) demonstrates pronounced tendency to a formation of co-continuous phase morphology. The melt-flow index (MFI) of TOR is roughly three times higher than MFI of used EOC30 (see Table 1). Therefore, in the 50EOC30/50TOR blend the TOR having markedly lower melt viscosity compared to

EOC30 forms a continuous phase with embedded coarse particles of disperse phase of EOC30. Interestingly, as proved by SEM images, the irregular-shaped EOC30 particles in the size range between 2 and 15 μm enclose nearly spherical fine-dispersed particles of TOR with diameter of about 0.3 to 1.5 μm. Thus, in 50EOC30/50TOR blend the simul-

taneous coexistence of continuous and fine-dispersed TOR phases is available.

4. Crystallization and melting behavior of heterogeneous SM polymer networks

The pronounced phase segregation, which was demonstrated in previous section for the majority of investigated blends, results in multiple crystallization and melting behavior but leads not always to multiple SM behavior.

Melting and crystallization behavior of binary and ternary HDPE/EOC30/TOR blends, which were slowly cooled or quenched before HEE cross-linking are demonstrated in Figure 5. Melting peaks corresponding to components of both binary and ternary blends are slightly more discrete for slowly cooled (*sc*) preparation than they are for samples quenched (*q*) before HEE cross-linking. Note that *sc* samples exhibit often peak splitting. Obviously, this is the result of phase separation depending on the thermal history before cross-linking and subsequent crystallization in crystallizable regions confined by cross-linking.

Melting and crystallization behavior of irradiated HDPE/EOC30/TOR blends, especially HDPE/TOR and EOC30/TOR binary blends, displays significantly discrete melting and crystallization peaks for all compositions (50HDPE/50TOR, 30HDPE/70TOR and 50EOC30/50TOR) in comparison to 50HDPE/50EOC30 blends. Discrete melting peaks point to a separation between crystalline TOR phase

and crystalline HDPE/EOC30 phases due to thermodynamic incompatibility between TOR and polyethylenes.

Melting (T_m) and crystallization (T_c) temperatures of HDPE phase decrease at decreasing HDPE content in EBR cross-linked blends compared to values for bulk cross-linked HDPE similarly as it was observed for HDPE/EOC30 blends cross-linked by peroxide [12]. At the same time, T_m and T_c values for EOC30 phase can increase in blends containing HDPE. If the increase of T_c and correspondingly T_m values of EOC30 can be explained as a result of the nucleating effect of crystallites in cooling run, both decrease of T_c and T_m values of HDPE as well as a multiple melting and fractionated crystallization behavior point indirectly at a significant molecular interaction of EOC30 and HDPE blends in molten state but solely in regions where the molecular level of mixing before cross-linking was achieved. Overlapped melting peaks obtained from DSC investigations for HDPE/EOC30 blends support the idea of weak phase separation due to the thermodynamic compatibility between HDPE and EOCs.

Apparent specific heat capacity as a function of temperature obtained for HDPE/PCL blends cross-linked by 1.3 wt% of DHBP peroxide reveals well separated distinct peaks (Figure 6) caused by crystallization (a) and melting (b) of both PCL and HDPE phases at temperatures of about 40 and 110°C as well as 50 and 120°C, respectively.

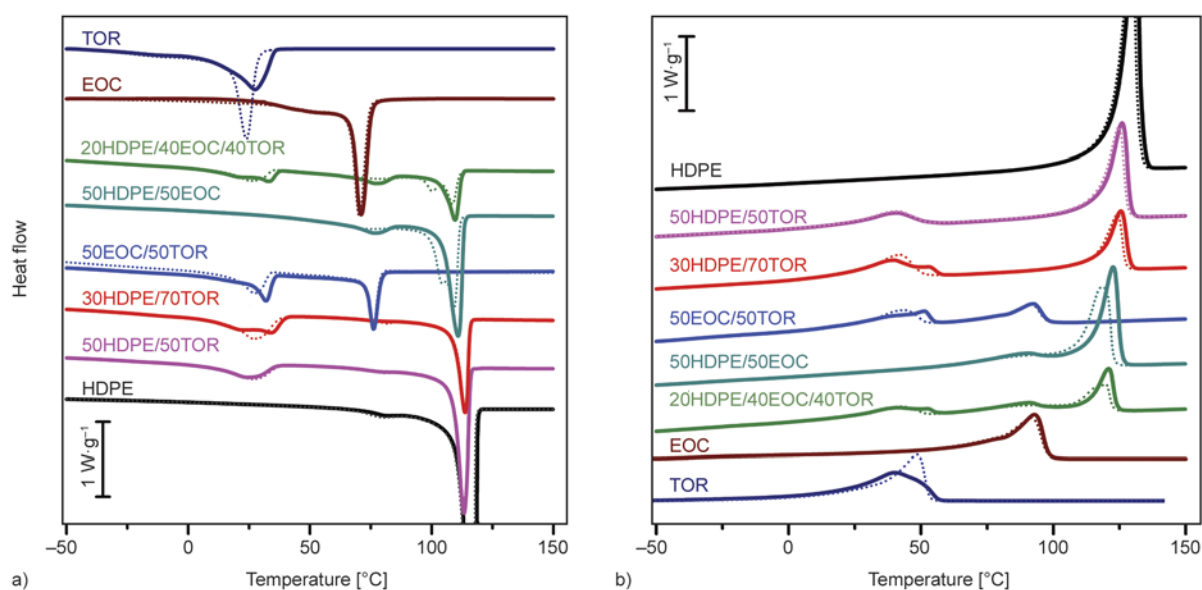


Figure 5. DSC traces of HDPE, EOC30 and TOR as well as their different binary and ternary blends, which were slowly cooled (*sc* – thick solid lines) or quenched (*q* – thin dotted lines) before HEE cross-linking, obtained during 1st cooling (a) and 2nd heating (b) runs [13]

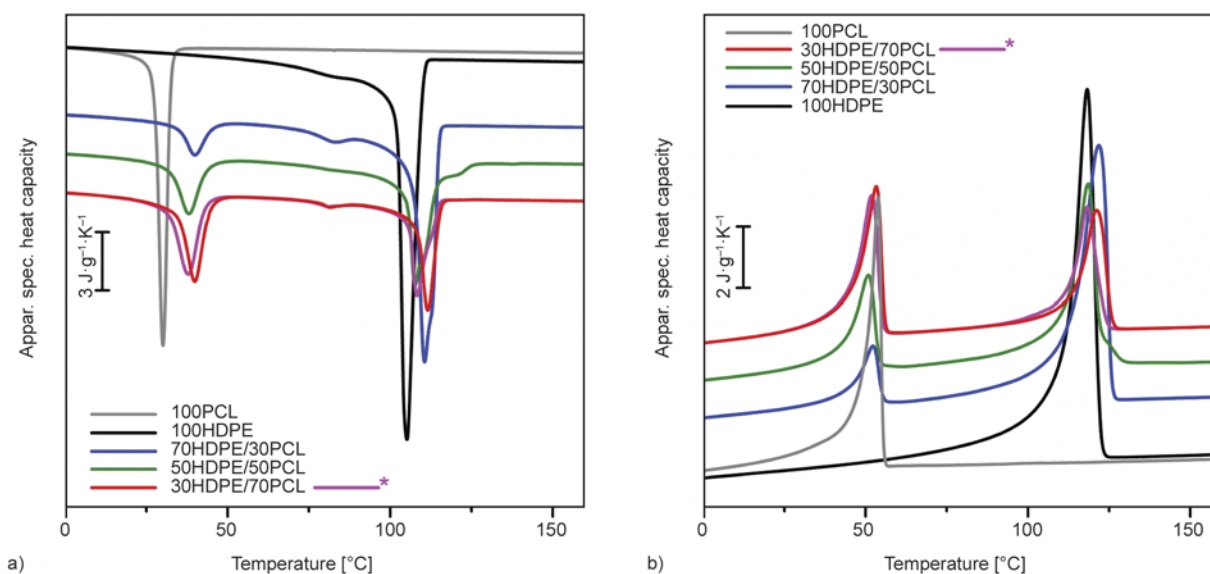


Figure 6. Apparent specific heat capacity as a function of temperature obtained for HDPE, PCL and their binary blends cross-linked by 1.3 wt% of DHBP, which demonstrate crystallization (a) and melting (b) of both PCL and HDPE phases. The magenta curves marked by asterisk present the 30HDPE/70PCL blends cross-linked by 2.0 wt% of DHBP.

Note that crystallization peak temperature T_c of bulk PCL is markedly lower than those of PCL phase in blends. This peculiarity can be explained by crystallization of PCL phase in the presence of already crystallized HDPE phase due to nucleating effect. At the same time, it is difficult to explain the lower T_c and T_m values of bulk HDPE compared to those of HDPE phase in blends by reason that during non-isothermal crystallization of HDPE phase in HDPE/PCL blends the PCL phase remains in amorphous state. It can be only assumed that PCL is a source of some nucleating impurities, which pollute the HDPE phase during the mixing process [48].

5. One-way SM behavior of heterogeneous SM polymer networks

Special thermo-mechanical tests were applied to investigate the multiple SM behavior in PE/TOR blends. Temperature dependences of SM recovery strain (ε_{rec}) and SM recovery rate obtained using time derivative of recovery strain ($-d\varepsilon_{rec}/dt$) are presented in Figure 7. Preliminary investigations of phase morphology pointed out that TOR owning the lowest melting temperature compared to other components is the continuous phase (matrix) of blends. Therefore, the TOR continuous phase with the lowest melting temperature does not constrain the SM recovery by

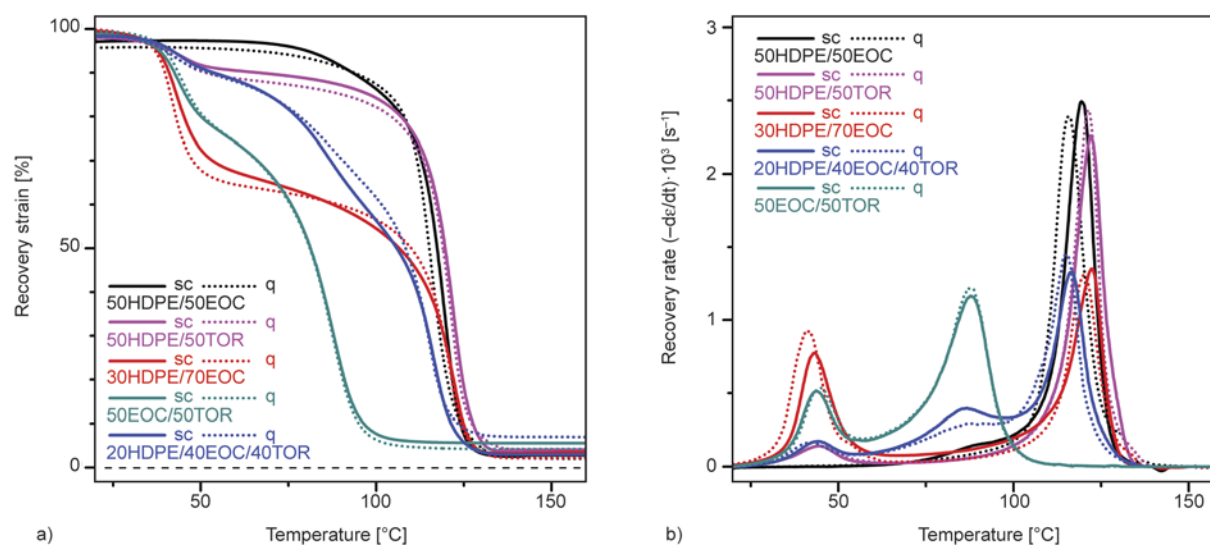


Figure 7. SM recovery strain (a) and SM recovery rate (b) of different binary and ternary blends on the basis of HDPE, EOC30 and TOR as function of temperature. The slowly cooled (*sc* – solid lines) and quenched (*q* – dotted lines) specimens were cross-linked by HEE.

melting of the disperse phase/-s. As a result, the blends on the basis of TOR forming the continuous phase evince a pronounced multiple SM behavior (see Figure 7). The SM blends cross-linked by HEE show high values of strain fixing and strain recovery ratios of 95 to 99 %.

The HDPE/TOR and EOC30/TOR blends of *q* preparation demonstrate more pronounced triple-shape behavior in comparison to blends of *sc* preparation that is reflected also by the higher peak values of SM recovery rate in particular of the TOR phase (see Table 4). Such triple-shape behavior correlates with finer phase separation and better phase segregation in blends of *q* preparation. Ternary 20HDPE/40EOC30/40TOR blend demonstrates some blurred indistinct quadruple-shape behavior. However, the detected temperature dependencies of SM recovery strain and rate allow to single out three steps and three peaks, respectively, in temperature ranges of melting of the continuous and both disperse phases.

The results of SM behavior investigation for HDPE, PCL, and HDPE/PCL blends cross-linked by 1.3 wt% of DHBP (see Figure 8) received during one-way unconstrained SM experiments demonstrate the pronounced triple-shape memory effect – two distinct steps of SM recovery strain at temperatures of above 53 and 121°C – in case of 30HDPE/70PCL blend, whose HDPE phase having higher melting and crystallization temperatures is dispersed in the continuous PCL phase/matrix.

The kinetics of unconstrained one-way SME as well as the switching temperatures (T_{sw}) of cross-linked

HDPE, PCL as bulk materials and as components of their blends have been estimated on the basis of peak values of SM recovery rate ($[-d\epsilon_{rec}/dt]_{max}$) and temperatures, at which these $[-d\epsilon_{rec}/dt]_{max}$ values arise, respectively.

These data along with T_c and T_m values obtained by DSC experiments are presented in Table 4 and demonstrate very good accordance between T_m and T_{sw} values as well as a considerable deceleration of SM recovery kinetics of PCL and HDPE phases in blends in comparison with bulk PCL and HDPE, which is exceedingly high for PCL phase dispersed in continuous HDPE phase having higher T_m . Thus, thermally induced macroscopic shape change of blends caused by SM recovery of each separate blend phase is restricted by other phases and especially by immobilized solidified phase, particularly when this solidified phase is continuous.

Note that all networks under study and in particular PCL show very high value of strain fixing (R_f) and strain recovery (R_r) ratios (see Table 4).

6. Two-way SM behavior of heterogeneous SM polymer networks

6.1. Singular two-way SM behavior

Invertible two-way SM effect can be observed in each crystallizable polymer network if the suitable v_c and load values are chosen [7–9, 17]. The results demonstrated in Figure 9 prove that HDPE cross-linked by peroxide is not an exception to this statement [48].

As can be seen from Figure 9a, the anomalous macroscopic elongation of a sample under constant

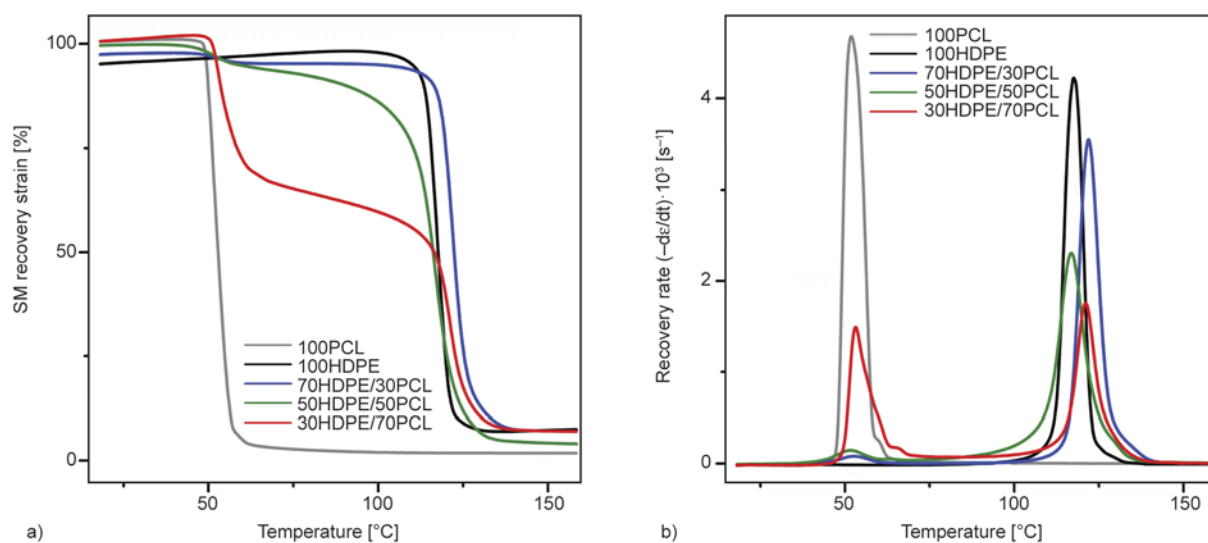


Figure 8. Temperature dependence of SM recovery strain (a) and SM recovery rate (b) for HDPE, PCL, and HDPE/PCL blends cross-linked by 1.3 wt% of DHBP. One-way unconstrained SM experiment performed after programming at 170°C and constant strain of 100% [48].

Table 4. Effect of composition and preparation route on the main characteristics of one-way unconstrained dual- and multi-shape memory effect of cross-linked HDPE, PCL, EOC30, and TOR as well as their blends

Sample	Cross-link type	TH*	Progr. steps	R _f [%]	R _r [%]	T _{sw} [°C]				dt _{rec} /dt _{max} · 10 ³ [s ⁻¹]				
						HDPE	EOC30	EOC60	TOR	PCL	HDPE	EOC30	EOC60	TOR
100HDPE	e	sc	1	95.4	96.2	122.5	–	–	–	–	3.65	–	–	–
	e	q	1	95.8	96.0	121.9	–	–	–	–	4.04	–	–	–
	p	–	1	95.2	93.9	117.6	–	–	–	–	4.20	–	–	–
100EOC30	e	sc	1	96.5	94.4	–	87.7	–	–	–	–	2.07	–	–
	e	q	1	97.1	95.9	–	87.1	–	–	–	–	2.11	–	–
	e	sc	1	98.8	98.1	–	–	–	41.2	–	–	–	3.38	–
100TOR	e	q	1	99.5	98.2	–	–	–	42.4	–	–	–	–	4.02
	e	sc	1	100.0	98.3	–	–	–	–	51.9	–	–	–	4.68
	p	–	1	95.0	94.0	111.1	78.5	–	–	–	1.32	0.41	–	–
50HDPE/50EOC30	e	sc	1	96.9	97.5	119.5	89.5	–	–	–	2.49	0.16	–	–
	e	q	1	95.5	98.0	115.7	–	–	–	–	2.39	–	–	–
	e	sc	1	99.5	96.8	122.4	–	–	43.1	–	1.35	–	–	0.78
30HDPE/70TOR	e	q	1	99.9	97.8	120.3	–	–	41.3	–	1.31	–	–	0.93
	e	sc	1	97.8	96.2	122.2	–	–	44.5	–	2.25	–	–	0.14
	e	q	1	97.9	96.0	121.6	–	–	44.1	–	2.43	–	–	0.18
50EOC30/50TOR	e	sc	1	98.8	94.5	–	87.8	–	43.8	–	–	1.16	–	–
	e	q	1	99.3	95.8	–	87.5	–	44.8	–	–	1.12	–	0.54
	p	–	1	97.4	93.0	121.9	–	–	–	–	3.52	–	–	0.08
50HDPE/50PCL	p	–	1	99.6	95.1	116.8	–	–	–	–	2.29	–	–	0.15
	p	–	1	100.0	92.8	121.0	–	–	–	–	1.74	–	–	1.48
	p	–	3	88.5	97.0	107.0	85.5	52.7	–	–	0.17	0.38	0.41	–
33HDPE/33EOC30/34EOC60	p	–	3	76.7	98.0	108.1	77.7	46.8	–	–	0.48	0.33	0.27	–
	e	sc	1	98.3	97.1	116.5	86.2	–	44.2	–	1.33	0.40	–	0.18
	e	q	1	98.1	93.0	115.4	86.6	–	41.9	–	1.45	0.30	–	0.17

p – cross-linked by peroxide

e – cross-linked via HEE

*thermal history (TH)

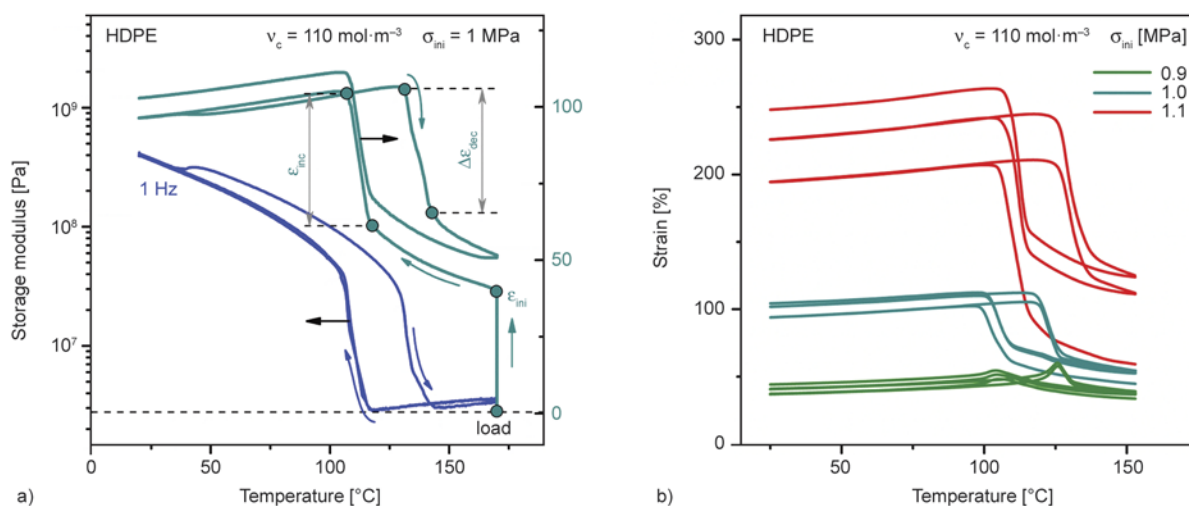


Figure 9. Temperature dependences of SM creep and recovery strain measured simultaneously along with dynamic-mechanical storage modulus under constant load with initial stress (σ_{ini}) of 1 MPa (a) and in cyclic two-way SM experiments carried out under three different σ_{ini} values (b) obtained for HDPE cross-linked by DHBP [48]

load is accompanied with simultaneous distinct increase of storage modulus during non-isothermal crystallization of the covalent polymer network, which is expected due to the increase of crystallinity. The repeating thermal cycling reveals good reproducibility for networks with relatively high crosslink density (Figure 9b). Generally, the repetition of thermal two-way SM cycles results in a tendency to improve reproducibility of SM cycling/performance similar to the thermomechanical ‘training’ treatment of SM alloys [49]. Temperature dependences of SM creep and recovery strain of HDPE obtained during two-way SM

experiment at different load values (loading temperature of 165°C) point to an increase of the strain increment ($\Delta\epsilon_{inc}$) with increasing load. However, load with initial stress (σ_{ini}) lower than 1 MPa is not sufficient to observe the anomalous elongation. On the contrary, HDPE sample under load of 0.9 MPa shrinks during crystallization, as it is normally expected. Thus, it can be concluded that the different polymer networks show very different threshold values of initial stress (constant force) required for the convenient occurrence of two-way SME that is definitely affected by crosslink density and crystallizability of the covalent polymer network.

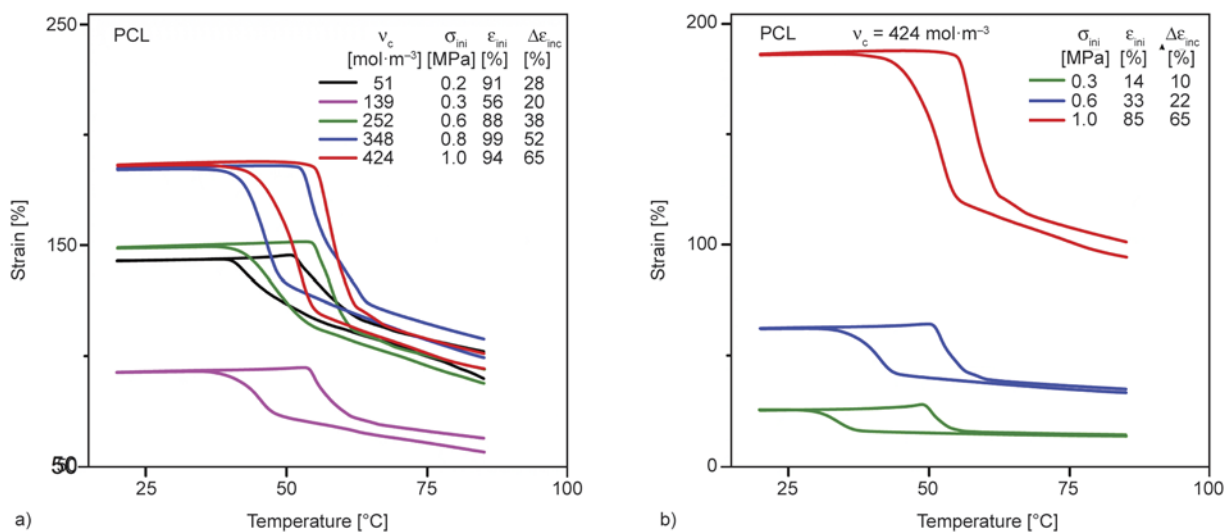


Figure 10. Temperature dependences of SM creep and recovery strain measured in the first cycle of two-way SM experiments using PCL cross-linked by different amounts of DHBP (a) and PCL with $v_c = 424 \text{ mol}\cdot\text{m}^{-3}$ under different permanent loads (b). Conditions of experiments and main parameters of performed two-way SM experiments are given in legends [48].

Temperature dependences of SM creep and recovery strain obtained during two-way SM experiment after loading performed at 100°C for PCL with different crosslink density ν_c and PCL with $\nu_c = 424 \text{ mol} \cdot \text{m}^{-3}$ under load with different initial stress shown in Figure 10 point to an increase of the crystallization-induced strain increment ($\Delta\varepsilon_{\text{inc}}$) and of the melting-induced strain decrement ($\Delta\varepsilon_{\text{dec}}$) as well as to a decrease of the initial strain after load (ε_{ini}) with increasing ν_c . The SM creep strain increment for PCL samples with enough high ν_c values gains with increasing load (see Figure 10b).

6.2. Triple two-way SM behavior

Temperature dependences of SM creep and recovery strain depicted in Figure 11 for binary HDPE/PCL blends cross-linked by 1.3 wt% of DHBP and 30HDPE/70TOR blend cross-linked by high energy electrons with dose of 200 kGy, which were obtained in the course of two-way SM experiment, demonstrate *invertible triple-shape memory effect* [4], which is more distinct for 30HDPE/70PCL and 30HDPE/70TOR blends, similar to one-way SM experiment [13].

The occurrence of two-way SM creep and recovery strain steps related to HDPE phase at σ_{ini} values less than 1 MPa is presumably explained by inhomogeneous distribution of load to blend phases. The local stress in areas of the HDPE phase possessing an enhanced modulus of elasticity is apparently considerably higher in comparison with nominal macroscopic stress applied to the sample.

In order to achieve a triple-shape behavior with requested performances, for instance comparable $\Delta\varepsilon_{\text{inc}}/\Delta\varepsilon_{\text{dec}}$ values for both SM strain steps, the crosslinkability and crystallinity of blend components should be taken into account because they are immediately responsible for the driving forces of SM creep and recovery. It also has to make allowance for mobility constraints, which are produced by the fixed semi-crystalline phase on the blend phase having lower T_m and T_c during its melting/crystallization. The considerably higher driving forces and correspondingly sufficient values of crosslink density and load are required for the characteristic sample shape change caused by the phase mobility with lower T_m/T_c . In this connection, the 50EOC30/50TOR blend is obviously a more suitable subject of such discussion because of peculiarity of phase morphology, comparable crystallinity of blend phases and enhanced cross-linkability of the TOR matrix based on the presence of double bonds regularly spaced along the polymer chains [50]. As may be clearly seen from Figure 11b (bottom), the 50EOC30/50TOR blend demonstrates pronounced triple-shape behavior with considerable but at the same time comparable $\Delta\varepsilon_{\text{inc}}$ and $\Delta\varepsilon_{\text{dec}}$ values connected with elongation and contraction of EOC30 and TOR blend phases, respectively.

The data presented in this section allow concluding that both one- and two-way multiple SM effect can be also achieved in covalent networks on the basis of polymer blends, if a suitable phase morphology is able to be generated. For blends of linear or short-

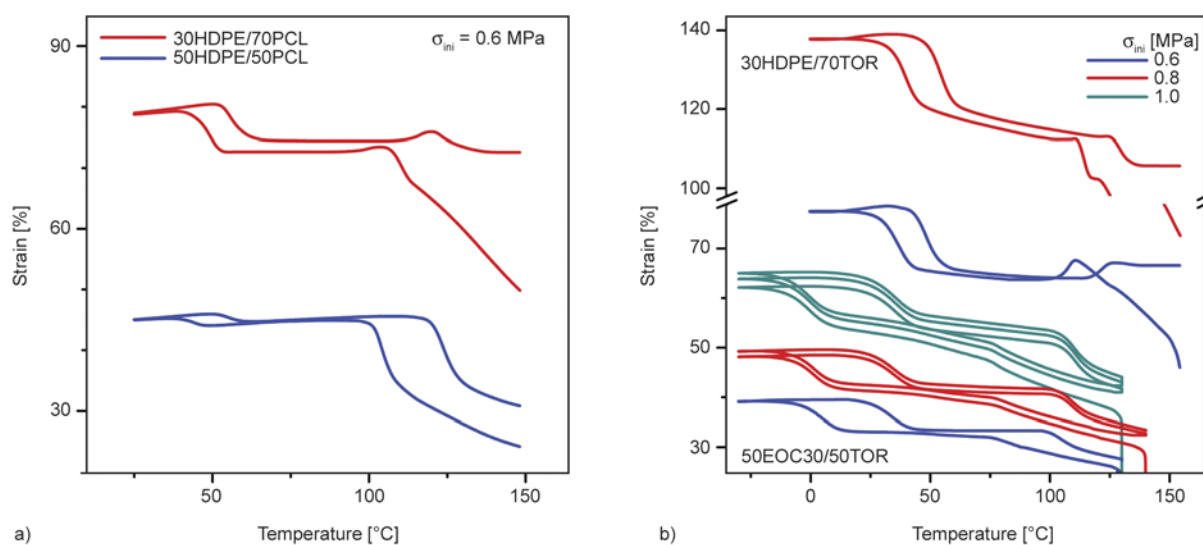


Figure 11. Temperature dependences of SM creep and recovery strain for binary HDPE/PCL blends (a), 30HDPE/70TOR, and 50EOC30/50TOR (b) blend obtained in the course of two-way SM experiment [48]

chain branched polyethylenes and poly(ϵ -caprolactone) (PCL) or trans-polyoctenamer (TOR) cross-linked by peroxide an appreciable *triple-shape* memory behavior with relatively good performances has been observed. The two-way SME performance in crystallizable covalent polymer networks gains with increasing crystallinity and crosslink density. In the special case of triple-shape behavior of polymer blends the situation becomes more complicated because of presumably inhomogeneous distribution and unlike efficiency of crosslinking agent in polymer blend components, which cannot be excluded. For this reason the obtainment of comparable values of crosslink density and normalized crystallinity defined as product of crystallinity and content of components for all blend phases is also very important. Thus, similar to one-way SME the key to proper occurrence and further improvement of the multiple two-way SM behavior of polymer blends is the generation of a well defined phase morphology including the well-developed separation/decoupling of the blend phases and an optimization of this phase morphology.

7. Modeling of SM behavior

7.1. Modeling of one-way SME

Recently, a new theoretical approach based on the modified three-element Eyring-Halsey model with non-Newtonian dashpot shown in Figure 12 was developed for the derivation of an equation describing the thermally induced recovery of pre-deformed and crystallized cross-linked polymers, in other words, describing SM recovery during one-way SME [50, 51]. The possibility of using such a model in case of creep/recovery process has been already pointed out in the works of Krausz and Eyring [53] and Ziabicki [54]. However, in the aforementioned study just non-isothermal recovery of preloaded (SM programmed) polymers is considered and the following specifications of elements in this model

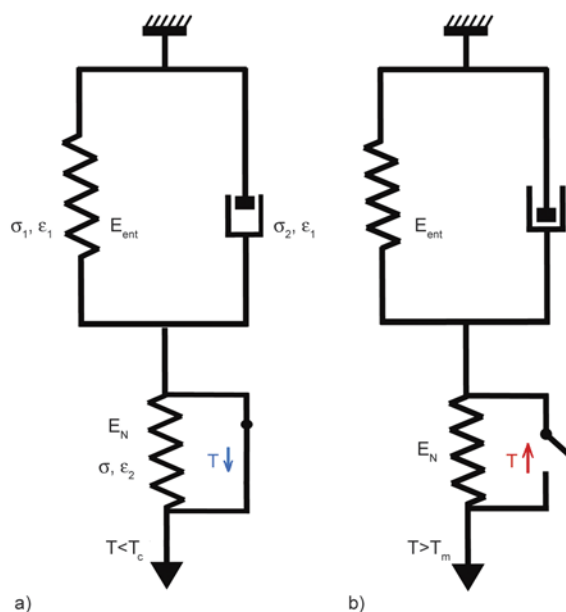


Figure 12. The three-element model proposed for the description of thermally induced recovery of semi-crystalline cross-linked polymers from deformed temporary (a) to a permanent shape (b) after heating above melting point [52]

are proposed. Firstly, a spring and a dashpot connected in parallel represent slipped entangled molecular chains containing loops and ends (Figure 12), but in contrast to Krausz and Eyring [53] another definition of the spring constant E_{ent} was used. Secondly, crystallizable covalent network is represented by the second spring. In addition, a trigger switch is connected in parallel with the second spring in order to illustrate shape fixing (Figure 12a) and shape recovery (Figure 12b) of covalent network caused by its crystallization and melting, respectively. Thus, the model in Figure 12 accounts for two basic mechanisms involved in SM performance – crystallization/melting of covalent network as well as slipping of entangled macromolecules. Basing on the reasonable assumptions, the thermally induced recovery strain was derived as described by Equations (2)–(4):

$$\varepsilon_{rec}(T) = C_0 \cdot T + \varepsilon_1 + \varepsilon_2 \quad (2)$$

$$\varepsilon_1 = \frac{8}{3V_h \nu_e N_A} \tanh^{-1} \left[\tanh \left(\frac{3}{8} V_h \nu_e N_A \varepsilon_{01} \right) \cdot \exp \left(\frac{3V_h^2}{4V_m} \frac{\nu_e U}{\alpha h} T \cdot \exp \left(- \frac{U}{RT} \right) \cdot \left[\frac{RT}{U} - 2 \right] \right) \right] \quad (3)$$

$$\varepsilon_2 = \varepsilon_{pr} - \varepsilon_{01} + \frac{4C_2^0 (1 - A)}{\nu_c R} - \frac{4C_2^0 \left[A \cdot \exp \left(- K \left(\frac{T}{T_{sw}} \right)^m \right) \cdot \left(\frac{3}{2} \nu_c RT - E_i \right) + E_i \right]}{\nu_c R E_i} \quad (4)$$

where physical and material constants are: N_A – the Avogadro constant, h – the Planck constant, α – heating rate, R – the gas constant, ε_{pr} – the programming strain, ν_c is the crosslink density, T_{sw} – the switching temperature of SM recovery. The values of material constants were determined by means of appropriate experimental investigation. The list of used fitting parameters and their definitions is given in Table 5. The modeling of thermally induced SM recovery strain and SM recovery rate detected at constant heating rate of $2 \text{ K} \cdot \text{min}^{-1}$ has been successfully performed on the basis of Equations (2)–(4) for cross-linked HDPE, EOC30, and EOC60. The results of modeling presented in Figure 13 demonstrate excellent coincidence between experimental and fitting curves. The values of material constants determined by fitting well agree with their estimations existing in literature and allow concluding that:

- crystallization plays a key role in SME of PEs under study;
- in high crystalline HDPE the crystallization of network is a dominant mechanism in SM recovery;
- decrease of the ability to crystallization in EOC30 and EOC60 leads to an increase of contribution of entangled slipped molecular chains to SM performance.

7.2. Modeling of two-way SME

The three-element mechanical model shown in Figure 12 was also employed to describe two-way SME [55]. However, it is emphasized that crystallizing/melting covalent network plays a key role in two-

Table 5. Parameters used for fitting one-way SME as well as their definitions

Effect of entangled slipped molecules		Effect of melting covalent network	
V_h	activation volume	E_i	modulus corresponding to the internal energetic deformation
V_m	volume of the slipping molecule	A	crystallinity at $T \rightarrow 0$
ν_e	density of the entangled molecules	K	material constant related to the heating rate
U	activation energy	m	material constant related to the rate of crystallization
ε_{01}	strain stored by entangled slipped molecules	C_2^0	coefficient responsible for the deviation from the theory of rubber elasticity
		C_0	linear expansion coefficient

way SME being suggested responsible for the anomalous elongation of a sample under constant load during non-isothermal crystallization. A theory of the stress-induced crystallization of cross-linked polymers developed by Gaylord [56] was used to reconsider the theoretical description of the behavior of crystallizable covalent network represented by the second spring in Figure 12. Though derived theoretical approach is based on the Gaylord's theory, it allows calculating the free energy change of a sample deformed under constant load (not constant deformation) and cooled down below crystallization temperature T_c at a constant cooling rate, i.e. in non-isometric and non-isothermal conditions, respectively. The free energy of crystallization of semi-crystalline network is written as shown by Equations (5)–(7):

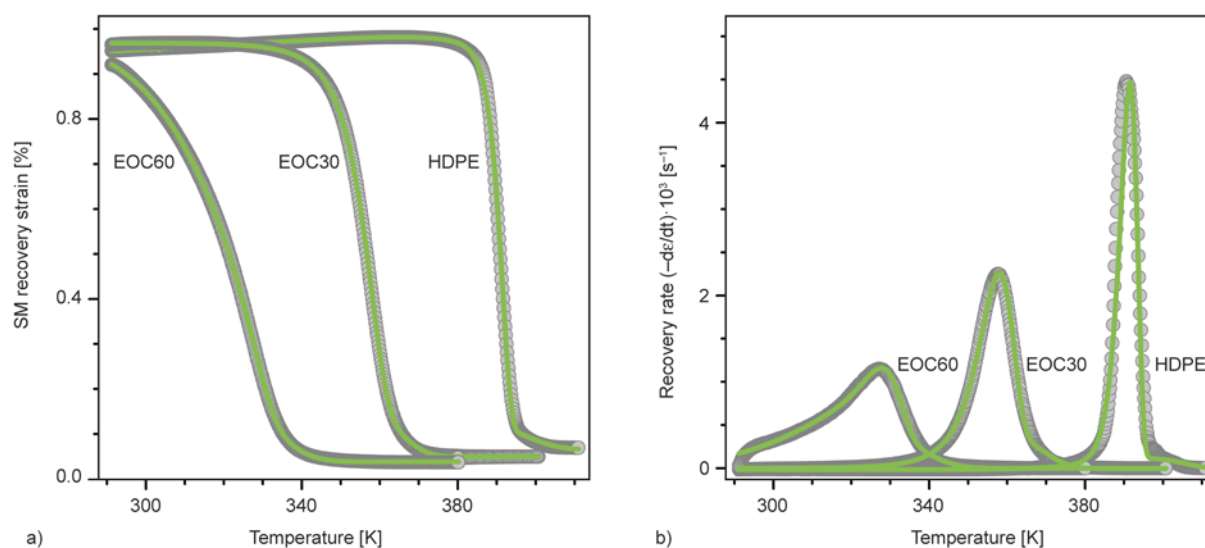


Figure 13. SM recovery strain (a) and SM recovery rate (b) for PEs with different degree of branching – HDPE, EOC30, EOC60. Grey points represent the experimental data, green lines represent the fitting results [52].

$$\Delta F_f(\chi_c, T, \lambda) = -N\chi_c\Delta H_\mu \left(1 - \frac{T}{T_m^0}\right) + U_{em} + fU_e + \frac{RT}{2\theta} \left[1 - \frac{1}{N\theta}\right] \cdot \left[\lambda^2 - 2\varphi\delta \left(1 + \frac{1}{20N}\right)\lambda + \frac{2}{\lambda} + \frac{3\varphi^2}{N} - 3\theta\right] + \frac{3RT}{20N\theta^3} \left[\lambda^4 + \frac{4}{3}\lambda + \frac{3\varphi^4}{N^2} + \frac{8}{3}\frac{1}{\lambda^2} + \frac{6\varphi^2}{N}\lambda^2 + \frac{4\varphi^2}{N}\frac{1}{\lambda} - \frac{8}{3}\varphi\delta(\lambda^3 + 1) - \frac{4}{N}\varphi^3\delta\lambda - \theta^2\left(5 - \frac{2}{N\theta}\right)\right] \quad (5)$$

$$\theta = \left(1 - \chi_c - \frac{\psi f}{N}\right) \quad (6)$$

$$\varphi = \left(\frac{f^2 a^2}{b^2} + \beta \zeta^2\right)^{1/2}, \quad \beta = 1, \text{ even folds} \\ \beta = 0, \text{ odd folds} \quad (7)$$

where N is the number of chain links, ΔH_μ is the enthalpy of fusion per link, U_{em} and U_e are the free energy of the interface between amorphous and crystalline regions and the surface free energy of a crystal with f folds, each with ψ links, respectively, T_m^0 is the equilibrium melting temperature, a is the chain thickness, b is the length of a chain link, ζ is the number of links traversing the crystallite, χ_c is the crystallinity.

Following Gaylord, it was assumed that the number of crystal folds f controls the orientation of crystallites formed during the two-way SME with respect to the applied force. Namely, the even number of folds results in perpendicular orientation of chains in crystal to the external force, while odd number of folds corresponds to the case when the orientation of chains in crystal is parallel to the stretch direction or makes a sharp angle with the external force. The free energies of crystallization as a function of temperature and draw ratio calculated for cross-linked HDPE on the basis of derived equations in case of different values of chain links N and different

numbers of crystal folds f are plotted in Figure 14. The results indicate that for given numbers of chain links the extended-chain morphology ($f=0$) has a lower free energy at the onset of crystallization, and further cooling results in forming the folded-chain crystals oriented nearly parallel ($f=4$, Figure 14a) or perpendicular to the stretch direction ($f=1$, Figure 14b). Evidently, these different cases of crystal orientation lead to dramatically different mechanical behavior of pre-deformed crystallizing covalent network. The theory predicts that perpendicular orientation of chain folds in crystals results in sample contraction during crystallization, as expected, whereas anomalous elongation of a sample under load during two-way SME can be observed when crystal chains are nearly parallel to the force direction.

The stress-strain-temperature relationship derived from the free energy change was used to fit the experimental findings of the temperature dependent strain under load, which were received by the authors for cross-linked HDPE loaded by 1 MPa, as

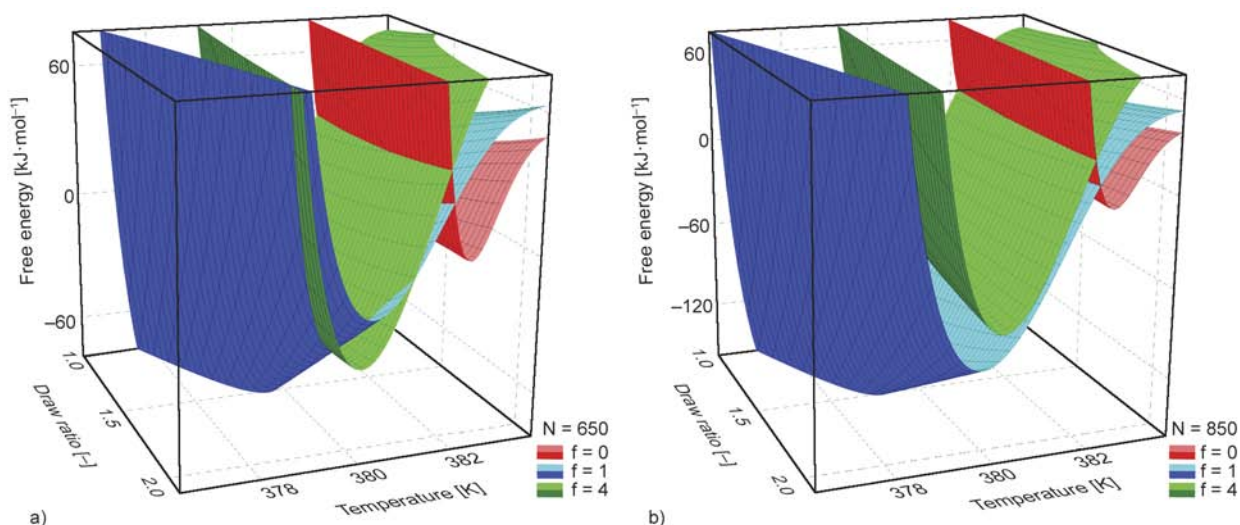


Figure 14. The free energy of crystallization as a function of temperature and draw ratio calculated for HDPE in case of different values of chain links $N = 650$ (a), $N = 850$ (b), and different numbers of crystal folds f [55]

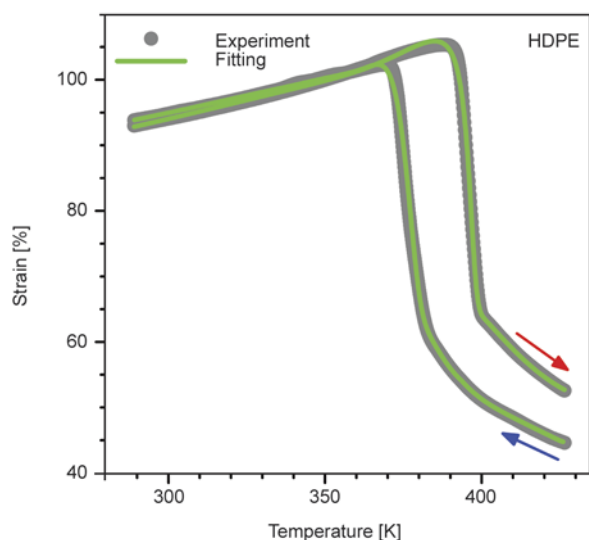


Figure 15. Fitting and experimental curves of two-way SME obtained for cross-linked HDPE loaded by 1 MPa. Blue and red arrows indicate cooling and heating runs, respectively [55].

shown in Figure 15. The fitting curves have shown excellent accordance with the experimental values. The fitting parameters used for the effect of entangled slipped macromolecules include all those listed in Table 5. Since the theoretical description of crystallizing/melting covalent network has been reconsidered, the corresponding fitting parameters are the number of chain links N , number of crystal folds f , crystallinity values χ_{co} and χ_{cf} corresponding to the lowest free energies of crystals with 0 and f folds, respectively, and linear expansion coefficient. Although presented modeling the one- and two-way SME has been performed for single polymers, like

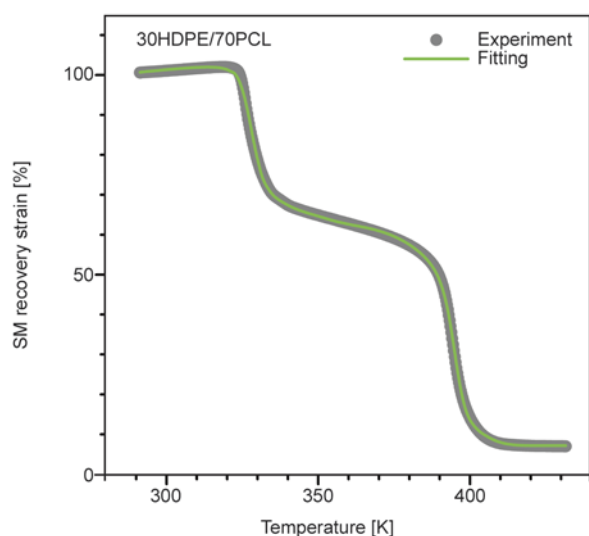


Figure 16. Fitting and experimental curves of multiple SM recovery obtained for cross-linked 30HDPE/70PCL blend

HDPE, EOC30, and EOC60, it opens broad prospects for modeling the SM phenomena in cross-linked blends of crystallizable polymers. First of all, the theoretical approach described above is accurate, physically grounded, and focused on the basic molecular mechanisms involved in one- and two-way SM behavior of both single polymers and polymer blends. In order to model the SM performance of polymer blends on the basis of presented theory, an account of phase morphology and its appropriate theoretical description are only needed. A potential of the present theoretical approach in modeling the one-way multiple SM behavior of cross-linked blends was verified for 30HDPE/70PCL blend. As it is seen from Figure 16, the fitting curve good coincides with the experimental findings. This encourages further development of the theory.

8. Conclusions

This mini-review about the generation and investigation of SM polymers on the basis of heterogeneous semi-crystalline polymer blends shows that such an approach has a great future potential. As an alternative to expensive synthesis of complex interpenetrating or block-copolymers networks both the one-way and two-way multiple SM effect can be also achieved in covalent networks on the basis of polymer blends, if a suitable phase morphology is able to be generated. For blends of crystallizable polymers covalently cross-linked by peroxide or electron irradiation an appreciable multiple-shape memory behavior with relatively good performances has been observed.

The main characteristics of both one-way and two-way SME in crystallizable covalent polymer network gain with increasing crystallinity and cross-link density. In the specific case of triple-shape behavior of polymer blends the situation becomes more complicated because of possible inhomogeneous distribution and efficiency of crosslinking agent in polymer blend components that cannot be excluded. For SM blends with high performance the obtainment of equal crosslink density and sufficient high crystallinity, which can be achieved by controlled technology of melt mixing, cooling, and cross-linking, is required.

The key to proper occurrence and further improvement of the multiple SM behavior of polymer blends is the generation of phase morphology including a well developed separation/decoupling of the blend

phases and an optimization of this phase morphology. Especially, the distinct manifestation of triple-SM behavior is possible only when the continuous phase of the blend has lower crystallization/melting temperatures in comparison to the disperse phase. The developed theoretical approach enabled not only the consistent and reliable description of the strain as a function of temperature obtained experimentally in the course of one- and two-way SME in crystallizable polymers but also the explanation of the anomalous elongation of crosslinked polymers under constant load during non-isothermal crystallization in terms of both crystal morphology and crystal orientation. Simultaneously, modeling of SME in heterogeneous networks on the basis of polymer blends requires the consideration of their phase morphology and of interaction of blend components using a suitable mechanical model. Further investigation on the effect of phase morphology on mechanical properties and peculiarities of the SM behavior of covalent networks on the basis of crystallizable polymer blends will enable the optimization of their multiple SM behavior. The investigation of constrained SME and especially the SM recovery of polymer networks loaded by constant forces could help to estimate the dynamic behavior of SME and in particular to evaluate the specific stored mechanical energy. On the basis of such a study on the capability of a SM network to accumulate mechanical energy, routes could be formulated to create energy storage devices in future. Development of theoretical description of SM polymer materials can point the operating ways to improve SM behavior of polymer networks by means of tailoring of their structure and morphology.

References

- [1] Lendlein A., Kelch S.: Shape-memory polymers. *Angewandte Chemie International Edition*, **41**, 2034–2057 (2002).
DOI: [10.1002/1521-3773\(20020617\)41:12<2034::AID-ANIE2034>3.0.CO;2-M](https://doi.org/10.1002/1521-3773(20020617)41:12<2034::AID-ANIE2034>3.0.CO;2-M)
- [2] Liu C., Qin H., Mather P. T.: Review of progress in shape-memory polymers. *Journal of Materials Chemistry*, **17**, 1543–1558 (2007).
DOI: [10.1039/b615954k](https://doi.org/10.1039/b615954k)
- [3] Behl M., Lendlein A.: Shape-memory polymers. *Materials Today*, **10**, 20–28 (2007).
DOI: [10.1016/S1369-7021\(07\)70047-0](https://doi.org/10.1016/S1369-7021(07)70047-0)
- [4] Behl M., Lendlein A.: Actively moving polymers. *Soft Matter*, **3**, 58–67 (2007).
DOI: [10.1039/b610611k](https://doi.org/10.1039/b610611k)
- [5] Rousseau I. A.: Challenges of shape memory polymers: A review of the progress toward overcoming SMP's limitations. *Polymer Engineering and Science*, **48**, 2075–2089 (2008).
DOI: [10.1002/pen.21213](https://doi.org/10.1002/pen.21213)
- [6] Mather P. T., Luo X., Rousseau I. A.: Shape memory polymer research. *Annual Review of Materials Research*, **39**, 445–471 (2009).
DOI: [10.1146/annurev-matsci-082908-145419](https://doi.org/10.1146/annurev-matsci-082908-145419)
- [7] Leng J., Lu H., Liu J., Huang W. M., Du S.: Shape-memory polymers – A class of novel smart materials. *MRS Bulletin*, **34**, 848–855 (2009).
DOI: [10.1557/mrs2009.235](https://doi.org/10.1557/mrs2009.235)
- [8] Jiang H-Y., Schmidt A. M.: The structural variety of shape-memory polymers. in ‘Shape memory polymers and multifunctional composites’ (eds.: Leng J., Du S.) CRC Press, Boca Raton, 27–63 (2010).
- [9] Bellin I., Kelch S., Langer R., Lendlein A.: Polymeric triple-shape materials. *Proceedings of the National Academy of Sciences of the United States of America*, **103**, 18043–18047 (2006).
DOI: [10.1073/pnas.0608586103](https://doi.org/10.1073/pnas.0608586103)
- [10] Behl M., Bellin I., Kelch S., Wagermaier W., Lendlein A.: One-step process for creating triple-shape capability of AB polymer networks. *Advanced Functional Materials*, **19**, 102–108 (2009).
DOI: [10.1002/adfm.200800850](https://doi.org/10.1002/adfm.200800850)
- [11] Luo X., Mather P. T.: Triple-shape polymeric composites (TSPCs). *Advanced Functional Materials*, **20**, 2649–2656 (2010).
DOI: [10.1002/adfm.201000052](https://doi.org/10.1002/adfm.201000052)
- [12] Kolesov I. S., Radusch H-J.: Multiple shape-memory behavior and thermal-mechanical properties of peroxide cross-linked blends of linear and short-chain branched polyethylenes. *Express Polymer Letters*, **2**, 461–473 (2008).
DOI: [10.3144/expresspolymlett.2008.56](https://doi.org/10.3144/expresspolymlett.2008.56)
- [13] Radusch H-J., Kolesov I. S., Gohs U., Heinrich G.: Multiple shape-memory behavior of polyethylene/polycyclooctene blends cross-linked by electron irradiation. *Macromolecular Materials and Engineering*, **297**, 1225–1234 (2012).
DOI: [10.1002/mame.201200204](https://doi.org/10.1002/mame.201200204)
- [14] Cuevas J. M., Rubio R., Germán L., Laza J. M., Vilas J. L., Rodrigues M., León L. M.: Triple-shape memory effect of covalently crosslinked polyalkenamer based semicrystalline polymer blends. *Soft Matter*, **8**, 4928–4935 (2012).
DOI: [10.1039/c2sm07481h](https://doi.org/10.1039/c2sm07481h)
- [15] Li F., Chen Y., Zhu W., Zhang X., Xu M.: Shape memory effect of polyethylene/nylon 6 graft copolymers. *Polymer*, **39**, 6929–6934 (1998).
DOI: [10.1016/S0032-3861\(98\)00099-8](https://doi.org/10.1016/S0032-3861(98)00099-8)
- [16] Xie T.: Tunable polymer multi-shape memory effect. *Nature*, **464**, 267–270 (2010).
DOI: [10.1038/nature08863](https://doi.org/10.1038/nature08863)

- [17] Zhao J., Chen M., Wang X., Zhao X., Wang Z., Dang Z.-M., Ma L., Hu G.-H., Chen F.: Triple shape memory effects of cross-linked polyethylene/polypropylene blends with cocontinuous architecture. *Applied Materials and Interfaces*, **5**, 5550–5556 (2013).
DOI: [10.1021/am400769J](https://doi.org/10.1021/am400769J)
- [18] Bai Y., Zhang X., Wang Q., Wang T.: A tough shape memory polymer with triple-shape memory and two-way shape memory properties. *Journal of Materials Chemistry A*, **2**, 4771–4778 (2014).
DOI: [10.1039/c3ta15117d](https://doi.org/10.1039/c3ta15117d)
- [19] Madbouly S. A., Lendlein A.: Degradable polyurethane/soy protein shape-memory polymer blends prepared via environmentally-friendly aqueous dispersions. *Macromolecular Materials and Engineering*, **297**, 1213–1224 (2012).
DOI: [10.1002/mame.201200341](https://doi.org/10.1002/mame.201200341)
- [20] Karger-Kocsis J., Kéki S.: Biodegradable polyester-based shape memory polymers: Concepts of (supra) molecular architecturing. *Express Polymer Letters*, **8**, 397–412 (2014).
DOI: [10.3144/expresspolymlett.2014.44](https://doi.org/10.3144/expresspolymlett.2014.44)
- [21] Ratna D., Karger-Kocsis J.: Recent advances in shape memory polymers and composites: A review. *Journal of Materials Science*, **43**, 254–269 (2008).
DOI: [10.1007/s10853-007-2176-7](https://doi.org/10.1007/s10853-007-2176-7)
- [22] Chung T., Romo-Urbe A., Mather P. T.: Two-way reversible shape memory in a semicrystalline network. *Macromolecules*, **41**, 87–96 (2008).
DOI: [10.1021/ma071517z](https://doi.org/10.1021/ma071517z)
- [23] Pandini S., Passera S., Messori M., Paderni K., Toselli M., Gianoncelli A., Bontempi E., Riccò T.: Two-way reversible shape memory behaviour of crosslinked poly(ϵ -caprolactone). *Polymer*, **53**, 1915–1924 (2012).
DOI: [10.1016/j.polymer.2012.02.053](https://doi.org/10.1016/j.polymer.2012.02.053)
- [24] Pandini S., Baldi F., Paderni K., Messori M., Toselli M., Pilati F., Gianoncelli A., Brisotto M., Bontempi E., Riccò T.: One-way and two-way shape memory behaviour of semi-crystalline networks based on sol–gel cross-linked poly(ϵ -caprolactone). *Polymer*, **54**, 4253–4265 (2013).
DOI: [10.1016/j.polymer.2013.06.016](https://doi.org/10.1016/j.polymer.2013.06.016)
- [25] Kolesov I. S., Kratz K., Lendlein A., Radosch H.-J.: Kinetics and dynamics of thermally-induced shape-memory behavior of crosslinked short-chain branched polyethylenes. *Polymer*, **50**, 5490–5498 (2009).
DOI: [10.1016/j.polymer.2009.09.062](https://doi.org/10.1016/j.polymer.2009.09.062)
- [26] Kolesov I. S., Radosch H.-J.: Investigation on the performances of the peroxidic initiated network in shape-memory materials on the basis of ethylene-1-octenecopolymers and their blends with HDPE by means of deformation behavior and stress relaxation. in ‘Proceeding of the Polymer Processing Society 24th Annual Meeting (PPS-24). Salerno, Italy’ 1–6, (2008).
- [27] Zotzmann J., Behl M., Hofmann D., Lendlein A.: Reversible triple-shape effect of polymer networks containing poly(pentadecalactone)- and poly(ϵ -caprolactone)-segments. *Advanced Materials*, **22**, 3424–3429 (2010).
DOI: [10.1002/adma.200904202](https://doi.org/10.1002/adma.200904202)
- [28] Basit A., L’Hostis G., Pac M. J., Durand B.: Thermally activated composite with two-way and multi-shape memory effects. *Materials*, **6**, 4031–4045 (2013).
DOI: [10.3390/ma6094031](https://doi.org/10.3390/ma6094031)
- [29] Imai S.: Operating methods for two-way behavior shape memory polymer actuators without using external stress. *IEEJ Transactions on Electrical and Electronic Engineering*, **9**, 90–96 (2014).
DOI: [10.1002/tee.21940](https://doi.org/10.1002/tee.21940)
- [30] Westbrook K. K., Mather P. T., Parakh V., Dunn M. L., Ge Q., Lee B. M., Qi H. J.: Two-way reversible shape memory effects in a free-standing polymer composite. *Smart Materials and Structures*, **20**, 065010/1–065010/9 (2011).
DOI: [10.1088/0964-1726/20/6/065010](https://doi.org/10.1088/0964-1726/20/6/065010)
- [31] Behl M., Kratz K., Noechel U., Sauter T., Lendlein A.: Temperature-memory polymer actuators. *Proceedings of the National Academy of Sciences of the United States of America*, **110**, 12555–12559 (2013).
DOI: [10.1073/pnas.1301895110](https://doi.org/10.1073/pnas.1301895110)
- [32] Behl M., Kratz K., Zotzmann J., Nöchel U., Lendlein A.: Reversible bidirectional shape-memory polymers. *Advanced Materials*, **25**, 4466–4469 (2013).
DOI: [10.1002/adma.201300880](https://doi.org/10.1002/adma.201300880)
- [33] Wu Y., Hu J., Han J., Zhu Y., Huang H., Li J., Tang B.: Two-way shape memory polymer with ‘switch–spring’ composition by interpenetrating polymer network. *Journal of Materials Chemistry A*, **2**, 18816–18822 (2014).
DOI: [10.1039/c4ta03640a](https://doi.org/10.1039/c4ta03640a)
- [34] Tobushi H., Okumura K., Hayashi S., Ito N.: Thermo-mechanical constitutive model of shape memory polymer. *Mechanics of Materials*, **33**, 545–554 (2001).
DOI: [10.1016/S0167-6636\(01\)00075-8](https://doi.org/10.1016/S0167-6636(01)00075-8)
- [35] Barot G., Rao I. J.: Constitutive modeling of the mechanics associated with crystallizable shape memory polymers. *Zeitschrift für angewandte Mathematik und Physik ZAMP*, **57**, 652–681 (2006).
DOI: [10.1007/s00033-005-0009-6](https://doi.org/10.1007/s00033-005-0009-6)
- [36] Barot G., Rao I. J., Rajagopal K. R.: A thermodynamic framework for the modeling of crystallizable shape memory polymers. *International Journal of Engineering Science*, **46**, 325–351 (2008).
DOI: [10.1016/j.ijengsci.2007.11.008](https://doi.org/10.1016/j.ijengsci.2007.11.008)
- [37] Qi H. J., Nguyen T. D., Castro F., Yakacki C. M., Shandas R.: Finite deformation thermo-mechanical behavior of thermally induced shape memory polymers. *Journal of the Mechanics and Physics of Solids*, **56**, 1730–1751 (2008).
DOI: [10.1016/j.jmps.2007.12.002](https://doi.org/10.1016/j.jmps.2007.12.002)

- [38] Husson J. M., Dubois F., Sauvat N.: A finite element model for shape memory behavior. *Mechanics of Time-Dependent Materials*, **15**, 213–237 (2011). DOI: [10.1007/s11043-011-9134-0](https://doi.org/10.1007/s11043-011-9134-0)
- [39] Böhl M., Reese S.: Micromechanical modelling of shape memory polymers. *Advances in Science and Technology*, **54**, 137–142 (2008). DOI: [10.4028/www.scientific.net/AST.54.137](https://doi.org/10.4028/www.scientific.net/AST.54.137)
- [40] Sinha R. P., Jarali C. S., Raja S.: Modelling the thermomechanical behaviour of shape memory polymer materials. *Indian Journal of Engineering and Materials Sciences*, **18**, 15–23 (2011).
- [41] Liu Y., Gall K., Dunn M. L., Greenberg A. R., Diani J.: Thermomechanics of shape memory polymers: Uniaxial experiments and constitutive modeling. *International Journal of Plasticity*, **22**, 279–313 (2006). DOI: [10.1016/j.ijplas.2005.03.004](https://doi.org/10.1016/j.ijplas.2005.03.004)
- [42] Ge Q., Yu K., Ding Y., Qi H. J.: Prediction of temperature-dependent free recovery behaviors of amorphous shape memory polymers. *Soft Matter*, **8**, 11098–11105 (2012). DOI: [10.1039/C2SM26249E](https://doi.org/10.1039/C2SM26249E)
- [43] Khonakdar H. A., Jafari S. H., Rasouli S., Morshedean J., Abedini H.: Investigation and modeling of temperature dependence recovery behavior of shape-memory crosslinked polyethylene. *Macromolecular Theory and Simulations*, **16**, 43–52 (2007). DOI: [10.1002/mats.200600041](https://doi.org/10.1002/mats.200600041)
- [44] Wang Z. D., Li D. F., Xiong Z. Y., Chang R. N.: Modeling thermomechanical behaviors of shape memory polymer. *Journal of Applied Polymer Science*, **113**, 651–656 (2009). DOI: [10.1002/app.29656](https://doi.org/10.1002/app.29656)
- [45] Heuchel M., Cui J., Kratz K., Kosmella H., Lendlein A.: Relaxation based modeling of tunable shape recovery kinetics observed under isothermal conditions for amorphous shape-memory polymers. *Polymer*, **51**, 6212–6218 (2010). DOI: [10.1016/j.polymer.2010.10.051](https://doi.org/10.1016/j.polymer.2010.10.051)
- [46] Westbrook K. K., Parakh V., Chung T., Mather P. T., Wan L. C., Dunn M. L., Qi H. J.: Constitutive modeling of shape memory effects in semicrystalline polymers with stretch induced crystallization. *Journal of Engineering Materials and Technology*, **132**, 041010/1–041010/9 (2010). DOI: [10.1115/1.4001964](https://doi.org/10.1115/1.4001964)
- [47] Kolesov I. S., Radusch H.-J.: Deformation behavior of random ethylene-1-octene-copolymers under long-term loading. in ‘Proceeding of the Polymer Processing Society 21st Annual Meeting (PPS-21). Leipzig, Germany’ 1–9 (2005).
- [48] Kolesov I., Dolynchuk O., Borreck S., Radusch H.-J.: Morphology-controlled multiple one- and two-way shape-memory behavior of cross-linked polyethylene/poly(ϵ -caprolactone) blends. *Polymers for Advanced Technologies*, **25**, 1315–1322 (2014). DOI: [10.1002/pat.3338](https://doi.org/10.1002/pat.3338)
- [49] Tadaki T.: Cu-based shape memory alloys. in ‘Shape memory materials’ (eds.: Otsuka K., Wayman C. M.) Cambridge University Press, Cambridge, 109–116 (1998).
- [50] Chen H. Y.: Carbon-13 NMR-spectra of polyalkenamers. in ‘Applications of polymer spectroscopy’ (ed: Brame E. G.) Academic Press, New York, 7–17 (1978).
- [51] Kolesov I., Dolynchuk O., Radusch H. J.: Modeling of shape-memory recovery in crosslinked semicrystalline polymers. *Advances in Science and Technology*, **77**, 319–324 (2012). DOI: [10.4028/www.scientific.net/AST.77.319](https://doi.org/10.4028/www.scientific.net/AST.77.319)
- [52] Kolesov I., Dolynchuk O., Radusch H.-J.: Theoretical description of unconstrained thermally induced shape-memory recovery in crosslinked polyethylenes. *Journal of Polymer Science Part B: Polymer Physics*, **52**, 815–822 (2014). DOI: [10.1002/polb.23491](https://doi.org/10.1002/polb.23491)
- [53] Krausz A. S., Eyring H.: Deformation kinetics. Wiley, New York (1975).
- [54] Ziabicki A.: Theoretical analysis of oriented and non isothermal crystallization. *Colloid and Polymer Science*, **252**, 207–221 (1974). DOI: [10.1007/BF01638101](https://doi.org/10.1007/BF01638101)
- [55] Dolynchuk O., Kolesov I., Radusch H.-J.: Thermodynamic description and modeling of two-way shape-memory effect in crosslinked semicrystalline polymers. *Polymers for Advanced Technologies*, **25**, 1307–1314 (2014). DOI: [10.1002/pat.3335](https://doi.org/10.1002/pat.3335)
- [56] Gaylord R. J.: A theory of the stress-induced crystallization of crosslinked polymeric networks. *Journal of Polymer Science: Polymer Physics Edition*, **14**, 1827–1837 (1976). DOI: [10.1002/pol.1976.180141008](https://doi.org/10.1002/pol.1976.180141008)

Spinning, drawing and physical properties of polypropylene nanocomposite fibers with fumed nanosilica

I. Dabrowska^{1,2}, L. Fambri^{1,2*}, A. Pegoretti^{1,2}, M. Slouf³, T. Vackova³, J. Kolarik⁴

¹Department of Industrial Engineering, University of Trento, via Sommarive 9, 38123 Trento, Italy

²National Interuniversity Consortium for Science and Technology of Materials (INSTM), Via G. Giusti 9, 50121 Firenze, Italy

³Institute of Macromolecular Chemistry, Academy of Sciences of the Czech Republic, Heyrovsky Sq. 2, 162 06 Prague 6, Czech Republic

⁴Visiting professor, Department of Industrial Engineering, University of Trento, via Sommarive 9, 38123 Trento, Italy

Received 30 September 2014; accepted in revised form 30 November 2014

Abstract. Nanocomposite fibers of isotactic polypropylene – fumed silica AR805 were prepared by melt compounding using a two-step process: melt-spinning and hot drawing at various draw ratios up to 15. Transmission electron microscopy revealed uniform dispersion of the silica nanoparticles in polypropylene matrix, although at higher concentrations and lower draw ratios the nanoparticles showed increasing tendency to form small agglomerates. On the other hand, at low concentrations the uniform distribution of fumed silica improved mechanical properties of the composite fibers, especially at higher draw ratios. Crystallinity and melting temperature of fibers were found to significantly increase after drawing. Elastic modulus at draw ratio = 10 rose from 5.3 GPa for neat PP up to 6.2–8.1 GPa for compositions in the range 0.25–2 vol% of the filler. Moreover, higher tensile strength and creep resistance were achieved, while strain at break was rather insensitive to the filler fraction. Considering all experimental results, a failure model was proposed to explain the toughness improvement during the drawing process by the induced orientation of polymer chains and the formation of voids.

Keywords: polypropylene, fibers, nanocomposites, drawing, mechanical properties

1. Introduction

Significant growth of polypropylene (PP) usage can be attributed to a combination of many factors, e.g. a good balance of physical and chemical properties. Owing to plausible melt rheology and thermal properties, PP-based materials can be processed by various technologies, e.g. injection molding, calendaring, air-quenched blow films, spinning technology, spunbond process [1]. Moreover, low density, excellent thermal stability, chemical inertness along with wide design flexibility and simplicity of recycling make PP an attractive construction material. Many studies have been performed to improve mechanical properties of PP fibers and films since 1964. PP

can easily be drawn and crystallized so that high degrees of orientation and crystallinity can be achieved. The maximum values of Young's modulus and tensile strength of PP fibers reported in the literature are 36–40 and 1.5 GPa, respectively [2]. Fibers of PP are employed in many end-use products thanks to their properties such as low density, resistance to moisture and chemicals, sufficient strength and easy processing [3]. PP fiber's properties can be enhanced by melt mixing with nano-sized particles like carbon nanotubes [4–6] and montmorillonite [7, 8]. Nowadays, many reports have been focused on the addition of silica and/or fumed nanosilica (FS) to enhance mechanical properties of

*Corresponding author, e-mail: luca.fambri@unitn.it

polyolefins [9–13], PP fibers [12–14] and synthetic rubbers [15].

Synthetic amorphous silicon dioxide is manufactured via the hydrolysis of chlorosilanes in an oxygen-hydrogen gas flame. Resulting fumed silica (FS) is a fine, white, odorless and tasteless amorphous powder. Owing to its completely amorphous state it is considered non-toxic and non-irritating, in contrast to crystalline silica which is carcinogenic. FS surface contains Si–O–Si units and Si–OH bonds which are highly reactive so that FS can easily be modified through chemical functionalization. Besides, the hydrophilic surface of fumed silica is characterized by high surface energy. In general, it is important to deactivate the FS surface by using alkylchlorosilanes or alkylsilazanes before mixing with polyolefines. This treatment lowers the surface energy and changes the FS character from hydrophilic to hydrophobic [16].

It has been demonstrated that the introduction of a small amount of FS into a polyolefin matrix may lead to substantial improvements of the mechanical properties of the resulting composite [11]. Rottstegge and coworkers [12] tested PP (MFI = 15 g/10 min) fibers reinforced by fumed silica. The obtained materials were of good quality, however, modulus, strain and stress at break were only slightly higher than those of neat PP. Srisawat and coworkers [13, 14] studied the influence of FS addition on the properties of PP fibers using PP with high melt flow rate (MFI = 25 g/10 min). They observed not only a higher thermal stability and nucleation effect of the nanofiller, but also a remarkable increase in the tensile strength, as consequence of the incorporation of elongated and flattened silica particles during the spinning process. D'Amato *et al.* [9] used high density polyethylene with low melt flow index as a matrix to produce fibers by means of a two-step process: extrusion and drawing. Fiber stiffness was remarkably improved by nanofiller presence, especially at elevated draw ratios, without affecting the tensile properties at break. Also creep compliance showed a reduction in comparison with neat HDPE fibers. Enhancement of these properties was related to the alignment of silica aggregates along the strain direction, which was confirmed by TEM analysis.

To the best of our knowledge, no papers can be found in the current literature dealing with the effect of fumed silica reinforcement in nanocomposite fibers made of PP with low melt flow rate. In this

contribution we have selected Aerosil®AR805 which – due to the surface modification obtained by octylsilane – has relatively long organic chains allowing for larger strains at break of the composites, as shown elsewhere [17]. In particular, our attention was focused on the addition of low amounts of FS to PP in order to improve the mechanical properties of resulting fibers. The fibers were melt-compounded by twin-screw extruder and then drawn at 145°C up to elevated draw ratio (DR). Mechanical and thermal measurements of the fibers were used to evaluate the effect of FS with regard to its concentration and to the selected processing procedure. Simultaneously, the effects of the fiber composition and of DR on resulting morphology were studied.

2. Experimental section

2.1. Materials and sample preparation

2.1.1. Materials

Isotactic polypropylene (Moplen HP500, melt flow rate 1.8 g/10 min at 230°C and 2.16 kg, density at 23°C = 0.9 g/cm³) in the form of pellets was supplied by Basell Polyolefins (Ferrara, Italy). Fumed silica Aerosil®R805 was kindly supplied by Evonik (Essen, Germany). Aerosil®R805 is a hydrophobic silica (surface treated with octylsilane) with a specific surface area 150 m²·g⁻¹, mean particle size of about 12 nm and a bulk density of 1.84 g·cm⁻³ at 23°C. Before the processing, FS powders were dried for 24 h at 80°C in a vacuum oven. Nanocomposites were marked with the silica abbreviation (AR805) and the filler content. As an example, AR805-2 indicates a nanocomposite sample filled with 2 vol% of fumed silica Aerosil®R805.

2.1.2. Fiber spinning

Monofilament fibers with the FS fraction between 0.25 and 2 vol% (Table 1) were produced by Thermo Haake (Karlsruhe, Germany) PTW16 intermeshing co-rotating twin screw extruder (screw diameter 16 mm, *L/D* ratio 25, rod die diameter 1.65 mm). The temperature profile from the hopper to rod die was gradually increased ($T_1 = 130^\circ\text{C}$, $T_2 = 200^\circ\text{C}$, $T_3 = 210^\circ\text{C}$, $T_4 = 220^\circ\text{C}$, $T_5 = 230^\circ\text{C}$). The extruder screws rotation was optimized in the range of 8–10 rpm depending on the material composition in order to produce fibers having a diameter of about 500 μm, as reported in Table 1, with an almost constant diameter ratio between die diameter and fiber diameter of 3.29±0.03. The spun fibers were fast

Table 1. Designation and composition of the PP nanocomposite fibers. Average diameter of as-spun fibers ($DR = 1$) and selected drawn fibers at nominal draw ratio DR 5, 10 and 15.

Material	PP [vol%]	Fumed silica [vol%]	Fiber diameter			
			DR = 1 [μm]	DR = 5 [μm]	DR = 10 [μm]	DR = 15 [μm]
PP	100	0	495±6	230±3	158±3	128±2
AR805-0.25	99.75	0.25	504±9	229±2	157±3	130±2
AR805-0.5	99.50	0.5	506±19	233±14	157±2	130±2
AR805-1	99.0	1	500±7	220±2	154±1	129±2
AR805-2	98.0	2	502±15	227±3	157±2	130±3

cooled in water at room temperature in order to eliminate orientation and drawing of the fibers immediately after the extrusion, and wrapped around a bobbin of diameter 40 mm rotating at 8 m/min.

2.1.3. Fiber drawing

The spun fibers were drawn in a hot-plate drawing apparatus 1.4 m length (SSM-Giudici srl, Galbiate, LC, Italy – www.ssm-giudici.it) at 145°C, similarly to the maximum drawing temperature (150°C) selected by Joshi and Viswanathan [18] in order to obtain highly extended fibers. As-spun fibers were unreel and wound by using acrylic bobbins of 40 mm diameter rotating from 10 up to 150 rpm, corresponding to a constant feeding rate of 1.26 m/min and maximum collecting rate of about 190 m/min (nominal draw ratio of 15).

The fiber draw ratio (DR) is commonly defined as the ratio between the collection (R_c) and the feeding (R_f) rate, and assuming a constant volume, it can be calculated according to Equation (1):

$$DR = \left(\frac{D_i}{D_f} \right)^2 \quad (1)$$

where D_i/D_f are the initial and final diameter of the fiber. The diameter was measured by using an optical microscope connected to image processing software (ImageJ®). Fibers with various draw ratios from $DR = 3$ up to $DR = 15$ were produced. Nominal draw ratio of 1 is referred to as-spun fibers, whereas $DR = 5, 10$ and 15 corresponds to the nominal draw ratio of drawn fiber with the diameter reported in Table 1.

2.2. Experimental techniques

Dispersion of FS in the PP matrix was visualized by transmission electron microscopy (TEM). Specimens for TEM analysis were prepared by means of an ultramicrotome by cutting the fibers perpendicularly to their axis. TEM micrographs were taken

with a microscope FEI Tecnai G2 Spirit (Brno, Czech Republic) using the bright field imaging at 120 kV. Differential scanning calorimetry (DSC) analysis was performed by using a Mettler DSC30 calorimeter (Schwarzenbach, Switzerland). Fiber samples of about 15 mg were placed in aluminum crucibles of 160 μL and were heated from 0 up to 250°C with a heating-cooling-heating cycle at ±10°C/min under flushing nitrogen at 100 mL/min. Melting temperature and crystallization temperature were registered during the scans. The crystallinity percentage X was calculated according to Equation (2) relating the measured melting enthalpy ΔH_i , the standard enthalpy of the fully crystalline PP (207 J·g⁻¹ [19]) and the weight fraction of nanofiller f :

$$X_{PP} = 100 \frac{\Delta H_i}{207 \cdot (1 - f)} \quad (2)$$

Quasi-static tensile mechanical properties of as-spun and all drawn fibers were measured at room temperature by using an Instron® 4502 (Norwood, MA, USA) tensile dynamometer equipped with a load cell of 100 N. Single filaments of various diameters (0.5 mm–0.1 mm) and of the gauge length 30 mm were uniaxially tested at a cross-head speed 50 mm/min. Elastic modulus was determined according to ISO 527 standard as a secant value between the strain levels of 0.05 and 0.25%. For each sample 5 specimens were tested and the average values were calculated.

Dynamic mechanical thermal analysis (DMTA) was conducted by a dynamic mechanical analyzer DMA Q800 from TA Instruments (New Castle, DE, USA). Experiments were carried out in the tensile mode by using a fiber clamp (gauge length of 10 mm; pre-stress of 0.01 N; sinusoidal strain with a frequency of 1 Hz and amplitude of 64 micron) from –125 to 100°C at a heating rate of 3°C/min.

Creep response of drawn (DR 10 and 15) and undrawn fibers at 30°C was studied by using a

dynamic mechanical analyzer DMA Q800 from TA Instruments (New Castle, DE, USA): gauge length of 10 mm; creeping time of 3600 s. A constant stress of 3 MPa corresponding to about 10% of the yield stress of undrawn fibers was chosen as the creep stress.

3. Results and discussion

It is well known that uniform filler dispersion and its good adhesion to polymer matrix are fundamental for improving mechanical properties of the composites. Complete and uniform dispersion is important for achieving a large interface and, consequently, extensive interfacial bonding that ensures a good interfacial stress transfer [20]. Thus, microstructure analysis by TEM was focused on the fumed silica distribution in PP matrix.

3.1. Microstructure characterization

TEM images of ultramicrotomed cross sections of the nanofilled PP-AR805 fibers with selected nanofiller fractions and/or draw ratios are presented in Figures 1, 2. A set of low-magnification micrographs

(Figure 1) of all studied composites shows that the silica particles are dispersed quite uniformly in the polymer matrix, but frequently they tend to form small agglomerates. In general, the amount and size of the agglomerates increases with the increasing filler percentage: at the lowest concentration (AR805-0.25; Figures 1a–1c) the agglomerates are rare, whereas at the highest concentration (AR805-2; Figures 1d–1f) the average number and size of the agglomerates grows; morphology of samples with medium concentrations (AR805-0.5 and AR805-1; not shown for the sake of brevity) is in between the two extremes. Further inspection of the TEM micrographs reveals that the silica nanoparticle agglomerates are partially destroyed at higher draw ratios. The effect is stronger for composites with higher nanoparticle concentrations (Figures 1d–1f). TEM micrographs with higher magnifications (Figure 2) evidence that silica nanoparticles are quite well fixed in the PP matrix even if they are agglomerated, because the matrix penetrates inside the agglomerates and the interface is not sharp but diffuse, which indicates good interfacial adhesion.

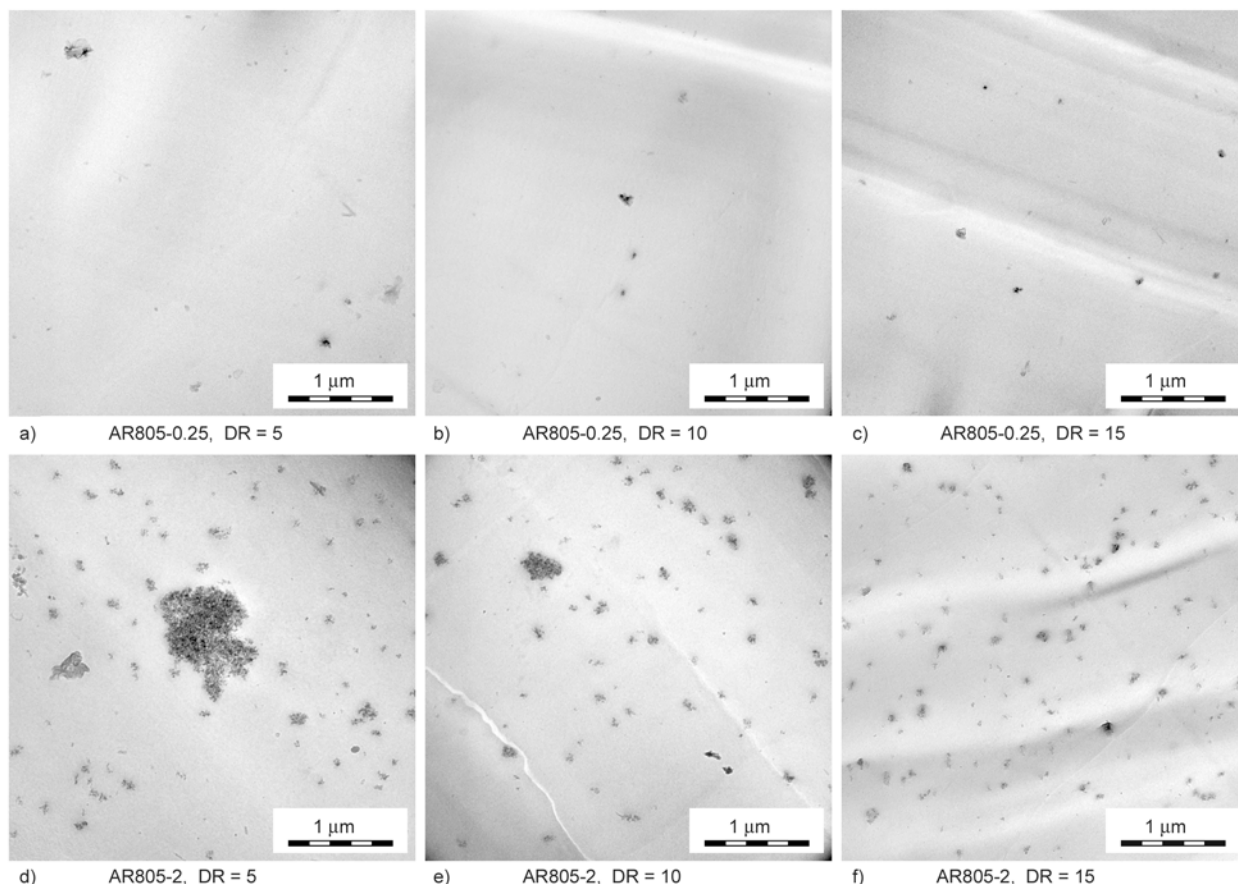


Figure 1. TEM micrographs of AR805 at various silica nanoparticle concentrations and draw ratios

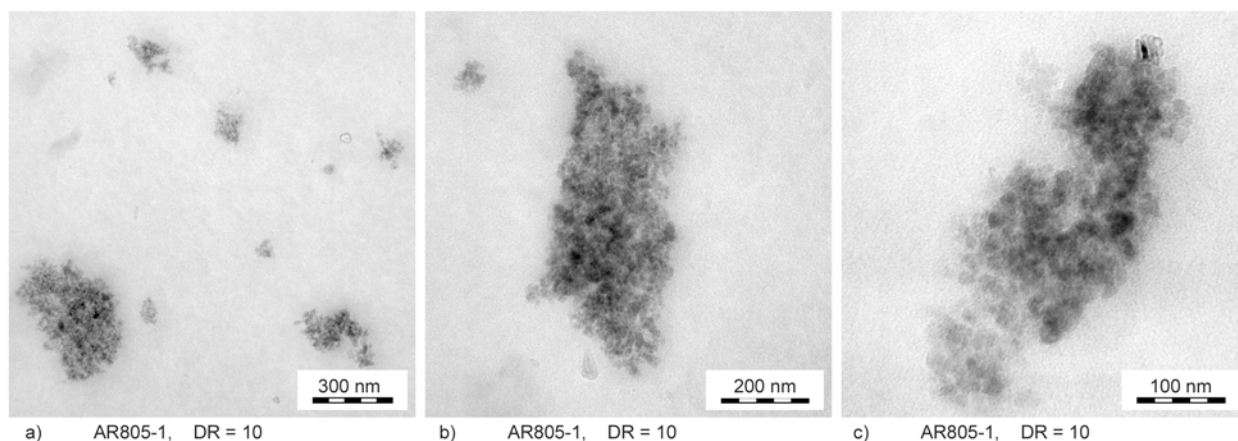


Figure 2. Higher magnification TEM micrographs of nanocomposite fibers AR805-1, illustrating good adhesion between nanosilica particles and iPP matrix

3.2. Differential scanning calorimetry

DSC results of the heating-cooling-heating cycle of the neat and nanocomposite PP fibers with different draw ratios are summarized in Table 2. Selected thermograms are depicted in Figure 3a–3c, where a single sharp melting peak is observed for the fibers with $DR = 1$ and 5, while for $DR = 10$ and 15 distinct multiple melting peaks appear. This behav-

Table 2. Results of the DSC analysis (1st heating – cooling – 2nd heating); onset of melting temperature (T_m onset), melting temperature (T_m), crystallinity (χ) and crystallization temperature (T_c) for neat and nanocomposite PP fibers at selected nominal draw ratio ($DR = 1, 5, 10$ and 15)

Material		1 st heating		Cooling		2 nd heating
		T_{m1} [°C]	X_c [%]	T_c [°C]	X_c [%]	T_{m2} [°C]
PP	$DR = 1$	165.1	36.4	111.5	44.7	167.1
	$DR = 5$	172.5	45.0	112.8	49.0	164.6
	$DR = 10$	179.7	50.4	114.1	47.2	164.7
	$DR = 15$	178.0	53.0	114.6	48.8	164.2
AR805-0.25	$DR = 1$	161.7	41.5	114.0	47.6	164.8
	$DR = 5$	170.0	49.6	115.8	47.8	164.5
	$DR = 10$	174.0	56.2	115.0	47.5	165.1
	$DR = 15$	180.7	53.0	112.0	46.4	164.9
AR805-0.5	$DR = 1$	160.7	43.0	114.3	48.6	164.6
	$DR = 5$	172.0	45.0	111.5	45.6	164.2
	$DR = 10$	174.1	49.2	111.1	45.6	165.8
	$DR = 15$	180.0	52.7	113.0	46.7	165.5
AR805-1	$DR = 1$	162.3	38.4	114.4	47.0	164.6
	$DR = 5$	165.2	45.7	112.1	46.2	165.4
	$DR = 10$	175.8	50.5	109.7	48.0	167.1
	$DR = 15$	182.4	52.0	112.7	42.0	165.4
AR805-2	$DR = 1$	162.5	41.1	114.4	49.2	165.4
	$DR = 5$	167.9	43.4	110.2	46.5	165.2
	$DR = 10$	179.0	51.2	114.0	47.3	165.5
	$DR = 15$	177.4	53.5	113.8	46.5	163.9

ior is related to the difference in the crystal forms and the degree of perfection and/or orientation achieved during drawing.

Comparison of the values of crystallinity, melting (T_m) and crystallization (T_c) temperatures indicates interesting differences between as-spun fibers for neat as well as nanofilled PP. Higher T_c (about 114°C vs. 111°C for neat PP) and crystallinity content (38–43% vs. 36% for neat PP), along with lower T_m values (160–162°C vs. 165°C for neat PP) were observed for as-spun nanocomposite fibers. In the literature, starting from PP at relatively high melt flow ($MF = 12$ and 25 g/10 min) slightly lower T_m values were already reported for both as-spun and drawn nanocomposite polyolefine fibers [18, 21], and correspondently lower crystallinity content and T_c values were observed. On the other hand, there are reports where growth of T_m was indicated along with lower crystallinity [7, 22]. Thus it can be concluded that higher crystallinity content and higher crystallization temperature in cooling reveal a possible nucleating role of FS.

The increase in the orientation of fiber structure upon the solid state drawing (Table 2) accounts not only for a higher degree of crystallinity (from about 36% up to 53%), but also for a significant increase in the melting temperature (from 161–165°C up to 174–182°C). Obviously, the higher the draw ratio, the higher the orientation of the polymer chains and, consequently, the faster the crystallization in the draw direction [23]. Higher crystallinity observed after the drawing is a typical effect, which is related to the high degree of the order and continuity of the crystalline phase, as presented by Srisawat *et al.* [13] for fibers drawn at 110°C with

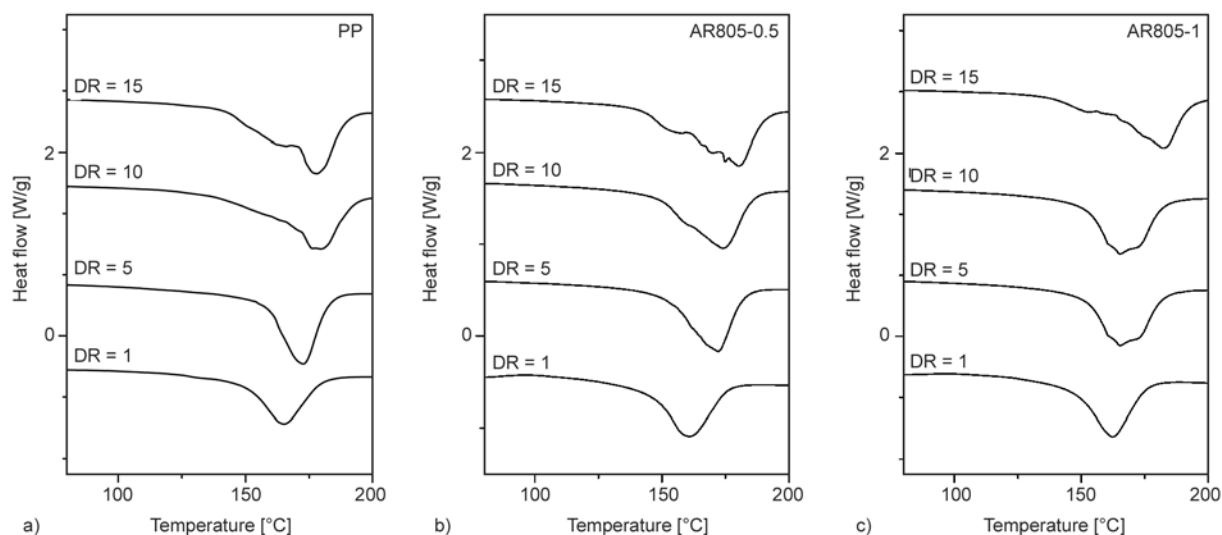


Figure 3. The first heating DSC thermograms of a) neat PP, b) AR805-0.5, and c) AR805-1 nanocomposite fibers at different draw ratios

fumed silica and high melt flow polypropylene (25 g/10 min), but showing also slight decrease of melting temperature. On the other hand, the parallel increase of crystallinity and melting temperature shown in Table 2, could directly be related to the low melt flow PP, as consequence of a combined effect of both the high drawing orientation and the high drawing temperature. Analogous results were obtained for nanocomposite fibers with low melt flow HDPE (0.9 g/10 min at 190°C/2.16 kg) containing organically modified hydrotalcite [24], that showed after drawing at 125°C a relevant increase of both melting temperature (from 132–133°C up to 140–146°C) and crystallinity content (from about 50% up to 74–78%). In both cases, the effect of drawing could be interpreted as the transformation of lower perfection crystals in highly ordered structure at higher melting temperature, and it is also proportional to the orientation of non-crystalline regions.

As already mentioned, polyolefin fibers show various kinds of improvements, so that it is difficult to obtain clear information on the effect of FS on the crystallization behavior of polypropylene fibers. If the fiber properties at the highest $DR = 15$ are compared, some slightly higher values of crystallinity and T_m can be seen for composites with FS.

It can be concluded from the data obtained for the as-spun fibers that the effect of FS on the nucleation process is quite evident, while in the case of the drawn fibers is rather blurred. The most significant result is the increase of the melting temperature of

both PP and nanofilled PP fibers after drawing, probably related to the high drawing temperature of high molecular weight polymer.

3.3. Mechanical properties

Representative stress – strain curves of the quasi-static tensile tests for as-spun ($DR = 1$) and drawn fibers with $DR = 15$ at various nanofiller content are reported in Figure 4a and 4b, respectively. The most relevant mechanical properties are summarized in Table 3. It is important to note that undrawn fibers manifest a clear yield point at a low strain followed by a wide plateau (of cold drawing at a constant stress) and a strain hardening region until the break point. Drawing process produces a strong orientation of the macromolecules along the draw direction and the strain-induced crystallization in the amorphous regions, which accounts for the increase in the fiber stiffness and the disappearance of yielding phenomena.

Tensile modulus (E) of the PP-FS fibers as a function of the draw ratio is shown in Figure 5. It is evident that FS particles raise the fiber stiffness, especially at higher draw ratios. The highest improvements were obtained for the compositions with 0.25 and 0.5 vol% FS, whose elastic modulus reached 8.1 and 7.3 GPa, respectively (in comparison to 5.3 GPa of the neat PP). A negative effect of high concentrations of nanosilica on modulus observed for composition with 2 vol% of filler is even more visible not only for $DR = 5$ (see Figure 1d), but also for higher draw ratio ($DR > 10$), which can be explained in

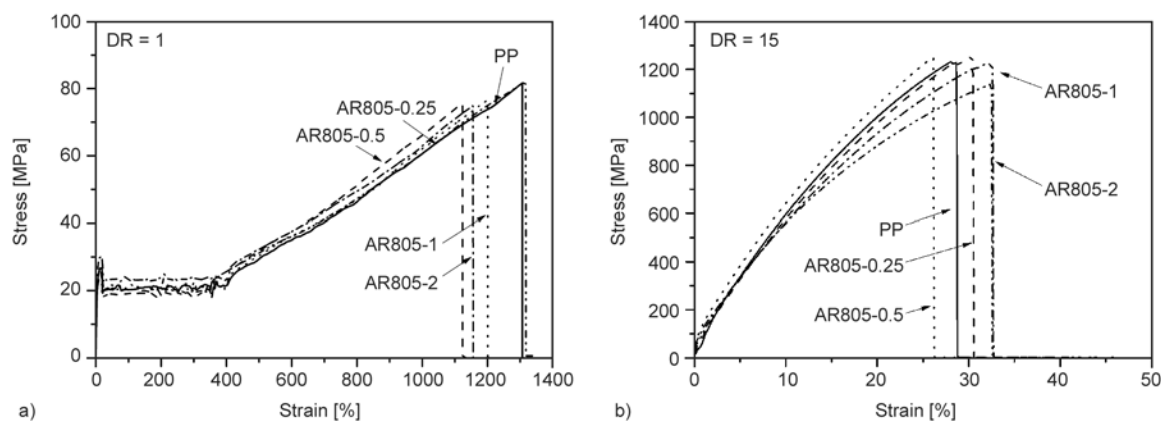


Figure 4. a) Representative stress-strain curves of neat and nanocomposite PP fibers a) as-spun fibers ($DR = 1$) and b) drawn fibers with draw ratio $DR = 15$

Table 3. Mechanical properties of neat and nanofilled PP fibers at selected nominal draw ratios ($DR = 1, 5, 10$ and 15)

Material	DR	Elastic modulus [GPa]	Stress at break [MPa]	Strain at break [%]	True strength ^a [MPa]	Mechanical draw ratio λ_{MEC}	Total draw ratio λ_{TOT}	Draw stiffening factor ^b
PP	1	0.48±0.01	83±4	1260±15	1123	13.6	148.1	1.0
	5	1.71±0.15	374±13	185±11	1066	2.85	153.3	3.6
	10	5.30±0.15	944±25	53±5	1444	1.53	173.4	11.0
	15	7.88±0.35	1240±50	34±3	1661	1.34	215.8	16.4
AR805-0.25	1	0.54±0.01	82±2	1275±55	1127	13.7	149.7	1.0
	5	2.27±0.15	538±14	70±10	914	1.7	91.4	4.2
	10	8.10±0.17	1117±25	41±3	1575	1.41	159.7	15.0
	15	9.10±0.52	1277±11	36±4	1737	1.36	219.1	17.0
AR805-0.5	1	0.60±0.01	78±3	1125±45	955	12.2	133.4	1.0
	5	2.16±0.01	404±11	126±13	913	2.26	121.5	3.6
	10	7.30±0.5	1260±25	39±5	1751	1.39	157.5	12.2
	15	9.00±0.35	1273±20	33±4	1693	1.33	214.2	15.0
AR805-1	1	0.61±0.01	76±2	1282±25	990	13.0	150.0	1.0
	5	2.36±0.15	414±20	71±3	824	2.0	92.0	3.9
	10	7.10±0.35	1172±35	36±10	1418	1.21	154.1	11.6
	15	8.40±0.24	1175±45	32±7	1492	1.27	212.6	13.8
AR805-2	1	0.65±0.02	72±2	1108±40	870	12.1	131.5	1.0
	5	1.93±0.12	376±15	100±12	752	2.0	107.6	3.0
	10	6.16±0.65	936±10	33±11	1245	1.33	150.7	9.5
	15	7.51±0.30	1175±40	31±3	1539	1.31	211.0	11.6

^acalculated according to Equation (4)

^bcalculated as the ratio of the modulus of drawn fiber and the modulus of as-spun fiber.

terms of the aggregate formation and incomplete filler dispersion as confirmed by TEM analysis (Figure 1).

Stress at break is plotted against DR in Figure 6 showing that drawn PP-FS fibers with low filler contents have higher strength than neat PP. If $DR = 10$ is taken for comparison, stress at break reached 1117 MPa for AR805-0.25 and 1260 MPa for AR805-0.5, with respect to 944 MPa for neat PP. It can be noticed that for the compositions up to 0.5 vol% of FS, stress at break was higher over the entire interval of DR in comparison to neat PP, while for the compositions with nanofiller fraction higher

than 1 vol% the obtained values were slightly lower. These findings are in conformity with available literature data. In the case of low nanofiller content, some authors attributed the enhancement of tensile properties to a better orientation of both silicate layers and polymer chains during the fiber spinning [20, 25]. Some other researchers [8, 13, 18] confirmed that better mechanical properties of PP fibers could be obtained with low nanofiller contents such as 0.25–0.5 vol%, whereas at higher filler concentrations (>1 vol%), the aggregation of the silica particles may deteriorate the fiber mechanical properties.

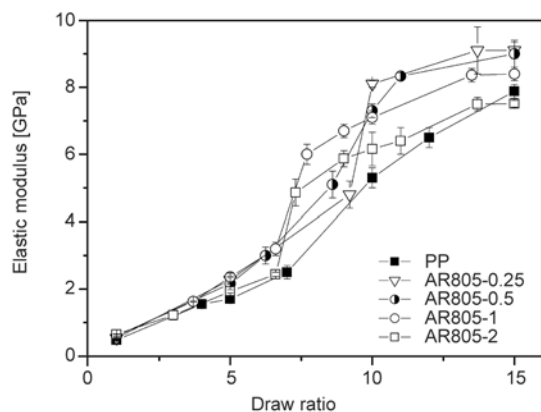


Figure 5. Elastic modulus of neat and nanocomposite PP fibers with different fractions of fumed silica as a function of draw ratio (*DR*)

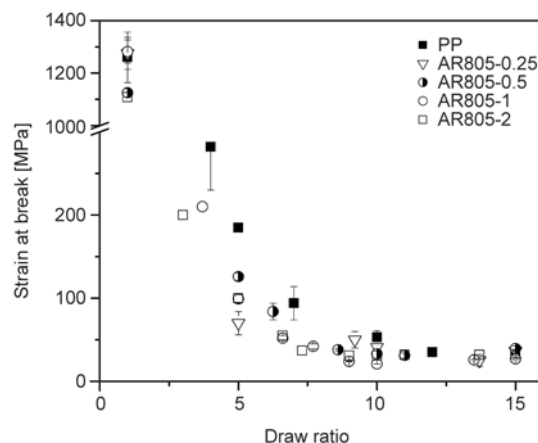


Figure 7. Strain at break of neat and nanocomposite PP fibers with different fractions of fumed silica as a function of draw ratio (*DR*)

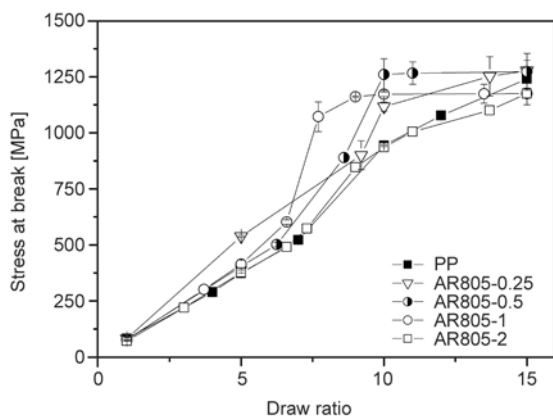


Figure 6. Stress at break of neat and nanocomposite PP fibers with different fractions of fumed silica as a function of draw ratio (*DR*)

Figure 7 confirms previous observations that the higher the draw ratio the lower the strain at break. In the case of the as-spun nanocomposite fibers, strain at break was slightly higher for the compositions with 0.25 and 1 vol% of the filler, when compared with that of neat PP (Table 3 and Figure 7). In general, the presence of the nanofiller does not markedly affect the strain at break of the prepared fibers. For example, both PP and AR805-1 fibers show similar strains at break of about 1270% and 33% for *DR* = 1 and *DR* = 15, respectively. We can conclude that the simultaneous increases in modulus and stress at break are not accompanied by significant changes of the strain at break. This kind of mechanical behavior is in agreement with previous reports on nanosilica composites where better mechanical properties were achieved through good dispersion of silica nanoparticles [9, 26, 27]. The observed toughening effect in the PP-FS fibers is

very particular and promising, because the stiffening effect in nanocomposites is commonly accompanied by the reduction of the tensile strain at break. In order to obtain more information on spinnability and drawability, the mechanical draw ratio (λ_{MEC}), the true strength (σ_{MAX}), the processing draw ratio (λ_{PRO}) and the total draw ratio (λ_{TOT}) of selected fibers were reported in Table 3. As previously defined by Dabrowska *et al.* [28], the mechanical draw ratio (λ_{MEC}), is calculated by Equation (3):

$$\lambda_{MEC} = 1 - \frac{\varepsilon_b}{100} \quad (3)$$

where ε_b is the strain at break expressed in percentage. The true strength (σ_{MAX}) is defined as the stress at break (σ_b) multiplied by the mechanical draw ratio Equation (4):

$$\sigma_{MAX} = \sigma_b \cdot \lambda_{MEC} \quad (4)$$

The processing draw ratio (λ_{PRO}) is calculated as the ratio between the sections of the die S_d and the section of the fibers S_f according to Equation (5):

$$\lambda_{PRO} = \frac{S_d}{S_f} \quad (5)$$

Total draw ratio (λ_{TOT}) can be calculated from Equation (6) [29]:

$$\lambda_{TOT} = \lambda_{PRO} \cdot \lambda_{MEC} \quad (6)$$

For the as-spun fibers, only the composite with 0.25 vol% of fumed silica exhibits values of true strength and total draw ratio almost equivalent to those of neat PP (see Table 3). For example, the true strength of the PP-fumed silica as-spun fibers is

located between $\sigma_{\text{MAX}} = 870\text{--}1127$ MPa and their total draw ratio between $\lambda_{\text{TOT}} = 131\text{--}150$, whereas the corresponding values for the neat as-spun PP fibers are 1123 MPa and 148, respectively. In the case of drawn fibers, for the compositions with 0.25–0.5 vol%. true strength and mechanical draw ratio are higher in comparison to those of neat PP fibers. Also, the total draw ratio indicates that fiber reinforced by a low amount of fumed nanosilica could be spun and drawn to the same levels as PP fiber, thus confirming the good processability of fumed silica nanocomposites.

In Table 3 the draw-stiffening factor, calculated as the ratio of the modulus of drawn fiber and the modulus of as spun fiber, is reported. This parameter can be useful for quantitative evaluation of the properties and drawability of composite fibers. Higher draw-stiffening factor of the nanocomposite PP fiber containing 0.25–0.5 vol% of fumed silica with respect to the neat PP fiber for DR up to 10 is quite evident, while slightly lower values for the composites with 2 vol% of silica are obtained.

The maximum attainable mechanical properties P_{∞} (either modulus or stress at break) can be predicted by using the following equation for fitting all experimental data plotted against $1/DR$ according to Equation (7):

$$P = P_{\infty} - k_p \left(\frac{1}{DR} \right) \quad (7)$$

where k_p is a constant taking into account the sensitivity of the property to the drawing [30]. Following this equation, the maximum attainable elastic moduli for all our nanocomposite fibers (from 10.5 GPa for AR805-1 up to 12.7 GPa for AR805-0.5) would be higher than that of neat PP, 9.6 GPa, as reported in Table 4. Similar tendency can also be observed for the maximum attainable stress at break, that is 1.59 GPa for AR805-1 and 1.63 GPa for AR805-

0.25, with respect to 1.49 GPa of neat PP. On the other hand, the composition with 2 vol% of FS shows the lowest extrapolated values.

3.4. Dynamical mechanical analysis

DMTA analysis was performed on the fibers with selected draw ratios to obtain deeper information on mechanical properties and molecular mobility. Due to a very high surface area of the nanoparticles in the PP-AR805 nanocomposites, the applied sinusoidal stress is expected to be easily transferred from the matrix onto the silica particles. Storage modulus (E') and loss modulus (E'') of the PP and PP-FS fibers in range $-125/100^{\circ}\text{C}$ are reported in Figure 8a–8c for as-spun and drawn fibers. For $DR = 1$ a marked rise in the storage moduli with the nanofiller content can be observed reaching the highest values for AR805-2 in the interval -100°C up to -30°C (Figure 8a). On the other hand, at temperatures higher than 0°C , all the composites exhibit almost the same values of storage modulus. With the drawing process, the storage modulus increases over the whole temperature range used, which can be attributed to the chain orientation induced by drawing. For drawn fibers the highest improvement was observed for the compositions with 1 vol% at $DR = 10$ (Figure 8b), and for 0.5 vol% of FS at $DR = 15$ (Figure 8c). Decreasing storage modulus of the composites with higher nanofiller fractions could be attributed to the formation of nanofiller aggregates (as observed by TEM analysis), which reduces the filler effectivity. Similarly to the storage modulus (E'), loss modulus (E'') of PP-AR805 composite fibers rises with the draw ratio and FS content (Figures 8a–8c). PP displays three relaxations (transitions, loss peaks) localized in the range of about -80°C (γ), 10°C (β) and 100°C (α), where β is the dominant relaxation. In the crystalline polymers the α transition is commonly considered to be associated with the molecular motion within the crystalline regions, the β transition corresponds to the glass transition of the amorphous regions, and the γ transition is believed to be related to limited molecular motions of short chain sections in both amorphous regions and crystalline domains [31, 32].

As already mentioned, the intensity of the β relaxation depends on various factors, such as crystalline fraction, orientation of the amorphous phase, and nanofiller fraction. For all as-spun fibers only one β relaxation peak at around 5°C can be observed (Fig-

Table 4. Maximum attainable values of elastic modulus (E_{∞}) and stress at break (σ_{∞}) of neat and nanofilled PP nanocomposite fibers, as predicted by Equation (7)

Drawn fiber	E_{∞} [GPa]	σ_{∞} [GPa]
PP	9.6±0.7	1.49±0.10
AR805-0.25	12.5±1.4	1.63±0.08
AR805-0.5	12.7±1.0	1.88±0.16
AR805-1	10.5±0.2	1.59±0.12
AR805-2	8.6±0.3	1.27±0.11

ure 8a), whose position does not significantly change with varying nanoparticle content (from 6.2°C for as-spun PP down to 0.5°C for AR805-0.5). After drawing process, T_β shifts to lower temperatures, from 6.2°C for neat PP to –26.7°C for

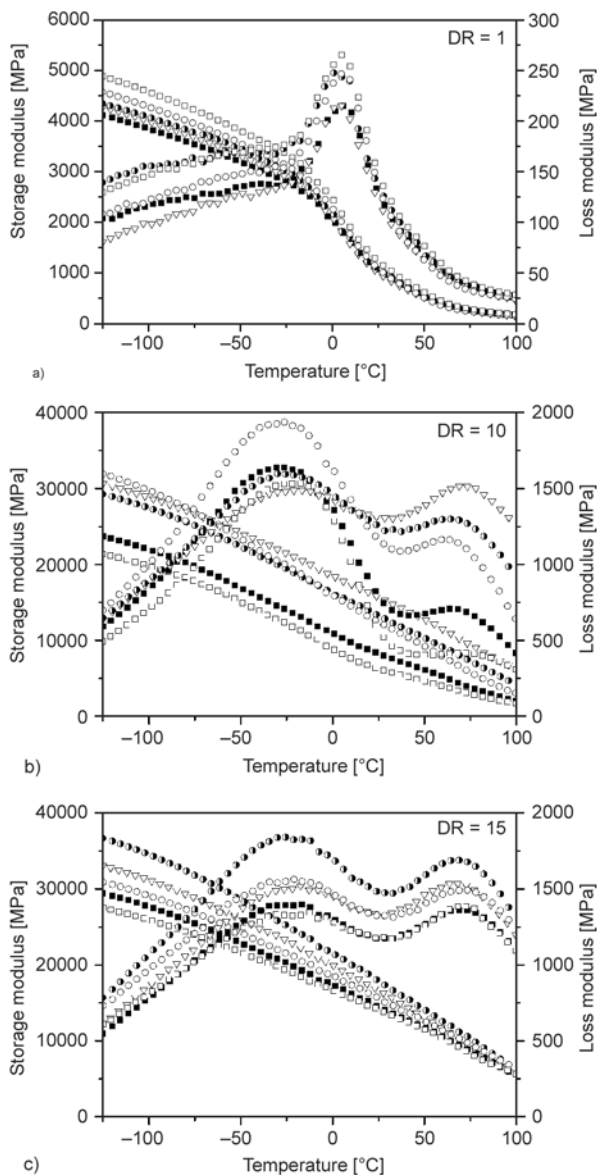


Figure 8. Storage modulus and loss modulus of neat PP (■) and nanocomposite PP fibers with different fractions of fumed silica (∇ – 0.25%, ● – 0.5%, ○ – 1% and □ – 2%) at selected draw ratios a) $DR = 1$, b) $DR = 10$ and c) $DR = 15$

Table 5. Temperature of the β (T_β), and α (T_α) loss peaks of the nanocomposite fibers with different fumed silica fraction and DR (heating rate: 3°C/min; frequency: 1 Hz)

Material	T_β [°C] / E'' peak [MPa]			T_α [°C] / E'' peak [MPa]		
	DR = 1	DR = 10	DR = 15	DR = 1	DR = 10	DR = 15
PP	6.2 / 215	–26.7 / 1637	–23.4 / 1393	–	68.6 / 703	71.4 / 1356
AR805-0.25	4.9 / 216	–20.7 / 1486	–21.6 / 1503	–	71.1 / 1516	68.3 / 1533
AR805-0.5	0.5 / 248	–27.7 / 1600	–25.5 / 1837	–	64.5 / 1300	68.6 / 1690
AR805-1	4.9 / 247	–26.3 / 1940	–23.3 / 1560	–	61.7 / 1163	71.1 / 1490
AR805-2	4.9 / 265	–21.9 / 1530	–22.0 / 1349	–	68.6 / 423	70.5 / 1390

$DR = 10$ and $\leq 23.4^\circ\text{C}$ for $DR = 15$. On the other hand, the nanofiller fraction slightly increases T_β , e.g. from $\leq 26.7^\circ\text{C}$ for neat PP up to -21°C for AR805-0.25 for $DR = 10$ and from -23.4 up to -21.6°C in case of composite AR805-0.25 with $DR = 15$ (Table 5). It is commonly observed that after the nanofiller addition T_β rises due to the adsorption of polymer chain on the surface of nanoparticles [33]. This effect is more pronounced after the drawing process which leads to more uniform distribution of the filler particles in the matrix. However, it is quite unusual the T_β values decrease due to the drawing process. The effect was observed for drawn fibers ($DR \geq 10$) and it can be attributed to the longitudinal defects developed during drawing that have been associated to a reduced density (and hence higher molecular mobility and lower T_β), in accordance to literature results. In fact, the higher the drawing, the longer the extension of the band defects, almost along all the fiber length [34, 35] at very high draw ratio.

As far as the α loss modulus peak is concerned, it can be seen that this relaxation is not observed for the as-spun fibers, while for drawn materials a peak occurs at 69°C . The magnitude of the α loss modulus peak (Table 5) increases proportionally to the draw ratio and/or filler fraction; the highest intensities were found for the compositions with 0.5vol% of FS. This enhancement observed after drawing is probably related to the increase in the fraction of crystalline phase induced by the drawing process, as confirmed by DSC analysis (Figure 3). This α relaxation shifts to higher temperatures with increasing nanoparticle content and/or draw ratio. Owing to the drawing process, the peak is shifted from 68°C for neat PP at $DR = 10$ to 71°C for $DR = 15$ (Table 5). It is believed that higher crystalline continuity and/or dimensions achieved at high draw ratios hinder the underlying molecular motion so that the onset of the transition is shifted towards higher temperatures [2, 36].

3.5. Creep test

The creep tests were carried out in order to determine the deformation behavior of the materials under a constant load. In this experiment, a constant stress equal to 3 MPa for 3600 s was applied to a fiber sample and the strain was monitored as a function of time. In Figures 9a–9c the creep compliance curves of the neat PP and nanofilled composites fibers at different draw ratio are reported. For as-spun fibers, the creep compliance of the nanocomposite fibers was higher than that of the neat PP. Interesting improvement of the creep resistance due to nanofiller intro-

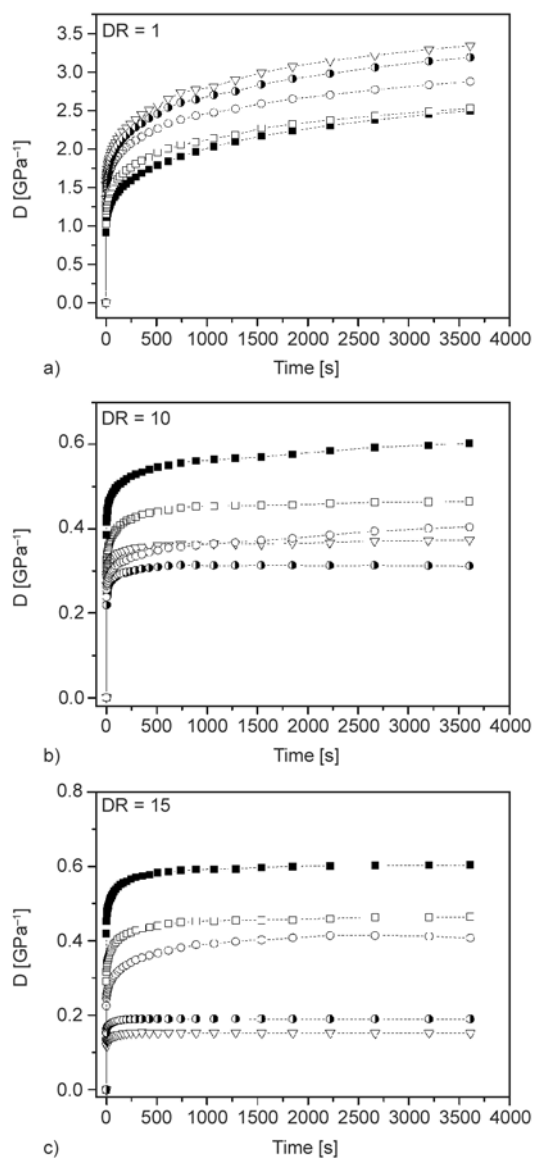


Figure 9. Tensile compliance of neat PP (■) and nanocomposite PP fibers with different fractions of fumed silica (∇ – 0.25%, \bullet – 0.5%, \circ – 1% and \square – 2%) as a function of time at selected draw ratios a) $DR = 1$, b) $DR = 10$ and c) $DR = 15$

duction was observed after the drawing process. For all drawn fibers ($DR = 10$ and 15), a lower creep compliance was obtained as shown in Figure 9b and 9c, respectively. However, at a higher draw ratio ($DR = 15$), the reduction of creep compliance was less significant for the composites with 1 and 2 vol% of nanofiller than that observed for the composites with 0.25 and 0.5 vol% of FS. The creep compliance of fibers drawn 15 times was found to decrease in the following order: PP > 805-2, 805-1 > 805-0.5, 805-0.25. Lower creep resistance of the composites with high nanofiller fractions could tentatively be related to the reduced thickness of the interphase and to poorer adhesion caused by defects formation (for instance voids) and possible debonding. According to the interpretation of Siengchin and Karger-Kocsis [37], a well-dispersed reinforcement with good bonding to the matrix (i.e. well-developed interphase and reduced formation of voids) may improve the creep resistance of nanocomposites. We can conclude that the creep behavior of nanocomposite fibres is mainly governed by the filler distribution and adhesion, which can be improved in the course of the drawing process.

3.6. Model of lamellae failure during drawing

According to the model proposed by Chen *et al.* [38], the improvement of PP fracture toughness observed in fracture tests, both at low (static) and at high strain (dynamic), was interpreted according to mechanisms of polymer chains and crystalline modification in the damage zone, such as via lamellae transformation, break-up of lamellae, and defolding with voids formation.

On the basis of the analysis of thermo-mechanical properties and TEM photographs described in previous paragraphs, a model of the lamella reorganization during the fiber drawing process is proposed. Figure 10 shows a sketch where lamellae are held together by tie molecules and start to separate from one another upon initial drawing that occurs already during extrusion. The lamellae involved in this network deform and break-up by tilting and slippages and their separation is accompanied by microvoid formation. This plastic deformation via break-up and defolding of the lamellae triggers the polymorphic transformation which occurs in the course of recrystallization process. Moreover, this structure rebuilding is also associated with volume contraction (see the contribution of crystallinity in Table 2); since

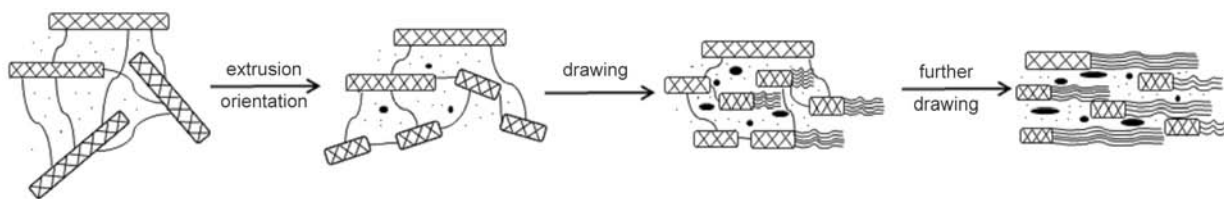


Figure 10. Scheme of the failure mode of the lamellae occurring during drawing process

the sample volume does not relax during the drawing process, the transition should amplify formation of microvoids. In the course of further drawing, the process of lamellae delamination and failure with the progressive chain orientation, and the voids formation becomes more intensive. In this latter critical step, the presence of some uniformly distributed nanoparticles, as in the case of 0.25–0.5 vol% FS, could promote a more regular voids formation and growth. The changes that occurred during the drawing process account – in term of this model – for enhancement of the mechanical properties of nanocomposite fibers, e.g. storage modulus, tensile strength, and creep resistance.

Better results obtained for the composites with low nanofiller content (0.25–0.5 vol%) can primarily attributes to good nanofiller dispersion/distribution, and to the orientation of the filler nanoparticles during drawing and creeping test, where fumed silica seems also to play the role of regulating agent in voids formation.

4. Conclusions

PP-fumed silica Aerosil®R805 fibers were produced by a combined melt-extrusion and hot-drawing process (up to the draw ratio 15). The incorporation of fumed silica into the PP matrix leads to improvement of a wide range of mechanical properties, which is more effective at low filler fractions. Higher crystallinity content and crystallization temperature in the cooling step of as-spun composite fibers can be ascribed to nucleating role of dispersed fumed nanosilica. After drawing, fibers exhibited a significant increase in both melting temperature and crystallinity content.

DMTA evidenced the stiffening effect of silica which is magnified by drawing composite fibers to high draw ratios. Similarly enough, creep tests demonstrated a significant reduction of the creep compliance of all drawn fibers. The improvements in mechanical properties observed in nanocompos-

ite fibers can mainly be attributed to a good dispersion of silica particles (observed by TEM) and to sufficient interfacial adhesion between matrix and filler. However, TEM micrographs revealed that the amount of nanoparticle agglomerates was proportional to the filler fraction in composites, but decreased with the fiber draw ratio.

The addition of low amounts of fumed silica (0.25–1 vol%) was found optimal to improve the tensile mechanical properties. Tested samples exhibited a marked increase in elastic modulus and stress at break, whereas no significant variations of strain at break were observed. For example, PP fiber with 0.5 vol% of nanosilica showed – in comparison to the neat PP – higher values of the maximum attainable modulus (about 12.7 GPa vs 9.6 GPa) and of the maximum attainable stress at break (1.88 GPa vs 1.49 GPa).

A failure model was proposed to interpret experimental data in terms of polymer chain orientation, re-crystallization of the amorphous regions, and void formation in the presence of fumed silica nanoparticles (up to 0.5–1 vol%), which are believed to have beneficial effects on mechanical properties of the prepared composites.

Acknowledgements

The authors thank to Evonik (Essen, Germany) for donating the fumed silica Aerosil®R805 used in this study. The authors are very indebted to Professor József Karger-Kocsis (Budapest University of Technology and Economics, Budapest) for his valuable comments. Electron microscopy at the Institute of Macromolecular Chemistry was supported through grant GACR P108/14-17921S.

References

- [1] Harutun G. K.: Handbook of polypropylene and polypropylene composites. Marcel Dekker, New York (1999).
- [2] Toshio K.: High-modulus and high-strength polypropylene fibers and films. in 'Polypropylene an a-z reference' (ed.: Karger-Kocsis J.) Kluwer Academic Publishers, Dordrecht, 295–300 (1999).

- [3] Wishman M., Hagler G. E.: Polypropylene fibers. in 'Handbook of fiber science and technology fiber chemistry' (eds.: Lewin P., Pearce E. M.) Marcel Dekker, New York, 371–497 (1985).
- [4] Kearns J. C., Shambaugh R. L.: Polypropylene fibers reinforced with carbon nanotubes. *Journal of Applied Polymer Science*, **86**, 2079–2084 (2002).
DOI: [10.1002/app.11160](https://doi.org/10.1002/app.11160)
- [5] Kumar S., Doshi H., Srinivasarao M., Park J. O., Schiraldi D. A.: Fibers from polypropylene/nano carbon fiber composites. *Polymer*, **43**, 1701–1703 (2002).
DOI: [10.1016/S0032-3861\(01\)00744-3](https://doi.org/10.1016/S0032-3861(01)00744-3)
- [6] López Manchado M. A., Valentini L., Biagiotti J., Kenny J. M.: Thermal and mechanical properties of single-walled carbon nanotubes–polypropylene composites prepared by melt processing. *Carbon*, **43**, 1499–1505 (2005).
DOI: [10.1016/j.carbon.2005.01.031](https://doi.org/10.1016/j.carbon.2005.01.031)
- [7] Rangasamy L., Shim E., Pourdeyhimi B.: Structure and tensile properties of nanoclay–polypropylene fibers produced by melt spinning. *Journal of Applied Polymer Science*, **121**, 410–419 (2011).
DOI: [10.1002/app.33619](https://doi.org/10.1002/app.33619)
- [8] Joshi M., Shaw A., Butola B. S.: Studies on composite filaments from nanoclay reinforced polypropylene. *Fibers and Polymers*, **5**, 59–67 (2004).
DOI: [10.1007/BF02875496](https://doi.org/10.1007/BF02875496)
- [9] D'Amato M., Dorigato A., Fambri L., Pegoretti A.: High performance polyethylene nanocomposite fibers. *Express Polymer Letters*, **6**, 954–964 (2012).
DOI: [10.3144/expresspolymlett.2012.101](https://doi.org/10.3144/expresspolymlett.2012.101)
- [10] Zhang Y., Yu J., Zhou C., Chen L., Hu Z.: Preparation, morphology, and adhesive and mechanical properties of ultrahigh-molecular-weight polyethylene/SiO₂ nanocomposite fibers. *Polymer Composites*, **31**, 684–690 (2010).
DOI: [10.1002/pc.20847](https://doi.org/10.1002/pc.20847)
- [11] Wu C. L., Zhang M. Q., Rong M. Z., Friedrich K.: Tensile performance improvement of low nanoparticles filled-polypropylene composites. *Composites Science and Technology*, **62**, 1327–1340 (2002).
DOI: [10.1016/S0266-3538\(02\)00079-9](https://doi.org/10.1016/S0266-3538(02)00079-9)
- [12] Rottstegge J., Qiao Y. K., Zhang X., Zhou Y., Xu D., Han C. C., Wang D.: Polymer nanocomposite powders and melt spun fibers filled with silica nanoparticles. *Journal of Applied Polymer Science*, **103**, 218–227 (2007).
DOI: [10.1002/app.25162](https://doi.org/10.1002/app.25162)
- [13] Srisawat N., Nithitanakul M., Srikulkit K.: Spinning of fibers from polypropylene/silica composite resins. *Journal of Composite Materials*, **46**, 99–110 (2011).
DOI: [10.1177/0021998311410477](https://doi.org/10.1177/0021998311410477)
- [14] Srisawat N., Nithitanakul M., Srikulkit K.: Characterizations of fibers produced from polypropylene/silica composite. *Journal of Materials and Minerals*, **19**, 53–58 (2009).
- [15] Ikeda Y., Kohjiya S.: *In situ* formed silica particles in rubber vulcanizate by the sol-gel method. *Polymer*, **38**, 4417–4423 (1997).
DOI: [10.1016/S0032-3861\(96\)01037-3](https://doi.org/10.1016/S0032-3861(96)01037-3)
- [16] Barthel H., Rösch L., Weis J.: Fumed silica – Production, properties, and applications. in 'Organosilicon Chemistry Set: From Molecules to Materials' (eds.: Auner N., Weis J.) Wiley, Weinheim, 761–778 (1996).
DOI: [10.1002/9783527620777.ch91a](https://doi.org/10.1002/9783527620777.ch91a)
- [17] Dorigato A., Sebastiani M., Pegoretti A., Fambri L.: Effect of silica nanoparticles on the mechanical performances of poly(lactic acid). *Journal of Polymers and the Environment*, **20**, 713–725 (2012).
DOI: [10.1007/s10924-012-0425-6](https://doi.org/10.1007/s10924-012-0425-6)
- [18] Joshi M., Viswanathan V.: High-performance filaments from compatibilized polypropylene/clay nanocomposites. *Journal of Applied Polymer Science*, **102**, 2164–2174 (2006).
DOI: [10.1002/app.24179](https://doi.org/10.1002/app.24179)
- [19] Van Krevelen D. W.: *Properties of polymers*. Elsevier, Amsterdam (1990).
- [20] Zhang M. Q., Rong M. Z., Ruan W. H.: Nanoparticles/polymer composites: Fabrication and mechanical properties. in 'Nano- and micro-mechanics of polymer blends and composites' (eds.: Karger-Kocsis J., Fakirov S.) Hanser, Munich, 91–140 (2009).
- [21] Chiu C-W., Lin C-A., Hong P-D.: Melt-spinning and thermal stability behavior of TiO₂ nanoparticle/polypropylene nanocomposite fibers. *Journal of Polymer Research*, **18**, 367–372 (2011).
DOI: [10.1007/s10965-010-9426-0](https://doi.org/10.1007/s10965-010-9426-0)
- [22] Lorenzi D., Sartori G., Ferrara G., Fambri L.: Spinnability of nanofilled polypropylene. *Macromolecular Symposia*, **301**, 73–81 (2011).
DOI: [10.1002/masy.201150310](https://doi.org/10.1002/masy.201150310)
- [23] Capaccio G., Crompton T. A., Ward I. M.: Ultra-high modulus polyethylene by high temperature drawing. *Polymer*, **17**, 644–645 (1976).
DOI: [10.1016/0032-3861\(76\)90288-3](https://doi.org/10.1016/0032-3861(76)90288-3)
- [24] Fambri L., Dabrowska I., Pegoretti A., Ceccato R.: Melt spinning and drawing of polyethylene nanocomposite fibers with organically modified hydrotalcite. *Journal of Applied Polymer Science*, **131**, 40277/1–40277/13 (2014).
DOI: [10.1002/app.40277](https://doi.org/10.1002/app.40277)
- [25] Lee S. H., Youn J. R.: Properties of polypropylene/layered-silicate nanocomposites and melt-spun fibers. *Journal of Applied Polymer Science*, **109**, 1221–1231 (2008).
DOI: [10.1002/app.28222](https://doi.org/10.1002/app.28222)
- [26] Kontou E., Niaounakis M.: Thermo-mechanical properties of LLDPE/SiO₂ nanocomposites. *Polymer*, **47**, 1267–1280 (2006).
DOI: [10.1016/j.polymer.2005.12.039](https://doi.org/10.1016/j.polymer.2005.12.039)

- [27] Dorigato A., D’Amato M., Pegoretti A.: Thermo-mechanical properties of high density polyethylene – fumed silica nanocomposites: Effect of filler surface area and treatment. *Journal of Polymer Research*, **19**, 9889/1–9889/11 (2012).
DOI: [10.1007/s10965-012-9889-2](https://doi.org/10.1007/s10965-012-9889-2)
- [28] Dabrowska I., Fambri L., Pegoretti A., Ferrara G.: Organically modified hydrotalcite for compounding and spinning of polyethylene nanocomposites. *Express Polymer Letters*, **7**, 936–949 (2013).
DOI: [10.3144/expresspolymlett.2013.91](https://doi.org/10.3144/expresspolymlett.2013.91)
- [29] Tomka J. G.: Textile fibres. in ‘Comprehensive polymer science and supplements’ (ed.: Allen G., Bevington J. C.) Pergamon, Amsterdam, Vol. 2, 487–510 (1989).
DOI: [10.1016/B978-0-08-096701-1.00051-3](https://doi.org/10.1016/B978-0-08-096701-1.00051-3)
- [30] Fambri L., Bragagna S., Migliaresi C.: Biodegradable fibers of poly-L, DL-lactide 70/30 produced by melt spinning. *Macromolecular Symposia*, **234**, 20–25 (2006).
DOI: [10.1002/masy.200650204](https://doi.org/10.1002/masy.200650204)
- [31] Matsuoka S.: Relaxation phenomena in polymers. Hanser, Munich (1992).
- [32] Boyd R. H.: Relaxation processes in crystalline polymers: Molecular interpretation – A review. *Polymer*, **26**, 1123–1133 (1985).
DOI: [10.1016/0032-3861\(85\)90240-X](https://doi.org/10.1016/0032-3861(85)90240-X)
- [33] Vladimirov V., Betchev C., Vassiliou A., Papageorgiou G., Bikiaris D.: Dynamic mechanical and morphological studies of isotactic polypropylene/fumed silica nanocomposites with enhanced gas barrier properties. *Composites Science and Technology*, **66**, 2935–2944 (2006).
DOI: [10.1016/j.compscitech.2006.02.010](https://doi.org/10.1016/j.compscitech.2006.02.010)
- [34] Abo El Maaty M. I., Bassett D. C., Olley R. H., Dobb M. G., Tomka J. G., Wang I-C.: On the formation of defects in drawn polypropylene fibres. *Polymer*, **37**, 213–218 (1996).
DOI: [10.1016/0032-3861\(96\)81090-1](https://doi.org/10.1016/0032-3861(96)81090-1)
- [35] Amornsakchai T., Olley R. H., Bassett D. C., Al-Hussein M. O. M., Unwin A. P., Ward I. M.: On the influence of initial morphology on the internal structure of highly drawn polyethylene. *Polymer*, **41**, 8291–8298 (2000).
DOI: [10.1016/S0032-3861\(00\)00144-0](https://doi.org/10.1016/S0032-3861(00)00144-0)
- [36] Alcock B., Cabrera N. O., Barkoula N-M., Reynolds C. T., Govaert L. E., Peijs T.: The effect of temperature and strain rate on the mechanical properties of highly oriented polypropylene tapes and all-polypropylene composites. *Composites Science and Technology*, **67**, 2061–2070 (2007).
DOI: [10.1016/j.compscitech.2006.11.012](https://doi.org/10.1016/j.compscitech.2006.11.012)
- [37] Siengchin S., Karger-Kocsis J.: Creep behavior of polystyrene/fluorohectorite micro- and nanocomposites. *Macromolecular Rapid Communications*, **27**, 2090–2094 (2006).
DOI: [10.1002/marc.200600539](https://doi.org/10.1002/marc.200600539)
- [38] Chen H. B., Karger-Kocsis J., Wu J. S., Varga J.: Fracture toughness of α - and β -phase polypropylene homopolymers and random- and block-copolymers. *Polymer*, **43**, 6505–6514 (2002).
DOI: [10.1016/S0032-3861\(02\)00590-6](https://doi.org/10.1016/S0032-3861(02)00590-6)

A statistical mechanical approach to the Payne effect in filled rubbers

G. Heinrich^{1*}, T. A. Vilgis²

¹Leibniz-Institut für Polymerforschung Dresden e.V., Hohe Str. 6, 01069 Dresden, Germany

²Max-Planck-Institut für Polymerforschung Mainz, Postfach 3148, 55021 Mainz, Germany

Received 1 October 2014; accepted in revised form 30 November 2014

Abstract. In this paper we apply and discuss some new aspects to the steric interaction of filler particles in reinforced elastomers under dynamic mechanical loading conditions. At certain concentration the filler particles (for example, carbon black, or silica) form loose clusters which themselves interact with each other and form a filler network with a significant contribution to the dynamic modulus of the rubber material. The filler concentration is relatively high, so that it is likely that the clusters undergo a ‘jamming transition’. With increasing strain amplitude under periodic mechanical deformation the disruption of the filler network resp. of finite filler cluster configurations leads to dejamming observed as softening of the rubber. As a theoretical approach we map the problem on a simple one dimensional Ising model. We present here a static model of this jamming (dejamming) and discuss the consequences on the mechanical and deformation properties of the filled rubber.

Keywords: rubber, mechanical properties, Payne effect, statistical mechanics

1. Introduction

Despite the technological significance of the Payne effect in rubber applications [1], this strain-induced softening phenomenon is often regarded as a special area of physics specific to filled elastomers [2]. Practically, the effect is measured as decreasing storage modulus with increasing strain amplitude at fixed temperature and fixed frequency during dynamic-mechanical testing of filled rubbers. Parallel, the corresponding loss modulus runs through a maximum value with increasing strain amplitude. Basic characteristics of the relationships between dynamic modulus and strain amplitude are similar for all kinds of investigated rubbers filled with conventional fillers like carbon black and silica (see, for example, reference [2]), or even for non-conventional rubber nanocomposites which were prepared, for example, via clay–NR latex dispersion and subsequent vulcanization [3, 4].

It is essential to note that dynamic strain-induced decrease of the stiffness of filled rubbers shows a striking similarity to what is known phenomenologically about the glass transition of solid materials and the jamming transition of granular materials [5, 6]. This analogy stems from the reality that shear strain in dynamic mechanical measurements introduces fluctuations in a filler network by forcing the system to explore different configurations. Such fluctuations can be described by an ‘effective temperature’ that has many attributes of a true temperature, and particularly is proportional to the strain amplitude [7, 8]. Thus, filled rubbers with respect to strain will display many unusual phenomena that are usually observed in glass-forming materials, but now demonstrated in filled rubbers, including asymmetric kinetics, crossover effects, and glasslike kinetic transitions [2, 5–7]. Indeed, the increase of the particle concentration may lead to jamming and

*Corresponding author, e-mail: gheinrich@ipfdd.de

a dramatically increase of the viscosity and cease of the diffusion in solutions, whenever the particles are anisotropic, so that only cooperative motion is possible.

Throughout the literature, there are two other processes that are known to show the same asymmetric behaviour as their thermodynamic properties approach equilibrium. One is the structural relaxation process in glassy materials, most notably the relaxation and recovery of enthalpy and volume [9–11]. In this case, the specific volume of a glass after abruptly cooling to a temperature T is known to approach equilibrium faster than a glass heated to the same temperature [9, 10]. The reason is that the cooled sample arrives at the temperature T with a larger free volume than the heated glass. Another situation with asymmetric relaxation behaviour is the density fluctuation in a vibrated granular material [12–17]. In this case, the granular material is in its jamming state. Once a void large enough to contain a grain is created, it will be quickly filled by a new particle. The rate of density settling from above or below equilibrium [12] depends on the rate of void creation and the initial density of the material. Nevertheless, in both cases, the free volume plays a crucial role in determining the rate of approaching equilibrium. Obviously, these two cases share a common ground of physics [15–17], when the rubber-like matrix is viewed as a (constant) elastic background, assigned to a modulus G_0 .

The existence of remarkable similarity between dynamic strain-induced nonlinearity in the modulus of filled rubbers and the physics of the glass transition of glass-forming materials and the jamming transition of vibrated granular materials has important implications with regard to our understanding of the strain amplitude dependency of the dynamic modulus of filled rubbers. The similarity stems from the fact that filler particles in the rubber matrix agglomerate and tend to form filler networks. The agglomeration and network formation of filler in elastomeric matrix are typically jamming processes that are analogous to glass formation. It is now reasonable that different routes, through strain, volume fraction, and temperature changes, can effectively lead filled rubbers to the same jammed state. A large unified physical picture in describing the dynamics in the frustrated systems would be a jamming phase diagram that is able to address the glass and jamming transitions [7, 8]. Based on the exper-

imental observations, a unified diagram was proposed as schematically shown in Figure 1 [7, 8]. The phase diagram for iso-viscosity lies in the vertical $(1/\Phi) - kT$ plane where Φ denotes the filler volume fraction. The line that separates the jammed solids and unjammed liquids (if the polymer is uncrosslinked) generally represents the glass transition. The classical empirical equation proposed by Doolittle and Doolittle [18] describes approximately the location of this transition. The transition line marks a critical viscosity of the system that in practice is impossible to track in the time scales accessible to experiment. The phase diagram for isoenergetic state lies in the horizontal $(1/\Phi) - \sigma\gamma$ plane where $\sigma\gamma$ describes a mechanical energy per unit volume and is taken from the corresponding amplitudes of stress and deformation. The isoenergetic behavior comes from experimental observation on various particle-filled systems [8]. The effects of the temperature on the jamming transition are illustrated in the $kT - \sigma\gamma$ plane. The magnitude of the energy is a function of the elasticity of the jammed fractal-like structure and the interaction strength between filler particles. The experimental data in [8] show that $\sigma_c\gamma_c$ increases as temperature decreases where the subscript c is attributed to the corresponding values for the transition line which marks a critical mechanical energy needed to dejam the system. Some years ago several authors [15–17] also proposed a phase diagram for jamming. In their phase diagram, however, other axes were selected; i.e., the temperature T , filler volume fraction Φ , and the shear stress σ . The quantities T and Φ are traditional axes for phase diagrams, but σ is not.

The physical origin of selecting σ in the phase diagram was not really clear, though recent mode-coupling theories have attempted to include the shear stress [19]. In the studies of Wang and Robertson

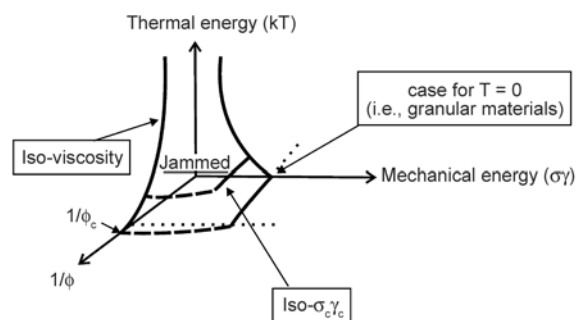


Figure 1. A schematic drawing of the jamming phase diagram in filled rubber [7]

[7, 8] was found experimentally that using $\sigma\gamma$ instead of σ as the critical parameter can significantly simplify the phase diagram (see also [5, 6]). It is also noteworthy that this mechanical energy density $\sigma\gamma$, similar to the thermal energy kT , is theoretically derivable from Hamiltonians, which makes it a natural choice as an axis in constructing phase diagrams.

2. Statistical mechanics of the Payne effect

In the following it will be assumed that filler network-like configurations in rubbers can be treated in the analogue of the ergodicity of thermal systems. Another known analogue is the ergodicity of compact systems like, e.g. powders or flocculated colloids where, in analogue to temperature T in thermal systems, a compactivity X was proposed by Edwards and Oakeshott [20], linked to an effective volume, Y . This effective volume has the role of free energy in thermal systems, which is easier to handle than the density of the powder. Furthermore, a similar analogue of the temperature has been introduced as an angoricity when angular momentum is a relevant variable in conventional thermal systems, leading, in addition to the traditional temperature, to a tensorial temperature as derivation of momentum to entropy [21, 22].

The key fact is that filler network and filler cluster configurations – inside a soft rubber matrix – for a given filler volume fraction can be realized in a strain sweep experiment with a variety of energy densities (= energy per volume unit), or, in other terms, with varying excess shear moduli G , depending on the magnitude of deformation amplitude during dynamic-mechanical excitations $\gamma(t) = \gamma_0 \sin(\omega t)$. In the following we only discuss the shear modulus (G^*) and its excess real part (storage modulus) denoted as G , however the discussion is similar for the dynamic tensile modulus E^* . We note that the total modulus contains additionally to this excess part a contribution from the rubber matrix (G_0) and from the pure hydrodynamical reinforcement of the solid filler particles [1, 2]. However, these contributions do not depend on the variable γ_0 during strain sweeps. There are two limiting cases: i) $G = \Delta G'$ for zero deformation $\gamma_0 = 0$ with $\Delta G'$ being the difference between low and high strain amplitude modulus $G'_0 - G'_\infty$ in the usual notation of viscoelasticity of filled rubbers and often termed as Payne amplitude;

ii) $G = 0$ for infinite deformation $\gamma_0 \rightarrow \infty$ where the filler network is completely destroyed and decomposed. Making the assumption that the filler network energy density (excess modulus G) is sufficient to characterize the filler network completely, one may formulate an analogy with normal statistical mechanics. There, the energy has a value E , so that the microcanonical probability (Equation (1)):

$$p = \exp\left(\frac{S}{k}\right) \delta(E - H); \int p d\Gamma = 1 \quad (1)$$

gives the probability that the system is found with E . Here, H is the Hamiltonian, S being the entropy, and k is the Boltzmann constant. In Equation (1), $d\Gamma$ symbolizes phase space integration, and $\delta(x)$ denotes Dirac's δ -functional. Note, the normalization is not necessary if, in the microcanonical ensembles, entropy S is introduced via the microcanonical hyper(phase)space volume Ω , i.e. $S = k \cdot \log \Omega$. One defines the traditional temperature $T = \partial E / \partial S$ and can transfer to the canonical ensemble with (Equation (2)):

$$p = \exp\left(\frac{F - H}{kT}\right) \quad (2)$$

and the Helmholtz free energy (Equations (3), (4)):

$$F = -kT \cdot \log Z = -kT \cdot \log \int e^{-H/kT} d\Gamma \quad (3)$$

where

$$E = F - T \frac{\partial F}{\partial T}, \quad S = -\frac{\partial F}{\partial T} \quad (4)$$

and Z denoting the phase state integral (partition function).

Suppose now for our imposed 'filler network' problem that there is a function W which plays the role of Hamiltonian H in the filler network in that the excess energy density G is the value taken by W for the particular configurations (= connectivity) of the constituents of the filler network. The constituents are usually filler particles (e.g., silica) as smallest entities, or specific aggregates in case of carbon black as industrial filler. Then, guided by [20] for compact powders, we define λ to be a constant which gives entropy the dimension of modulus (Equations (5), (6)):

$$p = \exp\left(-\frac{S}{\lambda}\right) \delta(G - W) \quad (5)$$

$$\exp\left(\frac{S}{\lambda}\right) = \int \delta(G - W) d\Gamma \quad (6)$$

The interesting step is now to go to the canonical ensemble, defining a ‘filler network connectivity’ (FNC), say τ , by Equations (7)–(9):

$$\tau = \frac{\partial G}{\partial S} \quad (7)$$

$$p = \exp\left(\frac{f - W}{\lambda\tau}\right) \quad (8)$$

$$G = f - \tau \frac{\partial f}{\partial \tau} \quad (9)$$

where we define f as the effective modulus. It plays in the presented analogy the role of free energy and, consequently, we may define S as Equation (10):

$$S = - \frac{\partial f}{\partial \tau} \quad (10)$$

In Equations (7)–(10), the FNC τ is a dimensionless quantity like the deformation amplitude γ_0 . Thus, just as it is easier to think of a temperature in a thermal system rather than its energy, we propose a filler network connectivity (FNC), linked to an effective modulus f , which is easier to handle than the macroscopic excess modulus of the filler network. This is very similar to the introduction of the compactivity X in granular systems [20], which is linked to an effective volume, and which is easier to handle than the density of the corresponding powder. This correspondence lights up the physical relationship between jamming physics in compact assemblages of particles and jammed filler networks in rubbers. The effect of FNC τ is most apparent in the coordination distribution it entails. The filler network with maximum number of connected subunits (filler particles), say N , has $\tau = 0$ and just as one cannot be larger than that, τ cannot be negative. The totally broken filler network at large deformation amplitudes $\gamma_0 \rightarrow \infty$ corresponds to $\tau = \infty$, where all configurations are equally probable corresponding to a random distribution of single subunits (filler particles or carbon black aggregates). The problem now is that it appears necessary that a corresponding statistical approach is introduced, which provides a basis for the analogy based on macroscopic quantities of the filled rubber systems.

A typical formula at the simplest level of approximation can be derived from the Ising-like model on

a closed $d = 1$ lattice where each site i has only two possible coordinations σ , say $\uparrow (+1)$ and $\downarrow (-1)$ [23]. The idea to the Ising approach – which is one of the simplest models for our problem – goes back to the above discussed similarity between softening of filled rubbers with increasing strain amplitudes and the jamming transition of granular matter. As a consequence we have defined the filler network connectivity as an analogy to the compactivity in granular systems. In the latter case, the search for the simplest example for a Hamiltonian led to the corresponding function for the problem of a binary mixture of spherical grains, mapped onto the Bragg-Williams problem of a binary alloy, and expressed by the Ising Hamiltonian without external magnetic field term [20, 36]. Assuming N sites and neighbour-neighbour interaction J yields (Equations (11)–(14)):

$$Z = \sum_{\sigma_1=\pm 1} \cdots \sum_{\sigma_N=\pm 1} \exp\left\{-\frac{1}{\lambda\tau} \sum_{i=1}^N (J\sigma_i\sigma_{i+1})\right\} \quad (11)$$

$$Z = \sum_{\sigma_1 \cdots \sigma_N} e^{-\frac{W}{\lambda\tau}} \quad (12)$$

that leads to

$$f = -N\lambda\tau \cdot \log\left(2 \cosh\left(\frac{J}{\lambda\tau}\right)\right) \quad (13)$$

and

$$G = -NJ \cdot \tanh\left(\frac{J}{\lambda\tau}\right) \quad (14)$$

where $\tau = 0$ gives $G = -NJ$, i.e. a filler network configuration consisting of N subunits which correspond to the low amplitude deformation state. Note, for the antiferromagnetic case $J < 0$ we have a positive G that corresponds to the so-called Payne amplitude $\Delta G'$. The other limit, $\tau = \infty$, yields $G = 0$, i.e. a totally broken filler network corresponding to a random distribution of single particles (or single aggregates in case of carbon black) as a result of infinite deformation amplitudes. Of course, this Ising approach assumes an equilibrium character of the filled polymer system, which appears very contradictory when the fabrication process of a filled rubber is considered (this process is known as the mixing and vulcanization process in rubber technology). Nevertheless, having the analogy proposed by Edwards and Oakeshott [20] in mind, it is worthwhile to proceed further. In the case of an original magnetic Ising model the two limiting cases corre-

spond to the two macroscopic states of alignment of all magnetic dipoles and statistically orientation of dipoles, respectively. Although these simple considerations are a gross oversimplification, it provides a flavour of a true description. In the next consequence we discuss the dynamic modulus.

3. The dynamic modulus and its strain dependence

Within the *Cole-Cole* approach to the Payne effect one introduces the reduced complex modulus as function of strain amplitude [24] (Equations (15)–(18)):

$$g^*(\gamma_0) = g'(\gamma_0) + ig''(\gamma_0) \equiv \frac{G^*(\gamma_0) - G'_\infty}{G'_0 - G'_\infty} = \frac{1}{1 + \left(i \frac{\gamma_0}{\gamma_{0c}}\right)^\beta} \quad (15)$$

With

$$g' \equiv \frac{G'(\gamma_0) - G'_\infty}{G'_0 - G'_\infty} = r^{-1} \cos\Phi$$

$$g'' \equiv \frac{G''(\gamma_0)}{G'_0 - G'_\infty} = r^{-1} \sin\Phi \quad (16)$$

where

$$r^2 = 1 + 2 \left(\frac{\gamma_0}{\gamma_{0c}}\right)^\beta \cos\left(\frac{\pi}{2}\beta\right) + \left(\frac{\gamma_0}{\gamma_{0c}}\right)^{2\beta} \quad (17)$$

$$\tan\Phi = \frac{\left(\frac{\gamma_0}{\gamma_{0c}}\right)^\beta \sin\left(\frac{\pi}{2}\beta\right)}{1 + \left(\frac{\gamma_0}{\gamma_{0c}}\right)^\beta \cos\left(\frac{\pi}{2}\beta\right)} \quad (18)$$

Equation (15) is a natural generalization of the original semi-phenomenological Kraus model [25] where the assumption was made for carbon black networks in rubber that under a periodic strain aggregate-aggregate contacts are continuously broken and reformed. This model is commonly applied in rubber technology for the evaluation of strain sweep characteristics of filled rubbers [2]. The characteristic deformation amplitude γ_{0c} marks the position of the maximum of the loss modulus in the strain scale and the parameter β characterizes the shape of the moduli functions. In the limit of low and high strain amplitudes the function g'' scales like (Equation (19)):

$$g'' \sim \gamma_0^\beta, (\gamma_0 \ll \gamma_{0c});$$

$$g'' \sim \gamma_0^{-\beta}, (\gamma_0 \gg \gamma_{0c}) \quad (19)$$

Earlier experimental investigations of the authors have shown that Equation (15)–(18) describe accurately the strain sweeps of several rubber compounds containing different grades of carbon black [24]. Obviously, the experiments suggest a characteristic universal non-integer exponent $\beta \approx 1/2$ which is even independent of the carbon black grade. The exponent β can be drawn back to various structural properties of the filler network, mainly its cluster structure, as has been proposed in [26] (see, also [27]) but for the purpose of the present study this is not of primary relevance.

4. A ‘relaxational behaviour’ analogy for the strain dependent dynamic modulus

The existence of similarity between dynamic strain-induced dependencies in the modulus of filled rubbers and the physics of the glass transition and the jamming transition of vibrated granular materials gives us a guideline to study a ‘relaxational behaviour’ in the domain of the canonical (to γ_0) conjugated variable α (Equations (20), (21)):

$$g^*(\gamma_0) = \int_0^\infty \dot{g}(\alpha) e^{i\gamma_0\alpha} d\alpha \quad (20)$$

where

$$\dot{g}(\alpha) = \frac{dg(\alpha)}{d\alpha} \quad (21)$$

Here, the shear amplitude γ_0 plays the role of frequency ω in the case of dielectric relaxation of a polymeric material, α plays the same role as time t in the time dependent dielectric permittivity $\epsilon_D(t)$ which is related to a function $\epsilon^*(\omega)$ by its Fourier transform. It is well known that the frequency dependence of this Fourier transform $\epsilon^*(\omega) = \epsilon' + i\epsilon''$ within a relaxation region can be quite well represented by the Havriliak-Negami model function [28] (Equation (22)):

$$\epsilon^*(\omega) - \epsilon_\infty = \frac{\Delta\epsilon}{\left(1 + \left(i \frac{\omega}{\omega_0}\right)^\beta\right)^\delta}, (0 < \beta, \beta \cdot \delta < 1) \quad (22)$$

which corresponds to the type of Equation (15) for $\delta = 1$ (often termed as *Cole-Cole* type equation). $\Delta\epsilon$ is the difference between high frequency limit of

permittivity and static low frequency permittivity limit. Both exponents in Equation (22) determine the power law behaviour of the loss function in the high frequency regime $\omega \gg \omega_0$, i.e. $\varepsilon'' \sim \omega^{-\beta\delta}$.

Similar like in the dielectric case we propose the validity of a linear response theorem [29] in the α -domain, where a mechanical stress, say $\sigma(\alpha)$, is related to a deformation, say $\gamma(\alpha)$ (Equation (23)):

$$\sigma(\alpha) = g_\infty \gamma(\alpha) - \int_{-\infty}^{\alpha} \dot{g}(\alpha - \alpha') \gamma(\alpha') d\alpha' \quad (23)$$

Such kind of relationship is well known for the theory of polarization [28, 29]. However, in the electric case, $\sigma(\alpha)$ plays the role of the polarization and $\gamma(\alpha)$ corresponds in this analogy to the external time dependent electric field. More important, according the fluctuation dissipation theorem [29], the temporal change of the dielectric permittivity, $\dot{\varepsilon}_D(t)$, is usually connected with the correlation function of the spontaneous polarization fluctuation, say $\varphi(t)$, which is proportional to the solution, say $p_D(t)$, of a corresponding diffusion equation (Equation (24)) [28, 34]:

$$\dot{\varepsilon}_D(t) = \frac{1}{kT} \frac{\partial}{\partial t} \varphi(t) \quad (24)$$

Guided by the discussed analogy we will propose a physical way of interpreting our function $g(\alpha)$. Our final conclusion will then be derived from a similar proportionality $g(\alpha) \sim p(\alpha)$ (see below). Especially, the introduction of the corresponding diffusion equation follows the model of damped diffusional propagation of conformational orientation in the dielectric case, as detailed in [34] (and references therein). Note, original models based on the concept of damped diffusional propagation of orientation along a polymer chain were developed in [30–33].

Going back to the ideas according the above already introduced simple Ising model we define here a two state Ising model as follows: state 0 is ascribed to broken aggregate contacts in a filler network, whereas state 1 is ascribed to a reformed, i.e. closed, contact. Physically, this is very similar to the basic assumptions for the phenomenological agglomeration-deagglomeration model of Kraus [25] that is often applied in rubber technology to quantify the strain amplitude dependence of the dynamic modulus of filled rubber. Then, a **probability** $p(x, \alpha)$ can be introduced that a contact marked by a coordinate x is in the state 1 at a certain strain amplitude $\gamma_0 \sim 1/\alpha$.

Initial condition is $p(x, \alpha=0) = 0$, i.e. the probability is zero for any closed contacts ($= 1$) if strain amplitude tends to infinity leading to a completely fractured filler network corresponding to a random distribution of single aggregates. We note that in the case of dielectric relaxation function at the glass transition of polymers the corresponding function $p_D(x, t)$ describes the probability that a polymer chain unit marked by the coordinate x is in the conformational state 1 (*gauche* conformation) at time t . The state 0 is then due to the *trans* conformation [34]. Most of the models for $p_D(x, t)$ which differ in the specific type of the mechanism of movement result in the hydrodynamic limit in a diffusion equation for $p_D(x, t)$, i.e. we can assume for our problem [34] (Equation (25)):

$$\frac{\partial p(x, \alpha)}{\partial \alpha} = -\frac{1}{\alpha_0} p(x, \alpha) + D \frac{\partial^2 p(x, \alpha)}{\partial x^2} \quad (25)$$

Similar to a certain time constant τ_0 in the polymer case [34] we introduced here the strain α_0 as a constant of the disappearance of the state 1 by direct coupling with a heat bath without diffusion. Indeed, it is well known and investigated that the filler network, when loaded at a low strain, can be disrupted by thermal motion and this disruption increases with increasing temperature (see, for example [2]). Filler networks exhibit a typical transition point of the $\log G'$ versus $1/T$ plot indication that the sample passes from a state characterized by a continuous filler network to another in which the network is thermally disrupted [2]. Obviously, this is related to thermal activation of the immobilized nanoscale polymer layer in between two adjacent filler units [27]. However, this disruption process can also be influenced by other energy sources like, for example, the precise external mechanical loading mode and loading history of the rubber. Recently, it could be shown how applied external strain history influences the local dynamics of filler particles in a rubber matrix [37]. Even significant differences in the local movement between different filler species (carbon black or silica) were detected.

In Equation (25), D is the diffusion coefficient of the Ising-state. The diffusion process along the filler network must therefore be regarded as a process in an inhomogeneous system; and each Ising-state during its diffusion meets with conditions which change with changing strain α . Thus, we can replace Equation (25) by the expression (Equation (26)):

$$\frac{\partial p(x, \alpha)}{\partial \alpha} = -\frac{1}{\alpha_0} p(x, \alpha) + \int_0^\alpha \frac{\partial D(\alpha - \alpha')}{\partial \alpha} \cdot \frac{\partial^2 p(x, \alpha')}{\partial x^2} d\alpha' \quad (26)$$

This equation represents the generalized master equation of non Markovian behaviour [35]. The diffusion coefficient D depends here on α which is expressed by a convolution integral, i.e. as a kind of linear response. Limiting cases are the ordinary diffusion equation for $D(\alpha - \alpha') \sim \delta(\alpha - \alpha')$ and the wave equation for $D(\alpha - \alpha') = const.$

After Laplace transformation and using the initial condition $p(x, \alpha=0) = 0$ it follows from Equation (26) (Equation (27)):

$$s\tilde{p}(x, s) = -\frac{1}{\alpha_0} \tilde{p}(x, s) + \tilde{D}(s) \cdot \frac{\partial^2 \tilde{p}(x, s)}{\partial x^2} \quad (27)$$

where s is the Laplace variable and Equation (27) corresponds to the above diffusion equation in the Laplace space. If we choose a scaling law [34] (Equation (28)):

$$\tilde{D}(s) = \frac{D_0}{s^\kappa}, \quad -1 \leq \kappa \leq 0 \quad (28)$$

we have with $\kappa = 0$ the ordinary diffusion case and with $-1 \leq \kappa < 0$ the so-called hindered diffusion.

Going back to the discussions after Equation (23), we have (Equation (29)):

$$\dot{g}(\alpha) \equiv \frac{\partial}{\partial \alpha} g(\alpha) \sim \frac{\partial}{\partial \alpha} p(\alpha) \quad (29)$$

Mathematical derivation of the function $p(\alpha)$ starting from Equation (27) is similar to the straight derivation of $p_D(t)$ (electrical case) as shown in Appendix 2 of reference [34].

The behaviour of $\dot{g}(\alpha)$ for $\alpha \ll \alpha_0$ (i.e., for large deformation amplitudes $\gamma_0 \gg \gamma_{0c}$) follows then as a power law (Equation (30)):

$$\dot{g}(\alpha) \sim \alpha^{-\frac{1-\kappa}{2}} e^{-\frac{\alpha}{\alpha_0}} \quad (30)$$

which leads with Equation (20) to the power law dependence of dynamic mechanical loss modulus from the deformation amplitude (Equation (31)):

$$g''(\gamma_0) \sim \gamma_{0c}^{-n} \text{ with } n = \frac{1 + \kappa}{2} \text{ for } \gamma_0 \gg \gamma. \quad (31)$$

The final result Equation (31) corresponds to experimental findings, i.e. a power law dependence for large deformation amplitudes according to Equa-

tion (19). Experimental data fitting with Equations (15)–(18) generated $\beta = n \approx 1/2$ [24]. Such values suggest $\kappa \approx 0$, which corresponds formally to ordinary diffusion of the Ising-states in the presumed model, see Equation (28). Consequently the filler networks breaks in simple non-delayed processes with a non-time (or space) dependent reaction constant.

5. Conclusions

We discussed already known remarkable similarities between strain dependence of the dynamic modulus of filled rubbers (Payne effect), glass transition of solid materials and the jamming transition of granular materials. These similarities allowed us to introduce a kind of statistical thermodynamics for strain dependent filler network configurations in analogy to classical thermodynamics and to Edwards-Oakeshott thermodynamics of compact powders [20]. The suggested simple Ising model approach to that kind of thermodynamics allows a consistent derivation of the so-called Payne amplitude which characterizes in rubber technology the decay of storage modulus from low strain to high strain amplitudes during strain sweeps at a certain temperature above glass transition region. Furthermore, scaling laws for the large strain behaviour of the corresponding loss modulus can be derived from a simple diffusion assumption of the Ising states. Clearly, there are more facets to the statistical thermodynamics of the discussed system and involved effects. We expect that more complex approaches instead of this simple diffusion model would lead to the near complete *Cole-Cole* like shape of the complex modulus as function of strain amplitude as observed in experiments and covering the whole range of accessible strain values. However, this was not the goal of the present paper, whose intention are the fundamental and basic physics approaches to the Payne effect in term of general jamming transitions. The open issues require more discussion and work.

References

- [1] Payne A. R.: Dynamic properties of filler-loaded rubbers. in ‘Reinforcement of elastomers’ (ed.: Kraus G.) Interscience Publishers, New York, 69–123 (1965).

- [2] Heinrich G., Klüppel M.: Recent advances in the theory of filler networking in elastomers. in 'Filled elastomers drug delivery systems series: Advances in polymer science' (ed.: Lee K-S.) Springer, Berlin, Vol 160, 1–44 (2002).
- [3] Varghese S., Karger-Kocsis J.: Natural rubber-based nanocomposites by latex compounding with layered silicates. *Polymer*, **44**, 4921–4927 (2003). DOI: [10.1016/S0032-3861\(03\)00480-4](https://doi.org/10.1016/S0032-3861(03)00480-4)
- [4] Karger-Kocsis J., Wu C-M.: Thermoset rubber/layered silicate nanocomposites. Status and future trends. *Polymer Engineering and Science*, **44**, 1083–1093 (2004). DOI: [10.1002/pen.20101](https://doi.org/10.1002/pen.20101)
- [5] Richter S., Kreyenschulte H., Saphiannikova M., Götz T., Heinrich G.: Studies of the so-called jamming phenomenon in filled rubbers using dynamical-mechanical experiments. *Macromolecular Symposia*, **306–307**, 141–149 (2011). DOI: [10.1002/masy.201000117](https://doi.org/10.1002/masy.201000117)
- [6] Richter S., Saphiannikova M., Stöckelhuber K. W., Heinrich G.: Jamming in filled polymer systems. *Macromolecular Symposia*, **291–292**, 193–201 (2010). DOI: [10.1002/masy.201050523](https://doi.org/10.1002/masy.201050523)
- [7] Wang X., Robertson C. G.: Strain-induced nonlinearity of filled rubbers. *Physical Review E*, **72**, 031406/1–031406/9 (2005). DOI: [10.1103/PhysRevE.72.031406](https://doi.org/10.1103/PhysRevE.72.031406)
- [8] Robertson C. G., Wang X.: Isoenergetic jamming transition in particle-filled systems. *Physical Review Letters*, **95**, 075703/1–075703/4 (2005). DOI: [10.1103/PhysRevLett.95.075703](https://doi.org/10.1103/PhysRevLett.95.075703)
- [9] Kovacs A. J.: La contraction isotherme du volume des polymères amorphes. *Journal of Polymer Science*, **30**, 131–147 (1958). DOI: [10.1002/pol.1958.1203012111](https://doi.org/10.1002/pol.1958.1203012111)
- [10] Kovacs A. J., Aklonis J. J., Hutchinson J. M., Ramos A. R.: Isobaric volume and enthalpy recovery of glasses. II. A transparent multiparameter theory. *Journal of Polymer Science: Polymer Physics Edition*, **17**, 1097–1162 (1979). DOI: [10.1002/pol.1979.180170701](https://doi.org/10.1002/pol.1979.180170701)
- [11] McKenna G. B.: Glass formation and glassy behavior. in 'Comprehensive polymer science' (eds.: Booth C., Price C.) Pergamon, Oxford, Vol 2, 311–363 (1989).
- [12] Nowak E. R., Knight J. B., Ben-Naim E., Jaeger H. M., Nagel S. R.: Density fluctuations in vibrated granular materials. *Physical Review E*, **57**, 1971–1982 (1998). DOI: [10.1103/PhysRevE.57.1971](https://doi.org/10.1103/PhysRevE.57.1971)
- [13] Barrat A., Loreto V.: Memory in aged granular media. *Europhysics Letters*, **53**, 297–303 (2001). DOI: [10.1209/epl/i2001-00100-3](https://doi.org/10.1209/epl/i2001-00100-3)
- [14] D'Anna G., Mayor P., Gremaud G., Barrat A., Loreto V.: Extreme events-driven glassy behaviour in granular media. *Europhysics Letters*, **61**, 60–66 (2003). DOI: [10.1209/epl/i2003-00245-y](https://doi.org/10.1209/epl/i2003-00245-y)
- [15] Trappe V., Prasad V., Cipelletti L., Segre P. N., Weitz D. A.: Jamming phase diagram for attractive particles. *Nature*, **411**, 772–775 (2001). DOI: [10.1038/35081021](https://doi.org/10.1038/35081021)
- [16] Liu A. J., Nagel S. R.: Jamming and rheology: Constrained dynamics on microscopic and macroscopic scales. Taylor and Francis, New York (2001).
- [17] Liu A. J., Nagel S. R.: Nonlinear dynamics: Jamming is not just cool any more. *Nature*, **396**, 21–22 (1998). DOI: [10.1038/23819](https://doi.org/10.1038/23819)
- [18] Doolittle A. K., Doolittle D. B.: Studies in Newtonian flow. V. Further verification of the free-space viscosity equation. *Journal of Applied Physics*, **28**, 901–905 (1957). DOI: [10.1063/1.1722884](https://doi.org/10.1063/1.1722884)
- [19] Fuchs M., Cates M. E.: Theory of nonlinear rheology and yielding of dense colloidal suspensions. *Physical Review Letters*, **89**, 248304/1–248304/4 (2002). DOI: [10.1103/PhysRevLett.89.248304](https://doi.org/10.1103/PhysRevLett.89.248304)
- [20] Edwards S. F., Oakeshott R. B. S.: The transmission of stress in an aggregate. *Physica D: Nonlinear Phenomena*, **38**, 88–92 (1989). DOI: [10.1016/0167-2789\(89\)90176-0](https://doi.org/10.1016/0167-2789(89)90176-0)
- [21] Wang K., Song C., Wang P., Makse H. A.: Anisotropy and compactness describe the jamming transition in soft particulate matter. *Europhysics Letters*, **91**, 68001/1–68001/6 (2010). DOI: [10.1209/0295-5075/91/68001](https://doi.org/10.1209/0295-5075/91/68001)
- [22] Blumenfeld R., Edwards S. F.: On granular stress statistics: Compactness, anisotropy, and some open issues. *The Journal of Physical Chemistry B*, **113**, 3981–3987 (2009). DOI: [10.1021/jp809768y](https://doi.org/10.1021/jp809768y)
- [23] Cipra B. A.: An introduction to the Ising model. *The American Mathematical Monthly*, **94**, 937–959 (1987). DOI: [10.2307/2322600](https://doi.org/10.2307/2322600)
- [24] Heinrich G., Vilgis T. A.: Effect of filler networking on the dynamic mechanical properties of crosslinked polymer solids. *Macromolecular Symposia*, **93**, 253–260 (1995). DOI: [10.1002/masy.19950930130](https://doi.org/10.1002/masy.19950930130)
- [25] Kraus G.: Mechanical losses in carbon-black-filled rubbers. *Applied Polymer Symposia*, **39**, 75–92 (1984).
- [26] Huber G., Vilgis T. A.: Universal properties of filled rubbers: Mechanisms for reinforcement on different length scales. *Kautschuk Gummi Kunststoffe*, **52**, 102–107 (1999).
- [27] Vilgis T. A., Heinrich G., Klüppel M.: Reinforcement of polymer nano-composites: Theory, experiments and applications. Cambridge University Press, New York (2009).
- [28] Kremer F., Schönhals A.: Broadband dielectric spectroscopy. Springer, Berlin (2003).
- [29] Landau L. D., Lifshitz E. M.: Course of theoretical physics, Vol 2: The classical theory of fields. Pergamon Press, Oxford (1971).

- [30] Shore J. E., Zwanzig R.: Dielectric relaxation and dynamic susceptibility of a one-dimensional model for perpendicular-dipole polymers. *The Journal of Chemical Physics*, **63**, 5445–5458 (1975).
DOI: [10.1063/1.431279](https://doi.org/10.1063/1.431279)
- [31] Skolnick J., Yaris R.: Damped orientational diffusion model of polymer local main-chain motion. 5. Comparison with three alternative models. *Macromolecules*, **18**, 1635–1637 (1985).
DOI: [10.1021/ma00150a020](https://doi.org/10.1021/ma00150a020)
- [32] Valeur B., Jarry J-P., Geny F., Monnerie L.: Dynamics of macromolecular chains. I. Theory of motions on a tetrahedral lattice. *Journal of Polymer Science: Polymer Physics Edition*, **13**, 667–674 (1975).
DOI: [10.1002/pol.1975.180130401](https://doi.org/10.1002/pol.1975.180130401)
- [33] Hall C. K., Helfand E.: Conformational state relaxation in polymers: Time-correlation functions. *The Journal of Chemical Physics*, **77**, 3275–3282 (1982).
DOI: [10.1063/1.444204](https://doi.org/10.1063/1.444204)
- [34] Schönhals A., Schlosser E.: Dielectric relaxation in polymeric solids Part 1. A new model for the interpretation of the shape of the dielectric relaxation function. *Colloid and Polymer Science*, **267**, 125–132 (1989).
DOI: [10.1007/BF01410350](https://doi.org/10.1007/BF01410350)
- [35] Kenkre V. M., Montroll E. W., Shlesinger M. F.: Generalized master equations for continuous-time random walks. *Journal of Statistical Physics*, **9**, 45–50 (1973).
DOI: [10.1007/BF01016796](https://doi.org/10.1007/BF01016796)
- [36] Edwards S. F., Grinev D. V.: Statistical physics of the jamming transition: The search for simple models. in ‘Jamming and rheology: Constrained dynamics on microscopic and macroscopic scales’ (eds.: Liu A. J., Nagel S. R.) Taylor and Francis, New York (2001)
- [37] Ehrburger-Dolle F., Morfin I., Bley F., Livet F., Heinrich G., Richter S., Pichè L., Sutton M.: XPCS investigation of the dynamics of filler particles in stretched filled elastomers. *Macromolecules*, **45**, 8691–8701 (2012).
DOI: [10.1021/ma3013674](https://doi.org/10.1021/ma3013674)

Biodegradable microfibrillar polymer-polymer composites from poly(L-lactic acid)/poly(glycolic acid)

L. D. Kimble*, D. Bhattacharyya, S. Fakirov

The Centre for Advanced Composite Materials, The University of Auckland, Building 740, Room 181, Tamaki Campus, 261 Morrin Rd, Glen Innes, Auckland, New Zealand

Received 1 October 2014; accepted in revised form 6 December 2014

Abstract. Biodegradable coronary stents have been under development for several years and a trend in biodegradable stent material development has emerged: reinforcement to enhance mechanical properties and creep resistance to improve vessel support. The aim of this work is to investigate the mechanical and viscoelastic characteristics of poly(L-lactic acid)/poly(glycolic acid) (PLLA/PGA) microfibrillar polymer-polymer composites (MFCs) at 37°C to determine the suitability of PGA fibrils as a reinforcement for polymeric, biodegradable stents. PLLA/PGA MFCs were produced via cold-drawing and subsequent compression moulding of extruded PLLA/PGA blend wires. Scanning electron microscopy revealed excellent fibril formation in the case of a 70/30 wt% PLLA/PGA MFC- the mean fibril diameter being 400 nm and aspect ratios exceeding 250. Tensile tests demonstrate Young's modulus and strength increases of 35 and 84% over neat PLLA in the case of a 70/30 wt% PLLA/PGA MFC. Creep resistance of the PLLA/PGA MFCs is lower than that of neat PLLA, as shown via relaxation. Dynamic mechanical thermal analysis demonstrates that it is the onset of glass transition of PGA that is the underlying cause for low creep resistance of the PLLA/PGA MFCs at 37°C.

Keywords: biocompatible polymers, biodegradable polymers, mechanical properties, microfibrillar polymer-polymer composites, viscoelasticity

1. Introduction

Stents have been used to treat coronary artery disease (the build-up of plaque in coronary arteries) for decades and they have evolved significantly. The stenting process begins with balloon angioplasty during which a balloon catheter is navigated to the target site and inflated to widen the vessel and flatten the plaque, as illustrated in Figure 1a–1c. A second balloon catheter with a stent over the balloon is then navigated to the target site and deployed via balloon expansion, Figure 1d–1e). Finally the balloon is deflated and removed, leaving the stent in place to support the vessel, Figure 1f–1g.

Early stents were made of medical grade stainless steel [1] and are known as bare metal stents (BMSs). Unfortunately the occurrence of restenosis (re-nar-

rowing of the vessel via either an inflammatory reaction [2] or formation of a clot/thrombus [3]) was common after BMS implantation. For this reason attempts were made at coating stents with various compounds, e.g. gold, silicon carbide, titanium-nitride-oxide, etc. to make them more inert [3, 4]. These stents are known as coated metal stents (CMSs); their efficacy results were mixed – in some cases yielding higher restenosis rates than BMSs [5]. The next step in stent evolution was the development of drug-eluting stents (DESs) which gradually release pharmaceutical agents after implantation to mitigate restenosis. However, clinical studies revealed that late stent thrombosis rates were higher in the case of DESs when compared with

*Corresponding author, e-mail: lkim009@aucklanduni.ac.nz

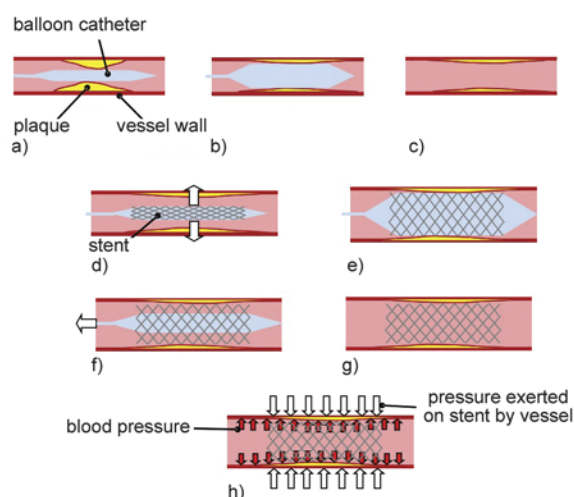


Figure 1. Stenting process: balloon catheter navigated to target site (a), inflation of balloon to deform plaque (b), vessel after removal of the balloon catheter (c), stent on balloon catheter is navigated to target site and deployed via balloon expansion (d–e), balloon is deflated and removed, leaving the stent in place to support the vessel (f–g). The stent is under continuous crushing load exerted by the vessel (h).

BMSs [6] and this has been attributed to endothelialisation being delayed by the eluted drugs [7]. Cardiologists have noted that vessel support is required for only 6 months while they heal [8]. For this reason biodegradable stents were developed which perform the required role and eventually degrade entirely, leaving no permanent object in the patients' bodies. Poly(L-lactic acid), PLLA, is a very prominent material in biodegradable stent material development but its major disadvantage is that it is brittle [9]. Ductility is required during balloon expansion in order for the stent to undergo sufficient plastic deformation without fracturing [10]. It is possible to modify PLLA via plasticiser addition or blending with rubbery polymers to produce a ductile material. Grabow and coworkers [10–12] have blended PLLA with tri-ethyl citrate (TEC), poly(ϵ -caprolactone) (PCL) and poly(4-hydroxybutyrate) (P4HB) for the intended application as biodegradable stent materials. Significant reduction in elastic moduli resulted ($\sim 50\%$ in the cases of PLLA/P4HB and PLLA/PCL/TEC blends [11, 12] and creep resistance of PLLA/TEC was reported to have greatly reduced by 1–2 orders of magnitude [10]. Blends of PLLA and poly(butylene succinate) (PBS) have been investigated by the authors and although they exhibit favourable mechanical properties, creep resistance reduces rapidly during degradation [13].

Creep resistance must be maintained because a stent is subjected to radial pressure by the vessel it supports and insufficient creep resistance could result in stent collapse or narrowing. Therefore, there is a need to investigate means of reinforcing polymeric biodegradable stent materials. Further motivation comes from evidence that the industry is moving in this direction – medical device companies have, in the last few years, published patents on reinforcement of biodegradable, polymeric stents. The patents cover the use of mineral reinforcements such as nanoclays [14, 15].

A common method of reinforcing polymers is to use particulate reinforcements such as nanoclays, a method which is widely used already. Furthermore, this method is covered by the aforementioned patents on reinforcement of biodegradable, polymeric stents [14, 15]. An alternative method is the use of microfibrillar or nanofibrillar polymer-polymer composites (MFCs or NFCs, respectively). The concept was developed by Fakirov *et al.* [16] with the knowledge that drawing of polymers enhances their mechanical properties. These polymer-polymer composites are created by fibrillising the dispersed component of an immiscible polymer blend, often by drawing during which the dispersed particles elongate and coalesce to form fibrils. The final step is to isotropise the matrix polymer by heating the material above the melting point of the matrix but below that of the dispersed polymer [17–22]. The MFC process has been shown to be successful for petrochemical-derived polymer pairs, including poly(ethylene terephthalate)/low-density poly(ethylene) [20], poly(propylene)/PET [22] and single polymer composites of polyamide 6 [23] with properties such as modulus and strength increasing manifold when compared with the neat, isotropic matrix polymer. Little work has been done on biodegradable, biocompatible MFCs or NFCs so there is enormous scope for research in this area for biomedical applications, as well as packaging or other consumer-oriented applications. Friedrich *et al.* [24] report briefly on MFCs from PLLA and poly(glycolic acid), PGA. They report improved bending modulus and strength compared with neat PLLA but importantly, their results were obtained at room temperature – despite the intended application being bone nails [24]. The mechanical characteristics of polymers are highly dependent on temperature, therefore for biomedical applications the properties should be measured at 37°C .

The aim of this work is to determine the mechanical properties and viscoelastic behaviour of PLLA/PGA MFCs at 37°C in order to assess the suitability of PGA fibrils for reinforcement of biodegradable stents based on PLLA.

2. Experimental methodology

2.1. Materials

PLLA grade 2002D (NatureWorks LLC, USA) was supplied in pellet form. Manufacturer's data indicates that the PLLA has a density of 1.24 g/cm³ and a melt flow index of 4–8 g/10 min (190°C, 2.16 kg). Its glass transition temperature (T_g) is 55–60°C and melting temperature, T_m , is 180°C according to Letchford *et al.* [25]. PGA (Kuredux, Kureha Corporation, Japan) was also supplied in pellet form. It is indicated by the manufacturer to have a T_m of 220°C, T_g of 40°C and density of 1.5–1.6 g/cm³, depending on the degree of crystallinity.

2.2. Specimen preparation

PLLA and PGA were dried overnight at 70 and 120°C, respectively, before melt blending in a twin-screw extruder (DSE 25, Brabender, Germany) at PLLA/PGA wt% ratios 70/30 and 80/20 – extrudate was collected on a spool as a wire. The temperature profile used for blending is shown in Table 1.

The extruded wire was cold-drawn (i.e. below the T_m but above the T_g of the PLLA matrix) at 60°C such that drawing occurred via necking. The drawing equipment was custom made at our facility and consists of a heated channel with rollers on either side. The rollers at the end of the channel were set to rotate faster than those feeding the wire in at the start of the channel. This provided the tension necessary for drawing. The MFCs were produced via compression moulding (using a hot press, Carver, USA) of drawn wire which had been wound around

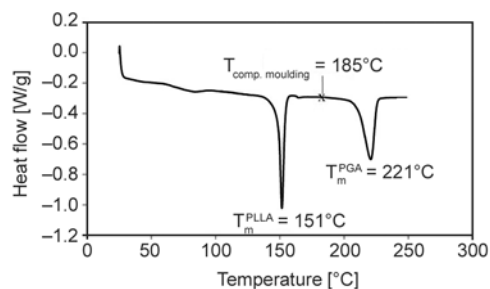


Figure 2. DSC scan of drawn PLLA/PGA30

a teflon-covered aluminum plate. Moulding was done at $T_{\text{comp.moulding}} = 185^\circ\text{C}$ since $T_{m,\text{PLLA}} < 185^\circ\text{C} < T_{m,\text{PGA}}$ as determined by differential scanning calorimetry (DSC), Figure 2. A DSC Q2000 (TA Instruments, USA) was used – a temperature ramp rate of 10°C/min was used.

The resulting unidirectional PLLA/PGA MFCs were cut into rectangular strips 150 mm×14 mm with thicknesses ~0.4 mm with the length parallel with the fiber direction for tensile and relaxation tests. Specimens from as-extruded blends were prepared in the same way and nomenclature of all specimen types is provided in Table 2).

2.3. Tensile and relaxation tests

A universal testing machine (5567, Instron, USA) was used for tensile and relaxation tests – all of which were performed in an environmental chamber at 37°C. Strain of a 50 mm gauge length marked on each specimen was measured using a video extensometer (Advanced Video Extensometer, Instron, USA). Tensile tests were performed in accordance with ASTM D882 – distance between the grips: 100 mm, crosshead speed: 10 mm/min. 5 specimens of each material were tensile tested. Young's moduli were determined using the gradient of the stress-strain data between 0.2 and 0.5% strain to mitigate the influence of the curves' toes. Relaxation tests

Table 1. Extrusion temperature profile for blending PLLA and PGA

Zone	1	2	3	4	5	6	7	8	DIE
Temperature [°C]	190	190	220	230	235	230	220	215	210

Table 2. Nomenclatures of PLLA/PGA blends and associated MFCs

Description	PLLA/PGA ratio [wt%/wt%]	Designation
PLLA/PGA blend, not drawn	80/20	PLLA/PGA20
	70/30	PLLA/PGA30
PLLA/PGA MFC resulting from compression moulding of drawn wire	80/20	PLLA/PGA20-MFC
	70/30	PLLA/PGA30-MFC

were done by applying 20 MPa initial stress and fixing the extension then monitoring stress over 15 mins.

2.4. Viscoelastic characterisation

Rectangular specimens 40 mm×5 mm were cut from compression moulded films of PLLA/PGA20-MFC, PLLA/PGA30-MFC and neat PLLA. Tensile mode dynamic mechanical thermal analysis (DMTA), with a strain amplitude of 0.05% and frequency of 1 Hz was done using a DMA Q800 (TA Instruments, USA).

2.5. Morphological characterisation

Scanning electron microscopy (SEM) was used to observe the morphology of PLLA/PGA blends and their corresponding MFCs. Specimens were prepared via cryofracture. Additional specimens were prepared via selective solvent extraction in a Soxhlet apparatus using tetrahydrofuran as the selective solvent. This resulted in the PLLA matrix being removed, leaving PGA fibrils behind. All specimens were coated with platinum before observation. A Philips (Netherlands), model XL30 S-FEG, scanning electron microscope was used.

3. Results and discussion

3.1. Morphology

SEM images of PLLA/PGA30 and PLLA/PGA20 demonstrate that in both cases PGA is very well dispersed within the PLLA, as shown in Figure 3a and 3b, respectively. PGA particle diameters are approximately 1–2 μm in diameter. In the case of PLLA/PGA30 there is a higher frequency of closely-clustered PGA particles compared with that observed in PLLA/PGA20. If one observes film made from non-drawn PLLA/PGA, fractured parallel to the direction of the wire before hot pressing, one may observe cigar shaped PGA particles, Figure 3e and 3f. This shows that during production of the wire there is some degree of hot drawing occurring during haul-off of the extrudate from the extruder. The materials produced by drawing and subsequent compression moulding were fractured parallel to the drawing direction for observation. It is clear from Figure 3e and 3f that fibrillation of the dispersed PGA component has occurred. Note the reduction in diameter of the cigars present in the non-drawn wire ($\sim 1 \mu\text{m}$) after fibrillation during cold drawing ($\sim 400 \text{ nm}$). In the case of PLLA/PGA30-MFC,

fibril formation is excellent and the PGA exists as long, well-oriented fibrils, Figure 3c. The morphology PLLA/PGA20-MFC, however, shows that drawing of PLLA/PGA20 only partially fibrillised the PGA, Figure 3d. Some fibrils can be seen but a significant proportion of the PGA present in PLLA/PGA20-MFC still exists as round particles. This poor fibrillation is attributed to the concentration of PGA in PLLA/PGA20 being too low, therefore the coalescence of PGA particles during drawing is hindered. Coalescence is essential for the formation of high aspect-ratio fibrils [26]. In order to determine key dimensions, fibrils were extracted from PLLA/PGA30-MFC using selective solvent extraction (tetrahydrofuran used as selective solvent) and are shown in Figure 3g and 3h. From these images and others a mean fibril diameter of 400 nm was determined. Fibrils exceeding 100 μm in length can be observed in Figure 3e and therefore fibrils with aspect ratios greater than 250 were created. The small diameters of the fibrils makes them well-suited to reinforcement of biodegradable stents since stent struts are only 150 μm thick, making some particulate reinforcements unsuitable since they have sizes of similar orders of magnitude.

3.2. Tensile properties

Properties of PLLA/PGA MFCs are compared with those of neat PLLA and the simple (not drawn) PLLA/PGA blends from which they were derived. It is important to make both comparisons because (i) PLLA is what is being reinforced whilst (ii) we must assess the gains obtained through MFC processing. Results from tensile testing are summarised in Table 3. Young's moduli of PLLA/PGA20 and PLLA/PGA30 are 5 and 16% higher than that of neat PLLA. The MFCs, PLLA/PGA20-MFC and PLLA/PGA30-MFC exhibited Young's moduli 15 and 36% higher than that of neat PLLA – clearly showing the enhancement of stiffness brought about by fibrillising the PGA, despite poor fibrillation in PLLA/PGA20-MFC. Note also that the PLLA/PGA blends are very brittle whilst the PLLA/PGA MFCs exhibit excellent toughness, as summarised by strains at break in Table 3 and which can be observed in stress-strain plots in Figure 4.

The enhancements of strength provided by the MFC process are evident- PLLA/PGA30-MFC exhibits a strength of 88.1 MPa: 84 and 69% higher than those of neat PLLA and PLLA/PGA30, respectively. The

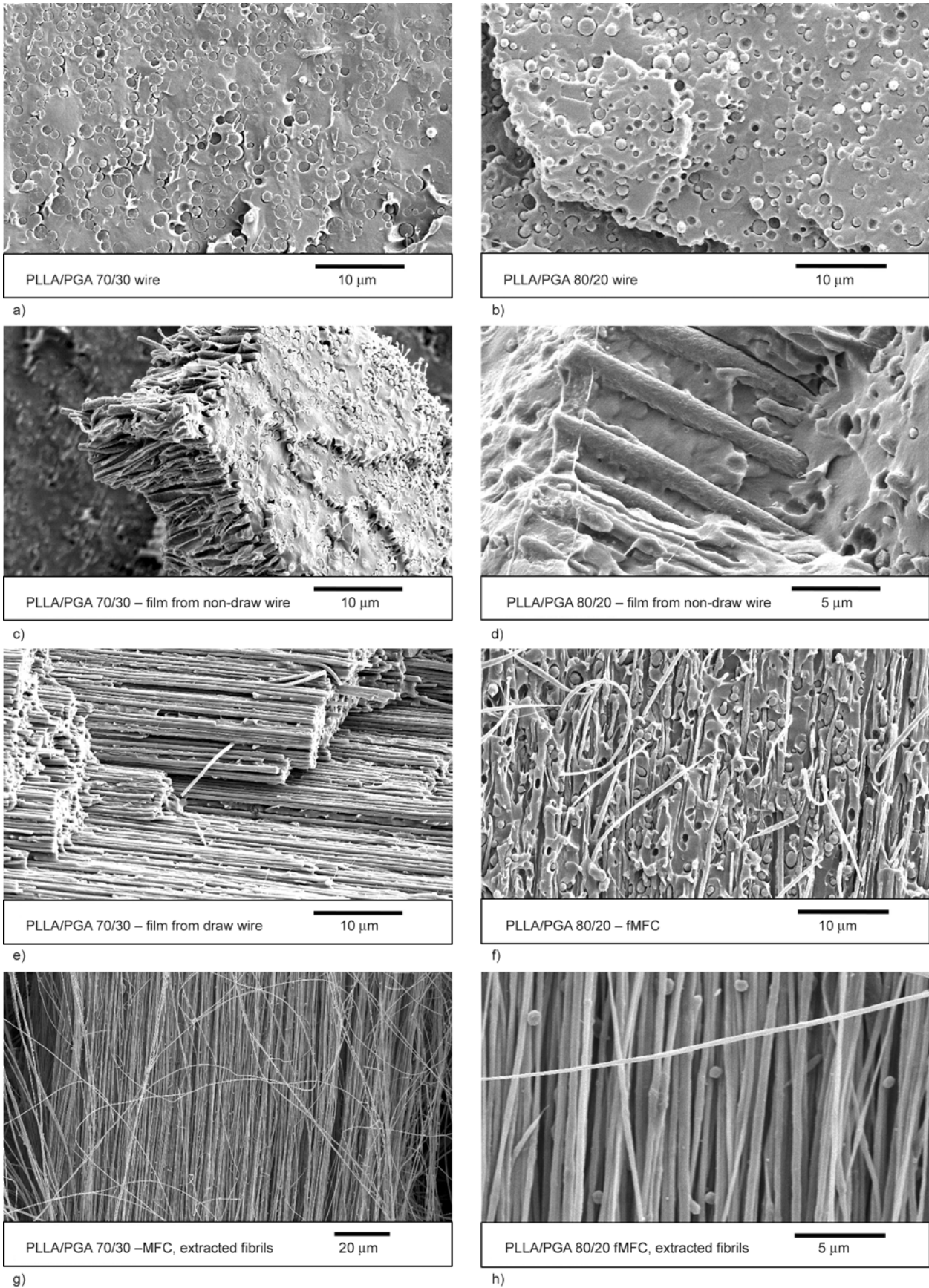


Figure 3. SEM images of non-drawn PLLA/PGA20 and PLLA/PGA30 (a and b) wires and film made from non-drawn wires (c and d). The MFCs resulting from drawing and subsequent compression moulding are shown (e and f). Fibrils extracted from PLLA/PGA30-MFC (g) and example diameter measurements of them are shown (h).

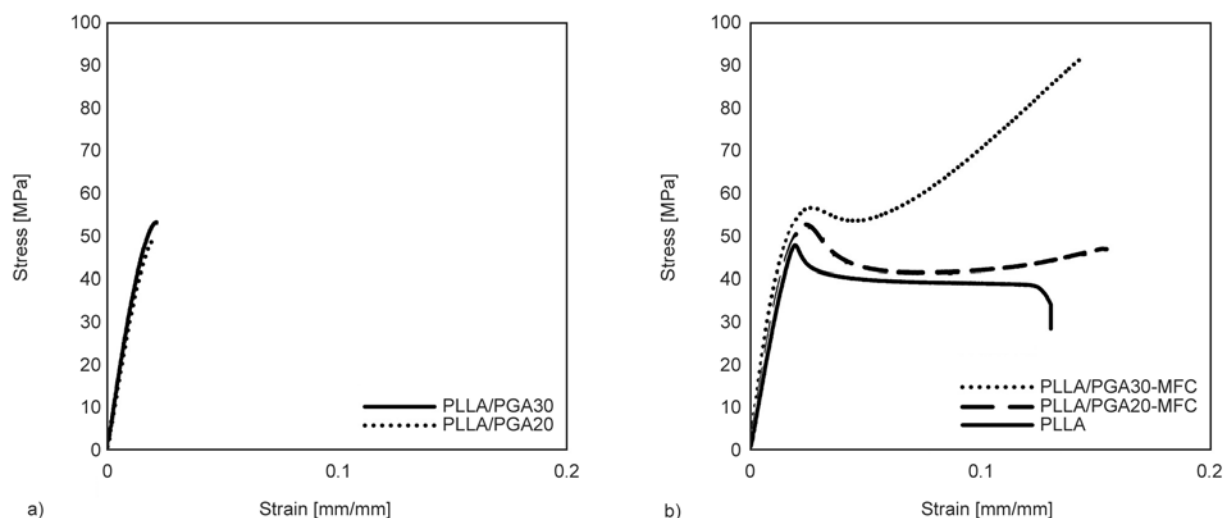


Figure 4. Stress-strain plots of PLLA/PGA blends (a) and their corresponding MFCs and neat PLLA (b)

Table 3. Strengths, Young's moduli and strains at break of PLLA, PLLA/PGA blends and their corresponding MFCs

Material	Young's modulus [GPa]	Tensile strength [MPa]	Strain at break [%]
PLLA	3.00±0.06	48.0±3.8	12.6*
PLLA/PGA20	3.16±0.07	51.5±1.6	2.2±0.2
PLLA/PGA30	3.47±0.11	52.0±1.8	2.2±0.3
PLLA/PGA20-MFC	3.44±0.14	52.5±0.6	15.3±1.1
PLLA/PGA30-MFC	4.08±0.14	88.1±6.8	13.7±1.2

*strain at break of the one PLLA specimen which failed within the gauge length, others failed at or near the grips.

lack of improvement of strength in the case of PLLA/PGA20-MFC versus its simple blend is again attributed to poor fibrillation, as observed by SEM, Figure 3d. The results of tensile testing demonstrate the successful improvement of mechanical properties of PLLA by microfibrillar reinforcement with PGA. However, the instantaneous response does not elucidate the behaviour of the material under long-term load. The results of relaxation tests and viscoelastic behaviour are now discussed to gain insight into this.

3.3. Relaxation behaviour

Results from relaxation tests of PLLA and PLLA/PGA MFCs show that both PLLA/PGA20-MFC and PLLA/PGA30-MFC exhibit quicker relaxation than neat PLLA does, Figure 5. Over a 1200 s duration, PLLA specimens relaxed from an initial stress of 20 MPa to 13–14 MPa whilst all of the PLLA/PGA MFC specimens relaxed to 10–11 MPa. Since quicker relaxation indicates lower creep resistance [27, 28] it can be concluded that the creep resist-

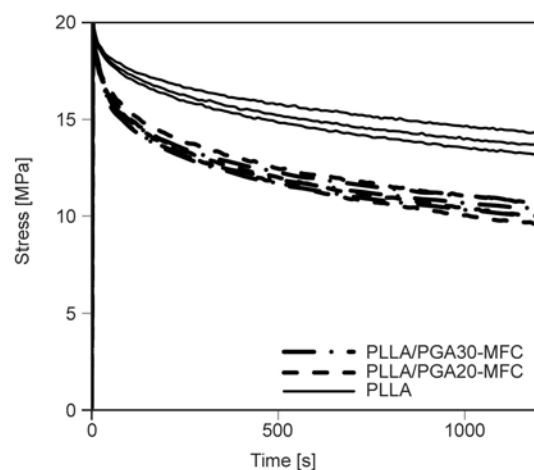


Figure 5. Stress-time curves from relaxation tests of PLLA, PLLA/PGA20-MFC and PLLA/PGA30-MFC specimens at 37°C

ances of PLLA/PGA MFCs are lower than that of neat PLLA. This is unfavourable for reinforcement of PLLA-based stents where sufficient creep resistance is required to provide vessel support for 6 months. The thermal history of all of the specimens is very similar, therefore physical ageing may be ruled out as a potential factor affecting the creep resistance of PLLA and the PLLA/PGA MFC specimens tested. A potential cause for the lower creep resistance of the PLLA/PGA MFCs is that 37°C is near the T_g of PGA – for this reason DMTA was used for further investigation, as discussed in the next section.

3.4. Viscoelastic behaviour

In order to verify the assertion that the onset of glass transition of the amorphous phase of PGA is the cause of the creep propensity of PLLA/PGA MFCs,

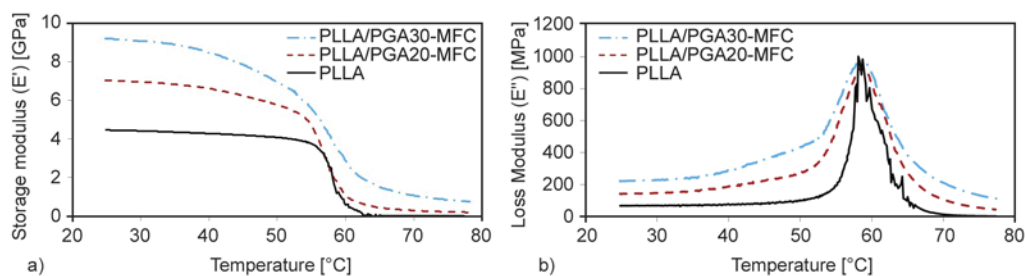


Figure 6. Storage (a) and loss moduli (b) of PLLA, PLLA/PGA20-MFC and PLLA/PGA30-MFC

their viscoelastic behaviours were compared to that of PLLA via DMTA. The storage modulus of PLLA begins to drop off at 50–55°C whilst those of the MFCs start to show this decline at much lower temperatures near 35°C, especially clear in the case of PLLA/PGA30-MFC, Figure 6a. The loss moduli, which indicate energy dissipated by viscoelastic effects, echo these trends, Figure 6b. The more rapid increases in loss moduli of the MFCs implies that from ~35°C the amorphous phase of PGA is becoming mobile resulting in more energy dissipation and less energy storage (as indicated by the declines in storage moduli). These results are an important consideration for load-bearing implants where creep failure is a concern. Nevertheless, other applications may benefit from the presence of PGA fibrils – note that the storage modulus of PLLA is practically negligible above 65°C whilst that of PLLA/PGA30-MFC is ~700 MPa because of the crystalline phase of PGA. Some applications, such as biodegradable cups for hot beverages, for example could take advantage of this. Additional drawing to increase the orientation of PGA molecules in the fibrils could be investigated to determine whether creep resistance and mechanical properties can be improved.

4. Conclusions

PGA was successfully fibrillised in a PLLA matrix via cold-drawing of extruded wires of PLLA/PGA blends. Fibril formation was excellent in the case of PLLA/PGA30-MFC whilst poor fibril formation was evident in PLLA/PGA20-MFC, owing to the lower concentration of PGA preventing coalescence during drawing. Tensile tests revealed the reinforcement gained via the MFC process. PLLA/PGA30-MFC has a 35% greater Young's modulus and is 84% stronger than neat PLLA in tension at 37°C. Relaxation tests at the same temperature indicate, however, that the creep resistance of PLLA/PGA MFCs

is poorer than that of neat PLLA. DMTA results reveal that it is the onset of glass transition of PGA which is the underlying cause for the creep propensity of PLLA/PGA MFCs. For biodegradable PLLA-based stents this highlights creep failure as a significant concern. Nevertheless, the fully biodegradable MFCs produced in this work exhibit properties which may be favourable for other applications. Furthermore, there is scope for further development of PLLA/PGA MFCs. Reduction of the initial PGA particle size and/or further drawing may be used to increase orientation of PGA molecules in an attempt to enhance creep resistance. Additionally, since PLLA and PGA are both condensation polymers the possibility of transreactions between them exists. This phenomenon could be leveraged to enhance interfacial adhesion between fibrils and matrix to improve mechanical performance [23].

Acknowledgements

The authors would like to thank the University of Auckland Doctoral Scholarship and the Ministry of Business, Innovation and Employment for funding this research.

References

- [1] Mani G., Feldman M. D., Patel D., Agrawal C.: Coronary stents: A materials perspective. *Biomaterials*, **28**, 1689–1710 (2007). DOI: [10.1016/j.biomaterials.2006.11.042](https://doi.org/10.1016/j.biomaterials.2006.11.042)
- [2] Kraitzer A., Kloog Y., Zilberman M.: Approaches for prevention of restenosis. *Journal of Biomedical Materials Research Part B: Applied Biomaterials*, **85**, 583–603 (2008). DOI: [10.1002/jbm.b.30974](https://doi.org/10.1002/jbm.b.30974)
- [3] Serruys P. W., Kutryk M. J. B., Ong A. T. L.: Coronary-artery stents. *New England Journal of Medicine*, **354**, 483–495 (2006). DOI: [10.1056/NEJMra051091](https://doi.org/10.1056/NEJMra051091)
- [4] O'Brien B., Carroll W.: The evolution of cardiovascular stent materials and surfaces in response to clinical drivers: A review. *Acta Biomaterialia*, **5**, 945–958 (2009). DOI: [10.1016/j.actbio.2008.11.012](https://doi.org/10.1016/j.actbio.2008.11.012)

- [5] Kastrati A., Schömig A., Dirschinger J., Mehilli J., von Welser N., Pache J., Schühlen H., Schilling T., Schmitt C., Neumann F.-J.: Increased risk of restenosis after placement of gold-coated stents results of a randomized trial comparing gold-coated with uncoated steel stents in patients with coronary artery disease. *Circulation*, **101**, 2478–2483 (2000). DOI: [10.1161/01.CIR.101.21.2478](https://doi.org/10.1161/01.CIR.101.21.2478)
- [6] Webster M. W. I., Ormiston J. A.: Drug-eluting stents and late stent thrombosis. *Lancet*, **370**, 914–915 (2007). DOI: [10.1016/s0140-6736\(07\)61424-x](https://doi.org/10.1016/s0140-6736(07)61424-x)
- [7] Finn A., Joner M., Nakazawa G., Kolodgie F., Newell J., John M. C., Gold H. K., Virmani R.: Pathological correlates of late drug-eluting stent thrombosis strut coverage as a marker of endothelialization. *Circulation*, **115**, 2435–2441 (2007). DOI: [10.1161/circulationaha.107.693739](https://doi.org/10.1161/circulationaha.107.693739)
- [8] Ormiston J., Webster M.: Absorbable coronary stents. *Lancet*, **369**, 1839–1840 (2007). DOI: [10.1016/s0140-6736\(07\)60829-0](https://doi.org/10.1016/s0140-6736(07)60829-0)
- [9] Yokohara T., Yamaguchi M.: Structure and properties for biomass-based polyester blends of PLA and PBS. *European Polymer Journal*, **44**, 677–685 (2008). DOI: [10.1016/j.eurpolymj.2008.01.008](https://doi.org/10.1016/j.eurpolymj.2008.01.008)
- [10] Grabow N., Schlun M., Sternberg K., Hakansson N., Kramer S., Schmitz K.-P.: Mechanical properties of laser cut poly(L-lactide) micro-specimens: Implications for stent design, manufacture, and sterilization. *Journal of Biomechanical Engineering*, **127**, 25–31 (2005). DOI: [10.1115/1.1835349](https://doi.org/10.1115/1.1835349)
- [11] Grabow N., Bünger C. M., Steinberg K., Mews S., Schmohl K., Schmitz K.: Mechanical properties of a biodegradable balloon-expandable stent from poly(L-lactide) for peripheral vascular applications. *Journal of Medical Devices*, **1**, 84–88 (2007). DOI: [10.1115/1.2355683](https://doi.org/10.1115/1.2355683)
- [12] Grabow N., Bünger C. M., Schultze C., Schmohl K., Martin D. P., Williams S. F., Sternberg K., Schmitz K.-P.: A biodegradable slotted tube stent based on poly(L-lactide) and poly(4-hydroxybutyrate) for rapid balloon-expansion. *Annals of Biomedical Engineering*, **35**, 2031–2038 (2007). DOI: [10.1007/s10439-007-9376-9](https://doi.org/10.1007/s10439-007-9376-9)
- [13] Kimble L., Bhattacharyya D.: *In vitro* degradation effects on strength, stiffness, and creep of PLLA/PBS: A potential stent material. *International Journal of Polymeric Materials and Polymeric Biomaterials*, **64**, 299–310 (2014). DOI: [10.1080/00914037.2014.945203](https://doi.org/10.1080/00914037.2014.945203)
- [14] Wang Y.: Bioabsorbable scaffolds made from composites. U.S. Patent 20120290073 A1, USA (2012).
- [15] Wu T.: Biodegradable stent formed with polymer-bioceramic nanoparticle composite and preparation method thereof. WO 2012100651 A1 (2012).
- [16] Fakirov S., Evstatiev M., Schultz J. M.: Microfibrillar reinforced composite from drawn poly(ethylene terephthalate)/nylon-6 blend. *Polymer*, **34**, 4669–4679 (1993). DOI: [10.1016/0032-3861\(93\)90700-K](https://doi.org/10.1016/0032-3861(93)90700-K)
- [17] Fakirov S., Evstatiev M.: Microfibrillar reinforced composites – New materials from polymer blends. *Advanced Materials*, **6**, 395–398 (1994). DOI: [10.1002/adma.19940060513](https://doi.org/10.1002/adma.19940060513)
- [18] Kargin V., Bakeev N., Fakirov S.: New direct observation technique of structure of polymer solutions with aid of electron microscope (in Russian). *Doklady Akademii Nauk SSSR*, **159**, 885–888 (1964).
- [19] Apostolov A. A., Fakirov S.: Effect of the block length on the deformation behavior of polyetheresters as revealed by small-angle X-ray scattering. *Journal of Macromolecular Science Part B: Physics*, **31**, 329–355 (1992). DOI: [10.1080/00222349208215520](https://doi.org/10.1080/00222349208215520)
- [20] Fakirov S., Kamo H., Evstatiev M., Friedrich K.: Microfibrillar reinforced composites from PET/LDPE blends: Morphology and mechanical properties. *Journal of Macromolecular Science Part B: Physics*, **43**, 775–789 (2004). DOI: [10.1081/mb-120030024](https://doi.org/10.1081/mb-120030024)
- [21] Fakirov S., Bhattacharyya D., Shields R. J.: Nanofibrillar reinforced composites from polymer blends. *Colloids and Surfaces A: Physicochemical and Engineering Aspects*, **313–314**, 2–8 (2008). DOI: [10.1016/j.colsurfa.2007.05.038](https://doi.org/10.1016/j.colsurfa.2007.05.038)
- [22] Fakirov S., Bhattacharyya D., Lin R. J. T., Fuchs C., Friedrich K.: Contribution of coalescence to microfibril formation in polymer blends during cold drawing. *Journal of Macromolecular Science Part B: Physics*, **46**, 183–194 (2007). DOI: [10.1080/00222340601044375](https://doi.org/10.1080/00222340601044375)
- [23] Bhattacharyya D., Maitrot P., Fakirov S.: Polyamide 6 single polymer composites. *Express Polymer Letters*, **3**, 525–532 (2009). DOI: [10.3144/expresspolymlett.2009.65](https://doi.org/10.3144/expresspolymlett.2009.65)
- [24] Friedrich K., Hoffmann J., Evstatiev M., Ye L., Mai Y. W.: Improvements of stiffness and strength of bioresorbable bone nails by the MFC-concept. *Key Engineering Materials*, **334–335**, 1181–1184 (2007). DOI: [10.4028/www.scientific.net/KEM.334-335.1181](https://doi.org/10.4028/www.scientific.net/KEM.334-335.1181)
- [25] Letchford K., Sodegraad A., Plackett D., Gilchrist S., Burt H.: Lactide and glycolide polymers. In ‘Biodegradable polymers in clinical use and clinical development’ (eds.: Domb A., Kumar N., Azra A.) Wiley, Chichester, 319–365 (2011).
- [26] Friedrich K., Evstatiev M., Fakirov S., Evstatiev O., Ishii M., Harrass M.: Microfibrillar reinforced composites from PET/PP blends: Processing, morphology and mechanical properties. *Composites Science and Technology*, **65**, 107–116 (2005). DOI: [10.1016/j.compscitech.2004.06.008](https://doi.org/10.1016/j.compscitech.2004.06.008)
- [27] Aklonis J. J., Tobolsky A. V.: Relationship between creep and stress relaxation. *Journal of Applied Physics*, **37**, 1949–1952 (1966). DOI: [10.1063/1.1708645](https://doi.org/10.1063/1.1708645)
- [28] Siengchin S., Psarras G. C., Karger-Kocsis J.: POM/PU/carbon nanofiber composites produced by water-mediated melt compounding: Structure, thermomechanical and dielectrical properties. *Journal of Applied Polymer Science*, **117**, 1804–1812 (2010). DOI: [10.1002/app.32133](https://doi.org/10.1002/app.32133)

Direct correlation between modulus and the crystalline structure in isotactic polypropylene

A. Menyhárd^{1*}, P. Suba³, Zs. László³, H. M. Fekete³, Á. O. Mester³, Zs. Horváth¹, Gy. Vörös¹, J. Varga¹, J. Móczó²

¹Laboratory of Plastics and Rubber Technology, Department of Physical Chemistry and Materials Science at Budapest University of Technology and Economics, H-1111 Budapest, Műgyetem rkp. 3., Hungary

²Hungarian Academy of Sciences, Chemical Research Centre, Institute of Environmental and Material Chemistry, H-1025 Budapest, Pusztaszeri út 59-67., Hungary

³Tisza Chemical Works Ltd., H-3581, P.O. Box 20., Hungary

Received 9 October 2014; accepted in revised form 15 December 2014

Abstract. Mechanical properties and crystalline structure of isotactic polypropylene (iPP) types were studied using polymers, which were polymerized differently in order to obtain diverse molecular architectures. The objective of this work is to describe quantitative correlation between the crystalline structure and the elastic modulus in order to predict structures with expectably advantageous properties. The molecular mass was measured by gel permeation chromatography (GPC) and the regularity of molecular structure was investigated by Fourier transform infrared spectroscopy (FTIR) and stepwise isothermal segregation technique (SIST). The chain regularity of the studied samples is varying in a wide range according to the results of SIST and FTIR measurements. The crystalline structure was characterized by differential scanning calorimetry (DSC) and wide angle X-ray scattering (WAXS). The tensile properties were determined by standardized tensile tests. The results indicate clearly that the increased chain regularity is accompanied by a proportional advancement in crystallinity and consequently proportionally larger stiffness. Moreover, the results of this work were compared to those obtained on other previously produced iPP samples and it can be established that the correlations found during this work are valid generally. An empirical model was developed also, which connects the stiffness to the structural parameters of iPP and makes possible the design and prediction of materials with targeted molecular structure and properties.

Keywords: mechanical properties, modeling and simulation, crystalline structure, structure-property correlation, stiffness

t1. Introduction

iPP is one of the commodity polymers used in large quantity nowadays [1]. Its advantageous price/performance ratio is the key to the success of this polymer. iPP is a crystalline polymer and its properties are determined by its complex crystalline structure [1]. The basic structural units of iPP are the chain-folded fibrillar or lamellar primary crystallites, which can be classified into supermolecular structures with diverse geometry (spherulites, cylindrites, hedrites, quadrites, etc.) [2–4]. Moreover, iPP has three crys-

talline modifications (α -, β - and γ -form) [2, 4–6], which influences also its mechanical properties. The monoclinic α -modification is the thermodynamically stable form, which is formed during the most frequently applied industrial practices [2]. In the past decades considerable attention was paid to the study of those parameters, which influence the mechanical properties of iPP. A short summary is given about these findings in the followings. Most of the related works describe that the stiffness depends on the crystalline structure developing during the

*Corresponding author, e-mail: amenyhard@mail.bme.hu

processing of the product [1, 7–10], i.e. the higher the crystallinity the larger the stiffness. The presence of nucleating agents promotes the formation of specific crystalline structures and improves crystallinity, lamella thickness is also larger in the case of effective nucleation [11–14]. Consequently, the stiffness of iPP containing nucleating agent is larger than that of non-nucleated samples [15]. Moreover, some special nucleating agents are selective to the β -form of iPP [16, 17]. The β -modification has lower stiffness and significantly larger impact resistance compared to the α -form [16, 18]. Stern *et al.* [19] have pointed out that the molecular mass can influence stiffness as well. He found that the increasing molecular mass results in decreased stiffness, because large molecular mass hinders the crystallization process of iPP with due to the kinetic effect. However, we have to note that he has not paid attention to the density and distribution of chain defects in those iPP polymers, which were used during his studies. Gahleitner *et al.* [20] found similar tendency, but the decreasing stiffness was explained by the different spherulitic structure formed in the polymers with different molecular masses.

The phenomenon that the molecular structure influences the overall crystallinity and consequently mechanical properties is known, however, only few work can be found according to our knowledge, which are linking the molecular architecture to the crystalline structure and to the mechanical properties quantitatively [21–27]. Pukánszky *et al.* [7] revealed that crystallinity and lamella thickness determines the stiffness of iPP, although the empirical correlation provided by him is applicable only in a limited crystallinity range. The aim of this work is to study the stiffness of iPP samples with diverse molecular architectures and to characterize the effect of molecular architecture (isotacticity and chain regularity) on the crystalline structure and consequently on the tensile properties of iPP. In addition our goal is the development of a theoretical model, which links the crystalline structure directly to the mechanical properties in the entire crystallinity range.

2. Experimental

2.1. Materials and sample preparation

Five iPP homopolymer grades produced by TVK (Hungary) were used in the experiments. The specification of iPP samples is included in Table 1. In order to produce polymers with significantly differ-

Table 1. The iPP samples used during the recent work

Sample		Donor type	MFR [g/10 min]
iPP1	ED1	Propyl-trimethoxy-silane	2.8
iPP2	ED1	Propyl-trimethoxy-silane	11.0
iPP3	ED1	Propyl-trimethoxy-silane	1.2
iPP4	ED2	Cyclohexyl-methyl dimethoxy-silane	16.0
iPP5	ED3	Dicyclopentyl- dimethoxy-silane	3.0

ent molecular architectures different external donors (ED) and the same Ziegler-Natta catalyst were applied during polymerization. The polymerization was carried out in a small scale vessel in batch mode at 70°C, 120 min and 250 L/min of stirring. The amount of hydrogen feed was modified, the final MFR is given together with the ED types also in Table 1.

The polymer powders were homogenized with additives (1500 ppm Irganox B 215, 400 ppm glycerol-monostearate, 400 ppm Ca-stearate (BASF, Switzerland)) in a Brabender W 50 EHT internal mixer (Brabender GmbH, Germany) at 190°C, 50 rpm for 10 min and subsequently were compression molded into 1 mm thick plates at 190°C for 5 min using a Fontijne SRA 100 laboratory compression molding machine (Fontijne, The Netherlands). The platelets were cooled with water in the compression molding machine and the pressure was kept constant during cooling. MFR values were measured after homogenization. DSC, WAXS, SIST, tensile, GPC measurements were carried out on samples cut from these plates. 100 μ m thick films were compression molded at 190°C from the samples for FTIR analysis. Cooling conditions used for films were the same as for the platelets.

2.2. Experimental techniques

Melting and crystallization of the polymers was studied by DSC technique using a Perkin Elmer DSC7 apparatus (Perkin Elmer, United States) at a heating and cooling rate of 10°C/min. The experiments were carried out on samples with mass of 3–5 mg under N₂ atmosphere. The samples were heated up to 220°C and held there in order to eliminate the thermal and mechanical prehistory. The crystallinity of the samples was determined based on the melting curve recorded during first heating according to Equation (1):

$$X = \frac{DH_m}{\Delta H_m^0} \quad (1)$$

ΔH_m and ΔH_m^0 are the experimentally recorded and equilibrium enthalpy of fusion. The value of ΔH_m^0 (146 J/g) has been taken from the work of Monasse and Haudin [28]. The SIST experiments were carried out on the same equipment between 160 and 100°C. After the thermal and mechanical prehistory of the samples had been eliminated at 220°C for 5 min the samples were cooled to 160°C at a cooling rate of 80°C/min and held there for 3 hours. Subsequently, the samples were cooled to next crystallization temperature (150°C) and held there for another 3 hours. Each temperature ramp took 3 hours and the step was 10°C. After the final crystallization step at 100°C was completed the samples were re-heated again and melting curves were recorded. The SIST method assumes; if the polymer is crystallized at high temperature, then only those fractions will be able to crystallize, wherein thick lamellas can develop proportionally to the crystallization temperature. Of course the holding time should be long enough, because the development of crystalline phase at high temperatures is slow. Based on this idea the crystalline structure of the polymer can be fractionated by using appropriate temperature program [29, 30]. We have to notice here that the accurate experimental condition would be if the sample could be held for endless time at higher temperatures. However, it can be established that if the holding time is longer than 2 hours the loss of fractions with long isotactic sequence is negligible. SIST can be used for characterization of distribution of stereo- and regiodeflects in iPP similarly to temperature rise elution fractionation (TREF) [31]. According to our earlier observation chain regularity estimated by calorimetry correlates strongly with properties, because they are determined by the crystalline structure [32]. After the samples were crystallized according to the SIST method they were melted at a heating rate of 10°C/min. The partial amount of different crystalline fractions can be calculated by separating the melting peaks refer to each crystallization step. From the upper and lower temperature limit of each fraction the characteristic range lamella thickness can be calculated according to Gibbs-Thomson equation (Equation (2)):

$$T_m = T_m^0 \left(1 - \frac{2\sigma_e}{\rho_c \Delta H_m^0 \ell} \right) \quad (2)$$

where T_m^0 is the equilibrium melting point, σ_e is the free energy of folding surface of the lamella, ρ_c is

the crystal density and ΔH_m^0 is the equilibrium heat of fusion of iPP. ℓ is the lamella thickness. The values of all constants appearing in Equation (2) are included in Table 2. Once the lamella thickness is known, the regular iPP sequence length can be obtained according to Equation (3):

$$I = 3 \frac{\ell}{c} \quad (3)$$

I is the length of the regular flawless isotactic PP sequence and c is the height of the unit cell of α -iPP, which is 6.5 Å according to crystallographic symmetry data [33]. ℓ/c has to be multiplied by 3 since iPP chains form 31 helices.

Crystalline structure was studied by WAXS technique as well. Diffractograms were recorded using a Philips PW 1830/PW type equipment (Philips, The Netherlands) with CuK_α radiation at 40 kV and 35 mA and X Pert PRO MPD type equipment (PANalytical, The Netherlands) with CuK_α radiation at 40 kV and 30 mA. The crystallinity of the samples was determined using the amorphous halo of iPP taken from the work of Boger *et al.* [35]

The isotacticity of the samples were characterized by FTIR. The spectra were recorded using a Mattson Galaxy 3020 apparatus (Unicam, England) in the wavelength range of 4000 and 400 cm^{-1} . Determination of isotacticity was carried out based on the work of Sundell *et al.* [36].

Mechanical properties were characterized by tensile testing using an Instron 5566 apparatus (Instron, Germany). Tensile modulus was determined at 0.5 mm/min cross head speed and 115 mm gauge length, while other tensile characteristics were measured at 5 mm/min speed.

Molecular mass and its distribution were characterized by gel permeation chromatography (GPC) as well. GPC measurements were carried out using a PL-GPC 210 (Polymer Laboratories Ltd., United Kingdom) equipment according to ISO 16014 standard procedure. The samples were dissolved in 1,2,4-trichloro-benzene (TCB) (1 mg/mL) at 160°C

Table 2. All constants, which were used during the calculation of lamella thickness during evaluation of SIST experiments

Constant	Value (dimension)	Literature
T_m^0	481 K	[2, 28]
σ_e	0.122 J/m ²	[28]
ρ_c	936 kg/m ³	[34]
ΔH_m^0	146 000 J/kg	[2, 28]

for 2 hours and stabilized by 2,6-di-tert-butyl-4-diethylphenol (BHT) (100 mg/L).

3. Results and discussion

3.1. Molecular architecture

The molecular mass and polydispersity values of the studied samples are presented in Table 3 and the distribution of molecular mass is represented in Figure 1. The results indicate clearly that iPP3 and iPP5 are so called bimodal polymers, because these grades contain a fraction with larger molecular mass. It appears as a shoulder on the GPC curves and it is reflected on the larger average M_w and Pd of iPP3 and iPP5.

The regularity of the polymer chains developed during polymerization using different EDs and hydrogen feed is characterized by the isotacticity and by the regular iPP sequence length. The isotacticity of the polymers was characterized by IR measurements, using the intensity ratio of bands at 998 and 973 cm^{-1} , which ratio is proportional to isotacticity [36]. The results are given in Table 4 indicating that the isotacticity of the samples varies in a wide range. The closer the ratio of I_{998}/I_{973} to 1 the larger the isotacticity, however, we have to mention that the correlation is not linear so the ratio is not equal

Table 3. The molecular mass data of selected materials

Sample	M_w [g/mol]	M_n [g/mol]	Pd
iPP1	231 707	68 882	3.4
iPP2	207 973	52 559	4.0
iPP3	420 731	87 589	4.8
iPP4	222 370	58 993	3.8
iPP5	311 667	63 971	4.9

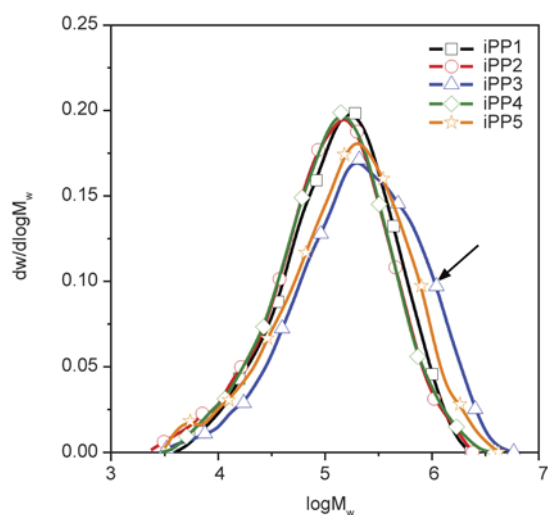


Figure 1. Distribution of molecular mass of the selected polymers

Table 4. The ratio of IR bands at 998 and 973 cm^{-1}

Sample	I_{998}/I_{973}
iPP1	0.81
iPP2	0.84
iPP3	0.90
iPP4	0.93
iPP5	0.97

to the isotacticity expressed in percentage. Based on IR results, ED2 and ED3 provide regular isotactic chain structures. The I_{998}/I_{973} value of iPP5 polymerized using ED3 suggests that this polymer has exceptionally regular stereo-structure. The isotacticity of the samples is important, but I_{998}/I_{973} value does not provide any information either about the amount of region-defects or about the distribution of all chain defects.

In order to characterize the distribution of chain defects SIST measurements were carried out. The results of these experiments are demonstrated in Figure 2. It is clear that the different ED systems are resulting in significantly different distribution of chain defects.

According to Figure 2 lots of chain defects are forming during polymerization in the presence of ED1 resulting in relatively low I (iPP1-iPP3). SIST distribution curve of iPP3, which has the largest M_w among iPP1-iPP3, indicate the longest isotactic chain sequence in polymers polymerized using ED1. The chain regularity is significantly larger if ED2 or ED3 were applied and ED3 results in the most regular structure, where the most frequent fraction is longer than 100 regular monomer units. The distri-

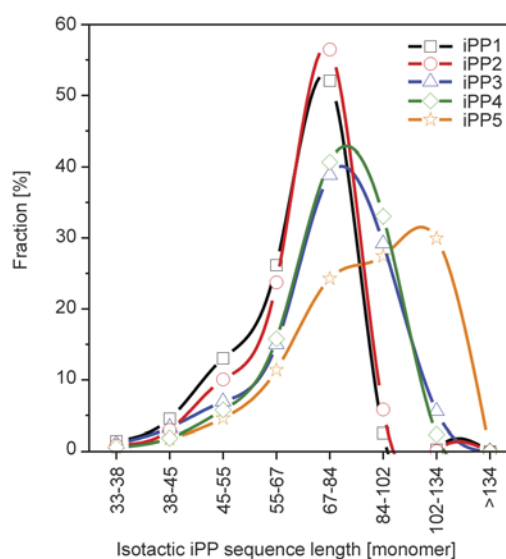


Figure 2. The distribution of length of flawless isotactic iPP sequences

bution curve reflects the chain regularity nicely, however it cannot be correlated directly to the properties of the polymer, thus the weight average of flawless isotactic sequence length (I_{av}) calculated from the distribution curve is used for characterization of chain regularity in the followings. If we know the crystallinity (X) of the sample, which can be calculated from the melting curve after the SIST treatment and M_w , the average length of folding chain can be obtained as well. The average number of repeating units (N) can be calculated according to Equation (4):

$$N = \frac{M_w}{M_m} \quad (4)$$

where M_m is the molecular mass of the repeating units. Consequently, the length of folding chain can be expressed as Equation (5):

$$F = \frac{N(1 - X)}{\frac{NX}{I_{av}}} \quad (5)$$

The expression of $N(1 - X)$ gives the number of repeating units, which are in the amorphous folding sequences and NX/I_{av} is the number parallel crystalline sequences. In the folded lamella the number of parallel chain sequences are equal to the number of folding of sequences (FS) or $FS + 1$. In our case '+ 1' is negligible, thus F can be calculated according Equation (5). In other words crystallinity can be expressed with the sequence lengths as well (Equation (6)):

$$X = \frac{I_{av}}{I_{av} + F} \quad (6)$$

The correlation between isotacticity and chain regularity and crystallinity is presented in Figure 3. I_{av} increases with increasing of isotacticity as it was expected, however F decreases much steeper as I_{av} increases. We have to remark here that I_{av} is also related to the lamella thickness. It is well discernible that crystallinity increases steeply with the enhancement in chain regularity. The tendencies reported here are very important, because they demonstrate clearly that the crystallinity of the sample can change significantly, while the lamella thickness increases slightly. Therefore, both key parameters – crystallinity and lamella thickness [7] – must be considered during the characterization of change in crystalline structure.

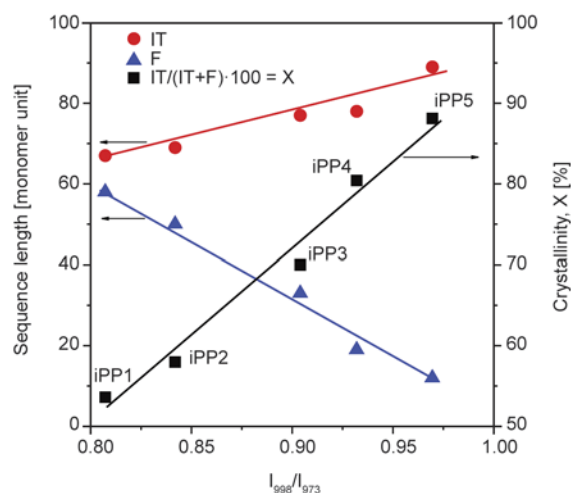


Figure 3. The correlation between sequence length and isotacticity and its effect on crystallinity

3.2. Crystalline structure of studied materials

The results of calorimetric experiments are summarized in Table 5. The crystallinity of the samples varies in a wide range. The application of ED1 results in significantly lower crystallinity compared to ED2 and ED3 due to the smaller chain regularity in its presence. The peak temperatures of melting (T_{mp}) of iPP1–3 are lower than that of iPP4 and iPP5, representing that thicker lamellas can form in samples with larger chain regularity during dynamic cooling at 10°C/min. The effect is pronounced in the case of ED3, which may result in the most regular chain structure.

The crystallinity of the samples was determined from WAXS pattern as well and the results obtained by the two different methods are compared in Figure 4. Although the points presented in Figure 4 scatter, the tendency demonstrates clearly that crystallinity determined by the two experimental tech-

Table 5. Crystallization and melting characteristics of studied samples recorded after elimination of the pre-history of the samples

Sample	ΔH_m [J/g]	X [%]	T_{mp} [°C]	T_m [°C]	T_{cp} [°C]
iPP1	69.2	46.7	161.8	166.5	106.1
iPP2	80.0	54.1	162.5	167.3	107.8
iPP3	84.1	56.8	163.2	169.2	110.1
iPP4	95.6	64.6	167.5	172.3	110.8
iPP5	100.5	67.9	168.2	172.8	112.6

ΔH_m is the enthalpy of fusion recorded during first heating run
 T_{mp} and T_m are the peak and end temperatures of melting respectively recorded during first heating run
 T_{cp} is the peak temperature of crystallization, which was recorded during cooling run

niques is the same. X was obtained from the first melting trace in DSC measurements, which was recorded before the elimination of thermal and mechanical prehistories in order to represent the complex structure formed during cooling as accurately as possible. Accordingly, X determined from WAXS patterns and DSC traces is characteristic for the crystallinity of compression molded platelets. The equal values of X indicate that the ΔH_m^0 determined by Monasse and Haudin is a reliable constant and we are using this constant throughout all of our calculations. We have to remark here that significantly different values of ΔH_m^0 can be found in the recent literature (see in the review of Varga [2]), consequently the crystallinity calculated using different ΔH_m^0 can be questionable. Figures 3 and 4 prove unambiguously that crystallinity increases steeply with the enhancement of parameters referring chain regularity (isotacticity and regular sequence length). Although, we have to remark here that crystallinity obtained during SIST measurements (Figure 3) and that determined by DSC and WAXS on compression molded specimens differ considerably, because of the different crystallization conditions. More perfect crystalline structure with larger ΔH_m forms during isothermal crystallization in SIST measurement at high temperatures. Data obtained by SIST, WAXS and DSC report similar tendency, thus the effect of chain regularity is the same under dynamic cooling (practical conditions) and isothermal conditions.

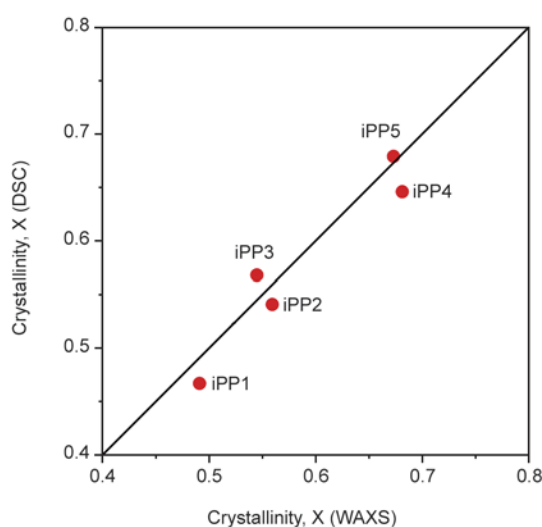


Figure 4. The crystallinity of compression molded platelets determined based on WAXS and DSC measurements

As we mentioned earlier lamella thickness is the second parameter, which should be considered independently, during characterization of crystalline structure. Lamella thickness can be estimated from the melting curves, because each point of the melting curves recorded by DSC can be attributed to a lamella thickness according to the well-known Gibbs-Thomson equation [13]. Romankiewicz and Stezyski [37] reported a possible way for estimation of lamella thickness distribution curve directly from the calorimetric melting curve. Accordingly, the distribution function of lamella thickness can be obtained using Equation (7):

$$\frac{1}{M} \cdot \frac{dM}{d\ell} = \frac{1}{M} \cdot \frac{dE}{dT} \cdot \frac{(T_m^0 - T_m)^2 \rho_c}{2\sigma_e T_m^0} \quad (7)$$

T_m is the actual melting temperature (each point of the DSC curve), T_m^0 is the equilibrium temperature of melting, σ_e (0.122 J/m^2) is the free energy of the folded surface of a lamella, and ℓ is the thickness of the lamella. M is the mass of the crystalline fraction. dE is the energy needed to melt the crystalline fraction with a mass of dM in the temperature range of $T + dT$. The $(1/M) \cdot (dE/dT)$ term of Equation (7) can be measured directly by DSC, because it equals to the recorded heat flow divided by the rate of heating. The second term of the right side of the distribution function (Equation (7)) can be calculated numerically. As a consequence, the lamella distribution curve can be plotted as a function of temperature. The melting curve and the distribution function of iPP1 are demonstrated in Figure 5 in order to illustrate the method. Figure 5a shows the melting trace and Figure 5b is the distribution function.

The distribution function of lamella thickness is difficult to use for the characterization of the material and it is impossible to compare with a modulus data. Thus, the distribution function has to be characterized with one quantity, which can be the thickness at the peak as well as the weight average of lamella thickness. We believe that an entire curve cannot be represented accurately using any of its points, therefore we decided using the weight average of lamella thickness function, which can be deduced according to Equation (8):

$$\bar{\ell} = \frac{\int f(\ell) \ell d\ell}{\int f(\ell) d\ell} \quad (8)$$

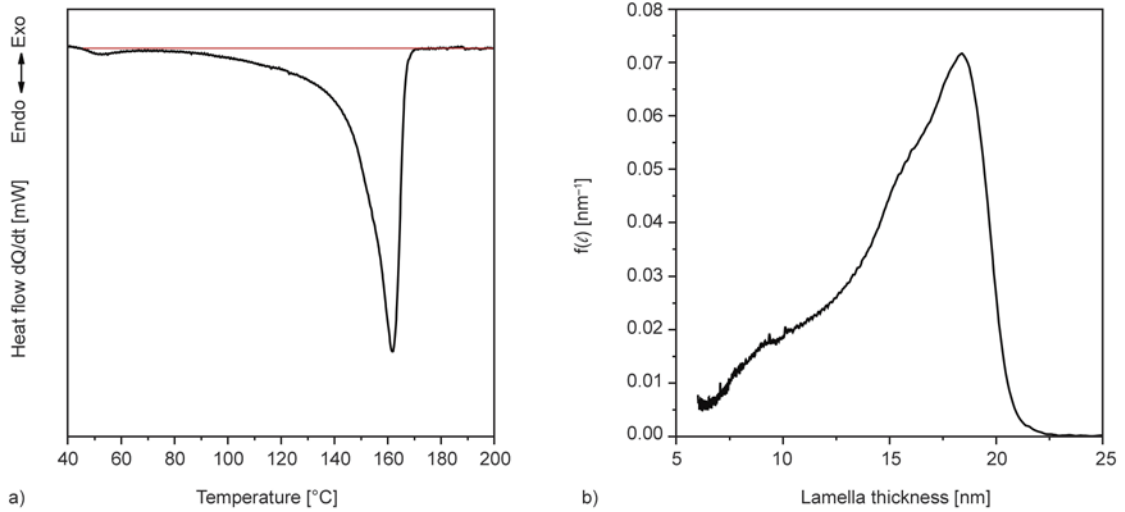


Figure 5. The melting curve recorded during first heating run of iPP1 (a) and the distribution function of lamella thickness (b) obtained according to Equation (7)

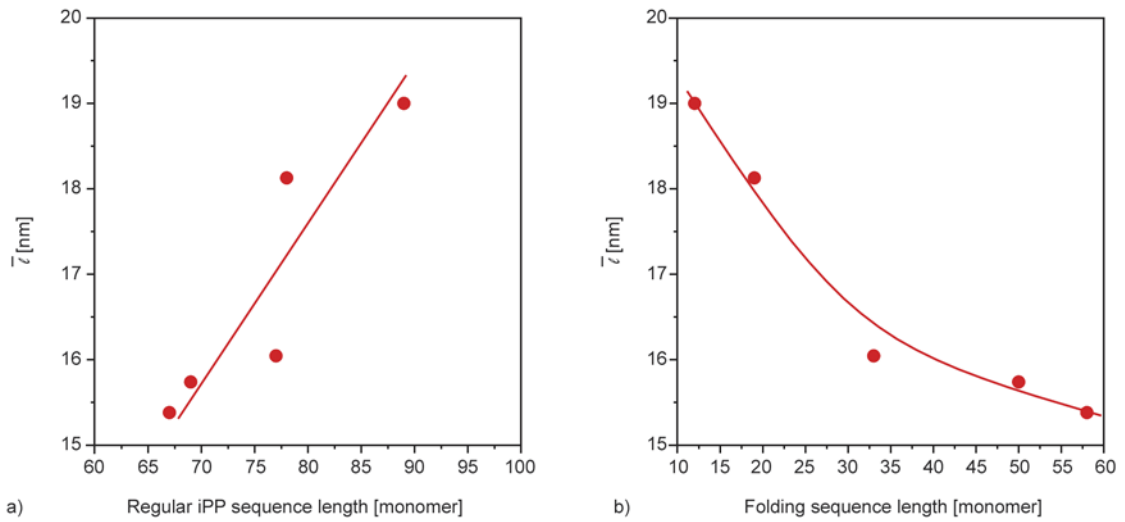


Figure 6. Relationship between \bar{l} value and (a) regular iPP sequence or (b) folding length

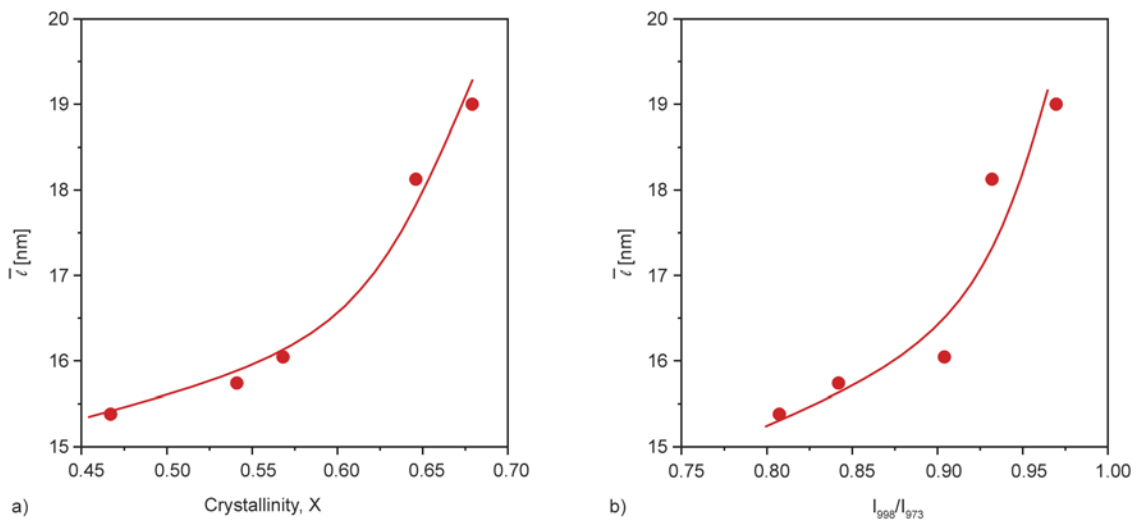


Figure 7. Correlation between \bar{l} value and (a) crystallinity or (b) isotacticity

$f(\ell)$ is the distribution function of lamella thickness and ℓ is the lamella thickness. The obtained $\bar{\ell}$ is the weight average of the distribution function and its value is plotted against the parameters of chain regularity in Figure 6 and 7.

It is well discernable that regular sequence length correlates strongly with lamella thickness. The longer the regular iPP chain, the thicker lamellas are formed in the polymer. The correlation seems to be close to linear in spite of the scattering of the points. F correlates strongly with lamella thickness as well, but the relationship is not linear. The results indicate unambiguously that high chain regularity results in the formation of thick lamellas. In the case of lower regularity lamella thickness decrease considerably, but crystallinity can be still relatively large. This tendency is represented by the non-linear relationship between lamella thickness and X (Figure 7).

3.3. Tensile properties

The results of tensile test are presented in Table 6. Mechanical properties of the studied samples differ considerably because of their significantly different crystalline structure indicating that the conditions of polymerization determine the properties of the product. In addition the stress at yield values correlate strongly with the modulus values, proving that the tensile measurements are reliable. The modulus values and their correlation with stress at yield are represented in Figure 8.

Effect of chain regularity on modulus is given in Figure 9. As it was suspected the chain regularity determined by the SIST measurement correlates

Table 6. The results of tensile tests

Sample	E [GPa]	σ_y [MPa]	ε_y [%]
iPP1	0.74±0.01	20.30±0.24	12.27±0.60
iPP2	0.93±0.02	24.15±0.40	11.71±0.36
iPP3	1.19±0.03	28.11±0.19	9.36±0.47
iPP4	1.77±0.02	36.92±0.36	6.31±0.39
iPP5	1.83±0.05	35.16±0.83	5.43±0.20

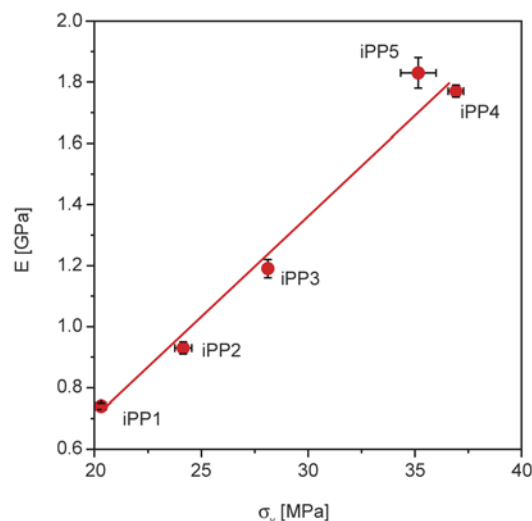


Figure 8. Modulus as a function of stress at yield values of studied samples

strongly with the modulus. The more regular chain structure is accompanied by proportionally larger modulus. Similar correlation can be found between the modulus and isotacticity as well. Since these molecular parameters are influencing the tendency for crystallization they affect the crystalline structure and consequently the modulus according to the same way (Figure 10).

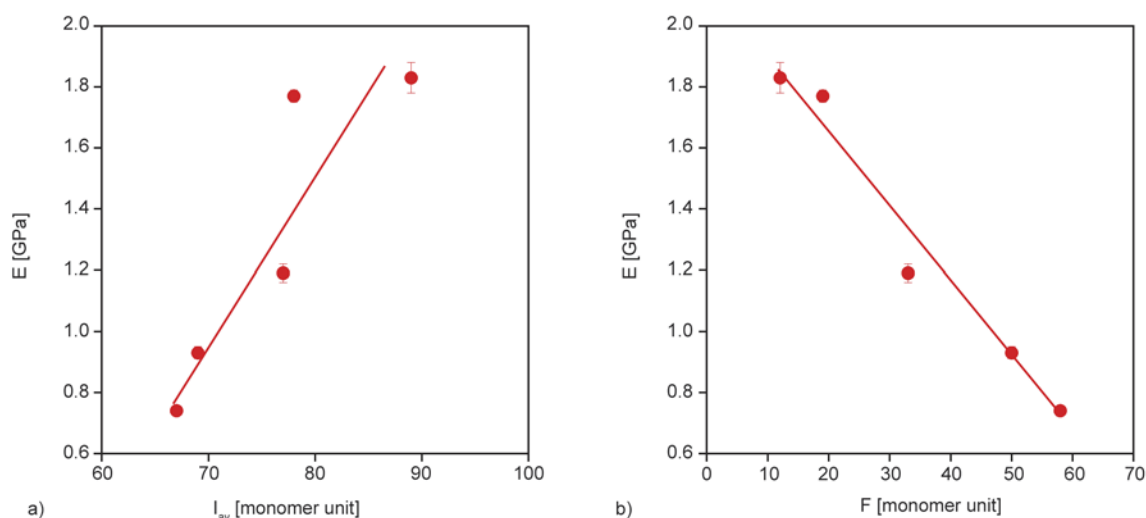


Figure 9. The effect of I_{av} (a) and F (b) on modulus

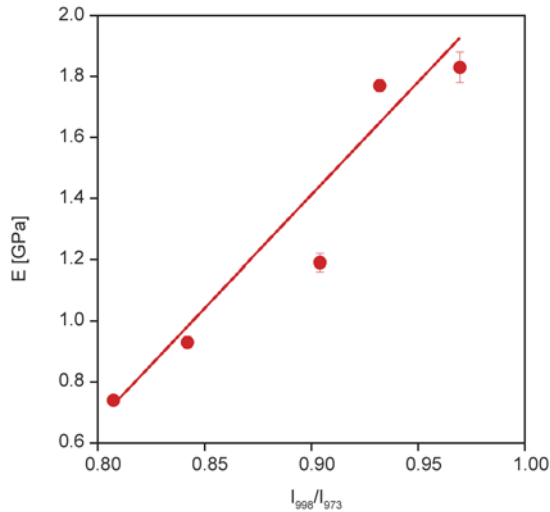


Figure 10. The modulus as a function of isotacticity

The modulus is plotted as a function of lamella thickness and crystallinity in Figure 11. It is clear that modulus depends strongly on both parameters, however the correlation seems not to be linear if the entire crystallinity range is demonstrated for example (Figure 11b). Although, a linear function can be fitted to the plots from $X \approx 0.5$ to 0.7 , which covers the range of iPP grades in the practice. That is why the linear correlation developed by Pukánszky and coworkers [7, 38] provides accurate results. The shape of the curve at lower lamella thickness and crystallinity can be speculated on (marked with dashed line in Figure 11), but the shape of the correlation at large lamella thickness and crystallinity is completely unknown. Therefore the modeling of stiffness in the upper region is an important question of material design and development, even if the modeling is based on empirical correlations.

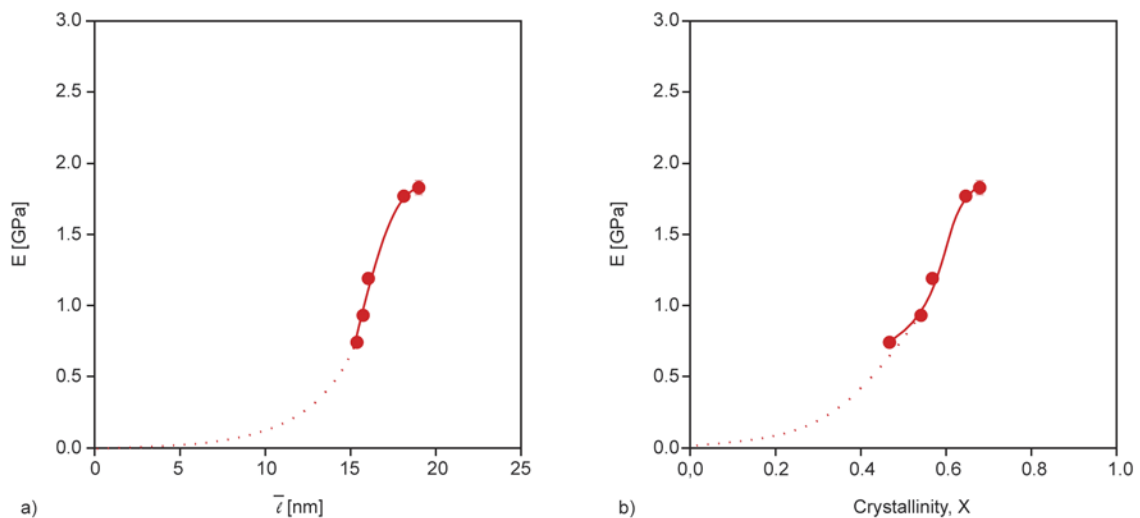


Figure 11. The modulus as a function of the two major parameters of crystalline structure – a) lamella thickness, b) crystallinity

3.4. Empirical modeling of stiffness using structural parameters

Based on the earlier results [7, 38] and our experimental data it can be concluded that stiffness depends predominantly on crystallinity and lamella thickness. Consequently, the following expression should be solved (Equation (9)):

$$E = f(X, \bar{l}) \quad (9)$$

E is the elastic moduli of iPP, X is the crystallinity and \bar{l} is the weight average of lamella thickness function in Equation (9). We have to note that stiffness changes from a minimum to a maximum value. The minimum stiffness (E_{\min}) is the stiffness of the amorphous iPP and it is in the range of 0.01–0.02 GPa depending on the molecular mass [39]. 0.01 GPa was used in our study as E_{\min} value. The maximum stiffness (E_{\max}) is the stiffness of the perfect iPP crystal, which value cannot be obtained experimentally. Moreover, it depends on the unit cell geometry of iPP, thus it should depend on the direction as well. E_{\max} can be calculated only theoretically from the propagation of longitudinal sound waves in the material according to the suggestion of van Krevelen and Nijenhuis [40]. The propagation rate depends on the crystallinity and experimental data can be extrapolated linearly to a perfect crystal ($X = 1$ in polymeric materials). The elastic modulus determines the vibration of the neighboring molecules, consequently the Equation (10) can be written:

$$E = u_L^2 \rho_{cr} \quad (10)$$

where E is the elastic modulus, u_L is the propagation rate of the sound wave. The extrapolated value of u_L

for iPP is 2650 m/s [40] and the crystal density is 936 kg/m³ (see in Table 2). Accordingly, the calculated E_{\max} is 6.6 GPa using the above data and Equation (10). We have to note that this value is much smaller than the theoretical stiffness along the polymer chain obtained by Kunugi [41] and Sawatari and Matuso [42] based on molecular dynamic calculations. The calculated $E_{\max} = 6.6$ GPa is more realistic, since it is valid without any orientation in the sample. Considering the abovementioned E_{\min} and E_{\max} data, an empirical function is suggested to describe the stiffness in the entire crystallinity range (Equation (11)):

$$E = E_{\min} + (E_{\max} - E_{\min})e^{\left(-\left(\frac{1-X}{X}\right)^\alpha \cdot \left(\frac{1}{\ell_{av}}\right)^\beta\right)^\gamma} \quad (11)$$

where E is the modulus, X is the crystallinity, ℓ_{av} is the average lamella thickness and α , β , γ are iterative parameters characteristics for iPP. Equation (11) gives back E_{\min} and E_{\max} for completely amorphous ($X = 0$ and $\ell_{av} = 0$) and perfectly crystalline ($X = 1$ and $\ell_{av} = \infty$) iPP respectively. We have to point out that X and ℓ_{av} are handled as independent parameters in Equation (11), despite the fact that larger X might be accompanied by proportionally thicker lamellas in iPP homopolymers (See in Figure 7a). The following formula is used to describe the correlation between ℓ_{av} and X presented in Figure 7a in the entire crystallinity range (Figure 12) (Equation (12)):

$$\ell_{av} = a + be^{\left(\frac{X}{1-X}\right)^c} \quad (12)$$

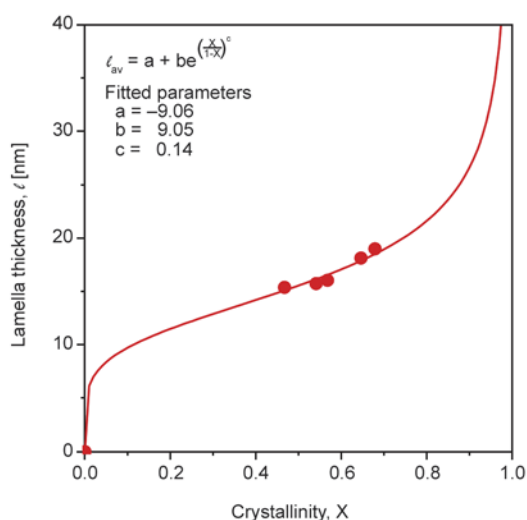


Figure 12. Fitting Equation (12) to lamella thickness – crystallinity data

The correlation demonstrated in Figure 12 is in good agreement with our expectations, because lamella thickness is infinite at $X = 1$ and decrease to zero at low crystallinity. Moreover, it demonstrates clearly that the lamella thickness increases steeply at low crystallinity, which means that the formation of thinner lamella than 5–8 nm is not probable even in the low crystallinity PP grades. Using Equation (3), we can recalculate that in average at least 20–30 regular monomer units are necessary to form crystalline structure. The variables of a , b and c are iterative parameters without any physical meaning, but using these values the number of independent variables in Equation (11) can be reduced to the crystallinity (X) only and Equation (11) can be fitted to the experimental data shown in Figure 11b. The fitted curve can be seen in Figure 13.

Once the parameter set of α , β and γ is determined the modulus of iPP samples can be predicted using Equation (11) in the entire crystallinity range if X and ℓ_{av} are available. Figure 14 represents the calculated and measured modulus values of several unpublished iPP samples studied earlier. Both random copolymers and homopolymers were included in this prediction in order to check the validity of the proposed empirical equation. The results indicate clearly that the prediction is accurate and reliable. Although, the results show some scattering, which may originate from experimental errors and inaccuracies, the predicted values are close to the measured ones consequently Equation (11) can be used for predicting of modulus from crystalline parameters obtained from calorimetric curves.

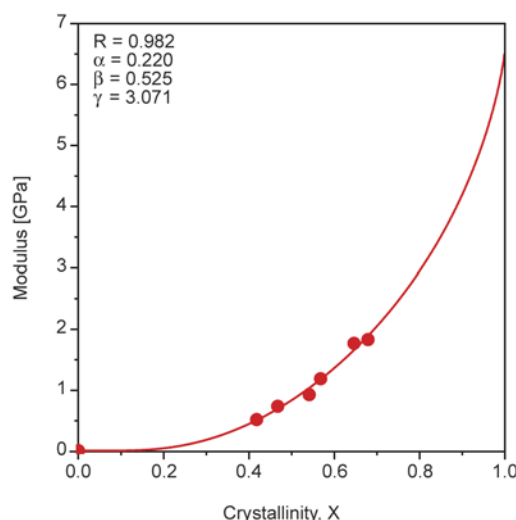


Figure 13. Fitting Equation (11) to modulus – crystallinity data

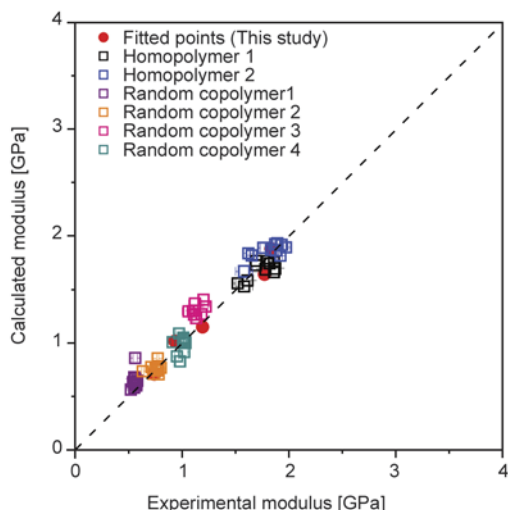


Figure 14. Correlation between the measured and calculated modulus values

3.5. Prediction of structure with desired properties

The improvement of stiffness is a crucial issue in the industrial practice. Polypropylene grades have stiffness in the range of 1.5–2.5 GPa, which is much smaller than the calculated 6.6 GPa. Recently, the desired limit value to be exceeded is 3 GPa. Using our simple equation the crystalline structure necessary to fulfill this need can be predicted, if we simulate the modulus using fixed crystallinity or lamella thickness data. Figure 15 presents such simulation. The data demonstrated in Figure 15 indicate clearly that 3 GPa is reachable. Figure 15a presents that lamella thickening has a limited effect. Only the lamella thickness below 30 nm influences stiffness. Although, it is also clearly demonstrated in this Fig-

ure, that thicker lamellas result in larger modulus at the same level of crystallinity. The effect of improvement in crystallinity can be seen in Figure 15b and it is well discernible that the 3 GPa cannot be exceeded if crystallinity is smaller than 70%. These simulated results indicate that the desired mechanical properties can be achieved if crystallinity is around 75% and lamella thickness is larger than 30 nm. This is in good agreement with our earlier results that 3 GPa of modulus can be reached by carefully designed annealing experiments [38].

4. Conclusions

iPP grades with significantly different chain regularities were studied in order to describe the effect of molecular architecture on the crystalline structure and consequently the influence on stiffness. The results support clearly the well-known fact that the increased chain regularity results in larger crystallinity and the formation of thicker lamellas and consequently proportionally larger modulus. Moreover, the deep analysis of chain structure revealed that crystallinity and lamella thickness are two independent parameters of crystalline structure despite of the fact that they show correlation in several cases. The results proved clearly that the modulus of the iPP products depends strongly on the crystallinity and lamella thickness, which correlation was characterized quantitatively. The upper lower boundary of modulus was determined and an empirical correlation was developed, which links the modulus to the crystalline structure. A parameter set was obtained for iPP and using the suggested empirical equation and these parameters, the modulus of

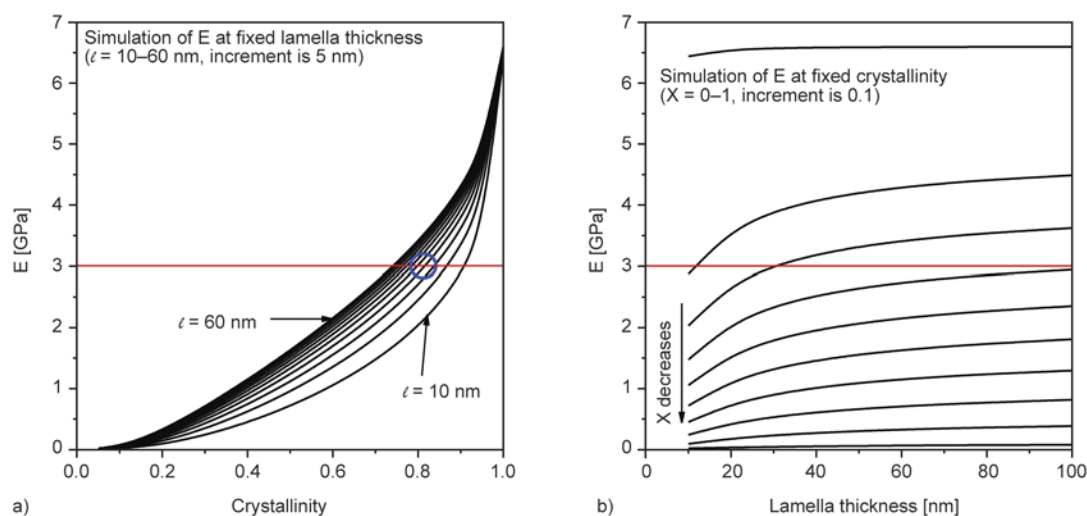


Figure 15. Modulus values predicted using (a) fixed lamella thickness or (b) fixed crystallinity values

injection molded iPP samples can be calculated from the crystallinity and lamella thickness data obtained from calorimetric experiments. A crystalline structure was predicted using the equation given this work for exceeding 3 GPa of elastic modulus without any reinforcement. Lamella thickness and crystallinity should be larger than 30 nm and 75% according to the prediction. We have to note that both parameters are influenced by chain regularity, which has to be increased significantly in order to fulfill this goal.

Acknowledgements

The Authors would like to express their gratitude to the János Bolyai Research Scholarship of the Hungarian Academy of Sciences and for the financial support of the National Scientific Research Fund of Hungary (OTKA Grant PD 109346) for the project on the structure-property correlations of polymeric materials.

References

- [1] Moore E. P.: Polypropylene handbook: Polymerization, characterization, properties, processing, applications. Hanser-Gardner Publications, Cincinnati (1996).
- [2] Varga J.: Crystallization, melting and supermolecular structure of isotactic polypropylene. in 'Polypropylene: Structure, blends and composites' (ed.: Karger-Kocsis J.) Chapman and Hall, London, Vol 1, 56–115 (1995).
- [3] Varga J.: Supermolecular structure of isotactic polypropylene. Journal of Materials Science, **27**, 2557–2579 (1992).
DOI: [10.1007/BF00540671](https://doi.org/10.1007/BF00540671)
- [4] Padden F. J., Keith H. D.: Spherulitic crystallization in polypropylene. Journal of Applied Physics, **30**, 1479–1484 (1959).
DOI: [10.1063/1.1734985](https://doi.org/10.1063/1.1734985)
- [5] Lotz B., Wittmann J. J., Lovinger A. J.: Structure and morphology of poly(propylenes): A molecular analysis. Polymer, **37**, 4979–4992 (1996).
DOI: [10.1016/0032-3861\(96\)00370-9](https://doi.org/10.1016/0032-3861(96)00370-9)
- [6] Phillips P., J., Mezghani K.: Polypropylene, isotactic (polymorphism). in 'The polymeric materials encyclopedia' (ed.: Salamone J. C.) CRC Press, Boca Raton, Vol 9, 6637–6649 (1996).
- [7] Pukánszky B., Mudra I., Staniek P.: Relation of crystalline structure and mechanical properties of nucleated polypropylene. Journal of Vinyl and Additive Technology, **3**, 53–57 (1997).
DOI: [10.1002/vnl.10165](https://doi.org/10.1002/vnl.10165)
- [8] Alberola N., Fugier M., Petit D., Fillon B.: Tensile mechanical behaviour of quenched and annealed isotactic polypropylene films over a wide range of strain rates. Journal of Materials Science, **30**, 860–868 (1995).
DOI: [10.1007/BF01178418](https://doi.org/10.1007/BF01178418)
- [9] Kalay G., Bevis M. J.: Processing and physical property relationships in injection-molded isotactic polypropylene. 1. Mechanical properties. Journal of Polymer Science Part B: Polymer Physics, **35**, 241–263 (1997).
DOI: [10.1002/\(SICI\)1099-0488\(19970130\)35:2<241::AID-POLB5>3.0.CO;2-V](https://doi.org/10.1002/(SICI)1099-0488(19970130)35:2<241::AID-POLB5>3.0.CO;2-V)
- [10] Fujiyama M.: Higher order structure of injection-molded polypropylene. in 'Polypropylene: Structure, blends and composites' (ed.: Karger-Kocsis J.) Chapman and Hall, London, Vol 1, 167–204 (1995).
- [11] Mitsuishi K.: Polypropylene, nucleating agents. in 'The polymeric materials encyclopedia' (ed.: Salamone J. C.) CRC Press, Boca Raton, Vol 9, 6602–6609 (1996).
- [12] Binsbergen F. L.: Heterogeneous nucleation in the crystallization of polyolefins: Part 1. Chemical and physical nature of nucleating agents. Polymer, **11**, 253–267 (1970).
DOI: [10.1016/0032-3861\(70\)90036-4](https://doi.org/10.1016/0032-3861(70)90036-4)
- [13] Wunderlich B.: Crystal nucleation, growth, annealing. Academic Press, London (1979).
- [14] Bassett D. C.: Polymer morphology: A guide to macromolecular self-organization. Macromolecular Symposia, **214**, 5–16 (2004).
DOI: [10.1002/masy.200451002](https://doi.org/10.1002/masy.200451002)
- [15] Avella M., dell'Erba R., Martuscelli E., Ragosta G.: Influence of molecular mass, thermal treatment and nucleating agent on structure and fracture toughness of isotactic polypropylene. Polymer, **34**, 2951–2960 (1993).
DOI: [10.1016/0032-3861\(93\)90620-P](https://doi.org/10.1016/0032-3861(93)90620-P)
- [16] Varga J.: β -modification of isotactic polypropylene: preparation, structure, processing, properties, and application. Journal of Macromolecular Science Part B: Physics, **41**, 1121–1171 (2002).
DOI: [10.1081/MB-120013089](https://doi.org/10.1081/MB-120013089)
- [17] Menyhárd A., Varga J., Molnár G.: Comparison of different -nucleators for isotactic polypropylene, characterisation by DSC and temperature-modulated DSC (TMDSC) measurements. Journal of Thermal Analysis and Calorimetry, **83**, 625–630 (2006).
DOI: [10.1007/s10973-005-7498-6](https://doi.org/10.1007/s10973-005-7498-6)
- [18] Mai J. H., Zhang M. Q., Rong M. Z., Bárány T., Ruan W. H.: Crystallization behavior and mechanical properties of nano-CaCO₃/ β -nucleated ethylene-propylene random copolymer composites. Express Polymer Letters, **6**, 739–749 (2012).
DOI: [10.3144/expresspolymlett.2012.79](https://doi.org/10.3144/expresspolymlett.2012.79)
- [19] Stern C., Frick A., Weickert G.: Relationship between the structure and mechanical properties of polypropylene: effects of the molecular weight and shear-induced structure. Journal of Applied Polymer Science, **103**, 519–533 (2007).
DOI: [10.1002/app.24156](https://doi.org/10.1002/app.24156)

- [20] Gahleitner M., Berneitner K., Neißl W., Paulik C., Ratajski E.: Influence of molecular structure on crystallization behaviour and mechanical properties of polypropylene. *Polymer Testing*, **14**, 173–187 (1995). DOI: [10.1016/0142-9418\(95\)93196-8](https://doi.org/10.1016/0142-9418(95)93196-8)
- [21] Halpin J. C., Kardos J. L.: Moduli of crystalline polymers employing composite theory. *Journal of Applied Physics*, **43**, 2235–2241 (1972). DOI: [10.1063/1.1661482](https://doi.org/10.1063/1.1661482)
- [22] McCullough R. L., Wu C. T., Seferis J. C., Lindemeyer P. H.: Predictions of limiting mechanical performance for anisotropic crystalline polymers. *Polymer Engineering and Science*, **16**, 371–387 (1976). DOI: [10.1002/pen.760160517](https://doi.org/10.1002/pen.760160517)
- [23] Boyd R. H.: Prediction of polymer crystal structures and properties. *Atomistic Modeling of Physical Properties*, **116**, 1–25 (1994). DOI: [10.1007/BFb0080195](https://doi.org/10.1007/BFb0080195)
- [24] Boyd R. H.: The mechanical moduli of lamellar semicrystalline polymers. *Journal of Polymer Science: Polymer Physics Edition*, **21**, 493–504 (1983). DOI: [10.1002/pol.1983.180210401](https://doi.org/10.1002/pol.1983.180210401)
- [25] Crist B., Fisher C. J., Howard P. R.: Mechanical properties of model polyethylenes: Tensile elastic modulus and yield stress. *Macromolecules*, **22**, 1709–1718 (1989). DOI: [10.1021/ma00194a035](https://doi.org/10.1021/ma00194a035)
- [26] Doyle M. J.: On the effect of crystallinity on the elastic properties of semicrystalline polyethylene. *Polymer Engineering and Science*, **40**, 330–335 (2000). DOI: [10.1002/pen.11166](https://doi.org/10.1002/pen.11166)
- [27] Fatahi S., Ajji A., Lafleur P. G.: Correlation between different microstructural parameters and tensile modulus of various polyethylene blown films. *Polymer Engineering and Science*, **47**, 1430–1440 (2007). DOI: [10.1002/pen.20836](https://doi.org/10.1002/pen.20836)
- [28] Monasse B., Haudin J. M.: Growth transition and morphology change in polypropylene. *Colloid and Polymer Science*, **263**, 822–831 (1985). DOI: [10.1007/BF01412960](https://doi.org/10.1007/BF01412960)
- [29] Varga J., Menczel J., Solti A.: The melting of high-pressure polyethylene subjected to stepwise heat treatment. *Journal of Thermal Analysis*, **17**, 333–342 (1979). DOI: [10.1007/BF01914024](https://doi.org/10.1007/BF01914024)
- [30] Varga J., Menczel J., Solti A.: Memory effect of low-density polyethylene crystallized in a stepwise manner. *Journal of Thermal Analysis*, **10**, 433–440 (1976). DOI: [10.1007/BF01909895](https://doi.org/10.1007/BF01909895)
- [31] Garoff T., Virkkunen V., Jääskeläinen P., Vestberg T.: A qualitative model for polymerisation of propylene with a MgCl₂-supported TiCl₄ Ziegler–Natta catalyst. *European Polymer Journal*, **39**, 1679–1685 (2003). DOI: [10.1016/S0014-3057\(03\)00069-7](https://doi.org/10.1016/S0014-3057(03)00069-7)
- [32] Horváth Zs., Menyhárd A., Doshev P., Gahleitner M., Varga J., Tranninger C., Pukánszky B.: Chain regularity of isotactic polypropylene determined by different thermal fractionation methods. *Journal of Thermal Analysis and Calorimetry*, **118**, 235–245 (2014). DOI: [10.1007/s10973-014-3999-5](https://doi.org/10.1007/s10973-014-3999-5)
- [33] Bai F., Li F., Calhoun B. H., Quirk R. P., Cheng S. Z. D.: Physical constants of poly(propylene). in ‘Polymer handbook’ (eds.: Brandrup J., Immergut E. H., Grulke E. A.) Wiley, New Jersey, Vol 1, V/21–30 (1999).
- [34] Clark E. J., Hoffman J. D.: Regime III crystallization in polypropylene. *Macromolecules*, **17**, 878–885 (1984). DOI: [10.1021/ma00134a058](https://doi.org/10.1021/ma00134a058)
- [35] Boger A., Heise B., Troll C., Marti O., Rieger B.: Mechanical and temperature dependant properties, structure and phase transitions of elastic polypropylenes. *European Polymer Journal*, **43**, 634–643 (2007). DOI: [10.1016/j.eurpolymj.2006.11.003](https://doi.org/10.1016/j.eurpolymj.2006.11.003)
- [36] Sundell T., Fagerholm H., Crozier H.: Isotacticity determination of polypropylene using *FT*-Raman spectroscopy. *Polymer*, **37**, 3227–3231 (1996). DOI: [10.1016/0032-3861\(96\)88466-7](https://doi.org/10.1016/0032-3861(96)88466-7)
- [37] Romankiewicz A., Sterzynski T.: The lamellar distribution in isotactic polypropylene modified by nucleation and processing. *Macromolecular Symposia*, **180**, 241–256 (2002). DOI: [10.1002/1521-3900\(200203\)180:1<241::AID-MASY241>3.0.CO;2-9](https://doi.org/10.1002/1521-3900(200203)180:1<241::AID-MASY241>3.0.CO;2-9)
- [38] Horváth Zs., Menyhárd A., Doshev P., Gahleitner M., Tranninger C., Kheirandish S., Varga J., Pukánszky B.: Effect of molecular architecture on the crystalline structure and stiffness of iPP homopolymers: Modeling based on annealing experiments. *Journal of Applied Polymer Science*, **130**, 3365–3373 (2013). DOI: [10.1002/app.39585](https://doi.org/10.1002/app.39585)
- [39] Mouzakis D. E., Gahleitner M., Karger-Kocsis J.: Toughness assessment of elastomeric polypropylene (ELPP) by the essential work of the fracture method. *Journal of Applied Polymer Science*, **70**, 873–881 (1998). DOI: [10.1002/\(sici\)1097-4628\(19981031\)70:5<873::aid-app6>3.0.co;2-q](https://doi.org/10.1002/(sici)1097-4628(19981031)70:5<873::aid-app6>3.0.co;2-q)
- [40] van Krevelen D. V., Nijenhuis K. T.: Properties of polymers. Elsevier, Amsterdam (2009).
- [41] Kunugi T.: High-modulus and high-strength polypropylene fibres and films. in ‘Polypropylene A-Z reference’ (ed.: Karger-Kocsis J.) Kluwer, Dordrecht, 295–300 (1999).
- [42] Sawatari C., Matsuo M.: Elastic modulus of isotactic polypropylene in the crystal chain direction as measured by X-ray diffraction. *Macromolecules*, **19**, 2653–2656 (1986). DOI: [10.1021/ma00164a036](https://doi.org/10.1021/ma00164a036)

Failure of compression molded all-polyolefin composites studied by acoustic emission

I. Z. Halász¹, G. Romhány¹, Á. Kmetty^{1,2}, T. Bárány^{1*}, T. Czigány^{1,2}

¹Department of Polymer Engineering, Faculty of Mechanical Engineering, Budapest University of Technology and Economics, Műegyetem rkp. 3., H-1111 Budapest, Hungary

²MTA–BME Research Group for Composite Science and Technology, Műegyetem rkp. 3., H-1111 Budapest, Hungary

Received 12 October 2014; accepted in revised form 24 December 2014

Abstract. This paper is aimed at studying the failure behavior of polyolefin-based self-reinforced polymer composites (SRPCs) via acoustic emission (AE). Three matrix materials (ethylene octene copolymer (EOC), polypropylene-based thermoplastic elastomer (ePP), random polypropylene copolymer (rPP), and three kinds of reinforcing structures of PP homopolymer (unidirectional (UD), cross-ply (CP) and woven fabric (WF)) were used. SRPCs were produced by compression molding using the film-stacking method. The composites were characterized by mechanical tests combined with in situ assessment of the burst-type AE events. The results showed that rPP matrix and UD reinforcement produced the greatest reinforcement, with a tensile strength more than six times as high as that of the matrix and a Young's modulus nearly doubled compared to the neat matrix. The number of the detected AE events increased with increasing Young's modulus of the applied matrices being associated with reduced sound damping. The AE amplitude distributions shows that failure of the SRPC structure produces AE signals in a broad amplitude range, but the highest detected amplitude range can be clearly linked to fiber fractures.

Keywords: polymer composites, all-polymer composite, compression molding, film-stacking method, acoustic emission

1. Introduction

Nowadays self-reinforced polymer composites (SRPCs) [1] are being developed dynamically. SRPCs can be produced by compaction [2], coextrusion [3], film-stacking [4, 5] or a combination of these methods [6]. The goal in each case is the production of a thermoplastic polymer composite that has excellent mechanical properties and can be recycled easily and cost effectively. In order to widely use these composites, however, it is necessary to investigate them with special regard of failure. An excellent method to characterize the failure is a tensile test combined with an acoustic emission (AE) test. When a material undergoes irreversible changes, for example crack formation, fracture of the matrix, delamination, or fiber fracture, then the release of

the stored energy produces a transient elastic wave on the surface which can be recorded and analyzed by AE. Considering some characteristics (amplitude, number) of these burst-type AE events and observing simultaneously the actual failure by suitable visual techniques the failure mechanisms and sequences in the composite can be identified.

Many researchers already used the AE to examine the failure of SRPCs. Zhuang and Yan [7] verified the viability of this method for an ultra-high molecular weight polyethylene (UHMWPE)/high density polyethylene (HDPE) based self-reinforced composite. They produced self-reinforced composites with 50% nominal UHMWPE fiber content and with different fiber alignments. According to their AE results fiber-matrix debonding caused AE sig-

*Corresponding author, e-mail: barany@eik.bme.hu

nals with amplitudes in the range of 30–45 dB. For matrix deformation and fracture an AE amplitude range of 30–60 dB, for fiber pullout 60–80 dB, while for fiber fracture and delaminations 60–85 dB were given. Scanning electron microscopic (SEM) images were used to corroborate the results. Cabrera *et al.* [8] successfully used AE method to record damage initiation events under static tensile measurements of coextruded self-reinforced PP composites. Romhány *et al.* [9] investigated the fracture toughness and compaction quality of PP-based self-reinforced composites (Curv[®]) with AE. In their tests single edge notched tensile loaded (SEN-T type) specimens were used. AE signals were collected with one and four microphones. It was shown that the damage development can well be assessed based on the localized AE events. The course of the AE hits as a function of loading of the specimens indicated well the consolidation quality. The relationship between consolidation quality and course of the AE events during loading was verified by Izer *et al.* [10]. In their tests 50 wt% α -PP fabric was used as reinforcement and self-reinforced composite specimens were manufactured from three (β -PP, random PP, and β -phase random PP) matrices by film-stacking at various pressing temperatures. The failure of each specimen was investigated in tensile test combined with AE recording. It was found that the number of AE events depends on the interfacial adhesion between reinforcement and matrix in the composite. With improving consolidation the number of AE events decreased markedly. In poorly consolidated composites the number of AE events reached several thousands by contrast to a well consolidated one with several tens. Low amplitude (40–50 dB) AE signals were assigned to sliding of tapes within the corresponding fabric or to delaminations, while signals' amplitudes above 65 dB were traced to fiber/tape fracture.

The goal of this study was to characterize the fracture behavior of polyolefin-based self-reinforced

composites by acoustic emission. The SRPCs are made by compression molding from different matrices with different Young's moduli, reinforced with various reinforcing structures composed of PP homopolymer (hPP). It was expected that the matrix characteristics, changing from 'soft' rubber to 'hard' thermoplastic, affect the AE characteristics.

2. Materials and processing

As matrix material three kinds of materials were used, which are listed in Table 1.

The basic composition of the ePP was the same as that of rPP according to Fourier-transform infrared (FTIR) analysis. Accordingly, rPP and ePP matrix materials belong to the same polymer family. From the matrix granulates a 50 μ m thick film was prepared by cast film extrusion.

As reinforcement woven polypropylene fabric from highly oriented split polypropylene homopolymer tapes (180 g/m², $T_m = 172.4^\circ\text{C}$ (determined by differential scanning calorimetry (DSC)), tensile strength 465 \pm 32 MPa (measured on a single tape)) Zwick Z050 tensile machine)) and a highly oriented polypropylene homopolymer (hPP) multifilament (linear density: 3300 dtex, $T_m = 172.1^\circ\text{C}$ (determined by DSC), number of single fibers: 400, tensile strength 581 \pm 30 MPa, (Stradom S.A., Czestochowa, Poland)) were applied. Three kinds of reinforcement structures were used: unidirectional reinforcement (UD), the cross-ply (CP) (0–90 $^\circ$) arrangement and the woven fabric (WF). The reinforcing hPP multifilaments were filament wound onto an aluminum core and matrix films were inserted in between the wound layers, as already published in the literature [6]. The woven fabric layers were inserted between the matrix films. The related 'package' was consolidated by compression molding (Schwabentan Polystat 300S). The production parameters are listed in Table 2. During preheating the 'package' to be consolidated was in the press without pressure.

Table 1. Matrix materials and their abbreviations

Matrix material	Abbreviation	T_m^* [$^\circ\text{C}$]	MFI [g/10 min]	Brand name	Producer
Ethylene-octene copolymer	EOC	100.3	30**	Engage 8402	Dow Chemical Company
Polypropylene based thermoplastic elastomer	ePP	84.2	25***	Versify 4200	Dow Chemical Company
Random PP copolymer	rPP	148.4	45***	Tipplen R959A	TVK Tiszaújváros, Hungary

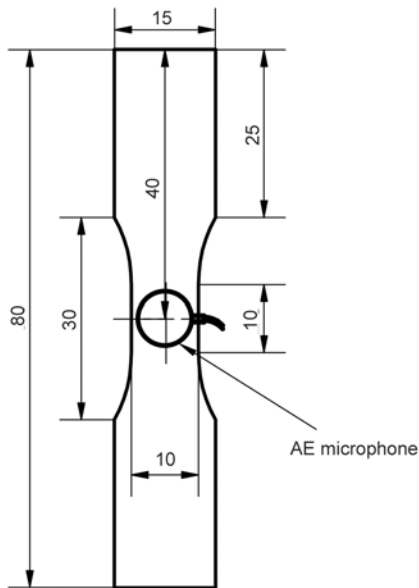
*determined by DSC from the first melting curve, 10 $^\circ\text{C}/\text{min}$

**190 $^\circ\text{C}$ with 2.16 kg

***230 $^\circ\text{C}$ with 2.16 kg

Table 2. Production parameters of SRPCs

Matrix	Reinforcing structure	Pressing temperature [°C]	Preheat time [min]	Pressing time [min]	Compression pressure [MPa]
EOC	UD	140	4	6	5.3
	CP		4	6	
	WF		1.5	4	
ePP	UD		4	8	
	CP		4	8	
	WF		1.5	4	
rPP	UD	180	4	4	
	CP		4	4	
	WF		1.5	4	

**Figure 1.** Measurement layout and the main dimensions of the specimen (dimensions in mm)

The thickness of the resulting composite plates was between 0.9...2.6 mm. Nominal fiber content was set to 75 wt%. From the composite plates the specimens (as shown in Figure 1) were cut with the help of a water-jet cutter.

3. Testing methods

The tensile tests were carried out on a Zwick Z020 (Zwick GmbH, Ulm, Germany) universal testing machine at a testing speed of 5 mm/min and a clamping length of 30 mm. Five parallel tests were run on each SRPC and the tensile strength (determined at maximal force), tensile modulus and strain at break were determined. AE measurements were carried out with a Sensophone AED-40 (Sensophone Kft, Hungary) apparatus and wideband (100–600 kHz) Micro30D (Physical Acoustics Corporation, USA) microphone and a logarithmic amplifier. The reference level for the amplitude of the signals was 1 μ V. The cumulated number of events and the amplitude

distribution of the measured values were evaluated to map the relationship between the failure of the materials and the emitted acoustic signals.

4. Results and discussion

Table 3 contains the results of the tensile tests. As expected, a considerable increase was observed in the Young's modulus and tensile strength due to the reinforcements. This strengthening effect was most pronounced for the UD reinforcing structure. The tensile strength and Young's modulus of the SRPCs reinforced with woven fabric and CP structure did not differ significantly as a function of the testing direction (i.e. warp, weft). There was, however, a large difference between the Young's moduli and tensile strength values of the composites with identical reinforcement structure: these values increased with increasing Young's moduli of the matrix materials. For all matrices the strain at break was the highest for the fabric (WF) reinforced composites. This was expected considering the fact that in the UD and CP structuring the fibers are straight, while they are wavy in the fabric and straighten in some extent only during loading.

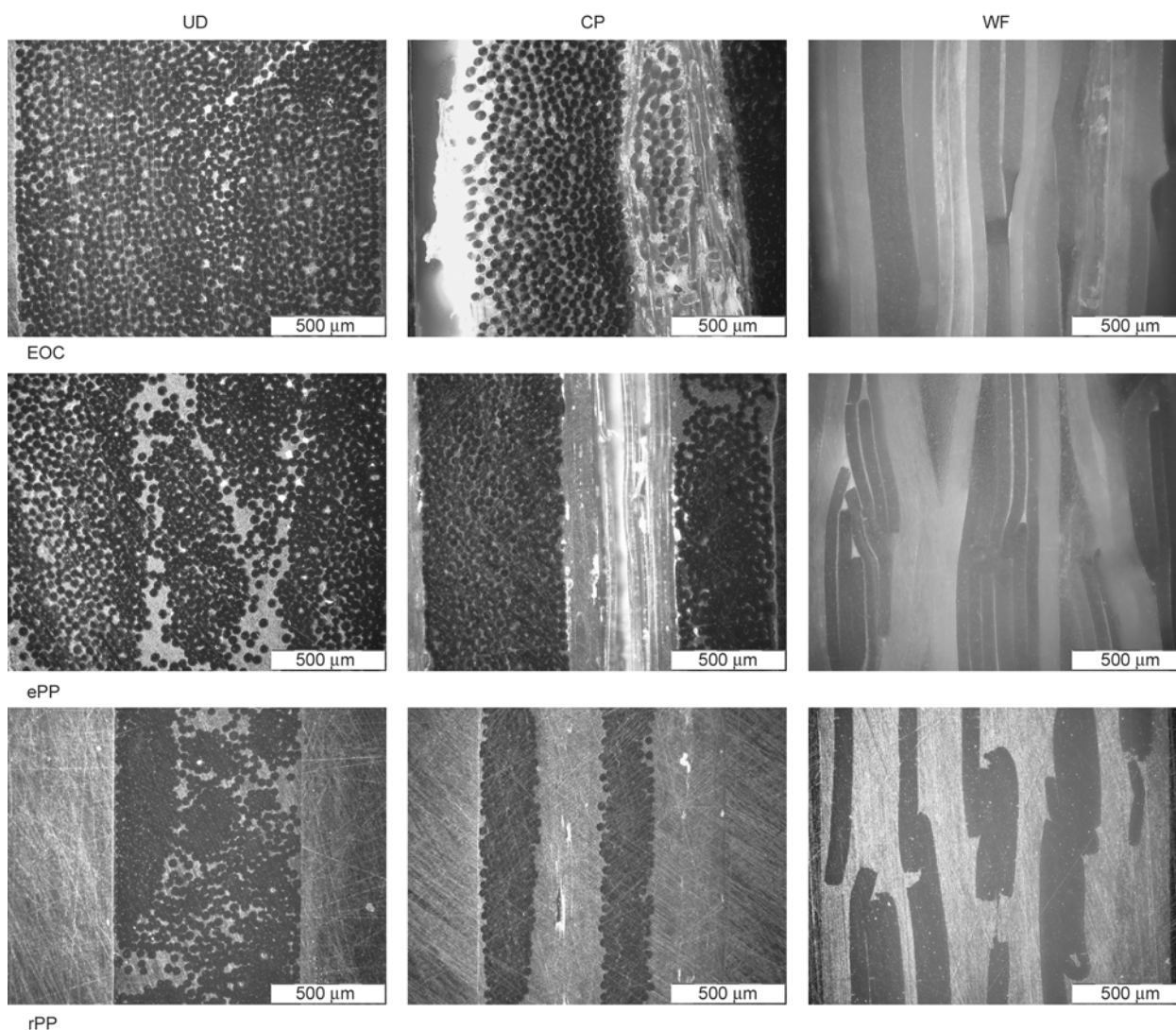
When the polished cross sections of the composites are examined (Figure 2), it can be seen that the distribution of the reinforcement fibers was better in the case of the EOC matrix (note that EOC had better flowability) than in the case of the ePP matrix. With CP reinforcement the original fiber directions became less distorted, while with UD it can also be seen that the fibers are more evenly distributed along the cross-section. Pressing at higher temperatures also led to a decrease in the thickness of the manufactured plates for the rPP matrix compared to the other two matrices (EOC: 2.0–2.5 mm, ePP: 2.1–2.6 mm rPP: 0.9–1.7 mm).

When evaluating the AE test results, first the amplitude distribution of the events was analyzed to find

Table 3. Mechanical properties of the composites

	Tensile strength [MPa]		Tensile modulus [MPa]		Strain at break [%]	
	Warp	Weft	Warp	Weft	Warp	Weft
	EOC					
Matrix	11.3*		72.6*			
UD	163.0±24.6		958.9±112		14.2±2.7	
CP	101.9±20.9	104.1±11.6	363.8±66.7	598.4±148.1	16.7±2.6	18.7±4.7
WF	131.8±5.1	110.6±5.6	613.2±56.5	483.0±110.0	34.1±1.3	27.0±0.9
	ePP					
Matrix	22.7*		112*			
UD	173.6±28.3		1573.6±234.8		17.0±2.6	
CP	126.3±6.7	154.6±14.5	925.9±317.1	797.9±144.1	26.8±2.0	30.0±2.5
WF	136.0±4.3	130.4±3.5	763.8±55.0	757.4±88.8	31.8±1.5	34.8±2.0
	rPP					
Matrix	30*		1250*			
UD	218.2±28		2419.1±438.5		25.9±2.8	
CP	154.1±11.3	161.1±2.6	1684.3±364.8	1467.2±290.8	21.5±1.4	21.8±1.3
WF	117.8±5.5	118.0±8.3	1467.3±169.4	1304.2±292.2	27.9±3.3	30.1±1.6

*The values for the matrix are values provided by the manufacturer

**Figure 2.** Polished cross-section images of the composites

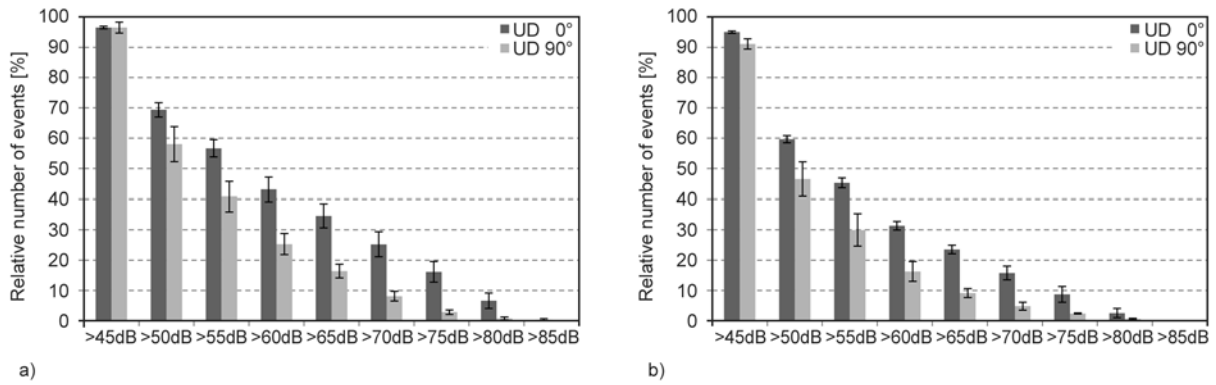


Figure 3. Relative number of events in the case of rPP (a) and ePP (b) matrix composites

a relationship between the amplitudes of the detected signals and the events of the various failures generating these signals. To assign AE signals specifically associated with fiber fracture, tests were run on UD reinforced SRPCs in both parallel and perpendicular directions to the loading and the collected AE signals were compared. Since fiber fracture does not occur when fibers are exposed to perpendicular load, a comparison of the amplitude distributions of the AE signals in these two directions provides information for fiber fracture. In the case of loading perpendicular to the reinforcing fibers no signals were detected until the maximal force was reached.

Figure 3 shows the relative number of AE events in the tensile tests of rPP and ePP matrix-based UD composites, representing the percentage of the events with higher amplitude than a given amplitude threshold. It can be seen that as amplitude increases, the difference between the two directions becomes larger. This points to the fact that signals associated with fiber fracture are detectable at higher intensity than signals associated with other failure modes (namely debonding). This is only true for AE events occurring in the immediate vicinity of the microphone because the amplitude values of long-range fiber fractures get lower due to the dampening effect of the material. Figure 3 shows that signals above 75 dB amplitude almost exclusively appear when the reinforcing hPP fibers are parallel to the loading direction. Therefore, if such signals are detected during AE test in an SRPC of unknown structure, one can surmise that the alignment of the reinforcing phase is parallel to the loading. The same tendency was observed in the case of SRPCs with EOC matrix. In this SRPC the detected signals were shifted to lower amplitudes due to the more effective dampening of this ‘rubbery’ EOC matrix.

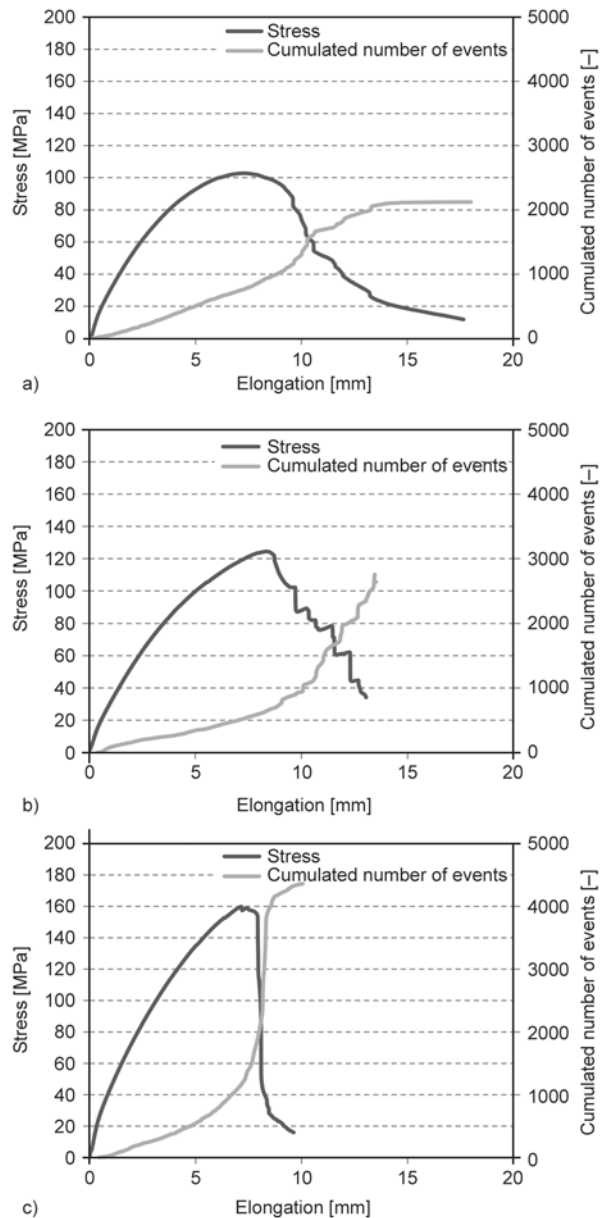


Figure 4. Tensile diagram and cumulated number of events of EOC (a), ePP (b) and rPP (c) CP SRPC

Figure 4 shows the course of the cumulated AE events as a function of tensile loading in CP-rein-

forced SRPCs. The shape of the cumulative events as a function of elongation is conform with the finding in the literature [10], namely, as the temperature of pressing increases (EOC and ePP versus rPP matrix), the course of the corresponding curves changes from gradual to a steep stepwise rise. The latter indicates that the majority of the AE events occurred close to final failure.

The amplitude distributions in Figure 5 show that after the maximal force (F_{max}) is reached the proportion of high amplitude events drastically increases. Before F_{max} the fibers of the reinforcement structure only changed position and stretched, coupled with fiber-matrix debonding. This does not influence the tensile strength because the force continuously

increases further on (cf. Figure 4). By contrast, above F_{max} the fibers started to break until the SRPC lost its load bearing capacity completely. In case of fabric reinforcement far more low-amplitude signals (45 dB) were detected for all the three matrices than for the other hPP reinforcing structures. These can be attributed to the tapes in the fabric which separate themselves from the matrix and start to slip within the composite [10]. This trend, but with different extent, was observed for all matrix materials and reinforcement structures.

Figure 6 shows the failure modes of SRPCs. As the processing temperature (EOC, ePP versus rPP), and fiber-matrix adhesion increased (EOC versus ePP, rPP) the characteristic failure mode of specimens

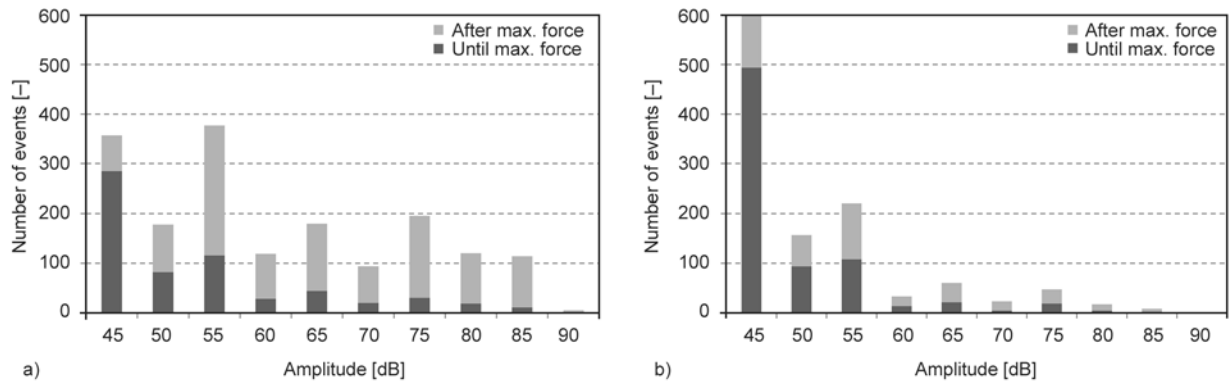


Figure 5. Amplitude distributions before and after maximal force in the case of an rPP matrix with CP (a), and fabric (b) reinforcement

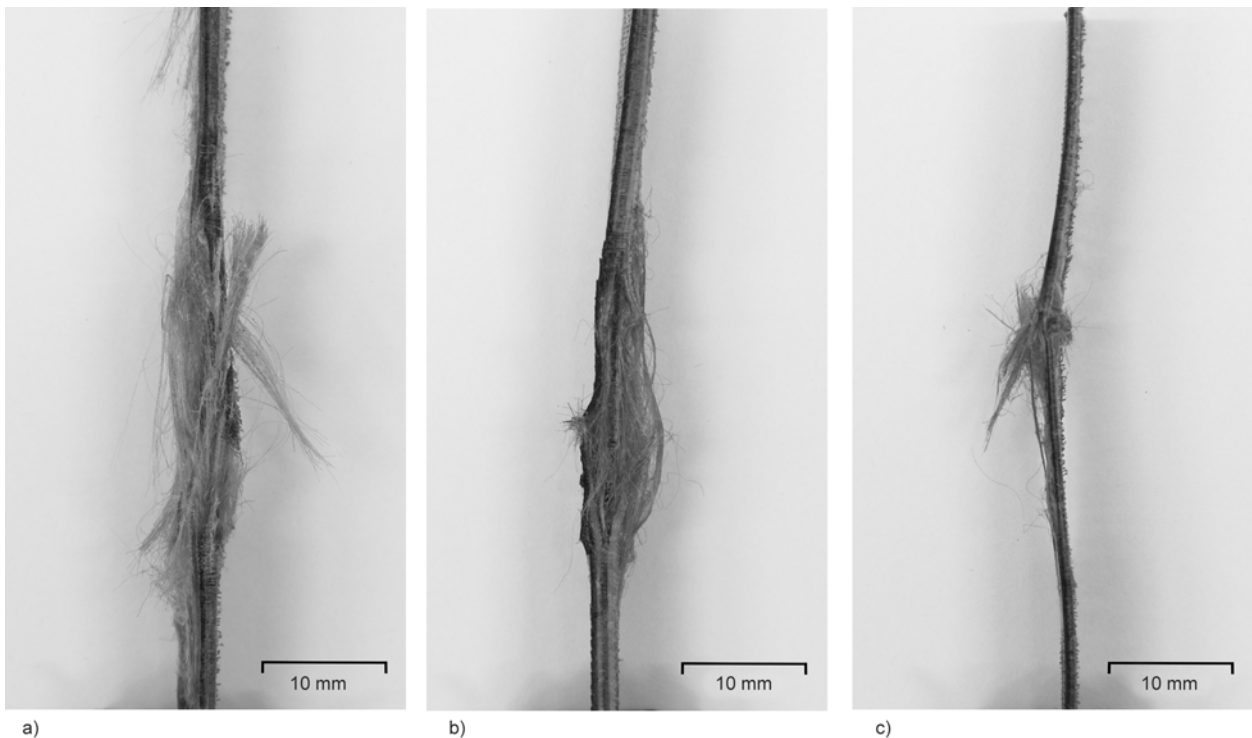


Figure 6. Failure modes in the case of composites of EOC (a), ePP (b) and rPP (c) matrix and CP reinforcement

shifted from fiber-matrix separation and layer delamination to fiber fracture. The fiber-matrix adhesion in the SRPC with EOC matrix was not as strong as in the other two cases because this is an ethyleneoctane copolymer and not PP as in the other SRPC combinations.

Figure 7 shows the number of events before reaching F_{\max} and during the whole tensile test for various matrix materials and reinforcement structures. It can be seen that in the case of CP and UD reinforcements the detected number of events is higher when the Young's modulus of the matrix is higher. This can be attributed to the fact that a higher Young's modulus results in decreased acoustic damping, and thus signals generated further away from the microphone can also be detected [11]. In the case of fabric-reinforced composites the SRPC with rPP matrix behaves differently. The images of the polished cross-sections also suggest some differences of the fabric-reinforced composites in their acoustic activity. It can be seen that some tapes of the fabric may be melted in the rPP matrix-based composite, which was processed at higher temperature than those with the two other matrices. Moreover, in this

WF-reinforced rPP the tapes were not pre-tensioned (as opposed to SRPCs reinforced by the UD and CP systems), thus the relaxation of the tapes was more prominent during the manufacturing of the composite. The lower number of AE events for the EOC-based SRPCs can be attributed to the followings: i) this matrix is not PP-based, therefore its adhesion to the hPP fibers and tapes within the fabric is not as strong as in the case of the other two matrix materials, and ii) EOC, being practically a rubber, has the highest acoustic damping among the matrices used. It can also be observed that in the case of a CP structure there is considerable difference between the two loading directions, which can be explained by the asymmetry of the cross-section. The order of layers was not symmetrical to the median, in one case the layer on the side of the microphone was parallel to the direction of the load, while in the other case it was perpendicular to it. Since in fiber direction the damping of the individual layers is much lower than perpendicular to it, during the measurements in weft direction far more events were recorded because the external layer on the side of the microphone was parallel to the load.

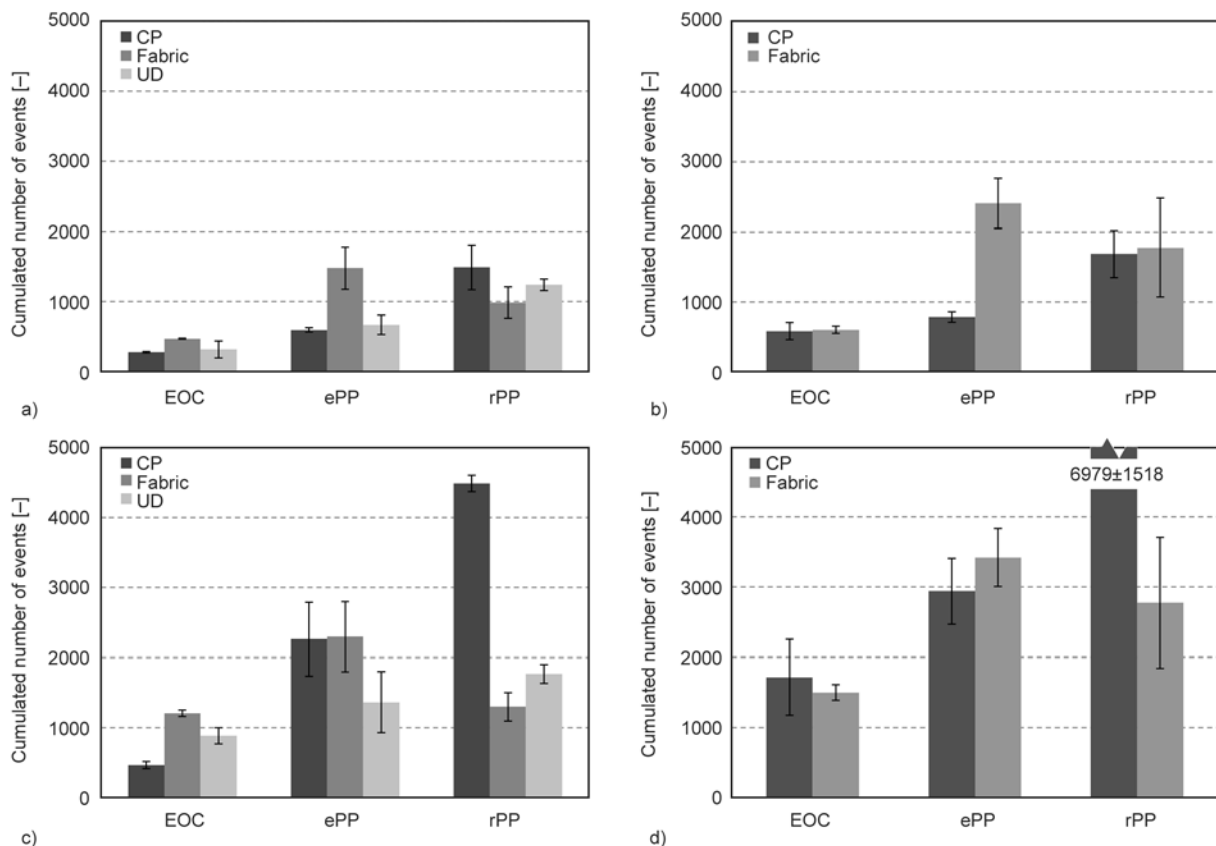


Figure 7. Cumulated number of events in the case of different matrix materials in warp (a and c) and weft (b and d) direction until reaching the maximum force (a and b) and total (c and d)

5. Conclusions

In this study polyolefin-based SRPCs were characterized in tensile tests during which the emitted acoustic signals were monitored. The mechanical properties of the composites significantly increased with all three kinds of reinforcement structures compared to those of the corresponding matrices. According to the results, rPP matrix and UD reinforcement produced the highest improvement in both tensile strength and Young's modulus. Tensile strength of this composite was more than six times higher than the matrix and the latter was nearly doubled. It was found that an increase in the Young's modulus of the matrix material is accompanied with an increase in the number of detected AE signals. This was attributed to the fact that a higher Young's modulus means lower acoustic damping, thus signals further away from the microphone can also be detected. It was shown that in the used test setup AE signals above 75 dB amplitudes can be unequivocally assigned to fiber fracture. Therefore it can be stated, that the real-time monitoring of the burst-type AE signals during loading is a useful tool to check the integrity of SRPC structures, to conclude failure initiation and failure sequence. AE signals in the highest amplitude range (specific amplitude values depend on the structure and experimental setup) can be assigned to the final fracture of the reinforcement aligned to the loading direction (usually fibers or tapes, also in woven architectures). It was also shown that an improvement in the fiber-matrix adhesion results in an increase in both the number and amplitude of acoustic events. Finally, the number of the emitted AE hits and their characteristics strongly depend on the matrix properties. A 'soft' rubbery matrix yields less signals and lower amplitude events than a 'hard' thermoplastic ones due to the difference in their acoustic damping.

Acknowledgements

This work was supported by OTKA Hungarian Scientific Research Fund by grants (K105257) in Hungary. This work is connected to the scientific program of the 'Development of quality-oriented and harmonized R+D+I strategy and functional model at BME' project. This project is supported by the New Széchenyi Plan (Project ID:TÁMOP-4.2.1/B-09/1/KMR-2010-0002).

References

- [1] Kmetty Á., Bárány T., Karger-Kocsis J.: Self-reinforced polymeric materials: A review. *Progress in Polymer Science*, **35**, 1288–1310 (2010).
DOI: [10.1016/j.progpolymsci.2010.07.002](https://doi.org/10.1016/j.progpolymsci.2010.07.002)
- [2] Hine P. J., Unwin A. P., Ward I. M.: The use of an interleaved film for optimising the properties of hot compacted polyethylene single polymer composites. *Polymer*, **52**, 2891–2898 (2011).
DOI: [10.1016/j.polymer.2011.04.026](https://doi.org/10.1016/j.polymer.2011.04.026)
- [3] Alcock B., Cabrera N. O., Barkoula N-M., Loos J., Peijs T.: Interfacial properties of highly oriented coextruded polypropylene tapes for the creation of recyclable all-polypropylene composites. *Journal of Applied Polymer Science*, **104**, 118–129 (2007).
DOI: [10.1002/app.24588](https://doi.org/10.1002/app.24588)
- [4] Chen J. C., Wu C. M., Pu F. C., Chiu C. H.: Fabrication and mechanical properties of self-reinforced poly(ethylene terephthalate) composites. *Express Polymer Letters*, **5**, 228–237 (2011).
DOI: [10.3144/expresspolymlett.2011.22](https://doi.org/10.3144/expresspolymlett.2011.22)
- [5] Bárány T., Izer A., Czigány T.: High performance self-reinforced polypropylene composites. *Materials Science Forum*, **567–538**, 121–128 (2007).
DOI: [10.4028/www.scientific.net/MSF.537-538.121](https://doi.org/10.4028/www.scientific.net/MSF.537-538.121)
- [6] Kmetty Á., Tábi T., Kovács J. G., Bárány T.: Development and characterisation of injection moulded, all-polypropylene composites. *Express Polymer Letters*, **7**, 134–145 (2013).
DOI: [10.3144/expresspolymlett.2013.13](https://doi.org/10.3144/expresspolymlett.2013.13)
- [7] Zhuang X., Yan X.: Investigation of damage mechanisms in self-reinforced polyethylene composites by acoustic emission. *Composites Science and Technology*, **66**, 444–449 (2006).
DOI: [10.1016/j.compscitech.2005.07.013](https://doi.org/10.1016/j.compscitech.2005.07.013)
- [8] Cabrera N. O., Alcock B., Klompen E. T. J., Peijs T.: Filament winding of co-extruded polypropylene tapes for fully recyclable all-polypropylene composite products. *Applied Composite Materials*, **15**, 27–45 (2008).
DOI: [10.1007/s10443-008-9055-5](https://doi.org/10.1007/s10443-008-9055-5)
- [9] Romhány G., Bárány T., Czigány T., Karger-Kocsis J.: Fracture and failure behavior of fabric-reinforced all-poly(propylene) composite (Curv®). *Polymers for Advanced Technologies*, **18**, 90–96 (2007).
DOI: [10.1002/pat.806](https://doi.org/10.1002/pat.806)
- [10] Izer A., Stocchi A., Bárány T., Pettarin V., Bernal C., Czigány T.: Effect of the consolidation degree on the fracture and failure behavior of self-reinforced polypropylene composites as assessed by acoustic emission. *Polymer Engineering and Science*, **50**, 2106–2113 (2010).
DOI: [10.1002/pen.21741](https://doi.org/10.1002/pen.21741)
- [11] Kim K. S., Lee K. I., Kim H. Y., Yoon S. W., Hong S. H.: Dependence of particle volume fraction on sound velocity and attenuation of EPDM composites. *Ultrasonics*, **46**, 177–183 (2007).
DOI: [10.1016/j.ultras.2007.01.010](https://doi.org/10.1016/j.ultras.2007.01.010)